UNIVERSITÉ DE STRASBOURG

École Doctorale de Physique et Chimie-Physique (ED 182)

Institut de Physique et Chimie des Matériaux de Strasbourg

(UMR 7504 CNRS-Unistra)

THÈSE

présentée par :

Yanhui WANG

soutenue le : **19 octobre 2016**

pour obtenir le grade de :

Docteur de l'université de Strasbourg

Spécialité : Chimie-Physique des Matériaux

Hybridation d'oxydes lamellaires: de l'insertion à la synthèse *in situ*

THÈSE dirigée par :

M. Guillaume Rogez	Dr., Université de Strasbourg
M. Pierre Rabu	Dr., Université de Strasbourg

RAPPORTEURS :

Mme Vanessa Prévot	Dr., Université de Clermont-Ferrand
M. Antoine Maignan	Dr., Université de Caen

AUTRES MEMBRES DU JURY :

Mme Anne Bleuzen	Pr., Université Paris XI
M. Clément Sanchez	Pr., Collège de France
M. Ovidiu Ersen	Pr., Université de Strasbourg

Remerciements

J’exprime mes profonds remerciements à mes directeurs de thèse M. Guillaume Rogez et M. Pierre Rabu. En chimie, je suis très reconnaissant pour leurs précieuses discussions, conseils utiles et l'encouragement continu. Dans la vie quotidienne, cet étranger (Chinois) est infiniment reconnaissant pour leur aide. Sous leur direction, je me sens très chanceux et fier.

A Emilie Delahaye, je voudrais exprimer ma gratitude. Elle est enthousiaste, patiente, bavarde et serviable. Je ne vais pas oublier son aide, ses conseils et ses encouragements.

J’exprime mes sincères remerciements à membres du jury qui ont aimablement accepté d’évaluer cette thèse. Leur présence me fait sentir honoré. Merci pour leurs suggestions, idées, commentaires et questions soulevées. Cela me permet d’avoir une compréhension plus profonde du sujet.

J’exprime mes profonds remerciements à mes encadrant de stage M2 au LCOS. M. Michel Miesch et M. Philippe Geoffroy. Je suis infiniment reconnaissant pour leur aide (ils m'ont recommandé comme candidat au doctorat), leurs conseils, instructions et encouragements.

Je tiens également à remercier sincèrement nos collaborateurs.

Je voudrais tout d'abord remercier M. Fabrice Leroux (Institut de Chimie de Clermont-Ferrand) pour beaucoup de manipulations sur RMN du solide, ce qui nous donne beaucoup de preuves utiles et même critiques.

Je voudrais aussi remercier M. Ovidiu Ersen et M. Dris Ihiawakrim (IPCMS) pour l’étudie microscopie électronique (MET, STEM). Leur patience et dévouement m'ont impressionné.

Je tiens également à remercier M. Philippe Turek et son équipe au laboratoire POMAM : Nathalie Parizel, Maxime Bernard pour l’aide des mesures en RPE. De plus, les explications apportées de RPE par Nathalie sont particulièrement important pour moi, qui n’ai jamais eu de contact avec cette technologie.

A Christine Taviot-Guého (Institut de Chimie de Clermont-Ferrand), je voudrais exprimer ma gratitude. Des profils de densité électronique 1D nous permettent de préciser les arrangements intracouche.

Ensuite, je tiens à remercier Grégory Taupier et Honorat Dorkenoo (IPCMS) pour des mesures ONL, ce qui nous donne une preuve nécessaire d’évaluer notre produit départ.

De plus, je n’oublie pas de remercier Cédric Leuvrey et Didier Burger pour les mesures MEB et ATG/ATD, respectivement, ce qui nous donne beaucoup de résultats utiles.

Je dois aussi remercier M. Marc Lenertz pour les affinements de diagrammes de diffraction et des discussions utiles.

Pour mademoiselle Capucine Loth (stagiaire), merci pour des manipulations expérimentales et des introductions chaleureuse de la culture française.

En outre, je tiens également à remercier les membres de notre groupe : Pierre Farger, Quentin Evrard et Oksana Toma pour leur aide et les discussions. Travailler avec eux pendant ce temps sera mes bons souvenirs.

Je n'oublie pas les autres membres du DCMI, je cite : Christophe Lefevre, Nathalie Viart, Céline Kieffer, Sylvie MAINGE, Mathilde Ménard, Damien Mertz, Elodie Martin, Mathias Dolci…

En outre, je tiens également à remercier le CNRS et la Région Alsace, qui ont mis à ma disposition trois ans durant les moyens financiers nécessaires.

A la fin, j'exprime mes profonds remerciements à mon père Yongchang Wang, ma mère Xuemei Ma et ma copine Shupei Luo. Grâce à votre soutien silencieux, je peux sentir à l'aise pour travailler.

Yanhui WANG

25/10/2016

Layout

General introduction 1

GI.1. Soft chemistry route-hybrid approach, a way to multifunctional materials 3
GI.2. Tempting multifunctional materials: multiferroic compounds 4
GI.3. Layered perovskites: potential candidates 5
GI.4. Applications of soft chemistry for the functionalization of layered perovskites 5
GI.4.1. Perovskites 5
GI.4.1.1. Definition 5
GI.4.1.2. Layered perovskites 6
GI.4.2. Common soft chemistry approaches to functionalization 6
GI.4.2.1. Ion exchange reactions 7
GI.4.2.1.1.Acid treatment 7
GI.4.2.1.1.1. Protonated forms of Dion-Jacobson and Ruddlesden-Popper phases 7
GI.4.2.1.1.2. Protonated forms of Aurivillius phases 8
GI.4.2.1.1.3. Reverse conversion 10
GI.4.2.1.1.4. Topochemical dehydration of the protonated forms of layered perovskites 10
GI.4.2.1.2. Mono or divalent cation exchange reactions 11
GI.4.2.1.3. Introduction of cationic structures 12
GI.4.2.2. Intercalation reactions 13
GI.4.2.2.1. Intercalation behaviors 13
GI.4.2.2.2. Factors influencing intercalation behaviors 15
GI.4.2.2.3. Mechanisms of intercalation 15
GI.4.2.2.4. Drawback of the published intercalation methods 16
GI.4.2.3. Grafting reactions 16
GI.4.2.3.1. Grafting behaviors 16
GI.4.2.3.2. Alcohol-alcohol exchange 17
GI.4.2.3.3. Mechanisms of alcohol grafting and alcohol-exchange reactions 18
GI.4.2.3.4. Drawback of published grafting methods 19
GI.4.2.4. Exfoliation 19
GI.4.2.4.1. Exfoliation behaviors 19
GI.4.2.4.2. 2D building blocks 20
GI.4.2.4.3. Layer-by-Layer (LBL) assembly 21
GI.5. Objective of this thesis 22
References 23

I. Efficient microwave-assisted functionalization of the Aurivillius phase $Bi_2SrTa_2O_9$ 27

I.1. Introduction 29
I.2. Results and discussion 30
I.2.1. Microwave-assisted synthesis of HST 30
I.2.1.1. Synthesis and structure 30

I.2.1.2. Thermal analyses 31
I.2.2. Microwave-assisted functionalization of HST by aliphatic amines 34
I.2.2.1. General synthetic procedures and structural characterization 34
I.2.2.1.1. Synthesis 34
I.2.2.1.2. XRD analysis 35
I.2.2.1.3. Elemental analysis 37
I.2.2.1.4. Infrared spectroscopy 37
I.2.2.1.5. SEM observation 39
I.2.2.1.6. TEM observation 39
I.2.2.2. Optimization of the reaction conditions, influence of some parameters 40
I.2.2.2.1. Role of water 40
I.2.2.2.2. An efficient pre-intercalation strategy 41
I.2.3. Microwave-assisted functionalization of HST by more complicated amines 42
I.2.3.1. Direct insertion 43
I.2.3.1.1. Synthesis 43
I.2.3.1.2. XRD and elemental analyses 43
I.2.3.2. Indirect insertion 44
I.2.3.2.1. Synthesis 44
I.2.3.2.2. XRD and elemental analyses 44
I.2.3.2.3. Solid state NMR study of cyclohexane-1,2-diamine-HST 45
I.2.3.3. Comparing the reactivates between complicated diamines and their corresponding mono amines 46
I.2.3.4. Examples of failed insertion 47
I.2.4. Inserting phenyl butylamine (PBA) into HST 47
I.2.4.1. The three PBA-intercalated phases with different interlayer distances 47
I.2.4.1.1. Synthesis 47
I.2.4.1.2. XRD analyses 47
I.2.4.1.3. Infrared spectroscopy 48
I.2.4.1.4. Thermal analyses 50
I.2.4.1.5. Solid state NMR study 51
I.2.4.1.6. TEM observation 52
I.2.4.2. Study the effect of reaction conditions on the interlayer distance of PBA-HST intercalated products 53
I.2.4.2.1. Reaction temperature 53
I.2.4.2.2. Reaction time 53
I.2.4.2.3. Molar ratio of PBA/HST 54
I.2.4.3. Mutual conversion between PBA2-HST and PBA3-HST 55
I.3. Conclusion 56
References 57

II. Alcohol grafting *vs.* amine insertion 59
II.1. Introduction 61
II.2. Results and discussion 61

II.2.1. Attempts of direct interlayer surface modification of HST with EtOH 61
II.2.1.1. Synthesis 62
II.2.1.2. XRD analysis 62
II.2.1.3. Infrared spectroscopy 62
II.2.2. Indirect interlayer surface modification of HST with *n*-alcohols. 63
II.2.2.1. Grafting reactions between amine pre-intercalated-HST and *n*-alcohols ($C_nH_{2n+1}OH$, n = 1, 2, 3, 4, 7, 12). 63
II.2.2.1.1. General syntheses 63
II.2.2.1.2. NH_3-HST as starting material 64
II.2.2.1.2.1. XRD analysis 64
II.2.2.1.2.2. Infrared spectroscopy 64
II.2.2.1.3. C_2N-HST as a starting material 65
II.2.2.1.3.1. XRD analysis 65
II.2.2.1.3.2. Infrared spectroscopy 66
II.2.2.1.4. C_4N-HST as a starting material 67
II.2.2.1.4.1. XRD analysis 67
II.2.2.1.4.2. Infrared spectroscopy 69
II.2.2.1.4.3. SEM observation 71
II.2.2.1.4.4. Solid state NMR 71
II.2.2.1.4.5. Thermal analyses 72
II.2.2.1.4.6. Proposed formulae 74
II.2.2.1.5. Discussion on the role of the intermediates 75
II.2.2.2. Grafting reactions between C_2OH-HST and *n*-alcohols ($C_nH_{2n+1}OH$, n = 3, 4, 7, 12): alcohol exchange reaction 75
II.2.2.2.1. Syntheses 75
II.2.2.2.2. XRD analysis 75
II.2.2.2.3. Proposed mechanism 76
II.2.3. Functionalization of HST by grafting α, ω-alkanediols, using C_4N-HST as an intermediate 76
II.2.3.1. Syntheses 76
II.2.3.2. Comparison between $C_2(OH)_2$-HST and $C_4(OH)_2$-HST 77
II.2.3.2.1. XRD analysis 77
II.2.3.2.2. Infrared spectroscopy 77
II.2.3.2.3. Solid state NMR 78
II.2.3.2.4. Thermal analyses 79
II.2.3.3. Comparison between $C_4(OH)_2$-HST, $C_8(OH)_2$-HST and $C_{12}(OH)_2$-HST 80
II.2.3.3.1. XRD analysis 80
II.2.3.3.2. Infrared spectroscopy 82
II.2.3.4. Discussion 83
II.2.4. Functionalization of HST with bulky alcohols, using C_4N-HST as an intermediate 83
II.2.4.1. Syntheses 83
II.2.4.2. XRD analysis 83
II.2.4.3. Infrared spectroscopy 84
II.2.4.4. Thermal analyses 85
II.2.5. Study of the role of water during the reaction process 86

II.2.5.1. Syntheses 86
II.2.5.2. Using C_4N-HST as intermediate 86
II.2.5.2.1. XRD analysis 86
II.2.5.2.2. Discussion 87
II.2.5.3. Using C_2OH-HST as intermediate 87
II.2.5.3.1. XRD analysis 87
II.2.5.3.2. Discussion 88
II.2.6. Comparison of the reactivity of *n*-alkylamine and *n*-alcohol towards insertion/grafting into HST: role of water 88
II.2.6.1. Syntheses 88
II.2.6.2. XRD analysis 89
II.2.6.3. Infrared spectroscopy 89
II.2.6.4. Solid state NMR 90
II.2.7. Study the effect of water for the reactivity of 5-amino-1-pentanol 91
II.2.7.1. Using C_2N-HST or C_4N-HST as starting materials 91
II.2.7.1.1. XRD analysis 91
II.2.7.1.2. Infrared spectroscopy 92
II.2.7.2. Using C_2OH-HST as starting material 93
II.2.7.2.1. XRD analysis 93
II.2.7.2.2. Infrared spectroscopy 94
II.2.7.3. Using HST as starting material 95
II.2.7.3.1. XRD analysis 95
II.2.7.3.2. Infrared spectroscopy 96
II.2.7.4. Post treatment: from bilayer to pillaring arrangement 97
II.2.7.4.1. Synthesis 97
II.2.7.4.2. XRD analysis 97
II.2.7.4.3. Infrared spectroscopy 98
II.3. Conclusions 98
References 100

III. Post modification of layered perovskite phases via microwave-assisted Copper (I) catalyzed Alkyne Azide Cycloaddition (CuAAC) 103

III.1. Introduction 105
III.2. Results and discussion 107
III.2.1. Preparation of precursors based on HST 107
III.2.1.1. Preparation of alkyne-terminated precursor (alkyne-HST) 107
III.2.1.1.1. Synthesis 107
III.2.1.1.2. XRD analysis 107
III.2.1.1.3. Infrared spectroscopy 108
III.2.1.1.4. Thermal analyses 109
III.2.1.1.5. Solid state NMR 110
III.2.1.2. Preparation of azide-terminated precursor (azide-HST) 110
III.2.1.2.1. Synthesis 110
III.2.1.2.2. XRD analysis 111
III.2.1.2.3. Infrared spectroscopy 111

III.2.1.2.4. Solid state NMR 112
III.2.2. Post-synthesis modification of alkyne-HST 113
III.2.2.1. Post-synthesis modification *via* 1, 3-dipolar cycloaddition reaction without using copper (I) catalyst 113
III.2.2.1.1. Synthesis 114
III.2.2.1.2. XRD analysis 114
III.2.2.1.3. Infrared spectroscopy 114
III.2.2.2. Post-synthesis modification of alkyne-HST via microwave-assisted Copper (I) catalyzed Alkyne-Azide Cycloaddition (CuAAC) reaction 115
III.2.2.2.1. Optimization of the reaction conditions, especially the amount of catalyst, using 1-azidohexane 115
III.2.2.2.1.1. Synthesis 115
III.2.2.2.1.2. XRD analysis 116
III.2.2.2.1.3. Infrared spectroscopy 116
III.2.2.2.2. Generalization of the above optimal conditions using 1-azidobenzene 117
III.2.2.2.2.1. Synthesis 117
III.2.2.2.2.2. XRD analysis 118
III.2.2.2.2.3. Infrared spectroscopy 118
III.2.2.2.3. Further characterizations of hexyl-click-HST and benzyl-click-HST 119
III.2.2.2.3.1. Solid-state NMR 119
III.2.2.2.3.2. Thermal analysis and proposed formulae 120
III.2.2.2.3.3. SEM observation 121
III.2.2.2.4. Deintercalation behaviors of hexyl-click-HST and benzyl-click-HST 122
III.2.2.2.4.1. Synthesis 122
III.2.2.2.4.2. Obtained solids 122
III.2.2.2.4.2.1. Collection 122
III.2.2.2.4.2.2. XRD analysis 122
III.2.2.2.4.2.3. Energy-dispersive X-ray spectroscopy (EDX) 123
III.2.2.2.4.2.4. Infrared spectroscopy 123
III.2.2.2.4.3. Obtained organic phases 124
III.2.2.2.4.3.1. Collection 124
III.2.2.2.4.3.2. NMR spectroscopy in solution 124
III.2.2.2.5. Discussion 125
III.2.3. Post-synthesis modification of azide-HST via CuAAC reaction 126
III.2.3.1. Synthesis 126
III.2.3.2. XRD analysis 126
III.2.3.3. Infrared spectroscopy 127
III.2.3.4. SEM observation 128
III.2.3.5. EDX analysis 129
III.2.4. Preparation of precursors based on $HLaNb_2O_7 \cdot xH_2O$ (HLN) 129
III.2.4.1. Preparation of alkyne-terminated precursor (alkyne-HLN) 129
III.2.4.1.1. Synthesis 129

III.2.4.1.2. XRD analysis 130
III.2.4.1.3. Infrared spectroscopy 130
III.2.4.1.4. Thermal analyses and proposed formula 131
III.2.4.2. Preparation of azide-terminated precursor (azide-HLN) 133
III.2.4.2.1. Synthesis 133
III.2.4.2.2. XRD analysis 133
III.2.4.2.3. Infrared spectroscopy 133
III.2.4.2.4. Thermal analyses and proposed formula 134
III.2.5. Post-modification of azide-HLN via microwave-assisted CuAAC with 1-hexyne. 135
III.2.5.1. Synthesis 135
III.2.5.2. XRD analysis 135
III.2.5.3. Infrared spectroscopy 136
III.3. Conclusion 137
References 139

IV. Soft-chemistry route for insertion of paramagnetic metals into layered perovskite 141

IV.1. Introduction 143
IV.2. Results and discussion 143
IV.2.1. Direct reaction between HST and $Cu^{II}(X)_2 \cdot yH_2O$ 143
IV.2.1.1. Synthesis 144
IV.2.1.2. XRD analysis, infrared spectroscopy and EDX analysis 144
IV.2.2. Indirect insertion of copper ions into HST via a precursor N3-HST 145
IV.2.2.1. Preparation of the precursor N3-HST 145
IV.2.2.1.1. Synthesis 145
IV.2.2.1.2. XRD analysis 146
IV.2.2.1.3. Infrared spectroscopy 146
IV.2.2.1.4. Thermal analyses 147
IV.2.2.1.5. Solid state NMR 148
IV.2.2.2. Reactions between N3-HST and $Cu(NO_3)_2 \cdot 2.5H_2O$ or $Cu(N3)(NO_3)_2$. 149
IV.2.2.2.1. Synthesis 149
IV.2.2.2.2. XRD analysis 149
IV.2.2.2.3. Infrared spectroscopy 150
IV.2.2.2.4. UV-Visible absorption spectroscopy 152
IV.2.2.2.5. SEM observation and EDX analysis 152
IV.2.2.2.6. Elemental analysis and proposed formulae 153
IV.2.2.2.7. STEM characterization 154
IV.2.2.2.7.1. STEM view of the cross section 154
IV.2.2.2.7.2. STEM-EDX profile analyses 155
IV.2.2.2.8. Squid magnetometry 155
IV.2.2.2.9. EPR spectroscopy 157
IV.2.2.3. Study of the mechanism: influence of the quantity of $Cu(NO_3)_2 \cdot 2.5H_2O$ 159
IV.2.2.3.1. Synthesis 159

IV.2.2.3.2. XRD analysis 159
IV.2.2.3.3. Infrared spectroscopy 160
IV.2.2.3.4. UV-Vis. absorption spectroscopy and elemental analysis 161
IV.2.2.3.5. Proposed mechanism 165
IV.2.2.4. Study of the mechanism: influence of the quantity of $CuN3(NO_3)_2$ 165
IV.2.2.4.1. Synthesis 165
IV.2.2.4.2. XRD analysis 166
IV.2.2.4.3. Infrared spectroscopy 167
IV.2.2.4.4. UV-Vis. absorption spectroscopy and elemental analysis 167
IV.2.2.4.5. Proposed mechanism 170
IV.2.3. Indirect insertion of copper ions into HST via a simpler precursor C_2N-HST 171
IV.2.3.1. Reactions between C_2N-HST and $Cu(NO_3)_2{\cdot}2.5H_2O$ or $Cu(N3)(NO_3)_2$ 171
IV.2.3.1.1. Synthesis 171
IV.2.3.1.2. XRD analysis 171
IV.2.3.1.3. Infrared spectroscopy 172
IV.2.3.1.4. UV-Visible absorption spectroscopy 172
IV.2.3.1.5. Elemental analysis and proposed formulae 173
IV.2.3.2. Study of the mechanism: influence of the quantity of $Cu(NO_3)_2{\cdot}2.5H_2O$ 173
IV.2.3.2.1. Synthesis 173
IV.2.3.2.2. XRD analysis 174
IV.2.3.2.3. Infrared spectroscopy 175
IV.2.3.2.4. UV-Vis. absorption spectroscopy and elemental analysis 176
IV.2.3.2.5. Proposed mechanism 179
IV.2.3.3. Study of the mechanism: influence of the quantity of CuN3 179
IV.2.3.3.1. Synthesis 179
IV.2.3.3.2. XRD analysis 180
IV.2.3.3.3. Infrared spectroscopy 181
IV.2.3.3.4. UV-Vis. absorption spectroscopy and elemental analysis 182
IV.2.3.3.5. Proposed mechanism 184
IV.2.4. Indirect insertion of nickel ions into HST via a precursor N3-HST 185
IV.2.4.1. Synthesis 185
IV.2.4.2. XRD analysis 185
IV.2.4.3. Infrared spectroscopy 186
IV.2.4.4. SEM observations and EDX analysis 186
IV.2.5. Preparation of other precursors 187
IV.2.5.1. Synthesis 187
IV.2.5.2. XRD analyses 188
IV.2.5.3. Infrared spectroscopy 188
IV.2.5.4. Proposed formulae 189

IV.3. Conclusion 189
References 191

General conclusion 193

Annex 199

A. Synthesis and characterization technics 201
A.1. Microwave synthesis reactor 201
A.2. Elemental analyses 201
A.3. Powder X-ray diffraction 201
A.4. Thermo Gravimetric and Thermo Differential Analyses (TGA-TDA) 201
A.5. Infrared spectroscopy 201
A.6. UV-visible spectroscopy 201
A.7. NMR in solution 201
A.8. Solid state ^{13}C NMR 201
A.9. Magnetic measurements 202
A.10. Electron Paramagnetic Resonance (EPR) 202
A.11. Scanning Electron Microscopy (SEM) 202
A.12. Transmission Electron Microscopy (TEM) and Scanning Transmission Electron Microscopy (STEM) 202
B. Syntheses 203
B.1. Chapter I 203
B.1.1. Starting materials 203
B.1.2. Intercalation of mono *n*-alkylamines and *α, ω*-diaminoalkanes 203
B.1.3. Intercalation of other amines and diamines 203
B.1.4. Preparation of the three phases PBA1-HST, PBA2-HST, PBA3-HST 205
B.2. Chapter II 205
B.2.1. Grafting of *n*-alcohols into C_4N-HST 205
B.2.2. Alcohol-exchange reactions between C_2OH-HST and *n*-alcohols ($C_nH_{2n+1}OH$, n = 3, 4, 7, 12). 206
B.2.3. Grafting of α, ω-alkyldiols ($HOC_nH_{2n}OH$, n = 2, 4, 8, 12) into C_4N-HST 206
B.2.4. Grafting of bulky alcohols (2-propanol, *tert*-butanol and benzyl alcohol) into C_4N-HST 207
B.2.5. Reactivity of 5-amino-pentan-1-ol with C_2N-HST as a function of the water content 207
B.3. Chapter III 208
B.3.1. Preparation of precursors based on HST 208
B.3.1.1. Alkyne-HST 208
B.3.1.2. Azide-HST 208
B.3.2. Post-modification reactions 209
B.3.2.1. Post-modification of alkyne-HST 209
B.3.2.1.1. Hexyl-click-HST 209
B.3.2.1.2. Benzyl-click-HST 210
B.3.2.2. Post-modification of azide-HST 210
B.3.3. Deintercalation reactions 211

B.3.3.1. Case of hexyl-click-HST 211
B.3.3.2. Case of benzyl-click-HST 211
B.3.4. Preparation of precursors based on $HLaNb_2O_7 \cdot xH_2O$ (HLN) 211
B.3.4.1. Preparation of HLN 211
B.3.4.2. C_3OH-HLN 212
B.3.4.3. alkyne-HLN 212
B.3.4.4. azide-HLN 212
B.3.5. Post-modification of azide-HLN via microwave-assisted CuAAC click reaction with 1-hexyne 212
B.4. Chapter IV 213
B.4.1. Non-linear optical measurements 213
B.4.2. In situ reactions between N3-HST and $Cu(NO_3)_2 \cdot 2.5H_2O$ or $CuN3(NO_3)_2$ 214
B.4.2.1. Preparation N3-HST 214
B.4.2.2. Reaction between N3-HST and $Cu(NO_3)_2 \cdot 2.5H_2O$ (green solid) 214
B.4.2.3. Reaction between N3-HST and $CuN3(NO_3)_2$ (blue solid) 215
B.4.3. In situ reactions between C_2N-HST and $Cu(NO_3)_2 \cdot 2.5H_2O$ or $CuN3(NO_3)_2$ 215
B.4.3.1. Reaction between C_2N-HST and $Cu(NO_3)_2 \cdot 2.5H_2O$ (green solid-2) 215
B.4.3.2. Reaction between C_2N-HST and $CuN3(NO_3)_2$ (blue solid-2) 215
B.4.4. In situ reactions between N3-HST and $Ni(NO_3)_2 \cdot 6H_2O$ or $NiN3(NO_3)_2$ 216
B.4.4.1. Reaction between N3-HST and $Ni(NO_3)_2 \cdot 6H_2O$ 216
B.4.4.2. Reaction between N3-HST and $NiN3(NO_3)_2$ 216
B.4.5. Other precursors N4-HST, PA-HST and cyclam$(NH_2)_4$-HST 216
References 218

Extended abstract (in French) 219

General introduction

The soft chemistry term,[1] has emerged in the last several decades in the field of materials chemistry.[2-8] The prosperity of soft chemistry, which involves topotactic reactions and sol-gel processes, benefits from its own unique advantages. Firstly, as the name suggests, this approach emphasizes mild reaction conditions.[3,6] The employed reaction temperatures are considerably lower than some conventional methods, for example the high-temperature solid state reaction (ceramic). As a result, the soft chemistry reaction products can preserve most of the bond connectivity of "parent" phases.[4,5] Secondly, comparing with conventional methods, this approach provides unparalleled access to various important metastable phases, which are thermodynamically unstable while kinetically stable, especially at low temperature.[2,3,5] Thirdly, it offers a potential retrosynthetic method.[5,7] One can work backward to design a sequence of reactions that will form the identified target structures from conventional starting materials. Lastly, the soft chemistry route owns low cost property and is potentially applicable for large-scale industrial production.[6,8]

GI.1. Soft chemistry route-hybrid approach, a way to multifunctional materials

The soft chemistry route offers an extraordinary promotion for the development of multifunctional materials by means of hybrid approach.[7] The hybrid approach, consisting in the controlled assembly at nanoscale of at least two functional components that dedicate their own properties to the final compound in a composite way or in synergy,[9,10] is becoming one of the most efficient ways to multifunctional materials (***Figure GI.1***).[10,11] Indeed the synthesis of hybrids via soft chemistry route presents numerous advantages: it allows for the relatively easy functionalization by molecular species, it may use various reactions and finally it enables the fine tuning of the properties. Depending on the nature of the interface, organic-inorganic hybrids can be divided into two distinct classes. The class I hybrids involve only weak bonds (hydrogen, van der Waals or ionic bonds) to embed the inorganic phases and organic phases while the class II hybrids involve strong chemical bonds (covalent or iono-covalent bonds) to link the two phases.[12]

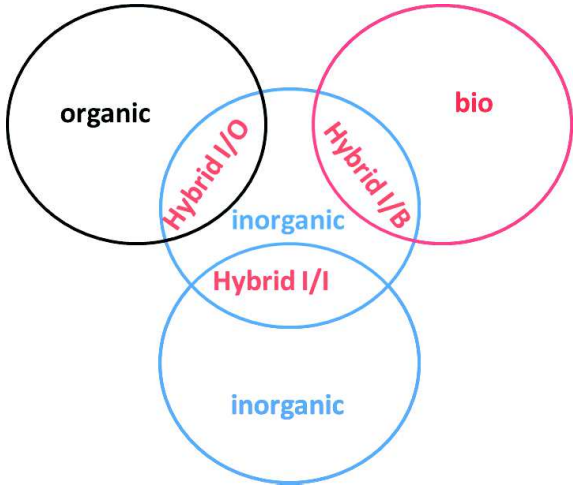

Figure GI.1. *Schematic illustration of the three main kinds of hybrid systems.*

Various interesting hybrid multifunctional materials have been obtained by the means of soft chemistry routes (insertion, sol-gel process, layer-by-layer (LBL) procedures…), for example organic-inorganic chiral hybrid layered magnet (***Figure GI.2***),[10,13] multiferroic

organic-inorganic hybrid,[14], inorganic-inorganic layered hybrid with the coexistence of superconductivity and magnetism[15] or bio-inorganic bioactive materials.[16,17]

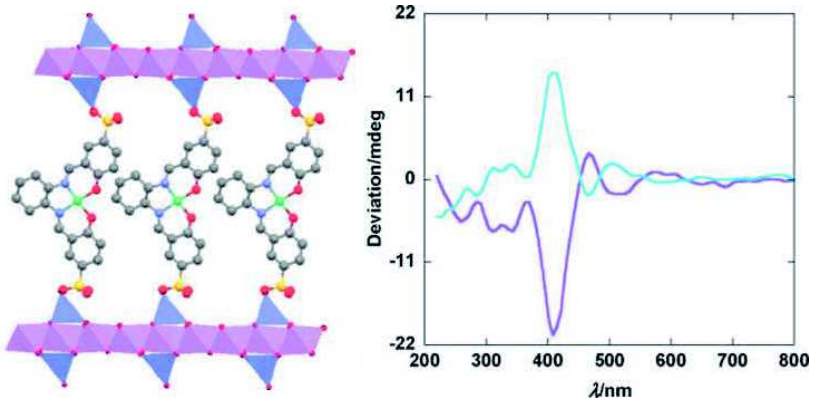

Figure GI.2. *A chiral hybrid magnet, obtained by functionalization of cobalt layered hydroxide by a chiral nickel salen complex.*[10]

GI.2. Tempting multifunctional materials: multiferroic compounds

Among the field of multifunctional materials, multiferroic compounds (*i.e.* materials presenting at least two coexisting electric, magnetic or elastic orders) have received much attention (***Figure GI.3***).[18,19] As potential applications, the compounds featuring a magneto-electric coupling are the most desirable. However, the intrinsic multiferroic materials are scarce, which is explained by the fact that electric and magnetic orders tend to be mutually exclusive.[20]

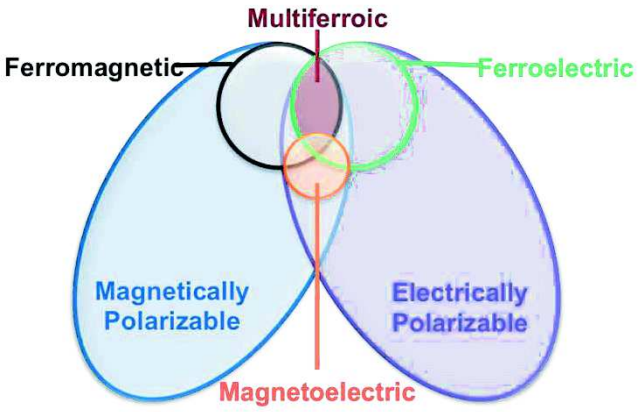

Figure GI.3. *Schematic illustration of the multiferroic compounds.*

Taking advantage of hybrid approach, based on soft chemistry routes, to design and prepare potential multiferroic compounds seems a promising option.[21] This is because of the numerous advantages of hybrids such as the possibility to design molecular building blocks to induce ferroelectric behavior, the higher magnetization or the interwoven subnetworks likely to induce magneto-electric coupling. However, apart from some examples (perovskite-like Metal Organic Frameworks,[21-25] AMX_4 or A_2MX_4 type layered perovskites[14] and layered bimetallic oxalates[26,27]), the hybrids approach via soft chemistry routes has not yet been thoroughly employed in the field of multiferroic compounds.

One approach to multiferroic hybrids is to functionalize a ferromagnetic structure in order to endow it with ferroelectric properties. This approach is being studied by Quentin Evrard in his PhD within the frame of an ANR project.
Another approach, symmetric of the previous one, is to functionalize a ferroelectric structure in order to endow it with ferromagnetic properties.

GI.3. Layered perovskites: potential candidates

Lamellar systems are particularly tailored for the hybrid approach, due to the versatility of insertion reactions which can be realized and the subsequent versatility of properties which results.[28] Among layered materials, layered perovskites and layered compounds with perovskite-related structures remain a favorite subject of study in solid state chemistry and materials science. They exhibit especially interesting physical properties such as fatigue-free ferroelectricity,[29-34] luminescence,[35] photovoltaic,[36] photocatalytic,[37] photoelectrochemical activities[38] or magnetic properties.[39] Therefore, the organic-inorganic hybrids based on layered perovskites are promising candidates to show multiferroic order since they possess at the same time flexible structures and magnetic or electrical properties.
These layered oxides are not so easy to functionalize due to the strong cohesion of the oxygen network. Fortunately in recent years, soft chemistry routes to design new materials based on perovskite structures have been considerably developed.[5,40] Therefore, lamellar perovskite oxides are still promising candidates to be functionalized in order to prepare potential multiferroic materials. Among the layered perovskites and layered compounds with perovskite-related structures, the Aurivillius phases, for example $Bi_2SrTa_2O_9$ which is well known as a ferroelectric material,[29] has naturally attracted our attention.
Our long-term thesis objective was to prepare new hybrid materials with multiferroic properties based on layered perovskite oxides by means of soft chemistry route. But it soon appeared that we had first to understand and to master the chemical functionalization mechanisms, especially topochemical manipulation with the principles of soft chemistry.

GI.4. Applications of soft chemistry for the functionalization of layered perovskites

GI.4.1. Perovskites

GI.4.1.1. Definition

Over decades, benefiting from the development of solid-state inorganic chemistry, various perovskites and compounds possessing perovskite-related structures have been synthesized.[41] The simple perovskites can be expressed as ABX_3, where A is a large electropositive cation (s-, d- or f- block),[5] B represents a transition metal cation and X is an anion. Since oxides are dominant, the formula can also directly be expressed as ABO_3. ***Figure GI.4*** presents the basic cubic perovskite structure. The B-site cation resides at the center of octahedral sites surrounded by oxygen anions, and A-site cation resides at the center of interstitial large cavity, surrounded by 8 BO_6 octahedrons.

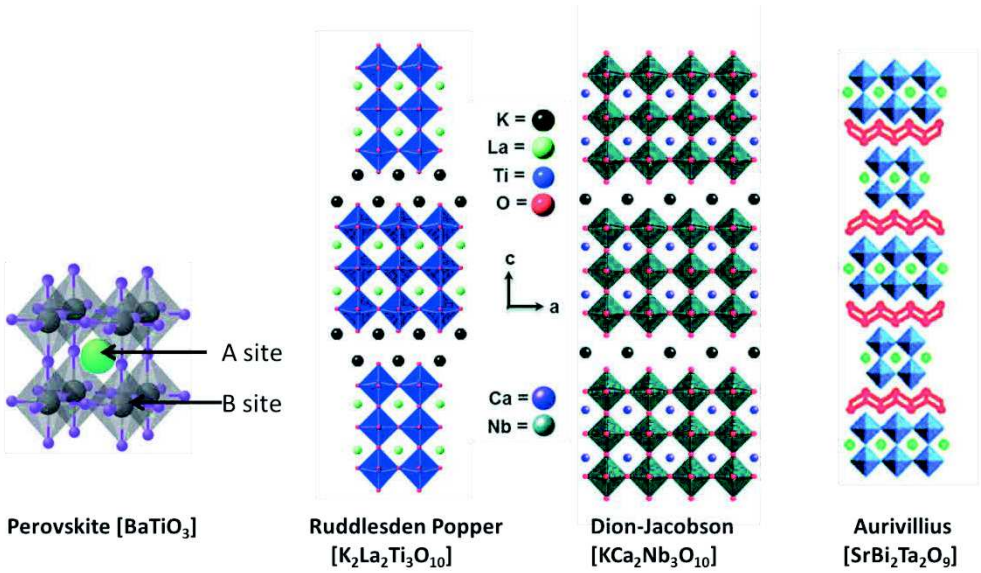

Figure GI.4. *Representative structure of selected perovskites and layered perovskites. The construction of the perovskite unit cell from the corner-sharing BO_6 octahedron and the three typical members of layered perovskites are shown.*[5,42,43]

GI.4.1.2. Layered perovskites

Among perovskite oxides, the layered ones are especially interesting for us for their further functionalization. The variants with layered perovskite structure include mainly Dion-Jacobson, Ruddlesden-Popper and Aurivillius phases.[5] These variants gained a growing interest within the past decades, due to their ion-exchangeable properties and their numerous interesting physical properties (photocatalytic,[37] photovoltaic,[36] etc…).
Dion-Jacobson phases and Ruddlesden-Popper phases can be expressed as $M[A_{m-1}B_mO_{3m+1}]$ and $M_2[A_{m-1}B_mO_{3m+1}]$, respectively.[5] The M and A are typically alkali-metal, alkaline-earth or rare-earth cations (M = Li, Na, K, Rb, Cs; A = Ca, Sr, La …), B is a transition metal cation (B = Ti, Nb, Ta) and m represents the layer thickness, $2 \leq m \leq 7$ for Dion-Jacobson phases and $1 \leq m \leq 4$ for Ruddlesden-Popper phases.[40] They consist of two-dimensional perovskite-like slabs ($[A_{m-1}B_mO_{3m+1}]$) interleaved with cations or cationic structural units. It is noteworthy that the layer charge per unit in Ruddlesden-Popper phases is twice that of the Dion-Jacobson phases. This difference has a considerable influence on the layer orientation and the interlayer local cation coordination.[40] Aurivillius phases constitute a closely related family, in which the perovskite layers are separated by α-PbO-type[44] bismuth oxide layers ($Bi_2O_2^{2+}$) instead of simple cation M that is found in Dion-Jacobson phases and Ruddlesden-Popper phases. Aurivillius can be expressed as $Bi_2O_2[A_{m-1}B_mO_{3m+1}]$ (A = Na, Ca, Sr, Bi, etc.; B= W, Nb, Ti, Ta, Mn, Mo, Fe, etc.; $1 \leq m \leq 8$)[45] with $[A_{m-1}B_mO_{3m+1}]$ denoting the perovskites-like slab.[46-48]

GI.4.2. Common soft chemistry approaches to functionalization

Nowadays, the functionalization of the above ion-exchangeable layered perovskites, based on the soft chemistry routes, has considerably developed.[5,40] Various metastable solid-state compounds possess remarkable physical/chemical properties have been obtained, which cannot be prepared by using the conventional solid-state reactions.[2,3,5] These soft chemistry approaches are mainly ion-exchange, insertion, grafting and exfoliation (***Figure GI.5***).

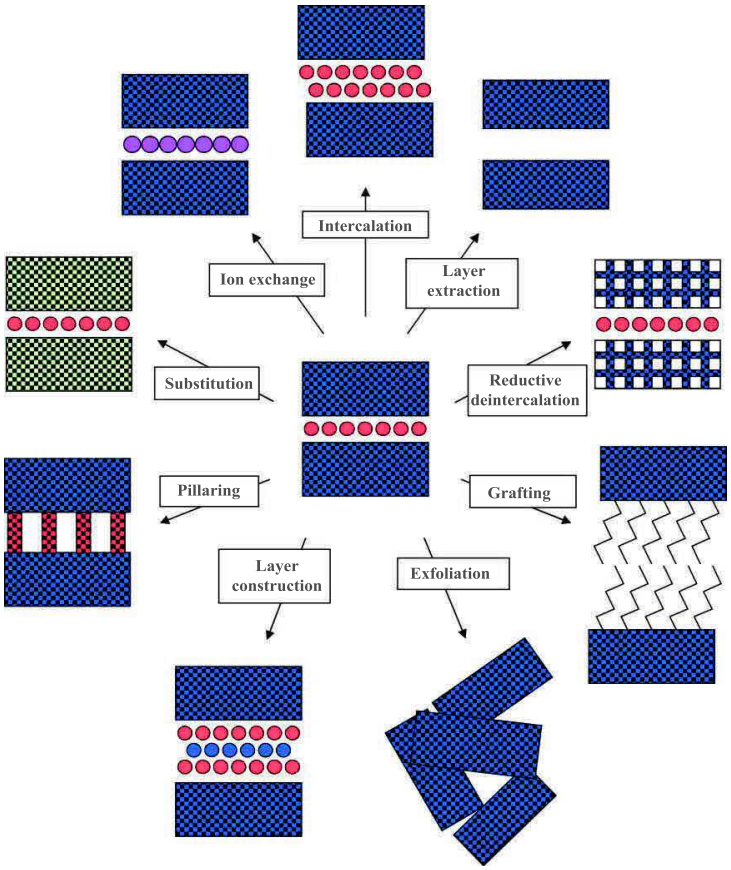

***Figure GI.5**. Common soft chemistry approaches to the functionalization of layered perovskites.*[40]

GI.4.2.1. Ion exchange reactions

GI.4.2.1.1. Acid treatment

Ion exchange reactions, as simple low-temperature methods, have been widely used. This is due to the existence of various cations or cationic units in the interlayer space of the three types of layered perovskites. Acid treatments of layered perovskites, which can be taken as cationic exchange reactions between protons and interlayer cations or other structural units, have extremely great importance, because the obtained protonated phases not only retain the corresponding layered perovskite structure but also become reactive with some kinds of organic molecules, which open the door to prepare various inorganic-organic hybrids based on perovskite structures or even to obtain nanoscale colloidal sheets. The nanoscale sheets exhibit various properties and can be utilized as hosts for various functional materials. This will be described in detail later.

GI.4.2.1.1.1. Protonated forms of Dion-Jacobson and Ruddlesden-Popper phases

Various protonated forms of Dion-Jacobson phases and Ruddlesden-Popper phases, $H[A_{m-1}B_mO_{3m+1}]$ and $H_2[A_{m-1}B_mO_{3m+1}]$, respectively, have been prepared *via* simple treatment by strong mineral acid aqueous solution (HCl or HNO_3). A protonated form of the Ruddlesden-Popper phase $K_2SrTa_2O_7$ can also be obtained by using a weak organic acid CH_3COOH.[49] Normally, the concentration of acid aqueous solution is relatively high (6.5 M

HNO_3 for $KLaNb_2O_7$,[50] 6 M HCl for $KCa_2Nb_3O_{10}$[51] and 4.0 M HNO_3 for $Li_2CaTa_2O_7$[52]) in order to ensure the entire transformation. However, the protonated transformation of $K_2SrTa_{2-x}Nb_xO_7$ (x= 0.0, 0.2, 0.4) can be carried out in very dilute HCl aqueous solution (pH = 5-6), and even a slight increasing of concentration can lead to the occurrence of hydrolysis.[53]

It is noteworthy that the protonated forms contain, as expected, one proton per $[A_{m-1}B_mO_{3m+1}]$ for Dion-Jacobson phases and two protons per $[A_{m-1}B_mO_{3m+1}]$ for Ruddlesden-Popper phases, which indicate the completely replacement of interlayer cations by protons. It is also possible to realize a partial replacement by strictly controlling the reaction conditions, for example the transformation from a Ruddlesden-Popper phase $Li_2SrTa_2O_7$ to its half-protonated phase $HLiSrTa_2O_7$.[54]

Finally, it appears that only alkali cations (Li^+, Na^+, K^+, Rb^+ and Cs^+) in the interlayer space can be replaced by protons *via* acid treatment. As an illustration, the acid treatment of $NaLaTiO_4$, in which the perovskite-like slabs $[TiO_4]$ are alternatively separated by Na^+ and La^{3+}, has been reported (***Figure GI.6***).[55,56] The protonated product is $HLaTiO_4$, in which only Na^+ cations have been replaced by protons.

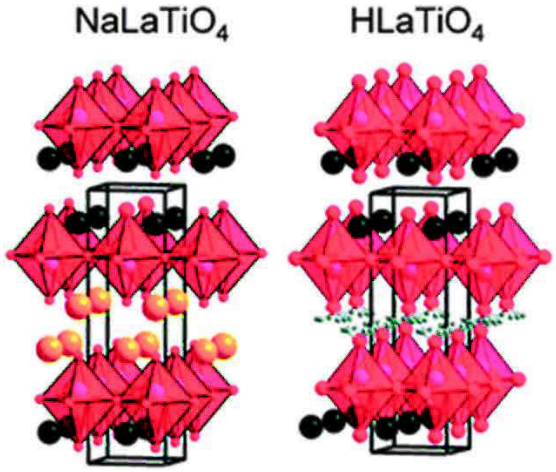

Figure GI.6. *Crystal structures of the layered perovskite phases $NaLaTiO_4$ and HLaTiO4. TiO_6 units are represented by red octahedra while black, orange and grey spheres represent La^{3+}, Na^+ and H^+, respectively.*[56]

GI.4.2.1.1.2. Protonated forms of Aurivillius phases

The conversion from an Aurivillius phase $Bi_2O_2[A_{m-1}B_mO_{3m+1}]$ into a corresponding proton form of Ruddlesden-Popper phase $H_x[A_yB_mO_{3m+1}]$ can also be realized by selective acid leaching,[37,45,57-59] based on the fact that the perovskite-like slabs are relatively stable (since the protonated forms of Dion-Jacobson phases and Ruddlesden-Popper phases have been obtained by means of acid treatment) while the bismuth oxide sheets between them are easily dissolved in acidic solutions (***Figure GI.7***).[60,61] Since the B-sites cations (W, Nb, Ti, Ta, Mn, Mo, Fe, etc…) of Aurivillius phases are more diverse than those of ion exchangeable Ruddlesden-Popper phases (limited to Nb, Ti or Ta),[62] the above protonated conversion has a great importance to enrich the kinds of ion exchangeable Ruddlesden-Popper phases.

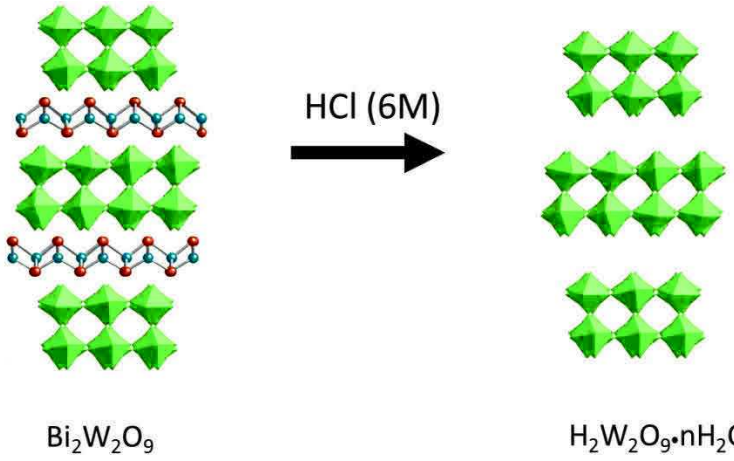

Figure GI.7. *Conversion from an Aurivillius phase $Bi_2W_2O_9$ into a corresponding proton form of Ruddlesden-Popper phase by selective acid leaching.*[61]

Normally, the employed acidic conditions should be strong mineral acid aqueous solution with relatively high concentration (6 M HCl for $Bi_2W_2O_9$[61] and 3 M HCl for $Bi_2SrTa_2O_9$[59]). But in some case, the concentration should not be too high. According to our experience, the Aurivillius phase $Bi_2SrNb_2O_9$ can be converted into its protonated form in 3 M HCl solution while it can be totally destroyed in 12 M HCl.

It is noteworthy that the nature of the strong acid employed is also very important. For example, the Aurivillius phase $Bi_2SrNaNb_3O_{12}$ can be converted to its protonated form by treatment with HCl, while treatments with HNO_3 or H_2SO_4 do not work.[63] In the same way, according to our experience the Aurivillius phase $Bi_2SrNb_2O_9$ as well cannot be converted into its protonated form by treatment with HNO_3 or H_2SO_4. It seems that the mineral acid HCl is the best choice to realize the conversion of Aurivillius phases into their protonated forms. One explication is the key role of Cl^-, which is very favorable to complex with Bi^{3+} leading to $BiCl_4^-$.[64] As a result, the bismuth oxide within Aurivillius phases can be leached *via* the following reaction:

$$BiO^+ + 2H_3O^+ + 4Cl^- \rightleftharpoons BiCl_4^- + 3H_2O$$

Yet, when other acids were employed, for example HNO_3, the initially formed $BiONO_3$ cannot be leached without the help of Cl^-,[64] this prevents the further leaching of bismuth oxide within Aurivillius phases.

The possibility of cation disorder between bismuth ions in the bismuth oxide sheet and A-site cations in the perovskite-like slab was first suggested to rationalize the broadened ferroelectric transition in an Aurivillius phase $Bi_2BaNb_2O_9$. This phenomenon has been further proved by the protonated conversion of Aurivillius phases $Bi_2ANaNb_3O_{12}$ (A= Sr or Ca)[65] and $Bi_2SrTa_2O_9$,[66] which showed slight amounts of residual bismuth, lost strontium and slightly lower numbers (1.8) of protons per $[A_{m-1}B_mO_{3m+1}]$ unit than theoretical value (2.0) in their corresponding protonated phases. In addition, a further investigation of three similar Aurivillius phases, $Bi_2CaNb_2O_9$, $Bi_2SrNb_2O_9$ and $Bi_2BaNb_2O_9$, lead to the conclusion that all the compounds exhibit disorder between the bismuth ions and A sites cations, which increases as the A site cation size increases.[30] In addition, the above investigation also proved that the A-site cations can affect the dielectric properties.[30]

GI.4.2.1.1.3. Reverse conversion

The protonated forms of Dion-Jacobson phases and Ruddlesden-Popper phases, $H[A_{m-1}B_mO_{3m+1}]$ and $H_2[A_{m-1}B_mO_{3m+1}]$, can be reversely converted into their corresponding alkali forms $M[A_{m-1}B_mO_{3m+1}]$) and $M_2[A_{m-1}B_mO_{3m+1}]$ (M= Li, Na, K, etc.), by reacting with melted or hot aqueous base MOH.[5] The above reverse conversion is particularly interesting for the design of new Ruddlesden-Popper phases. For example, $KLnTiO_4$ and $LiLnTiO_4$ (Ln = lanthanide), which cannot be directly prepared by solid-state reactions, can be indirectly obtained by means of reactions between $HLnTiO_4$ (protonated form of $NaLnTiO_4$)[55] and the corresponding MOH base.[67] In addition, there is also an example for the reverse conversion from the protonated form of the Aurivillius phase $Bi_2SrTa_2O_9$, $H_{1.8}Sr_{0.8}Bi_{0.2}Ta_2O_7$, into itself by the reaction with BiOCl (***Figure GI.8***).[68]

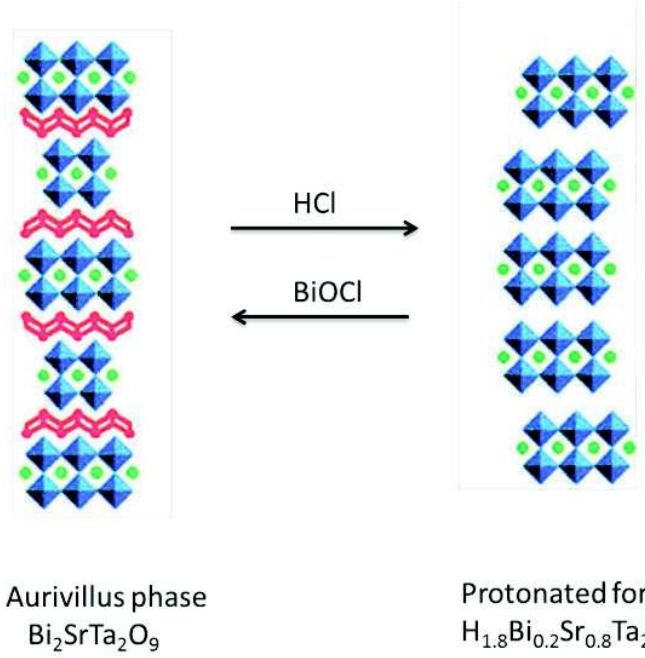

Figure GI.8. *Reversible conversion between the Aurivillius phase $Bi_2SrTa_2O_9$ and its protonated form.*

GI.4.2.1.1.4. Topochemical dehydration of the protonated forms of layered perovskites

The protonated forms of Ruddlesden-Popper phases have been employed to prepare new perovskite related structures that possess defects via topochemical dehydration.[53] The calcination of $H_2La_2Ti_3O_{10}$ results in a three-dimensional perovskite with one-third vacant or defective A-sites.[69] The calcination of $H_2SrTa_2O_7$ has been reported to produce a defective perovskite $SrTa_2O_6$ with half A-sites defects.[53] The protonated triple-layer Ruddlesden-Popper phases $H_2CaNaTa_3O_{10}$ and $H_2Sr_{1.5}Nb_3O_{10}$ have also been reported to lead to A-site defective phases $CaNaTa_3O_9$ and $Sr_{0.5}NbO_3$, respectively (***Figure GI.9***).[70,71] It is noteworthy that the protonated forms of Dion-Jacobson phases are not suitable for preparing new defective perovskite phases by means of topochemical dehydration, which is proposed to be due to the insufficient number of interlayer protons.[5]

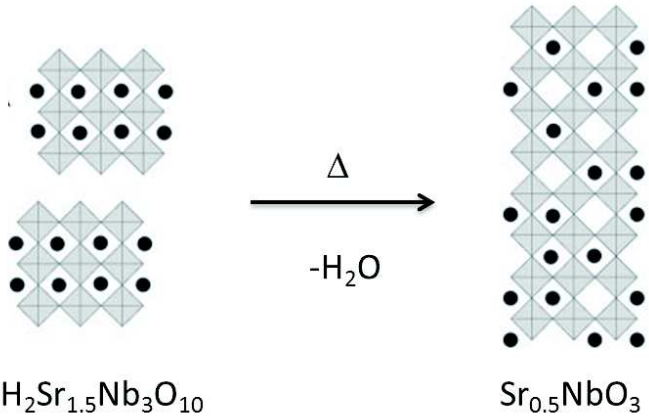

Figure GI.9. *$H_2Sr_{1.5}Nb_3O_{10}$ and the formation of the metastable $Sr_{0.5}NbO_3$, which possess A-sites defects, through topochemical dehydration.*[71]

GI.4.2.1.2. Mono or divalent cation exchange reactions

For Dion-Jacobson phases, the ion-exchange reactions have focused on monovalent cations including alkali metal ions but also Ag^+, Cu^+, Tl^+ and NH_4^+. The relatively large cations (Cs^+, Rb^+ or K^+) in the interlayer spacing can be replaced by relatively small cations (Na^+, Li^+, NH_4^+ or Tl^+) using molten nitrate salts as ion-exchange medium.[62,72-74] The aqueous monovalent ion exchange reactions between Cu^+ and $ALaNb_2O_7$ (A = H, K or Cs) or Ag^+ and $ALaNb_2O_7$ (A = H or K) have also been reported.[75,76]

A few examples of divalent cation exchange have also been reported. The partial ion exchange reactions between Sr^{2+} and Ba^{2+} with the triple-Dion-Jacobson phase $RbCa_2Nb_3O_{10}$ lead to $Rb_{1-x}Sr_{x/2}Ca_2Nb_3O_{10}$ (x=0.45) and $Rb_{1-x}Ba_{x/2}Ca_2Nb_3O_{10}$ (x=0.55), respectively.[77] In addition, the intercalation of Cu^{2+} (in the form of $Cu(NO_3)^+$ or $Cu(OH)^+$) into the interlayer spacing of $ALaNb_2O_7$ (A = octylamine) has also been described.[75]

For Ruddlesden-Popper phases, the ion-exchange reactions are much more various. Using molten salts as ion-exchange medium, these phases not only undergo monovalent cation exchange reactions between the interlayer cations (Na^+, K^+, Rb^+) and other smaller cations (Li^+, Na^+, Ag^+, respectively)[69,78-80] but also divalent cation exchange reactions between the interlayer alkali cations and divalent ions (Co^{2+}, Cu^{2+}, Zn^{2+}, etc…).[81] It is noteworthy that even aqueous divalent ion exchange reactions have been reported by Schaak and Mallouk (Ca^{2+}, Sr^{2+}, Ni^{2+}, Cu^{2+}, Zn^{2+}).[82]

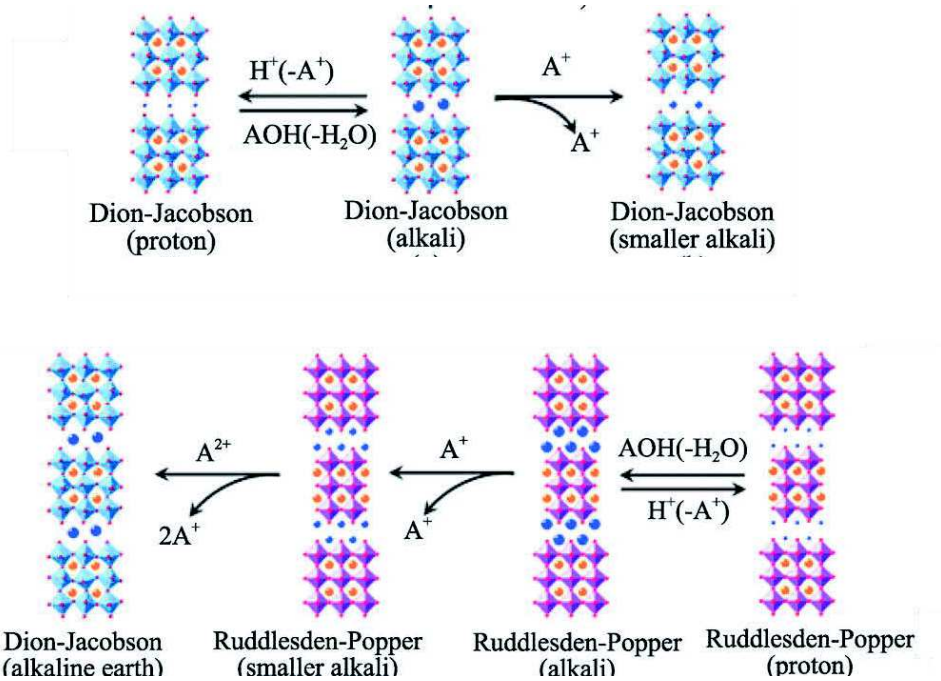

Figure GI.10. *Ion-exchange reactions of layered perovskites.*[5]

GI.4.2.1.3. Introduction of cationic structures

Ion-exchange reactions can also not only simply introduce cations but also can lead to formation of cationic networks in the interlayer space of perovskite-like slabs. For Dion-Jacobson phases, a co-exchange reaction of both cations and anions between $RbLaNb_2O_7$ and CuX_2 (X = Cl or Br) leads to the formation of copper halide layers in the interlayer space of perovskite-like slabs, where the cations Rb^+ have been replaced (***Figure GI.11***).[83]

$$RbLaNb_2O_7 + CuX_2 \longrightarrow (CuX)LaNb_2O_7 + RbX\ (X = Cl, Br)$$

Until now, this type of copper-halide exchange reactions has been expanded to various Dion-Jacobson phases ($ALaNb_2O_7$ (A = H, Li, Na, K, Rb, etc…), $RbLaTa_2O_7$, $RbA'Nb_2O_7$ (A' = Bi, Nd), $RbCa_2Nb_3O_{10}$).[84-86] In addition, these exchange reactions are not limited to copper but have been extended to other transition metals, leading to $(MCl)LaNb_2O_7$ (M = V, Cr, Mn, Fe, Co) possessing intergrowth structures.[87-89] $(CuCl)LaNb_2O_7$ can also be employed to prepare other intergrowth structures ($(A_2X)LaNb_2O_7$, A = Rb, Cs; X = Cl, Br) with alkali-metal halide layers in the interlayer space of perovskite-like slabs.[40]

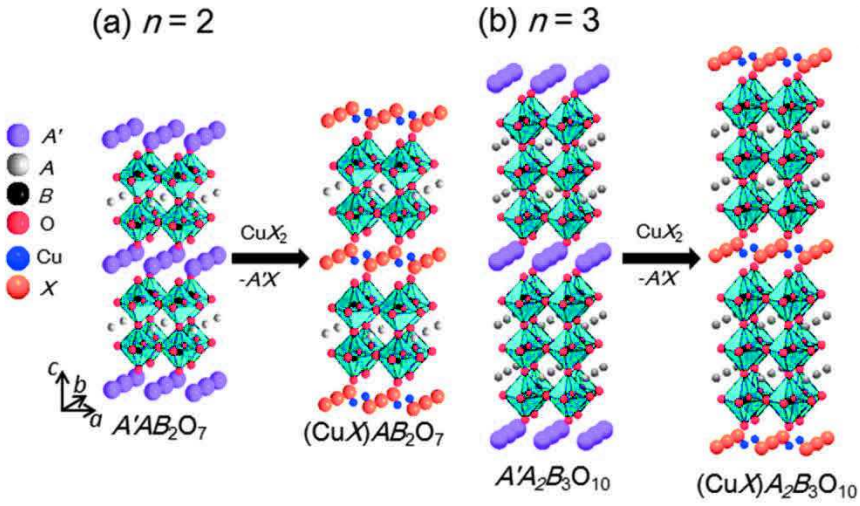

Figure GI.11. *Ion-exchange reaction involving the insertion of copper halide layer into the interlayer space of the Dion-Jacobson type layered perovskites A´[$A_{n-1}B_nO_{3n+1}$] for (a) n = 2 and (b) n = 3.*[86]

For Ruddlesden-Popper phases, in a typical example, $K_2La_2Ti_3O_{10}$ have been functionalized by a α-PbO-type bismuth oxide layers ($Bi_2O_2^{2+}$) to become an Aurivillius phase $Bi_2O_2[La_2Ti_3O_{10}]$ by ion-exchange reactions.[68] The intergrowth of a vanadium oxide layer and perovskite host has also been obtained *via* reaction of $K_2La_2Ti_3O_{10}$ with aqueous $VOSO_4$.[68]
The successful preparation of new intergrowth structures, using Dion-Jacobson or Ruddlesden-Popper phases as hosts, leads to new solids with interesting new properties. For example, (CuCl)$LaNb_2O_7$, derived from $RbLaNb_2O_7$, was reported to be a frustrated magnetic system showing spin gap behavior.[90] The above results inspired us to attempt the preparation of new ferroelectric Aurivillius phases, in which interlayer structure units possessing magnetic properties are introduced, which would potentially lead to new multiferroic materials (or at least to hybrid paramagnetic ferroelectric materials). Yet we realized that the processes of soft-chemistry functionalization of such phases had first to be investigated further, and possibly improved.

GI.4.2.2. Intercalation reactions

Various protonated forms of Aurivillius, Dion-Jacobson and Ruddlesden-Popper phases can react with various organic molecules, which leads to the preparation of various organic-inorganic class I hybrids based on perovskite structures.

GI.4.2.2.1. Intercalation behaviors

The protonated forms of layered perovskites can be seen as solid acids. Therefore the intercalation processes are assumed to be acid-base type reactions.[5] The amine intercalation reactions have been essentially reported on Dion-Jacobson phases, but more recently amine intercalation reactions into protonated forms of Aurivillius and Ruddlesden-Popper phases have also been reported (***Table GI.1***).

Nature of the starting phase	Protonated form	Organic molecule	Reaction conditions			
			Solvent	Method	Temperature	Time
Dion-Jacobson	$HCa_2Na_{n-3}Nb_nO_{10}$ ($3 \le n \le 7$)	*n*-octylamine[91]	*n*-heptane	Classical heating	98°C	
	$HLaNb_2O_7$	*n*-alkylamines[92]	*n*-heptane	Classical heating	98°C	2 d
		pyridine[92]	*n*-heptane	Classical heating	98°C	20 d
		n-alkylamines[93] ($1 \le nc \le 4$)	water	Microwave	100°C	1h
	$HCa_2Nb_3O_{10}$	*n*-alkylamines ($4 \le nc \le 18$) [94]	*n*-heptane	Classical heating	98°C	3 – 20 d
		methylamine[94]	water	Hydrothermal	50°C	3 – 20 d
		ethylamine[94]	water	Stirring	R. T.	3 – 20 d
		n-propylamine[94]	∅	Classical heating	48°C	3 – 20 d
		aniline[95]	acetone	Classical heating	56°C	14 d
		methylviologen[96]	water	Hydrothermal	80°C	14 d
	$HSr_2Nb_3O_{10}$	metylamine [97]	water	Hydrothermal	60°C	1 d
		ethylamine[97]	water	Hydrothermal	120°C	2 d
		n-alkylamines[97] ($3 \le nc \le 6$)	ethanol	Solvothermal	120°C	2-3 d
		α,β-diamino alkane[98] ($2 \le nc \le 8$)	water	Classical heating	60 – 90°C	3 d
		α,β-diamino alkane[98] (nc=10,12)	*n*-heptane	Classical heating	60 – 90°C	3 d
	$HLa_2Ti_2TaO_{10}$	*n*-alkylamine[99]	water	Stirring	R.T.	1 d
	$HCa_2Nb_2MO_{10}$ (M = Fe, Al)	*n*-alkylamine ($6 \le nc \le 18$), aniline or pyridine[100]	*n*-heptane	Classical heating		Several days
	$HCa_2(CaSr)_{n-3}Nb_3TiO_{3n+1}$ (n = 4, 5)	*n*-alkylamine[101]	water	Classical heating	100 °C	2–3 d
Ruddlesden-Popper	$H_2SrTa_2O_7$	*n*-alkylamine[102] (nc = 4, 8, 12,16)	water	Classical heating	70°C	1 d
	$H_2La_{2/3}Ta_2O_7$	*n*-alkylamine[102]	water	Classical heating	70°C	1 d
	$H_2La_2Ti_3O_{10}$	*n*-alkylamine[43]	water	Hydrothermal	50°C	21 d
	$H_2CaTa_2O_7$	*n*-alkylamines[93] ($1 \le nc \le 4$)	water	Microwave	100 °C	1h
Aurivillius	$H_{1.8}Bi_{0.2}Sr_{0.8}Ta_2O_7$	*n*-alkylamine[66]	THF	Classical heating	70°C	7 d
		n-alkylamine[103]	water	Hydrothermal	70°C	14 d
		α,β -diaminoalkane (nc = 2, 4, 8)[104]	water	Classical heating		3 d
		1,12-diaminododecane[104]	water/THF	Classical heating		3 d
		n-alkylamine (nc = 3, 8, 12, 18) and tetraphenylporphyrin[105]	propanone	Chromatography	R.T.	1 d
	$H_{1.8}Bi_{0.2}A_{0.8}NaNb_3O_{10}$ (A = Sr or Ca)	*n*-alkylamine[65] (nc = 4, 8)	*n*-heptane	Classical heating		
	$H_2W_2O_7$	*n*-alkylamine[61]	*n*-heptane	Stirring	R.T.	7 d

Table GI.1. *Typical Intercalation reactions between organic amines and layered perovskites (adapted from reference[106]).*

As seen in ***Table GI.1***, Dion-Jacobson phases present the most various reactions with organic bases. Apart from *n*-alkylamine and α,β-diaminoalkane (pKa *ca.* 10), some Dion-Jacobson phases can even accommodate pyridine or aniline (pKa *ca.* 5), which are much weaker bases. The variety of intercalation reactions is less for the protonated forms of Aurivillius and Ruddlesden-Popper phases, limited to *n*-alkylamine (Ruddlesden-Popper, Aurivillius) and α,β-diaminoalkane (Aurivillius).

GI.4.2.2.2. Factors influencing intercalation behaviors

Table GI.1 shows that various solvents can be employed. For Dion-Jacobson phases, they can be polar protic (water), polar aprotic (acetone, ethanol) and non-polar aprotic (*n*-heptane). It thus seems that there is no special requirement about the type of solvent. A similar observation can be made in the case of Aurivillius phases. Yet, it seems that water is the most suitable solvent for the intercalation reactions in Ruddlesden-Popper phases. As an example, $H_2La_2Ti_3O_{10}$ can be intercalated by *n*-alkylamine using water as solvent,[107] but intercalation does not occur when water is replaced by *n*-heptane.[108]

It seems that the type of A-site cations does not have considerable effect on the reactivity of the three layered perovskites with organic bases. As shown in ***Table GI.1***, $HSr_2Nb_3O_{10}$ and $HCa_2Nb_3O_{10}$, Dion-Jacobson phases, have the similar high reactivity with organic bases. In addition, $H_2SrTa_2O_7$ and $H_2La_{2/3}Ta_2O_7$, Ruddlesden-Popper phases, also have similar reactivity with *n*-alkylamines. We can observe the same phenomenon in the case of Aurivillius phases, for example $H_{1.8}Bi_{0.2}Sr_{0.8}Nb_3O_{10}$ and $H_{1.8}Bi_{0.2}Ca_{0.8}Nb_3O_{10}$.

However, the type of B-site cations can really affect the reactivity of layered perovskites with organic bases. Actually, the reactivity of the protonated forms of the layered perovskites towards organic bases depends on the acidity of the protons attached to the terminal oxygen atoms of the interface of perovskite-like slabs. The acidity of the protons mainly depends on the B-site cations (mainly limited to Ta, Nb and Ti),[62] which are at the center of octahedrons surrounded by oxygen anions. Normally, niobates and tantalates exhibit stronger acidity than titanates.[107] As an example to illustrate this point, $HLa_2Ti_2NbO_{10}$, derived from $CsLa_2Ti_2NbO_{10}$, was found to intercalate alkylamines, while $HLa_2Ti_2NbO_{10}$, derived from $KLa_2Ti_2NbO_{10}$, has no reactivity with alkylamines.[72] The interesting phenomenon is due to that the former has a sufficient number of protons attached to NbO_6 octahedron while in the later, protons are essentially attached to TiO_6 octahedron.[72]

Finally, the Dion-Jacobson phase $HCa_2Nb_3O_{10}$ (which can react with aniline[95]) shows much higher acidity than Ruddlesden-Popper phase $H_{1.8}Bi_{0.2}Ca_{0.8}NaNb_3O_{10}$ (which can react with *n*-alkylamine[65]). Since both of them only have protons attached to NbO_6 octahedrons, structural factors need to be taken into account. The proton-proton distances on the interlayer surface of $HCa_2Nb_3O_{10}$ is larger than that of $H_{1.8}Bi_{0.2}Ca_{0.8}NaNb_3O_{10}$, since only half terminal oxygen atoms are attached to protons in the case of Dion-Jacobson phases.[109] In addition, although the protonated Ruddlesden-Popper phase $H_{1.8}Bi_{0.2}Ca_{0.8}NaNb_3O_{10}$ was proposed to possess *P*-type stacking sequence,[58] the same as protonated Dion-Jacobson phase $HCa_2Nb_3O_{10}$,[110], the coexistence of local *I*-type stacking sequence is also possible by analogy with what has been described on $H_{1.8}Sr_{0.8}Bi_{0.2}Ta_2O_7$.[59] As a result, the proton-proton distance and the local stacking sequence may also affect the acidity of layered perovskites.

GI.4.2.2.3. Mechanisms of intercalation

Although the mechanisms of the intercalation reactions between organic bases and protonated forms of layered perovskites have been generally accepted as acid-base reactions, some special examples have been reported to be ion exchange processes. $H_2La_2Ti_3O_{10}$ can be intercalated by *n*-alkylamines and *n*-butylammonium ions, using water as solvent.[107] Yet, it shows no reactivity with *n*-alkylamines when non-polar aprotic solvent *n*-heptane was employed which has been explained by the ion-exchange nature of the reaction, rather than acid base.[108]

The reaction between $HCa_2Nb_3O_{10}$ and cationic aminoundecanoic acid has also been described as an ion-exchange process.[111]

GI.4.2.2.4. Drawback of the published intercalation methods

Although the intercalation behaviors of layered perovskites have been discovered over decades, the published intercalation methods are essentially limited to reflux or solvothermal and they have the important drawback of being very long (typically several days). One example reports the use of a faster (about one day) room temperature chromatographic process.[105] Due to these very long reaction times, only a limited number of amines (n-alkylamines, α, β -diaminoalkane, pyridine, etc.) have been tested for insertion into protonated layered perovskites. Moreover, this reaction timescale intrinsically limits the type of molecules which can be inserted to very stable and very simple ones. During the course of this PhD work, the microwave-assisted functionalization of Dion-Jacobson and Ruddlesden-Popper layered perovskites by *n*-alkylamines was reported, with a significant reduction of the reaction times, and no loss in conversion rates.[93]

GI.4.2.3. Grafting reactions

GI.4.2.3.1. Grafting behaviors

In addition to class I hybrids, class II hybrids based on layered perovskites have also been reported. By means of grafting reactions with organic molecules, the hybrids based on layered perovskites possess covalent bonds between organic phases and inorganic ones. As illustrations, some typical examples are listed in the following table (***Table GI.2***).

Nature of the starting phase	Protonated form	Intermediate	Organic phase	Reaction conditions			
				Solvent	Method	Temperature	Time
Dion-Jacobson	$HLaNb_2O_7$ (HLN)	∅	methanol[50]	water	Stirring	R.T.	1d
		∅	ethanol[50]	water	Stirring	R.T.	7d
		∅	*n*-alcohol[50] nc = 3-6, 8, 10, 12	water	Classical heating	80°C	7d
		n-decoxyl-HLN	2-propanol, or ethylene glycol[112]	∅	Solvothermal	80°C	7d
		n-decoxyl-HLN	*tert*-butyl alcohol[112]	∅	Solvothermal	80°C	14d
		n-decoxyl-HLN	*n*-$C_nH_{2n+1}PO(OH)_2$[113] $4 \leq nc \leq 18$	2-butanone	Stirring	80°C	2-3d
		n-decoxyl-HLN	*n*-$CH_3(OCH_2CH_2)_nOH$[114] $1 \leq nc \leq 4$	∅	Classical heating	80°C	14d
		n-decoxyl-HLN	$CF_3(CF_2)_7C_2H_4OH$[115]	2-butanone	Classical heating	80°C	7d
		n-decoxyl-HLN	D-glucopyranose[116]	2-butanone	Solvothermal	70°C	3d
		propoxyl-HLN	CF_3COOH[117]	∅	Solvothermal	70°C	3d
		propoxyl-HLN	4-penten-1-ol[118]	∅	Solvothermal	80°C	7d
		∅	methanol or propanol[93]	water	Microwave	100°C	1h
		methoxyl-HLN	*n*-propanol[93]	water	Microwave	100°C	1h
		methoxyl-HLN or propoxyl-HLN	*n*-pentanol[93]	water	Microwave	120°C	1h
		methoxyl-HLN or propoxyl-HLN	*n*-decanol[93]	water	Microwave	150°C	0.5h
	$HCa_2Nb_3O_{10}$ (HCN)	∅	methanol or ethanol[51]	water	Hydrothermal	150°C	7d
		methoxyl-HCN	*n*-propanol[51]	∅	Solvothermal	150°C	7d
		propoxyl-HCN	*n*-alcohol[51] $4 \leq nc\ (pair) \leq 18$	∅	Solvothermal	150°C	7d
	$HSr_2Nb_3O_{10}$ (HSN)	∅	methanol[119]	∅	Microwave	Non-mentioned	4h
		methoxyl-HSN	*n*-propanol[119]	∅	Microwave	Non-mentioned	4h
		propoxyl-HSN	*n*-hexanol[119]	∅	Microwave	Non-mentioned	3.5h
Ruddlesden-Popper	$H_2CaTa_2O_7$ (HCT)	methylamine-HCT	methanol[52]	water	Hydrothermal	100°C	3d
		methoxyl-HCT	*n*-propanol[52]	water	Hydrothermal	80°C	7d
		propoxyl-HCT	*n*-alcohol nc = 6, 10[52]	water	Hydrothermal	80°C	7d
		n-decoxyl-HCT	D-glucopyranose[120]	2-butanone/ water	Solvothermal	70°C	3d
		propylamine-HCT	n-propanol[93]	water	Microwave	110°C	1h
		propoxyl-HCT	*n*-alcohol[93] nc = 5, 10	∅	Microwave	120°C	1h
	$H_2La_2Ti_3O_{10}$ (HLT)	*n*-butylamine-HLT	*n*-propanol[107]	∅	Solvothermal	180°C	5d
		propoxyl-HLT	*n*-alcohol [107] nc = 4, 8, 10, 12	∅	Solvothermal	150°C	5d

Table GI.2. *Typical grafting reactions into layered perovskites in literature.*

Relatively few Dion-Jacobson phases and Ruddlesden-Popper phases have been reported to undergo grafting reactions, essentially with simple alcohols. There is one example of grafting of a diol (ethylene glycol),[112] and two with a more complicated alcohol (a sugar, D-glucopyranose).[116,120] Finally, there is one single example of grafting with a molecule other than alcohol, a phosphonic acid.[113] Until now, there is no report about the grafting behavior of the protonated forms of Aurivillius phases.

GI.4.2.3.2. Alcohol-alcohol exchange

Alcohol-alcohol substitution is a very useful approach to prepare various alkoxy derivatives, which cannot be prepared directly. It has been first employed to realize the modification of

the interlayer surface of $HLaNb_2O_7$ with some relatively complex alcohols, 2-propanol, *tert*-butanol and ethylene glycol by using *n*-decoxy derivative as an intermediate.[112] It is interesting that only one of the two –OH groups of ethylene glycol is linked to the interlayer surface through the formation of covalent bond while the other –OH group retains free.
For the bulky alcohol *tert*-butanol, the alcohol-exchange-type reaction works only partly, and there is a coexistence of *n*-decoxy groups and *tert*-butoxy groups in the obtained product. For $H_2La_2Ti_3O_{10}$ and $HCa_2Nb_3O_{10}$, the direct grafting reactions with alcohols with long carbon chains do not work, but when using propoxy derivative as an intermediate, much longer alcohols can be grafted.[52,107] Finally, with the help of this alcohol-exchange-type reaction, grafting of polyether chains,[114] D-glucopyranose (***Figure GI.12***)[116] with reductive property and 4-penten-1-ol[118] with a functional group have been reported.

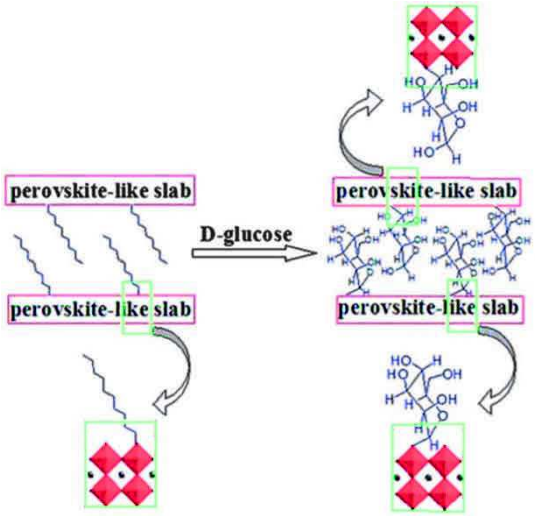

Figure.GI.12. *Scheme of the reaction between the n-decoxyl derivative of $HLaNb_2O_7$ with D-glucopyranose.*[116]

GI.4.2.3.3. Mechanisms of alcohol grafting and alcohol-exchange reactions

Among the layered perovskites, the grafting reactions between $HLaNb_2O_7$ and *n*-alcohols were first reported by Takahashi *et al.*.[50] In fact, the reactions with *n*-alcohols were once reported to be simple intercalation.[121] Yet, according to the work of Takahashi *et al.*, using solid state NMR, the obtained hybrids were proved to be *n*-alkoxy derivatives with formation of a covalent bond Nb-O-C.
In addition, apart from the direct reactions between $HCa_2Nb_3O_{10}$ with methanol or ethanol, $HLaNb_2O_7$ is the unique phase that can directly react with *n*-alcohols. For the other phases, $H_2La_2Ti_3O_{10}$ and $H_2CaTa_2O_7$, the intermediates are necessary for the occurrence of grafting reaction with *n*-alcohols to form covalent bond Ti-O-C and Ta-O-C, respectively. The intermediates are usually alkylamine intercalated layered perovskites. Until now, the mechanisms of these indirect grafting reactions with the help of amine pre-intercalation are unclear. According to the work of Van Der Voort, P. *et al.*, the ammonium groups are known as catalysts to promote the silylation of silica surface and formation of Si-O-Si linkage.[122]

The mechanism of alcohol-exchange-type reactions can be proposed as a nucleophilic reaction, where a new alcohol directly attacks the C-O-Nb bonds of the intermediate and replaces the previous alkoxy group to obtain the new alkoxy derivative in a single step. It can be expressed as follows:

$$(RO)NbO_5 + R'OH \longrightarrow (R'O)NbO_5 + ROH$$

Yet, after mechanistic investigation by Suzuki *et al.*, the crucial role of water was proved and $(HO)NbO_5$ was proposed as an intermediate.[112] A new mechanism with two steps was proposed, where the exchange reaction proceeds first *via* hydrolysis with the help of water to release the previously grafted alcohol and then in a second step, the new alcohol grafts the $(HO)NbO_5$ intermediate with esterification. The above process can be expressed as follows:

$$(RO)NbO_5 + H_2O \xrightarrow{-ROH} (HO)NbO_5 \xrightarrow[-H_2O]{R'OH} (R'O)NbO_5$$

In fact, the alcohol-exchange-type reactions have been updated as ligand-exchange-type reactions along with the successful interlayer surface modification of $HLaNb_2O_7$ with organophosphonic acids and trifluoroacetic acid through the formation of covalent bond P-O-Nb and CO-O-Nb, respectively.[113,117] The major advantages of the hybrids possessing covalent bond P-O-Nb are the high stability and the insensitivity to water.[113]

GI.4.2.3.4. Drawback of published grafting methods

Apart from the Dion-Jacobson phase $HLaNb_2O_7$, the grafting reactions based on layered perovskites are limited to simple alcohols. Until now, there is not an example of protonated forms of Aurivillius phases undergoing similar grafting reactions. Although the alcohol-exchange-type reactions are helpful, they cannot be employed to prepare alkoxy derivatives at will, for example the pure *tert*-butoxy derivative. In addition, the published methods are limited to reflux and hydrothermal, and they have the important drawback of being very long (typically several days). During the course of this PhD work, the microwave-assisted functionalization of Dion-Jacobson and Ruddlesden-Popper layered perovskites by *n*-alcohols was reported, with a significant reduction of the reaction times, and no loss in conversion rates.[93,119]

GI.4.2.4. Exfoliation

GI.4.2.4.1. Exfoliation behaviors

Exfoliation of layered compounds is wildly considered as a promising method for preparing unilamellar sheet units (nanosheets).[123-128] Layered perovskites are suitable for exfoliation because of their structural properties: strong covalent bonds in the perovskite-like slabs with weaker interlayer linkages (van der Waals or electrostatic interactions).[129] Exfoliation can be viewed as an extreme of intercalation.[129] The general idea is to weaken the layer-to-layer interactions by enlarging extremely the interlayer distance. Upon intercalation of specific molecules into the interlayer space of perovskite hosts, excess solvent molecules, usually water, enter the interlayer space, which results in a high degree of swelling.[129] The 3D phase collapse after the layers are completely solvated and the 2D nanosheets are obtained (***Figure GI.13***).

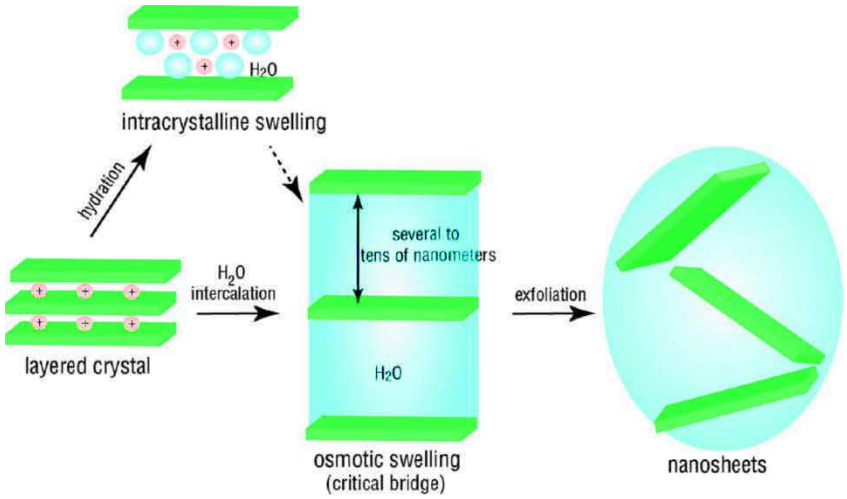

Figure GI.13. *Schematic illustration of the swelling and exfoliation processes.*[129]

Over decades of development, there have been various reports about the successful exfoliations of the three families of layered perovskites.

The use of a bulky organic base such as tetra-(*n*-butyl)ammonium hydroxide (TBA^+OH^-) is a very common approach to realize the exfoliation which has been employed for example for the Dion-Jacobson phases $HCa_2Nb_3O_{10}$[126] or $HLa_2TiTa_2O_{10}$[130] and for the Ruddlesden-Popper phases $H_2SrLaTi_2TaO_{10}$ or $H_2Ca_2Ta_2TiO_{10}$.[124]

Apart from the use of a bulky organic base, in some cases the intercalation of simple alkylamines can also lead to exfoliation. For example $H_{1.8}Bi_{0.2}Sr_{0.8}Ta_2O_7$, which is derived from Aurivillus phase $Bi_2SrTa_2O_9$, has been reported to exfoliate to nanosheets upon reaction with ethylamine aqueous solution.[131] The triple-layer Ruddlesden-Popper phase $H_2La_2Ti_2O_{10}$ has been reported to behave similarly when intercalated by *n*-butylamine.[124] For the exfoliation of $HLaTa_2O_7$, two-step intercalation is necessary: first reaction with ethylamine and then reaction with TBA^+OH^-.[132] Intercalation of a cationic amino acid into $HCa_2Nb_3O_{10}$ by ion-exchange reaction can also induce exfoliation.[111]

GI.4.2.4.2. 2D building blocks

The obtained 2D nanosheets present an extraordinarily rich structural diversity and electronic properties. They have wildly potential applications in the field of catalysis and electronics.[133,134]

The obtained colloidal sheets of layered perovskites are negatively charged and they present a high 2D anisotropy of crystallites: thickness is about 1 nm while lateral size ranges from sub-micrometers to about 100 micrometers.[134] As a result, they are very suitable as 2D building blocks to create new materials with controlled structures at the nano-scale (***Figure GI.14***).[124]

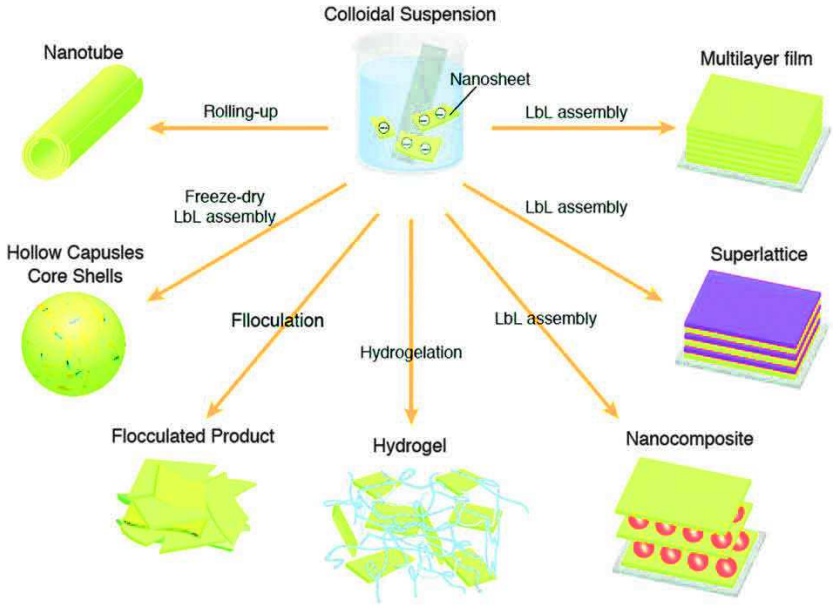

Figure GI.14. *Examples of different nanoarchitectures that can be produced from colloidal suspension of nanosheets.*[135,136]

GI.4.2.4.3. Layer-by-Layer (LBL) assembly

Taking advantage of hybrid approach, building up various functional nanosheets together to create potential multifunctional materials is a promising option.[131] A convenient and efficient way to prepare multilayer thin film materials with specific stacking sequences is Layer-by-Layer (LBL) assembly.[126,137-139] Through this method, the negatively charged nanosheets of layered perovskites can be combined with polycations (for example poly (diallyldimethylammonium chloride): PDDA),[126] metal complex, clusters or even positively charged nanosheets[140,141] (for example the nanosheets of layered Double Hydroxides (LDHs)).

The multilayer film with the stacking sequence $HCa_2Nb_3O_{10}/HLaNb_2O_7/HSr_2Nb_3O_{10}/HLaNb_2O_7$ (alternatively combined with PDDA) have been reported by LBL method.[126] Another multilayer film with a stacking sequence $Mg_{2/3}Al_{1/3}(OH)_2/Ca_2Nb_3O_{10}$ or $Mn_2Al(OH)_6/Ca_2Nb_3O_{10}$ have also reported by combining the positively charged nanosheets of LDHs and the negatively charged nanosheets of Dion-Jacobson phases using the LBL method (***Figure GI.15***).[142,143]

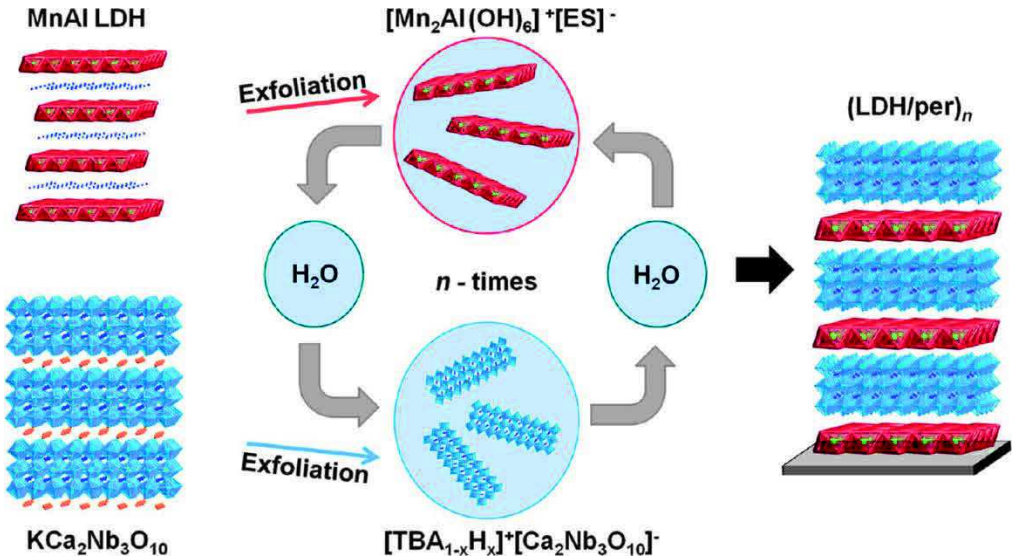

Figure GI.15. *Schematic representation of the liquid-phase process employed to construct hybrid superlattices. Exfoliation of the layered bulk materials into* $Mn_2Al(OH)_6^+$ *and* $Ca_2Nb_3O_{10}^-$ *nanosheets is followed by electrostatic LBL assembly with intermediate washing steps in order to achieve 3D (LDH/perovskite)*$_n$ *heterostructures immobilized on a substrate.*[143]

The development of exfoliation and restacking technology is extraordinary meaningful, which provide an efficient way to design at will new materials with well structural control at nanoscale. This is unrealizable through the traditional high-temperature methods. Combining several types of layered perovskites into a single thin film or a bulk solid with specific stacking sequences is very promising to produce multifunctional materials. Various new perovskites with intergrowth will be prepared.

C. Objective of this thesis

Taking advantage of hybrid approach (based on soft chemistry routes), using layered perovskite oxides as hosts, especially $Bi_2SrTa_2O_9$ which possessing ferroelectricity, to design and prepare new potential multiferroic compounds is our fundamental objective. In order to realize the above objective, the well study of the chemistry functionalization mechanism is a must step. The time-consuming chemistry functionalization processes published in literature (more than a week) should be improved. In this thesis, we manage to establish new procedure, using microwave, allowing considerably decrease the reaction time necessary for functionalization (intercalating, grafting, etc.). In addition, the diversity of the guest organic phases should be expanded but not be limited to some simple organic molecules reported in literature. We also established post-synthesis strategy to further enrich the functionalization methods of layered perovskite oxides by means of click chemistry. In order to prepare hybrids possess potential multiferroic properties, the *in situ* complexation reactions or ion exchange reactions between protonated phase of Aurivillius $Bi_2SrTa_2O_9$ functionalized with polyamines and metal ions in aqueous have been carried out.

References

[1] C. Delmas, Y. Borthomieu, C. Faure, *Solid State Ionics* **1988**, *26*, 152.
[2] J. Gopalakrishnan, *Chem. Mater.* **1995**, *7*, 1265-1275.
[3] D. M. Schleich, *Solid State Ionics* **1994**, *70*, 407-411.
[4] J. Rouxel, M. Tournoux, *Solid State Ionics* **1996**, *84*, 141-149.
[5] R. E. Schaak, T. E. Mallouk, *Chem. Mater.* **2002**, *14*, 1455-1471.
[6] G. A. Seisenbaeva, V. G. Kessler, *Nanoscale* **2014**, *6*, 6229-6244.
[7] C. Sanchez, G. J. d. A. A. Soler-Illia, F. Ribot, T. Lalot, C. R. Mayer, V. Cabuil, *Chem. Mater.* **2001**, *13*, 3061-3083.
[8] S. Gai, C. Li, P. Yang, J. Lin, *Chem. Rev.* **2014**, *114*, 2343-2389.
[9] P. Gomez-Romero, *Adv. Mater.* **2001**, *13*, 163-174.
[10] E. Delahaye, S. Eyele-Mezui, M. Diop, C. Leuvrey, P. Rabu, G. Rogez, *Dalton Trans.* **2010**, *39*, 10577-10580.
[11] *Functional Hybrid Materials*; P. Gómez-Romero, C. Sanchez, Eds.; Wiley-VCH: Weinheim, **2004**.
[12] P. Judeinstein, C. Sanchez, *J. Mater. Chem.* **1996**, *6*, 511-525.
[13] C. Train, R. Gheorghe, V. Krstic, L.-M. Chamoreau, N. S. Ovanesyan, G. L. J. A. Rikken, M. Gruselle, M. Verdaguer, *Nat. Mater.* **2008**, *7*, 729-734.
[14] A. O. Polyakov, A. H. Arkenbout, J. Baas, G. R. Blake, A. Meetsma, A. Caretta, P. H. M. van Loosdrecht, T. T. M. Palstra, *Chem. Mater.* **2012**, *24*, 133-139.
[15] E. Coronado, C. Martí-Gastaldo, E. Navarro-Moratalla, A. Ribera, S. J. Blundell, P. J. Baker, *Nat. Chem.* **2010**, *2*, 1031-1036.
[16] D. Avnir, T. Coradin, O. Lev, J. Livage, *J. Mater. Chem.* **2006**, *16*, 1013-1030.
[17] N. Nassif, J. Livage, *Chem. Soc. Rev.* **2011**, *40*, 849-859.
[18] W. Eerenstein, N. D. Mathur, J. F. Scott, *Nature* **2006**, *442*, 759-765.
[19] S.-W. Cheong, M. Mostovoy, *Nat. Mater.* **2007**, *6*, 13-20.
[20] N. A. Hill, *J. Phys. Chem. B* **2000**, *104*, 6694-6709.
[21] P. Jain, V. Ramachandran, R. J. Clark, H. D. Zhou, B. H. Toby, N. S. Dalal, H. W. Kroto, A. K. Cheetham, *J. Am. Chem. Soc.* **2009**, *131*, 13625-13627.
[22] X.-Y. Wang, L. Gan, S.-W. Zhang, S. Gao, *Inorg. Chem.* **2004**, *43*, 4615-4625.
[23] X.-Y. Wang, Z.-M. Wang, S. Gao, *Chem. Commun.* **2008**, 281-294.
[24] A. Stroppa, P. Jain, P. Barone, M. Marsman, J. M. Perez-Mato, A. K. Cheetham, H. W. Kroto, S. Picozzi, *Angew. Chem. Int. Ed.* **2011**, *50*, 5847-5850.
[25] G. Rogez, N. Viart, M. Drillon, *Angew. Chem. Int. Ed.* **2010**, *49*, 1921-1923.
[26] E. Pardo, C. Train, H. Liu, L.-M. Chamoreau, B. Dkhil, K. Boubekeur, F. Lloret, K. Nakatani, H. Tokoro, S.-i. Ohkoshi, M. Verdaguer, *Angew. Chem. Int. Ed.* **2012**, *51*, 8356-8360.
[27] B. Kundys, A. Lappas, M. Viret, V. Kapustianyk, V. Rudyk, S. Semak, C. Simon, I. Bakaimi, *Phys. Rev. B* **2010**, *81*, 224434.
[28] P. Rabu, M. Drillon, *Adv. Eng. Mater.* **2003**, *5*, 189-210.
[29] E. C. Subbarao, *J. Phys. Chem. Solids* **1962**, *23*, 665-676.
[30] S. M. Blake, M. J. Falconer, M. McCreedy, P. Lightfoot, *J. Mater. Chem.* **1997**, *7*, 1609-1613.
[31] N. C. Bristowe, J. Varignon, D. Fontaine, E. Bousquet, P. Ghosez, *Nat. Commun.* **2015**, *6*.
[32] C. A. P. de Araujo, J. D. Cuchiaro, L. D. McMillan, M. C. Scott, J. F. Scott, *Nature* **1995**, *374*, 627-629.
[33] K. Amanuma, T. Hase, Y. Miyasaka, *Appl. Phys. Lett.* **1995**, *66*, 221-223.
[34] A. Kingon, *Nature* **1999**, *401*, 658-659.
[35] H. Abid, A. Samet, T. Dammak, A. Mlayah, E. K. Hlil, Y. Abid, *J. Lumin.* **2011**, *131*, 1753-1757.
[36] A. Kojima, K. Teshima, Y. Shirai, T. Miyasaka, *J. Am. Chem. Soc.* **2009**, *131*, 6050-6051.

[37] M. Kudo, S. Tsuzuki, K.-i. Katsumata, A. Yasumori, Y. Sugahara, *Chem. Phys. Lett.* **2004**, *393*, 12-16.
[38] K. Gurunathan, P. Maruthamuthu, *J. Solid State Electrochem.* **1998**, *2*, 176-180.
[39] S. Kataoka, S. Banerjee, A. Kawai, Y. Kamimura, J.-C. Choi, T. Kodaira, K. Sato, A. Endo, *J. Am. Chem. Soc.* **2015**, *137*, 4158-4163.
[40] K. G. Sanjaya Ranmohotti, E. Josepha, J. Choi, J. Zhang, J. B. Wiley, *Adv. Mater.* **2011**, *23*, 442-460.
[41] B. R. C. N. R. Rao, *Adv. Mater.* **1995**, *9*.
[42] J. Boltersdorf, N. King, P. A. Maggard, *CrystEngComm* **2015**, *17*, 2225-2241.
[43] Z. Tong, G. Zhang, S. Takagi, T. Shimada, H. Tachibana, H. Inoue, *Chem. Lett.* **2005**, *34*, 632-633.
[44] S. Liu, W. Miiller, Y. Liu, M. Avdeev, C. D. Ling, *Chem. Mater.* **2012**, *24*, 3932-3942.
[45] W. Sugimoto, M. Shirata, Y. Sugahara, K. Kuroda, *J. Am. Chem. Soc.* **1999**, *121*, 11601-11602.
[46] B. Aurivillius, *Ark. Kemi* **1949**, *1*, 463.
[47] B. Aurivillius, *Ark. Kemi* **1949**, *1*, 499.
[48] B. Aurivillius, *Ark. Kemi* **1950**, *2*, 519.
[49] M.-P. Crosnier-Lopez, F. Le Berre, J.-L. Fourquet, *J. Mater. Chem.* **2001**, *11*, 1146-1151.
[50] S. Takahashi, T. Nakato, S. Hayashi, Y. Sugahara, K. Kuroda, *Inorg. Chem.* **1995**, *34*, 5065-5069.
[51] S. Tahara, Y. Sugahara, *Langmuir* **2003**, *19*, 9473-9478.
[52] Y. Wang, C. Wang, L. Wang, Q. Hao, X. zhu, X. Chen, K. Tang, *RSC Adv.* **2014**, *4*, 4047-4054.
[53] P. J. Ollivier, T. E. Mallouk, *Chem. Mater.* **1998**, *10*, 2585-2587.
[54] C. Galven, J.-L. Fourquet, E. Suard, M.-P. Crosnier-Lopez, F. Le Berre, *Dalton Trans.* **2010**, *39*, 3212-3218.
[55] S.-H. Byeon, J.-J. Yoon, S.-O. Lee, *J. Solid State Chem.* **1996**, *127*, 119-122.
[56] T. W. S. Yip, E. J. Cussen, D. A. MacLaren, *Chem. Commun.* **2010**, *46*, 698-700.
[57] Z. Liang, K. Tang, S. Zeng, D. Wang, T. Li, H. Zheng, *J. Solid State Chem.* **2008**, *181*, 2565-2571.
[58] W. Sugimoto, M. Shirata, K. Kuroda, Y. Sugahara, *Chem. Rev.* **2002**, *14*, 2946-2952.
[59] Y. Tsunoda, M. Shirata, W. Sugimoto, Z. Liu, O. Terasaki, K. Kuroda, Y. Sugahara, *Inorg. Chem.* **2001**, *40*, 5768-5771.
[60] *Gmelins Handbuch der Anorganischen Chemie: Bismuth*; Springer-Verlag: Berlin, **1964**.
[61] M. Kudo, H. Ohkawa, W. Sugimoto, N. Kumada, Z. Liu, O. Terasaki, Y. Sugahara, *Inorg. Chem.* **2003**, *42*, 4479-4484.
[62] K. Toda, M. Sato, *J. Mater. Chem.* **1996**, *6*, 1067-1071.
[63] M. Shirata, Y. Tsunoda, W. Sugimoto, Y. Sugahara, *MRS Proceedings* **2000**, *658*, 1-6.
[64] M. N. Ackermann, *J. Chem. Educ.* **1998**, *75*, 523.
[65] W. Sugimoto, M. Shirata, K. Kuroda, Y. Sugahara, *Chem. Mater.* **2002**, *14*, 2946-2952.
[66] Y. Tsunoda, W. Sugimoto, Y. Sugahara, *Chem. Mater.* **2003**, *15*, 632-635.
[67] R. E. Schaak, T. E. Mallouk, *J. Solid State Chem.* **2001**, *161*, 225-232.
[68] J. Gopalakrishnan, T. Sivakumar, K. Ramesha, V. Thangadurai, G. N. Subbanna, *J. Am. Chem. Soc.* **2000**, *122*, 6237-6241.
[69] J. Gopalakrishnan, V. Bhat, *Inorg. Chem.* **1987**, *26*, 4299-4301.
[70] R. E. Schaak, T. E. Mallouk, *J. Solid State Chem.* **2000**, *155*, 46-54.
[71] N. S. P. Bhuvanesh, M.-P. Crosnier-Lopez, H. Duroy, J.-L. Fourquet, *J. Mater. Chem.* **2000**, *10*, 1685-1692.
[72] J. Gopalakrishnan, S. Uma, V. Bhat, *Chem. Mater.* **1993**, *5*, 132-136.
[73] M. Sato, J. Abo, T. Jin, *Solid State Ionics* **1992**, *57*, 285-293.
[74] M. Dion, M. Ganne, M. Tournoux, *Mater. Res. Bull.* **1981**, *16*, 1429-1435.
[75] T. Matsuda, T. Fujita, N. Miyamae, M. Takeuchi, I. Kunoua, *J. Mater. Chem.* **1994**, *4*, 955-958.
[76] T. Matsuda, T. Fujita, M. Kojima, *J. Mater. Chem.* **1991**, *1*, 559-562.
[77] C. H. Mahler, B. L. Cushing, J. N. Lalena, J. B. Wiley, *Mater. Res. Bull.* **1998**, *33*, 1581-1586.

[78] K. Toda, J. Watanabe, M. Sato, *Solid State Ionics* **1996**, *90*, 15-19.
[79] K. Toda, J. Watanabe, M. Sato, *Mater. Res. Bull.* **1996**, *31*, 1427-1435.
[80] R. E. Schaak, D. Afzal, J. A. Schottenfeld, T. E. Mallouk, *Chem. Mater.* **2002**, *14*, 442-448.
[81] K.-A. Hyeon, S.-H. Byeon, *Chem. Mater.* **1999**, *11*, 352-357.
[82] R. E. Schaak, T. E. Mallouk, *J. Am. Chem. Soc.* **2000**, *122*, 2798-2803.
[83] T. A. Kodenkandath, J. N. Lalena, W. L. Zhou, E. E. Carpenter, C. Sangregorio, A. U. Falster, W. B. Simmons, C. J. O'Connor, J. B. Wiley, *J. Am. Chem. Soc.* **1999**, *121*, 10743-10746.
[84] T. A. Kodenkandath, A. S. Kumbhar, W. L. Zhou, J. B. Wiley, *Inorg. Chem.* **2001**, *40*, 710-714.
[85] H. Kageyama, L. Viciu, G. Caruntu, Y. Ueda, J. B. Wiley, *J. Phy. Condens. Matter* **2004**, *16*, S585.
[86] Y. Tsujimoto, H. Kageyama, *Ion-Exchange Reactions for Two-Dimensional Quantum Antiferromagnetism*, **2012**.
[87] L. Viciu, G. Caruntu, N. Royant, J. Koenig, W. L. Zhou, T. A. Kodenkandath, J. B. Wiley, *Inorg. Chem.* **2002**, *41*, 3385-3388.
[88] L. Viciu, J. Koenig, L. Spinu, W. L. Zhou, J. B. Wiley, *Chem. Mater.* **2003**, *15*, 1480-1485.
[89] L. Viciu, V. O. Golub, J. B. Wiley, *J. Solid State Chem.* **2003**, *175*, 88-93.
[90] H. Kageyama, T. Kitano, N. Oba, M. Nishi, S. Nagai, K. Hirota, L. Viciu, J. B. Wiley, J. Yasuda, Y. Baba, Y. Ajiro, K. Yoshimura, *J. Phys. Soc. Jpn.* **2005**, *74*, 1702-1705.
[91] A. J. Jacobson, J. W. Johnson, J. T. Lewandowski, *Inorg. Chem.* **1985**, *24*, 3727-3729.
[92] J. Gopalakrishnan, V. Bhat, B. Raveau, *Mater. Res. Bull.* **1987**, *22*, 413-417.
[93] S. Akbarian-Tefaghi, E. Teixeira Veiga, G. Amand, J. B. Wiley, *Inorg. Chem.* **2016**, *55*, 1604-1612.
[94] A. J. Jacobson, J. W. Johnson, J. T. Lewandowski, *Mater. Res. Bull.* **1987**, *22*, 45-51.
[95] S. Uma, J. Gopalakrishnan, *Mater. Sci. Eng. B* **1995**, *34*, 175-179.
[96] T. Nakato, K. Ito, K. Kuroda, C. Kato, *Microporous Mater.* **1993**, *1*, 283-286.
[97] Z. Zhong, W. Ding, W. Hou, Y. Chen, X. Chen, Y. Zhu, N. Min, *Chem. Mater.* **2001**, *13*, 538-542.
[98] Y.-S. Hong, S.-J. Kim, *Bull. Korean Chem. Soc.* **1996**, *17*, 730-735.
[99] M. Matsuda, T. Hioki, K. Okada, S. Nishimoto, M. Miyake, *J. Phys. Chem. Solids* **2006**, *67*, 1325-1329.
[100] S. Uma, J. Gopalakrishnan, *Chem. Mater.* **1994**, *6*, 907-912.
[101] R. A. M. Ram, A. Clearfield, *J. Solid State Chem.* **1991**, *94*, 45-51.
[102] K.-i. Shimizu, S. Itoh, T. Hatamachi, Y. Kitayama, T. Kodama, *J. Mater. Chem.* **2006**, *16*, 773-779.
[103] Z. Tong, S. Takagi, T. Shimada, H. Tachibana, H. Inoue, *Chem. Lett.* **2005**, *34*, 1406-1407.
[104] S. Tahara, T. Yamashita, G. Kajiwara, Y. Sugahara, *Chem. Lett.* **2006**, *35*, 1292-1293.
[105] Z. Peng, X. Xing, X. Chen, *J. Alloys Compd.* **2006**, *425*, 323-328.
[106] S. Tahara, PhD thesis, Waseda University, **2007**.
[107] S. Tahara, T. Ichikawa, G. Kajiwara, Y. Sugahara, *Chem. Mater.* **2007**, *19*, 2352-2358.
[108] S. Uma, A. R. Raju, J. Gopalakrishnan, *J. Mater. Chem.* **1993**, *3*, 709-713.
[109] S. Tani, Y. Komori, S. Hayashi, Y. Sugahara, *J. Solid State Chem.* **2006**, *179*, 3357-3364.
[110] A. J. Jacobson, J. T. Lewandowski, J. W. Johnson, *J. Less Common Met.* **1986**, *116*, 137-146.
[111] Y.-S. Han, I. Park, J.-H. Choy, *J. Mater. Chem.* **2001**, *11*, 1277-1282.
[112] H. Suzuki, K. Notsu, Y. Takeda, W. Sugimoto, Y. Sugahara, *Chem. Mater.* **2003**, *15*, 636-641.
[113] A. Shimada, Y. Yoneyama, S. Tahara, P. H. Mutin, Y. Sugahara, *Chem. Mater.* **2009**, *21*, 4155-4162.
[114] Y. Takeda, T. Momma, T. Osaka, K. Kuroda, Y. Sugahara, *J. Mater. Chem.* **2008**, *18*, 3581-3587.
[115] Y. Asai, Y. Ariake, H. Saito, N. Idota, K. Matsukawa, T. Nishino, Y. Sugahara, *RSC Adv.* **2014**, *4*, 26932-26939.
[116] C. Wang, K. Tang, D. Wang, Z. Liu, L. Wang, Y. Zhu, Y. Qian, *J. Mater. Chem.* **2012**, *22*, 11086-11092.

[117] Y. Takeda, H. Suzuki, K. Notsu, W. Sugimoto, Y. Sugahara, *Mater. Res. Bull.* **2006**, *41*, 834-841.
[118] S. Yoshioka, Y. Takeda, Y. Uchimaru, Y. Sugahara, *J. Organomet. Chem.* **2003**, *686*, 145-150.
[119] J. R. Boykin, L. J. Smith, *Inorg. Chem.* **2015**, *54*, 4177-4179.
[120] Y. Wang, X. Zhu, X. Li, L. Wang, Y. Wang, Q. Hao, K. Tang, *J. Mater. Chem. A* **2014**, *2*, 15590-15597.
[121] T. Matsuda, N. Miyamae, M. Takeuchi, *Bull. Chem. Soc. Jap.* **1993**, *66*, 1551-1553.
[122] P. V. Der Voort, E. F. Vansant, *J. Liq. Chromatogr.Relat. Technol.* **1996**, *19*, 2723-2752.
[123] T. Sasaki, M. Watanabe, H. Hashizume, H. Yamada, H. Nakazawa, *J. Am. Chem. Soc.* **1996**, *118*, 8329-8335.
[124] R. E. Schaak, T. E. Mallouk, *Chem. Mater.* **2000**, *12*, 3427-3434.
[125] S. Ida, D. Shiga, M. Koinuma, Y. Matsumoto, *J. Am. Chem. Soc.* **2008**, *130*, 14038-14039.
[126] R. E. Schaak, T. E. Mallouk, *Chem. Mater.* **2000**, *12*, 2513-2516.
[127] J. N. Coleman, M. Lotya, A. O'Neill, S. D. Bergin, P. J. King, U. Khan, K. Young, A. Gaucher, S. De, R. J. Smith, I. V. Shvets, S. K. Arora, G. Stanton, H.-Y. Kim, K. Lee, G. T. Kim, G. S. Duesberg, T. Hallam, J. J. Boland, J. J. Wang, J. F. Donegan, J. C. Grunlan, G. Moriarty, A. Shmeliov, R. J. Nicholls, J. M. Perkins, E. M. Grieveson, K. Theuwissen, D. W. McComb, P. D. Nellist, V. Nicolosi, *Science* **2011**, *331*, 568-571.
[128] V. Nicolosi, M. Chhowalla, M. G. Kanatzidis, M. S. Strano, J. N. Coleman, *Science* **2013**, *340*.
[129] F. Geng, R. Ma, Y. Ebina, Y. Yamauchi, N. Miyamoto, T. Sasaki, *J. Am. Chem. Soc.* **2014**, *136*, 5491-5500.
[130] T. Wang, C. N. Henderson, T. I. Draskovic, T. E. Mallouk, *Chem. Mater.* **2013**, *26*, 898-906.
[131] S. Ida, C. Ogata, U. Unal, K. Izawa, T. Inoue, O. Altuntasoglu, Y. Matsumoto, *J. Am. Chem. Soc.* **2007**, *129*, 8956-8957.
[132] L. Won-Jae, Y. Hyun Jung, K. Do-Yun, P. Seung-Min, K. Young-Il, *Bull. Korean Chem. Soc.* **2013**, *34*, 2041-2043.
[133] R. Ma, T. Sasaki, *Adv.Mater.* **2010**, *22*, 5082-5104.
[134] M. Osada, T. Sasaki, *J. Mater. Chem.* **2009**, *19*, 2503-2511.
[135] W. J. Roth, B. Gil, W. Makowski, B. Marszalek, P. Eliasova, *Chem. Soc. Rev.* **2016**, *45*, 3400-3438.
[136] M. Osada, T. Sasaki, *Polym. J.* **2015**, *47*, 89-98.
[137] H. Hata, S. Kubo, Y. Kobayashi, T. E. Mallouk, *J. Am. Chem. Soc.* **2007**, *129*, 3064-3065.
[138] T. Sasaki, Y. Ebina, M. Watanabe, G. Decher, *Chem. Commun.* **2000**, 2163-2164.
[139] Y. Zhou, R. Ma, Y. Ebina, K. Takada, T. Sasaki, *Chem. Mater.* **2006**, *18*, 1235-1239.
[140] F. Leroux, M. Adachi-Pagano, M. Intissar, S. Chauviere, C. Forano, J.-P. Besse, *J. Mater. Chem.* **2001**, *11*, 105-112.
[141] Q. Wang, D. O'Hare, *Chem. Rev.* **2012**, *112*, 4124-4155.
[142] L. Li, R. Ma, Y. Ebina, K. Fukuda, K. Takada, T. Sasaki, *J. Am. Chem. Soc.* **2007**, *129*, 8000-8007.
[143] C. Ziegler, S. Werner, M. Bugnet, M. Wörsching, V. Duppel, G. A. Botton, C. Scheu, B. V. Lotsch, *Chem. Mater.* **2013**, *25*, 4892-4900.

Chapter I

Efficient microwave-assisted functionalization of the Aurivillius phase $Bi_2SrTa_2O_9$

This chapter is essentially based on the article we have published during my Ph-D (Y. Wang et al., *Inorg. Chem.* **2016**, *55,* 4039). I have added some results and discussions which were not treated in the published paper.

I.1. Introduction

Functionalization of ion-exchangeable layered perovskites by intercalation of organic compounds has been widely described in the literature, following the pioneering work on the functionalization of layered niobiates,[1] titanates[2] and titano-nobiates[3,4] by acid-base reactions with amines. Such functionalization process involves first the transformation of the layered perovkites into their protonated forms.[5-7] For Aurivillius phases, this initial transformation involves the selective leaching of the bismuth oxide layers.[8-12] Then the protonated layered perovskites can be functionalized by amines, *via* cation exchange or acid-base reaction.[13-17]

Yet, the published synthetic methods have the important drawback of being very long (typically one week), usually in tetrahydrofuran (THF) or ethanol in reflux or room temperature conditions. One example reports the use of a faster (about one day) room temperature chromatographic process.[18] Due to these very long reaction times, only a limited number of amines have been tested for insertion into protonated layered perovskites. Moreover, this reaction timescale intrinsically limits the type of molecules which can be inserted to very stable and very simple ones.

To overcome this problem, we have explored the use of microwave irradiation applied to protonation of the $Bi_2SrTa_2O_9$ Aurivillius phase (BST) to obtain the protonated form $H_2Bi_{0.1}Sr_{0.85}Ta_2O_7$ (HST) and its subsequent functionalization by various amines. Microwave assisted reactions have essentially been used in organic chemistry,[19] but also in coordination chemistry[20-22] and in materials chemistry.[23-25] It has been also used for the post-functionalization of nanoparticles,[26] MOFs,[27-31] or Layered Simple Hydroxides.[32] Microwave activation has proved to be particularly useful to accelerate reactions, to increase the yields and the purity of compounds under milder reaction conditions and to obtain products which cannot be obtained otherwise. Very recently, the microwave-assisted functionalization of Dion-Jacobson and Ruddlesden-Popper layered perovskites by *n*-alcohols and *n*-alkylamines was reported, with a significant reduction of the reaction times, and no loss in conversion rates.[33,34]

We describe in this chapter the microwave-assisted protonation and functionalization of $Bi_2SrTa_2O_9$ Aurivillius phase, which requires the prior removal of bismuth oxide layers, which is not the case for Dion-Jacobson and Ruddlesden-Popper phases. This method enables synthesizing functionalized hybrid materials from the starting BST phase in only a few hours, with similar conversion rates and crystallinity than more classical routes. In addition, we report how a pre-intercalation strategy may help to functionalize HST. Besides linear aliphatic mono- or di-amines, it is thus possible to functionalize the interlamellar space by other amines, such as 1, 2-cyclohexane diamine or amines bearing an aromatic group for instance.

Among the various amines with which we have functionalized HST, an amine with aromatic group, the phenyl butylamine (PBA), has shown a very peculiar behavior. Indeed, the obtained hybrid materials, HST intercalated by PBA (PBA-HST), could have a variable interlayer distance depending on the preparation methods. We will detail in this chapter the

various studies we have performed in order to better understand this behavior, which was not encountered for the other amines we have tried.

I.2. Results and discussion

I.2.1. Microwave-assisted synthesis of HST

I.2.1.1. Synthesis and structure

HST was synthesized by acid treatment of the starting Aurivillius phase $Bi_2SrTa_2O_9$ (BST) which was synthesized according to published procedures.[35]
The XRD pattern of BST (***Figure I.1***) can be indexed on the basis of an orthorhombic cell (a = 0.5523(4) nm, b = 0.5519(4) nm, c = 2.507(2) nm), in accordance with the reported powder patterns[12,18] and the previously reported structure.[36]
The microwave-assisted acid treatment of BST leads to a compound of elemental formula $H_2Bi_{0.1}Sr_{0.85}Ta_2O_7{\cdot}2H_2O$, hereafter denoted HST. The formula is in good accordance with the one of the room temperature acid-treated BST, $H_{1.8}Bi_{0.2}Sr_{0.8}Ta_2O_7$ which was obtained for the first time by Tsunoda *et al.*.[12] The small difference in the final Bi:Sr:Ta metal composition ratios can be ascribed to a small difference in cation-disorder (Bi↔Sr) in the starting BST products.[11,12,37] The XRD pattern of HST can be indexed in a tetragonal cell (a = 0.3912(3) nm, c = 0.977(1) nm) (***Figure I.1***), in accordance with what was reported previously.[12]

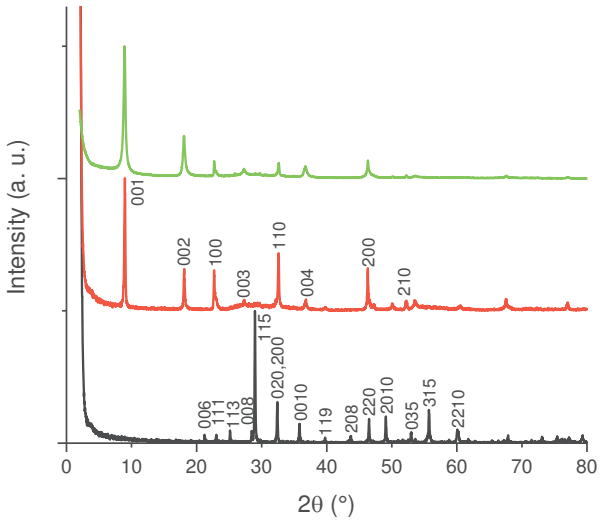

Figure I.1. *Powder XRD patterns of BST (black), "classic-route" HST (red), and HST synthesized using microwave heating (green).*

The size of the crystallites can be evaluated using the Scherrer formula, and compared with the ones obtained when the classical protonation method is used (HCl 4M, room temperature, 5 days).[12] For the *00l* direction, the crystallite size is estimated around 40 nm (70 nm for the "classic-route" HST). For the *h00* direction, the size is estimated around 70 nm (60 nm for the "classic-route" HST). For this comparison, the same batch of BST was used for the classical and for the microwave assisted methods. It appears that the microwave-assisted protonation does not alter significantly the size of the crystallites in the lateral

dimensions. In the *00l* direction the size is reduced with respect to our own classically-made HST sample, but remains within the range of what has been reported in the literature for HST.[12,18] It is worth noticing though that a temperature higher than 70°C leads very rapidly to a significant decrease of crystallinity.
A representative SEM image of HST is presented (***Figure I.2***). The shape and size of the particles are very similar to the ones of our own classically-made HST sample or of the previously reported HST.[12] Therefore, without changing much the crystallinity of the obtained compound, microwave heating allows decreasing considerably the reaction time necessary for the protonation of the Aurivillius phase BST.

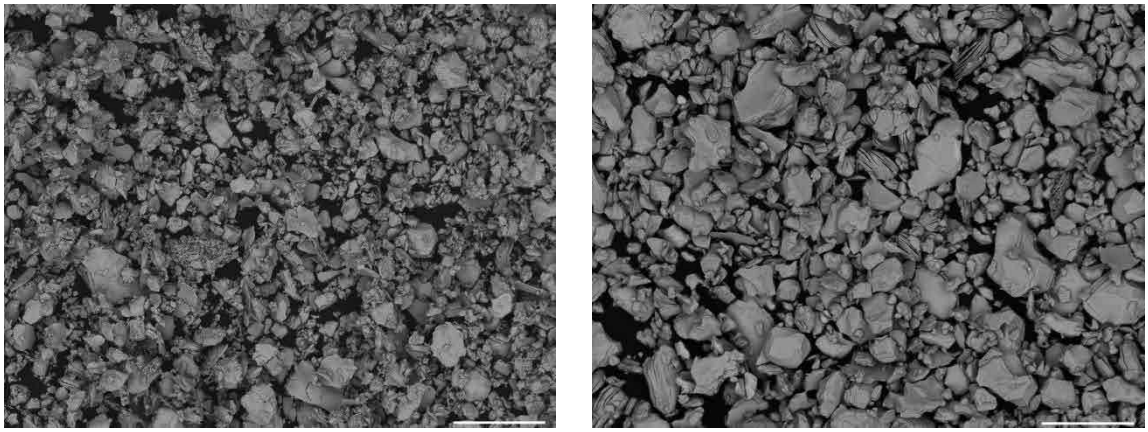

Figure I.2. *SEM images of "classic-route" HST (left), and "microwave" HST (right) (the scale bars correspond to 10 µm).*

I.2.1.2. Thermal analyses

The thermal behaviors of HST have been studied with the help of Thermo Gravimetric and Thermo Differential Analyses (TGA-TDA) (***Figure I.3***). The mass loss before 150°C can be ascribed to the water loss (despite it is not clearly endothermic). Yet this loss is far smaller than expected from the elemental analysis (*ca.* 6 %) probably due to partial dehydration of the sample before the thermal analysis. Apart from the slightly improved crystallinity, the XRD pattern after heating at 150 °C is the same as the one of HST itself (***Figure I.4***). Between 150 °C and 500 °C, a very obvious mass loss occurs (2.7 %) which can be ascribed to the loss of protons on interlayer surface of HST in the form of water (theoretical value *ca.* 3 %).[12] By analogy with what has been described on $H_2SrTa_2O_7$,[38,39] the disappearance of *00l* lines in the XRD pattern at 700 °C might be due to the formation Ta-O-Ta linkages between layers leading to adhesions of perovskite-like slabs.[38] The obtained phase is likely a three-dimensional perovskite with A sites unoccupied or occupied with Sr/Bi ions, the formula of which can be proposed as $Bi_{0.1}Sr_{0.85}Ta_2O_6$ (***Figure I.4a***). Finally, an exothermic event, associated with a weight loss of about 0.9 % occurs at around 850 °C. The XRD pattern of the compound obtained after heating at 1000 °C can be ascribed to a mixture of tungsten bronze phase α-$Bi_{0.1}Sr_{0.85}Ta_2O_6$ and to another phase with the same formula $Bi_{0.1}Sr_{0.85}Ta_2O_6$, by analogy with what has been described on $H_2SrTa_2O_7$,[38,39] with the formation of the tungsten bronze phase α-$SrTa_2O_6$ (isostructural with the tetragonal $K_{0.57}WO_3$)[40] and another orthorhombic phase with the same formula $SrTa_2O_6$ (***Figures I.4a*** **and** ***I.4b***). The transformation between perovskite and tungsten bronze phases normally does not lead to a

change in mass since they possess the same formula. The observed weight loss around 850 °C can be explained by partial Bi removal.

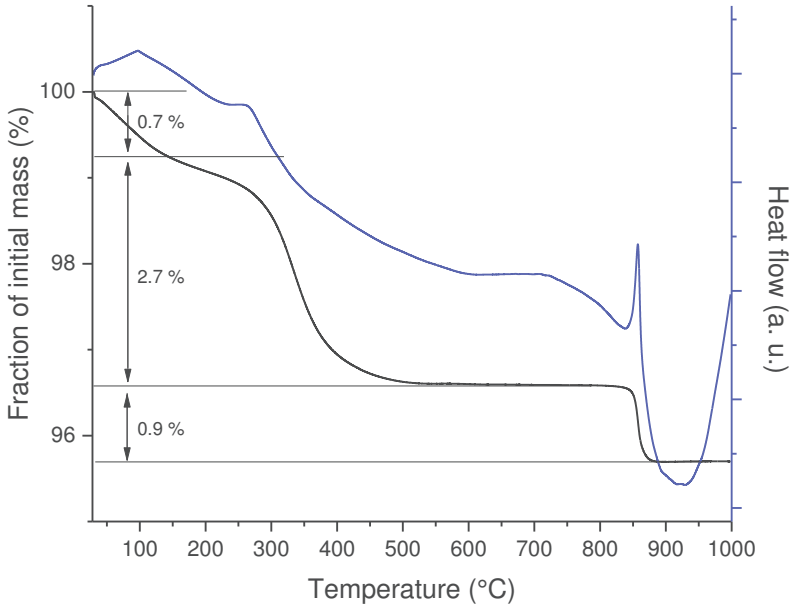

Figure I.3. *TGA (black) and TDA (blue) curves for HST.*

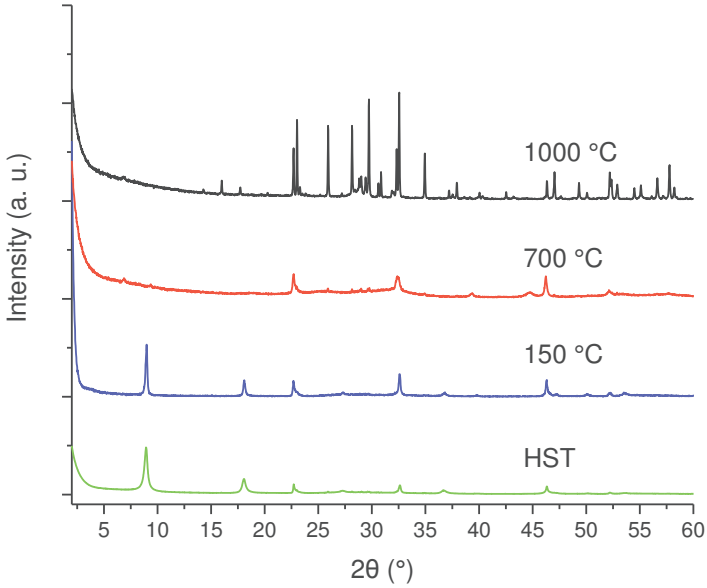

a

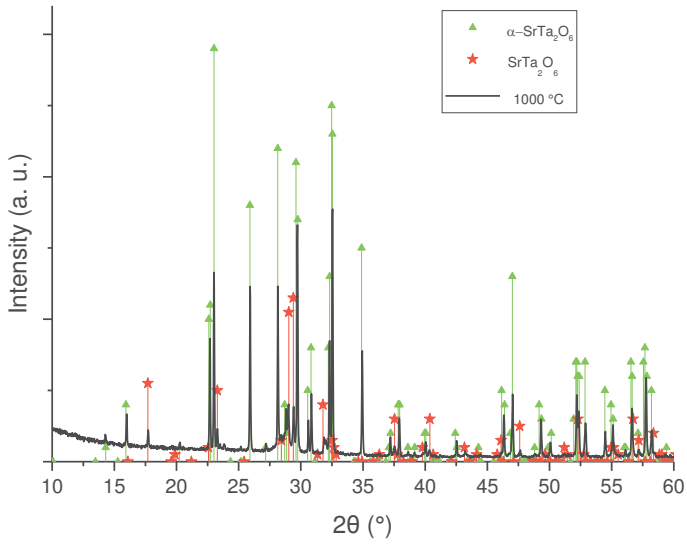

b

Figure I.4. (a): *XRD patterns of the products obtained after thermal treatments of HST at 150 °C (blue), 700 °C (red) and 1000 °C (black);* ***(b):*** *Comparison between the pattern of the product obtained after thermal treatment at 1000 °C and the patterns of the tungsten bronze phase* α*-*$SrTa_2O_6$ *and of* $SrTa_2O_6$*.*

The corresponding SEM images (***Figure I.5)*** clearly display the change of morphology during the heating temperature from 700 °C (left) to 1000 °C (right). It appears that the platelet morphology was retained at 700 °C and lost after the thermal treatment at 1000 °C, where the SEM image also displays a multiphasic aspect, in accordance with the XRD patterns.

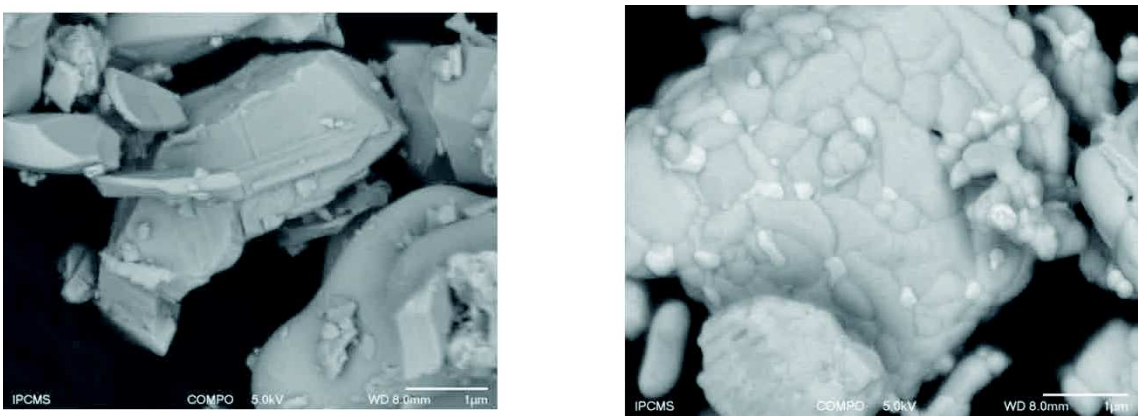

Figure I.5. *SEM images after thermal treatments of HST at 700 °C (left) and 1000 °C (right).*

I.2.2. Microwave-assisted functionalization of HST by aliphatic amines

I.2.2.1. General synthetic procedures and structural characterization

I.2.2.1.1. Synthesis

The insertion of mono-*n*-alkylamines (C_nN-HST) and *α, ω*-diaminoalkanes (C_nN_2-HST) was performed using a large excess (*ca.* ×100) of amine with respect to HST, in a THF/H_2O mixture (5:1 v:v). Large excesses of organic molecule (alcohols, amines or phosphonates) are commonly used to functionalize layered perovskites (Dion-Jacobson, Ruddlesden-Popper or Aurivillius phases) using classical methods.[15,16,18,41-45] Despite many attempts and the use of microwave activation, we have not been able to reduce significantly this ratio. The conditions established for the functionalization of HST (***Table I.1***) are rather general, yet some parameters need to be adjusted finely to achieve the complete insertion of the desired amines. The parameters reported in ***Table I.1*** result from optimization of time and temperature of the reactions.

Product	Starting compound	Temperature (°C)	Duration (min)
C_2N-HST	HST	110	60
C_3N-HST	HST	110	60
C_4N-HST	HST	110	60
$C_{12}N$-HST	HST	130	60
C_2N_2-HST	C_2N-HST	110	60
C_3N_2-HST	C_2N-HST	110	60
C_4N_2-HST	HST	110	60
$C_{12}N_2$-HST	HST	110	60

Table I.1. *Experimental conditions for the insertion of amines into HST.*

I.2.2.1.2. XRD analysis

The XRD patterns of the reaction products are given in ***Figure I.6***. In the low 2θ range, the XRD patterns of the hybrid compounds show essentially series of intense (00*l*) reflections, which evidence their lamellar structure. These (00*l*) reflections are shifted to lower angles with respect to the ones of the starting product HST which are no longer present in the final compounds. This indicates the completeness of the reaction after the exchange process. On the contrary, the out-of-plane reflections of HST are still present and unshifted (for instance the characteristic reflections (100) at 22.68°, (110) at 32.59° and (200) at 46.32° (CuKα1)). This shows that the perovskite-like slab structure has remained essentially unchanged upon the insertion, thus underlining a topotactic reaction.

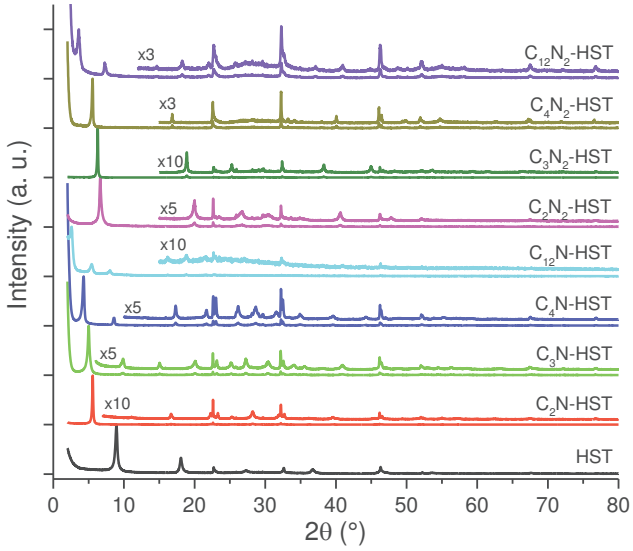

Figure I.6. *Powder XRD patterns (PXRD) of* ***HST*** *and compounds functionalized by linear aliphatic primary amines and diamines.*

The interlayer distance (*c* parameter) can be determined from the (00*l*) reflection. It increases linearly with the number of carbon atoms in the alkyl chain. One finds c parameters of 1.57 nm (C_2N-HST), 1.77 nm (C_3N-HST), 2.07 nm (C_4N-HST) and 3.45 nm (C_{12}N-HST) for *n*-alkylamines, which fits well the relation d (nm) = 1.24 + 0.19 n_C. For *α, ω*-diaminoalkanes, values of 1.32 nm (C_2N_2-HST), 1.41 nm (C_3N_2-HST), 1.56 nm (C_4N_2-HST) and 2.45 nm ($C_{12}N_2$-HST) were observed, leading to the relation d (nm) = 1.09 + 0.11 n_C (***Figure I.7***).

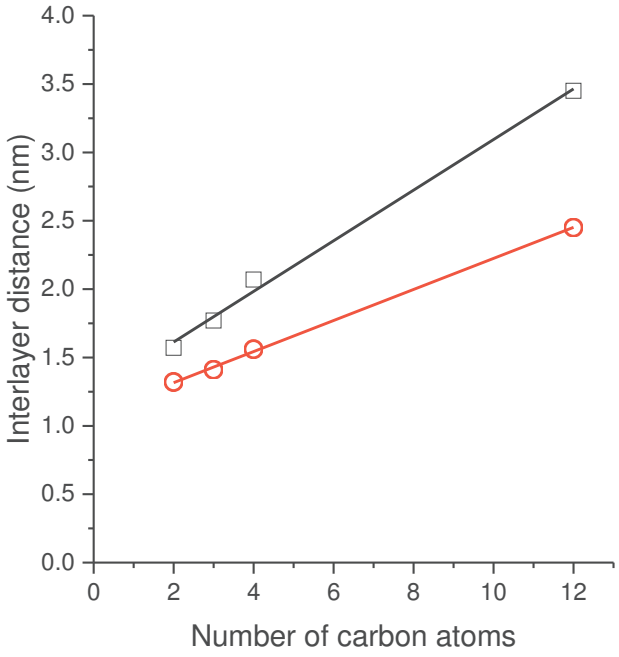

Figure I.7. *Relationship between the number of carbon atoms in the aliphatic chain and the interlayer distance (black: monoamines, red: diamines; open symbols: experimental points, full lines: best linear fit).*

These results suggest a bilayer arrangement in the case of monoamines, and a pillaring of the inorganic layers in the case of diamines, and are in accordance with the ones obtained by classical functionalization.[15,16] The values of the intercepts match well with the expected ones considering the thickness of the inorganic layers (*ca.* 1 nm)[35,36] and, in the case of the bilayer arrangement, with the additional expected distance between the methyl ends of the alkyl chains (*ca.* 0.3 nm).[46] The tilt angles (with respect to the normal to the layers) can be estimated around 40° for the mono-*n*-alkylamines and around 30° for the *α,ω*-diaminoalkanes (***Scheme I.1***), similar to the ones obtained for classical insertion.[15,16]

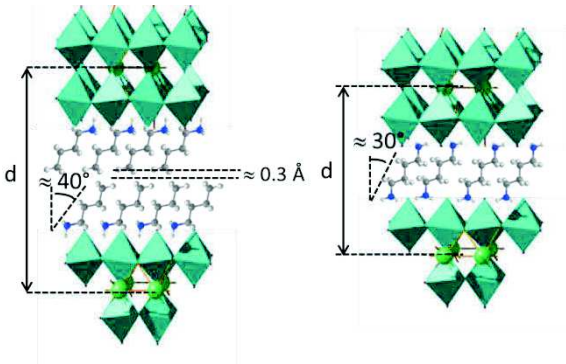

Scheme I.1. *Scheme of the bilayer arrangement of mono-n-alkylamines (left) and of the pillaring arrangement of α, ω-diaminoalkanes (right).*

I.2.2.1.3. Elemental analysis

The formulae of the different compounds have been established by elemental analyses (**Annex**), and are collected in ***Table I.2***.

Product	Formula
C_2N-HST	$(C_2NH)_{0.8}H_{1.2}Bi_{0.1}Sr_{0.85}Ta_2O_7 \cdot 3\ H_2O$ (M = 651 g/mol)
C_3N-HST	$(C_3NH)_{0.8}H_{1.2}Bi_{0.1}Sr_{0.85}Ta_2O_7 \cdot 4.9\ H_2O$ (M = 707 g/mol)
C_4N-HST	$(C_4NH)_{0.9}H_{1.1}Bi_{0.1}Sr_{0.85}Ta_2O_7 \cdot 3.8\ H_2O$ (M = 706 g/mol)
$C_{12}N$-HST	$(C_{12}NH)_{0.7}H_{1.3}Bi_{0.1}Sr_{0.85}Ta_2O_7 \cdot 5.8\ H_2O$ (M = 806 g/mol)
C_2N_2-HST	$(C_2N_2H_2)_{0.4}H_{1.2}Bi_{0.1}Sr_{0.85}Ta_2O_7 \cdot 4.6\ H_2O$ (M = 678 g/mol)
C_3N_2-HST	$(C_3N_2H_2)_{0.4}H_{1.6}Bi_{0.1}Sr_{0.85}Ta_2O_7 \cdot 3.7\ H_2O$ (M = 668 g/mol)
C_4N_2-HST	$(C_4N_2H_2)_{0.6}H_{0.8}Bi_{0.1}Sr_{0.85}Ta_2O_7 \cdot 5.6\ H_2O$ (M = 725 g/mol)
$C_{12}N_2$-HST	$(C_{12}N_2H_2)_{0.7}H_{0.6}Bi_{0.1}Sr_{0.85}Ta_2O_7 \cdot 8.7\ H_2O$ (M = 867 g/mol)

Table I.2. *Proposed formulae.*

For most aliphatic amines the elemental analyses show that out of two potentially reactive protons, only 0.7 to 0.9 react with amines in accordance with what was established by Sugahara *et al.* based on steric considerations and considering the amines can occupy only the cavity sites on the (100) surface of the perovskite layers.[15,16] In the present case though, for C_4N_2 and $C_{12}N_2$, elemental analyses show a slight excess of amines with respect to what is expected with the previous assumptions. This excess may be explained by a denser packing of the amine groups (either quadratic, or even hexagonal) which is still physically acceptable considering steric hindrance of the amines groups.

I.2.2.1.4. Infrared spectroscopy

The infrared spectra of the compounds (***Figure I.8***) show the characteristic vibration bands of the samples. The Ta-O elongation vibration is the dominant feature at 580 cm^{-1}. This band is slightly shifted depending on the sample, without any clear correlation with the functionalization.

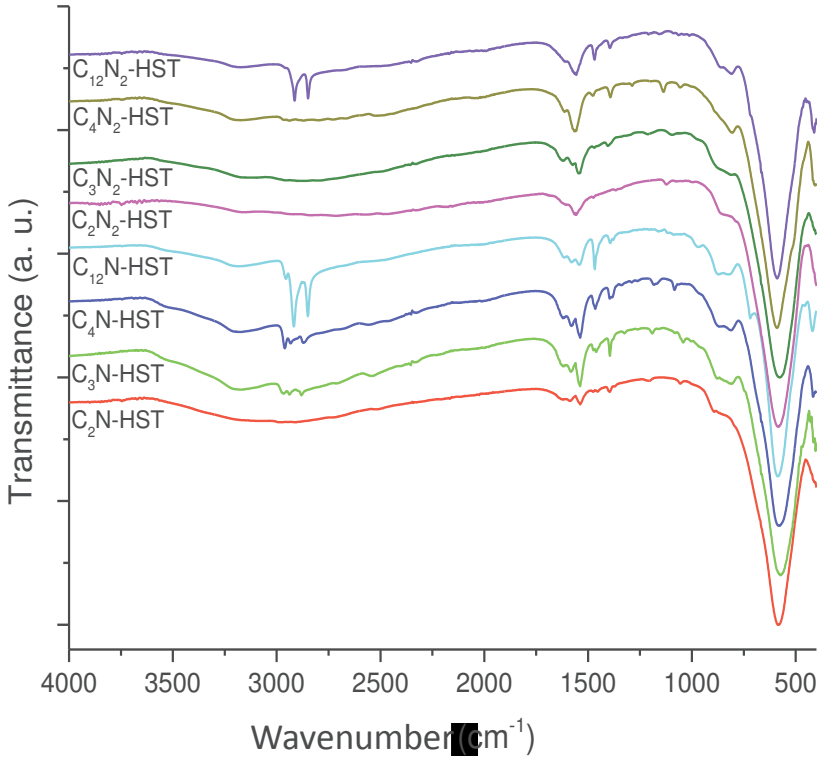

Figure I.8. *Infrared spectra of C_2N-HST, C_3N-HST, C_4N-HST, $C_{12}N$-HST, C_2N_2-HST, C_3N_2-HST, C_4N_2-HST and $C_{12}N_2$-HST (ATR mode).*

The other important features are the vibrations due to the inserted alkylamines. For compounds functionalized with monoamines, the stretching band of the CH_3 groups is visible at 2967, 2962 and 2956 cm^{-1} for C_3N-HST, C_4N-HST and $C_{12}N$-HST respectively, and hardly visible at around 2980 cm^{-1} for C_2N-HST. The position of the asymmetric (ν_{as}) and symmetric (ν_s) CH_2 stretching bands are collected in ***Table I.3*** (for C_2N-HST, C_2N_2-HST and C_3N_2-HST these bands are of too low intensity to be clearly identified).

Product	ν_{as} (CH_2) (cm^{-1})	ν_s (CH_2) (cm^{-1})
C_3N-HST	2940	2880
C_4N-HST	2930	2870
$C_{12}N$-HST	2920	2850
C_4N_2-HST	2940	2870
$C_{12}N_2$-HST	2915	2850

Table I.3. *Position of the IR absorption bands of the methylene groups in C_xN_y-HST compounds.*

The values of ν_{as} and ν_s observed for $C_{12}N$-HST correspond to *all-trans* conformation.[47] When the length of the alkyl chains decreases, the frequencies of these bands increase as expected in the case of gauche conformation,[47] yet, the ratio of gauche conformation is too low to have an influence on the basal spacing, as evidenced by the linear variation of the basal spacing (***Figure I.7***). The bending vibrations for all methylene groups can be seen at 1470 cm^{-1}, whereas the C-N elongation modes of the ammonium can be seen around 1550 cm^{-1}.[48]

I.2.2.1.5. SEM observation

SEM observation for all compounds shows the same morphology of crystallites (see ***Figure I.9*** for representative examples), with stratification typical of lamellar compounds. Crystallites are rather inhomogeneous in size, around several μm.

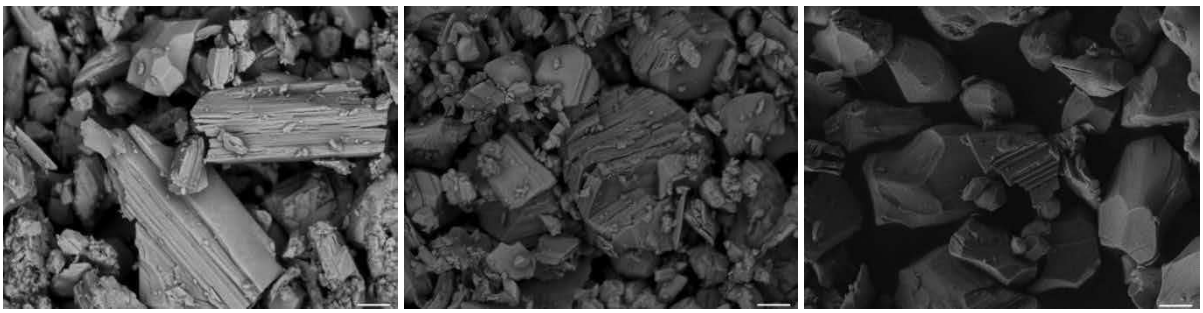

Figure I.9. *SEM images of C_2N_2-HST (left), C_4N-HST (middle) and HST (right) (the scale bar corresponds to 1 μm).*

I.2.2.1.6. TEM observation

The electron diffraction (ED) images of all compounds have been obtained (see ***Figure I.10*** for representative examples), and the calculated lattice parameters (a, b and γ) have been collected in ***Table I.4***. The products intercalated by mono-*n*-alkylamines (except dodecylamine) have almost the same lattice parameters as HST. But for the products intercalated by *α, ω*-diaminoalkanes (except 1, 12-diaminododecane), the parameters, especially the angle γ are slightly modified with respect to HST, indicating that the structure is more constrained by the insertion of the amine molecules.

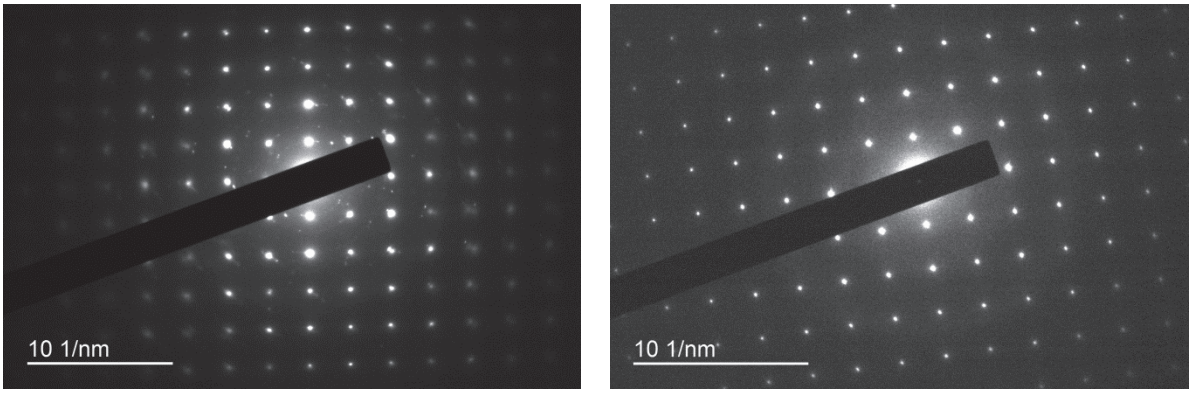

Figure I.10. *ED images for C_4N_2-HST (left) and C_4N-HST (right).*

Product	a (nm)	b (nm)	γ (°)	symmetry
HST	0.3960	0.3940	90	Tetragonal
C_2N-HST	0.3952	0.3952	90	Tetragonal
C_3N-HST	0.3968	0.3968	90	Tetragonal
C_4N-HST	0.3937	0.3937	90	Tetragonal
$C_{12}N$-HST	0.3817	0.3937	92	
C_2N_2-HST	0.3876	0.3745	87.23	
C_3N_2-HST	0.3968	0.3891	87.57	
C_4N_2-HST	0.3861	0.3550	88	
$C_{12}N_2$-HST	0.3869	0.3869	90	Tetragonal

Table I.4. *Calculated lattice parameters according to the obtained ED patterns of the various intercalated products.*

I.2.2.2. Optimization of the reaction conditions, influence of some parameters

I.2.2.2.1. Role of water

During the course of our exploration of the microwave-assisted functionalization of HST, we have been able to evidence the importance of water for the successful insertion of amines. This role was not explicitly mentioned in the initial report of the intercalation of *n*-alkylamines into HST using classical heating in THF (probably because THF was not anhydrous),[16] yet it has been underlined for the intercalation of *α, ω*-diaminoalkanes in HST[15] or for the grafting of alcohols into Dion-Jacobson phases (in this case, it was related to an hydrolysis-etherification mechanism).[41,43] It is worth noticing that the amount of water needed depends on the nature of the amine. For short amines, the amount of water contained into HST is enough to enable the reaction, whereas for more hydrophobic amines, with longer aliphatic chains, typically dodecyl amine and dodecyl diamines, the addition of a certain volume of water is necessary (***Figure I.11***), to increase the polarity of the solvent, and thus its ability to absorb microwaves.[19,33] The standard and optimum THF/water ratio has been determined to be about 5/1 v:v.

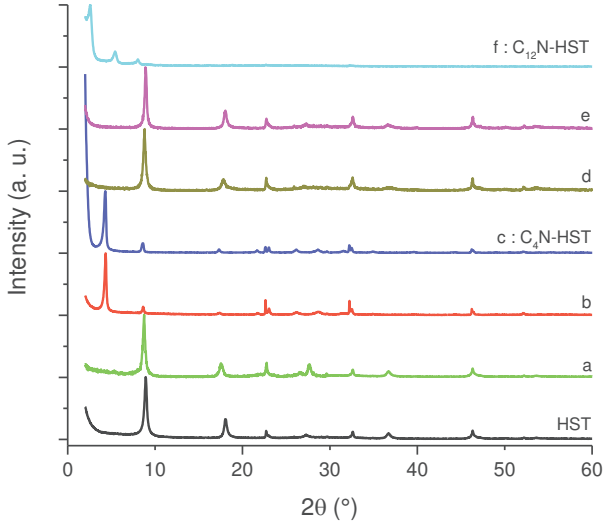

Figure I.11. *Powder XRD patterns of HST, the product of the reaction between dried butylamine and HST (dried at 130°C overnight) in 5 mL of dried THF (microwave, 110°C, 1h) (a), the product of the reaction between dried butylamine and native HST in 5 mL of dried THF (microwave, 110°C, 1h) (b), C_4N-HST (see* ***Annex****) (c), the product of the reaction between dried dodecylamine and HST (dried at 130°C overnight) in 5 mL of dried THF (microwave, 130°C, 1h) (d), the product of the reaction between dried dodecylamine and native HST in 5 mL of dried THF (microwave, 130°C, 1h) (e) and C_{12}N-HST (see* ***Annex****) (f).*

I.2.2.2.2. An efficient pre-intercalation strategy

Despite the great advantage presented by the use of microwave activation for the functionalization of HST in terms of duration of the reactions, it appears that the standard protocol for the insertion is sometimes not totally efficient. This is typically the case for the insertion of short diamines, C_2N_2 and C_3N_2 (***Figure I.12***, graphs a and b), for which the standard insertion protocol from HST leads to multiphasic compounds, even with longer reaction time, or higher temperatures. This might be due to the lower basicity of such diamines which might reduce their reactivity towards HST. The impurity phase is essentially the starting HST, with a slightly modified interlamellar distance probably due to partial insertion of solvent molecules (water and/or THF) during the insertion procedure. To overcome this difficulty, an efficient preinsertion strategy was developed, consisting in using C_2N-HST instead of HST as a starting material for functionalization (***Figure I.12***).

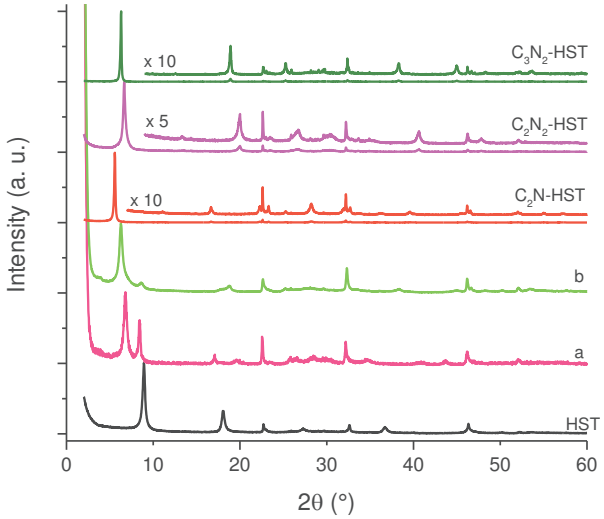

Figure I.12. *Powder XRD patterns of HST, the product of the reaction between 1, 2-diaminoethane and HST (THF/H_2O 5/1 v:v, 110°C, 1h) (a), the product of the reaction between 1, 3-diaminopropane and HST (THF/H_2O 5/1 v:v, 110°C, 1h) (b), C_2N-HST, C_2N_2-HST (from C_2N-HST, see experimental procedure) and C_3N_2-HST (from C_2N-HST, see experimental procedure).*

Such a preintercalation approach was already used for the synthesis of other lamellar hybrid compounds such as hexathiohypodiphosphates (MPS_3), preintercalated by ammonium cations,[49,50] zirconium phosphate, preintercalated by sulfophenylphosphonate,[51-53] Layer Double Hydroxides (LDH) preswelled by formamide,[54] or Layered Simple Hydroxides (LSH), prefunctionalized by dodecylsulfate or dodecylsulfonate.[55,56] Concerning layered oxides, Dion-Jacobson phases have been grafted by *n*-propanol and further by *n*-dodecanol before being functionalized by alkylphosphonic acids.[41]

To the best of our knowledge, associating a preintercalation step with microwave activation is really new.[34] Contrarily to the case of layered hydroxides or Dion-Jacobson phases for which preintercalation is efficient when compounds with long alkyl chains are used, in the case of HST the best results were obtained with prefunctionalization by ethylamine. This observation confirms the result obtained very recently by Wiley and coworkers on Ruddlesden-Popper and Dion-Jacobson derivatives.[34] For instance, long-alkyl chain amines were intercalated in HCT ($H_2CaTa_2O_7$) from pre-intercalated intermediates with short chain alkyl amine, $C_nH_{2n+1}NH_2$-CT (n = 3 or 4). In our case, the functionalization of C_3N-HST or C_4N-HST by exchange reaction with other amines and diamines led to satisfactory results but necessitated longer reaction times or higher temperatures than when the shorter chain C_2N-HST was used.

I.2.3. Microwave-assisted functionalization of HST by more complicated amines

Finally, using this strategy, microwave activation and, when necessary, prefunctionalization, we have been able to insert amines that had never been inserted before in an Aurivillius phase.

I.2.3.1. Direct insertion

I.2.3.1.1. Synthesis

We report here three examples of direct insertion of new amines, bearing a cyclic aliphatic group (cyclohexylamine and aminomethyl-cyclohexane) or an aromatic group (benzylamine) (***Scheme I.2***). The reactions proceed as described above, from HST, without need for preintercalation, although higher temperatures (130°C) and longer reaction times (90 min) were requested.

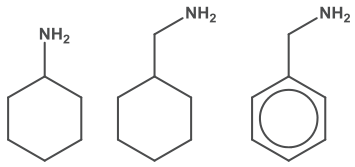

Scheme I.2. *From left to right : cyclohexylamine ($C_6H_{11}NH_2$), aminomethyl-cyclohexane ($C_6H_{11}CH_2NH_2$) and benzylamine ($C_6H_5CH_2NH_2$).*

I.2.3.1.2. XRD and elemental analyses

The XRD patterns of the obtained products are given in ***Figure I.13***. The interlamellar distances are in accordance with a bilayer arrangement of the alkyl groups between the inorganic layers (d = 2.05 nm for $C_6H_{11}NH_2$-HST, 2.07 nm for $C_6H_5CH_2NH_2$-HST and 2.20 nm for $C_6H_{11}CH_2NH_2$-HST). The proposed formulae (***Table I.5***), established from elemental and thermogravimetric analyses (see **Annex**) show that about only one half of the protons of HST have reacted with the amine groups, in accordance with what was observed for linear aliphatic amines, suggesting a similar packing of the organic molecules within the interlamellar space.

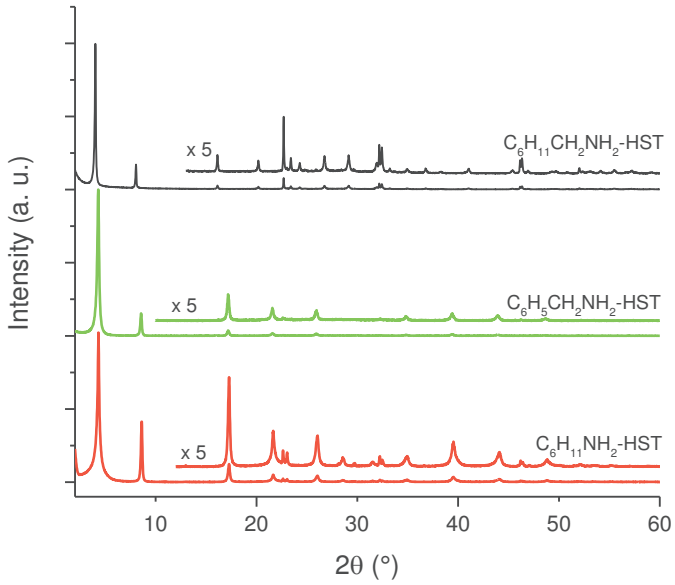

Figure I.13. *Powder XRD patterns of $C_6H_{11}NH_2$-HST, $C_6H_5CH_2NH_2$-HST and $C_6H_{11}CH_2NH_2$-HST.*

Product	Formula
$C_6H_{11}NH_2$-HST	$(C_6H_{11}NH_3)_{0.8}H_{1.2}Bi_{0.1}Sr_{0.85}Ta_2O_7{\cdot}6.0H_2O$ (M = 759 g/mol)
$C_6H_5CH_2NH_2$-HST	$(C_6H_5\ CH_2NH_3)_{0.9}H_{1.1}Bi_{0.1}Sr_{0.85}Ta_2O_7{\cdot}5.5H_2O$ (M = 767 g/mol)
$C_6H_{11}CH_2NH_2$-HST	$(C_6H_{11}CH_2NH_3)_{0.8}H_{1.2}Bi_{0.1}Sr_{0.85}Ta_2O_7{\cdot}1.0H_2O$ (M = 680 g/mol)

Table I.5. *Proposed formulae.*

I.2.3.2. Indirect insertion

I.2.3.2.1. Synthesis

We report here several examples of indirect insertion of complicated diamines bearing cyclic aliphatic group (cyclohexane-1,2-diamine, cyclohexane-1,4-diamine, and 1,4-bis(aminomethyl)-cyclohexane) or an aromatic group (1,4-bis(aminomethyl)-benzene) (***Scheme I.3***) with the help of preintercalation strategy, which employs C_2N-HST instead of HST as a starting material. The reactions proceed as described above with modified reaction temperatures and durations (***Table I.6***).

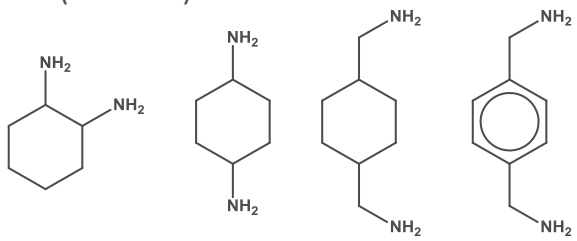

Scheme I.3. *From left to right : cyclohexane-1,2-diamine, cyclohexane-1,4-diamine, 1,4-bis(aminomethyl)-cyclohexane and 1,4-bis(aminomethyl)-benzene.*

Product	Starting compound	Temperature (°C)	Duration (min)
cyclohexane-1,2-diamine-HST	C_2N-HST	90	90
cyclohexane-1,4-diamine-HST	C_2N-HST	130	60
1,4-bis(aminomethyl)-cyclohexane-HST	C_2N-HST	130	60
1,4-bis(aminomethyl)-benzene-HST	C_2N-HST	130	60

Table I.6. *Experimental conditions for the insertion of complicated amines into C_2N-HST.*

I.2.3.2.2. XRD and elemental analyses

The interlamellar distances of the obtained products, except cyclohexane-1, 2-diamine, are in accordance with a pillaring arrangement of the alkyl groups between the inorganic layers (d = 1.57 nm for cyclohexane-1,4-diamine-HST, 1.70 nm for 1,4-bis(aminomethyl)-cyclohexane-HST and 1.61 nm for 1,4-bis(aminomethyl)-benzene-HST). For cyclohexane-1,2-diamine-HST , the interlamellar distance is in accordance with a bilayer arrangement (d = 2.05 nm). The proposed formulae (***Table I.7***), established from elemental and thermogravimetric analyses (see **Annex**) show that the molar ratio between cyclohexane-1,2-diamine and HST is 0.8 (similar as for *n*-alkylamines) and the ones of the three other

diamines are 0.4 (similar as *α, ω*-diaminoalkanes). This further supports the above hypothesis of a different arrangement based on XRD patterns.

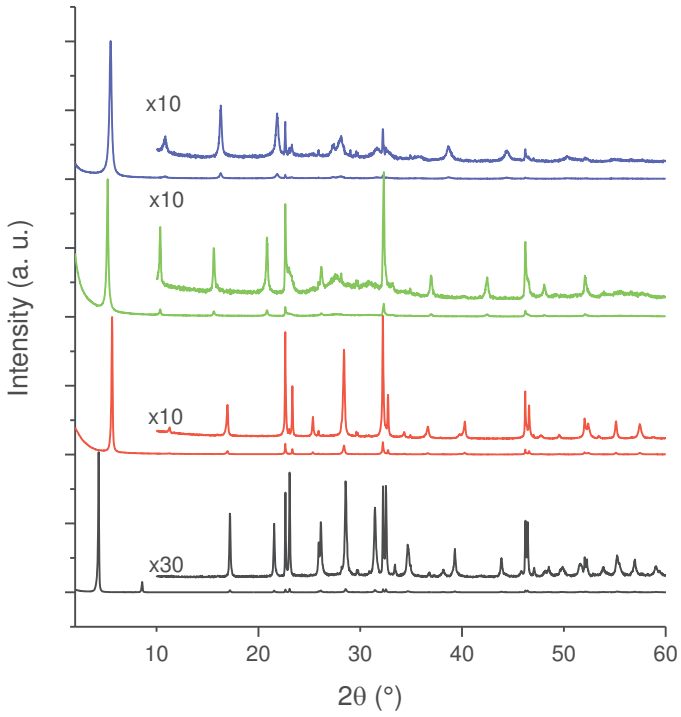

Figure I.14. *Powder XRD patterns of cyclohexane-1,2-diamine-HST (black) (d = 2.05 nm), cyclohexane-1,4-diamine-HST (red) (d = 1.57 nm), 1,4-bis(aminomethyl)-cyclohexane-HST (green) (d = 1.70 nm), 1,4-bis(aminomethyl)-benzene-HST (blue) (d = 1.61 nm).*

Product	Formula
cyclohexane-1,2-diamine-HST	$(C_6H_{10}(NH_3)_2)_{0.8}H_{0.4}Bi_{0.1}Sr_{0.85}Ta_2O_7{\cdot}5.0H_2O$ (M = 753 g/mol)
cyclohexane-1,4-diamine-HST	$(C_6H_{10}(NH_3)_2)_{0.4}H_{1.2}Bi_{0.1}Sr_{0.85}Ta_2O_7{\cdot}1.4H_2O$ (M = 651 g/mol)
1,4-bis(aminomethyl)-cyclohexane-HST	$(C_6H_{10}(CH_2NH_3)_2)_{0.4}H_{1.2}Bi_{0.1}Sr_{0.85}Ta_2O_7{\cdot}1.2H_2O$ (M = 660 g/mol)
1,4-bis(aminomethyl)-benzene-HST	$(C_6H_4(CH_2NH_3)_2)_{0.4}H_{1.2}Bi_{0.1}Sr_{0.85}Ta_2O_7{\cdot}1.3.0H_2O$ (M = 650 g/mol)

Table I.7. *Proposed formulae.*

I.2.3.2.3. Solid state NMR study of cyclohexane-1,2-diamine-HST

For cyclohexane-1,2-diamine-HST, the protonation state of the second amine group remains unclear. Actually, considering its steric hindrance, cyclohexane-1,2-diamine cannot act as a pillar between the inorganic layers. Accordingly, the measured interlamellar spacing is far larger than expected in the case of pillaring (it would then be around the one observed for C_2N_2-HST, *i.e.* 1.3 nm). Yet, the protonation of both amine groups cannot be discarded,

considering they may have reacted with two protons from the same inorganic layer. To further scrutinize this point, solid state NMR study was performed (^{13}C CP/MAS) (collaboration with F. Leroux, Institut de Chimie de Clermont-Ferrand). The spectrum of $C_6H_{10}(NH_2)_2$-HST shows three signals, at 54, 32 and 24 ppm (***Figure I.15***). The upfield shift of the signals with respect to the signals of the unprotonated free amine (56, 33 and 24.5 ppm (^{13}C NMR in D_2O)), and especially of the carbon in β position (33 *vs.* 32 ppm) is attributable to the protonation of the amine groups into ammonium.[15] Moreover the ^{13}C CP/MAS NMR spectrum of $C_6H_{10}(NH_2)_2$-HST shows only three signals, which is in favour of a protonation of both amine groups. Yet the differences between the positions of the signals for $C_6H_{10}(NH_2)_2$-HST and for the free amine are small, and the solid state signals are rather broad, which may mask the presence of two families of signals.

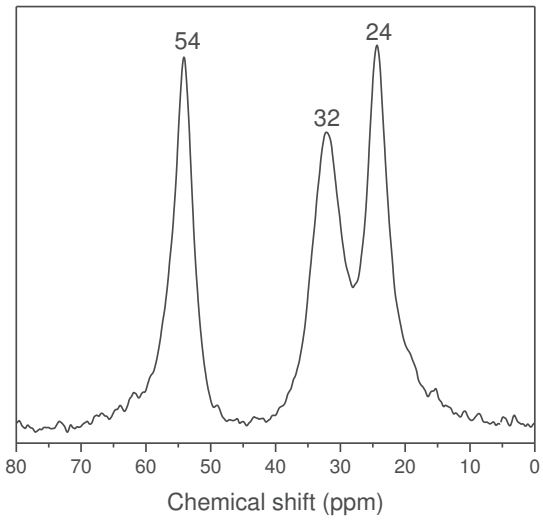

Figure I.15. *^{13}C CP/MAS NMR spectrum of $C_6H_{10}(NH_2)_2$-HST.*

I.2.3.3. Comparing the reactivates between complicated diamines and their corresponding mono amines

It is noteworthy that the attempts of direct intercalation into HST with the above relatively complicate diamines (cyclohexane-1,2-diamine, cyclohexane-1,4-diamine, 1,4-bis(aminomethyl)-cyclohexane and 1,4-bis(aminomethyl)-benzene, ***Scheme I.3***) lead to recover unreacted HST, even with relatively extreme conditions (160 °C, 3h by microwave heating or 160 °C, 3d with a classical oven). Yet, their corresponding monoamines display direct reactivities with HST (***Figure I.13).*** This phenomenon cannot be ascribed to the difference of basicity, since the employed diamines have similar values of pKa (at least pKa_1) with that of their corresponding monoamines. Considering the smaller reactivity towards HST of ethylenediamine with respect with other simple diamines longer carbon chains, for example 1,12-dodecyldiamine, one hypothesis is that the weaker pKa_2 may have a negative role. In addition, the diamines bearing cyclic aliphatic group or aromatic group have higher rigidity with respect to *α,ω*-diaminoalkanes and to their corresponding monoamines. This increased rigidity may also play a role in the decreased reactivity. Finally, considering the successful insertions of the complicated diamines with the help of pre-intercalation

approach, which significantly enlarges the interlayer distance of starting material, the "inertia" of the above complicated diamine is proposed to be ascribed to kinetic barriers.

I.2.3.4. Examples of failed insertion

Combining with pre-intercalation strategy, the established procedure based on microwave irradiation becomes an efficient tool to realize the functionalization of HST with much more various amines than previous reports. Yet, our procedure still seems powerless to functionalize HST with some amines possessing too low pKa values, for example aniline and pyridine, even when the preintercalation strategy was employed. The impossibility to functionalize HST with pyridine had already been reported by using reflux in THF for 7 days.[16] In conclusion, despite great advantages, our strategy based on microwave irradiation and preintercalation cannot overcome thermodynamic limitations.

I.2.4. Inserting phenyl butylamine (PBA) into HST

Among the various amines with which we tried to functionalize HST, phenyl-butylamine (PBA) led to interesting observations. The obtained hybrid materials could have a variable interlayer distance, which can be dominated by the preparation protocols.

I.2.4.1. The three PBA-intercalated phases with different interlayer distances

I.2.4.1.1. Synthesis

The preparations were always performed using a large excess (*ca.* ×100) of PBA with respect to HST or C_2N-HST, in a THF/H_2O mixture (5:1 v:v). The phases obtained by direct intercalation between HST and PBA via microwave irradiation (130 °C, 1.5 h) or via oven (130 °C, 18 h) were called PBA1-HST or PBA3-HST, respectively. The phase PBA2-HST was obtained via microwave irradiation (130 °C, 1.5 h) by using C_2N-HST as an intermediate (pre-intercalation strategy) (see **Annex**).

I.2.4.1.2. XRD analyses

Figure I.16 shows the XRD patterns of HST, C_2N-HST and the three reaction products. After reactions the interlayer distances increase from that of HST (0.98 nm) to 2.20 nm for PBA1-HST and to 3.00 nm for PBA3-HST. For PBA2-HST, the interlayer distance increases from that of C_2N-HST (1.57 nm) to 2.67 nm. In contrast, the characteristic reflections assigned to (100) and (110) in the XRD pattern of HST, are observed at the same positions (22.68° and 32.59°, respectively) for the three phases. Therefore, after the intercalation reactions, the structures of the inorganic perovskite-like slabs are retained.

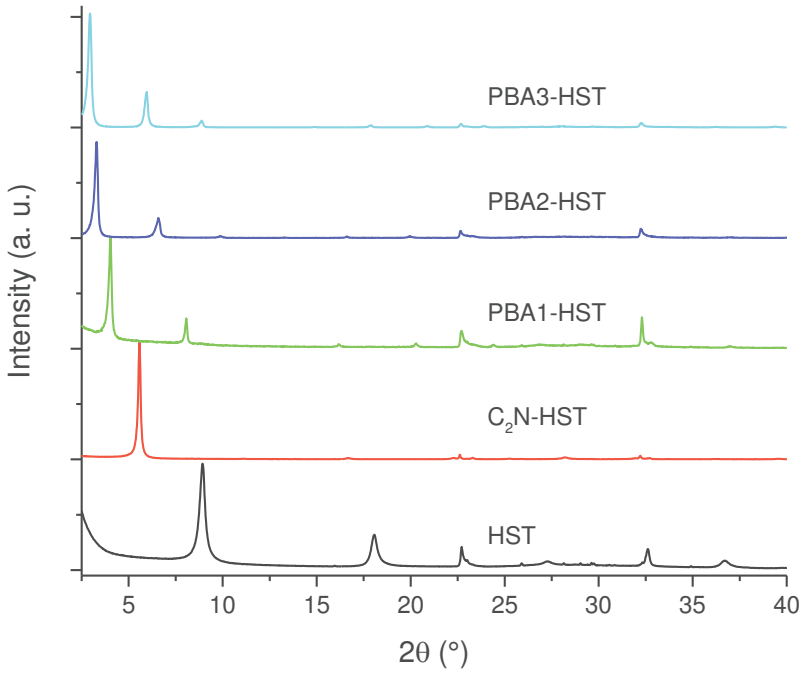

Figure I.16. *PXRD patterns of HST, C_2N-HST, PBA1-HST, PBA2-HST and PBA3-HST.*

I.2.4.1.3. Infrared spectroscopy

The corresponding IR spectra are displayed in **Figure I.17.** For the three obtained phases, very similar IR spectra can be observed. The signals of aromatic group at 3062 and 3026 cm^{-1} and the signals of C-C bond and C-N bond between 1500 cm^{-1} and 1700 cm^{-1} are clearly observed.

The antisymmetric and symmetric stretching bonds of CH_2 groups can also clearly be observed. In order to well study the structure, the values of $\nu_s(CH_2)$, $\nu_{as}(CH_2)$ and $\delta(CH_2)$ of the three products are collected in ***Table I.8***. The antisymmetric stetching bond $\nu_{as}(CH_2)$ decreases from 2929.6 cm^{-1} to 2925.5 cm^{-1} and further to 2920.5 cm^{-1} for PBA1-HST, PBA2-HST and PBA3-HST respectively. In general, the frequency and width of $\nu_{as}(CH_2)$ are sensitive to the gauche/trans conformer ratio and the packing density of methylene chains.[47] The band shifts from lower frequencies, characteristic of highly ordered all-trans conformations , to higher frequencies and increased widths as the number of gauche conformations along the hydrocarbon chain (chain disorder) increases.[47] Therefore, the above results show that the number of all-trans conformations increases and the number of gauche conformations decreases along with the increase of the interlayer distance of PBA-intercalated products.

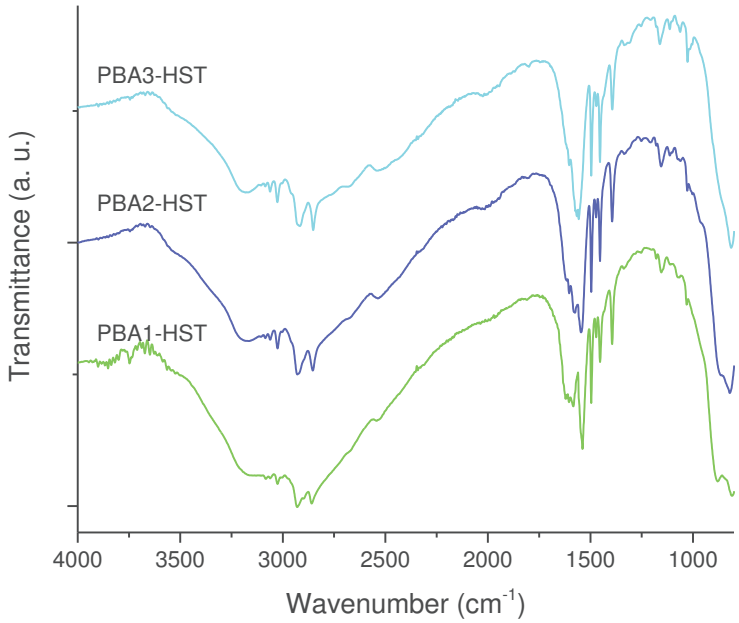

Figure I.17. *Infrared spectra of PBA1-HST, PBA2-HST and PBA3-HST.*

Product	ν_{as} (CH_2) (cm^{-1})	ν_s (CH_2) (cm^{-1})	δ (CH_2) (cm^{-1})
PBA1-HST	2929.6	2860.1	1471.8
PBA2-HST	2925.5	2853.7	1471.8
PBA3-HST	2920.5	2851.9	1471.1

Table I.8. Position of the IR absorption bands of the CH_2 groups in *PBA1-HST, PBA2-HST and PBA3-HST.*

In addition, δ(CH_2) decreases from 1471.8 cm^{-1} to 1471.8 cm^{-1} and to 1471.1 cm^{-1} for PBA1-HST, PBA2-HST and PBA3-HST, respectively. And the intensity of δ(CH_2) also decreases. The δ(CH_2) is sensitive to inter-chain intercalation and the packing arrangement of the chains with frequencies ranging from 1466 to 1472 cm^{-1}.[47] In general, higher frequencies (*ca.* 1472 cm^{-1}) indicate ordering of the methylene chains in an all-trans crystalline state and the lower frequency (ca.1466 cm^{-1}), band broadening and decreasing intensity indicate a decrease in inter-chain interactions and an increase in chain motion which is normally associated with a liquid state.[47] According to the values of δ (CH_2) (about 1472 cm^{-1}), it appears that PBA in three phases have ordered methylene chains in an all-trans crystalline state. In addition, the slight decrease of the values and the intensity of δ (CH_2) observed at the spectra of PBA-3 indicates the decreasing of the inter-chain interactions and the increasing of chain motion as the interlayer distance of the reaction products increases. This seems to imply the reduced degree of overlap of the two PBA layers (bilayer arrangement) within the interlayer space of PBA-3.

I.2.4.1.4. Thermal analyses

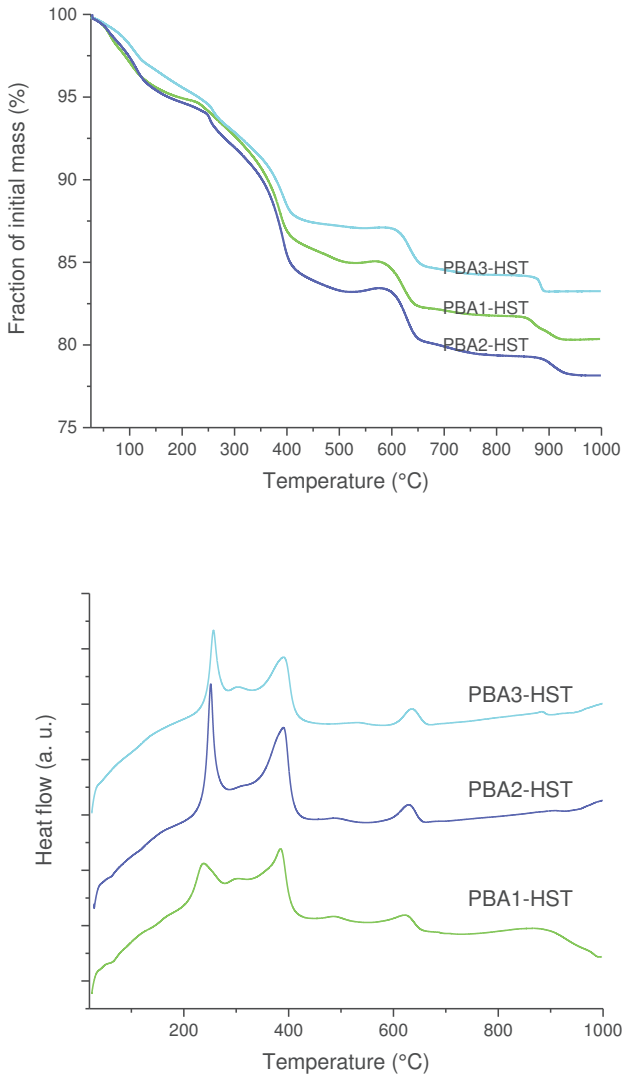

Figure I.18. *TGA (top) and DTA (bottom) curves for PBA1-HST, PBA2-HST and PBA3-HST.*

Figure I.18 shows the TG and DTA curves of PBA1-HST, PBA2-HST and PBA3-HST. The first mass losses occur before 125 °C (4%, 4% and 3% for PBA1-HST, PBA2-HST and PBA3-HST, respectively) and are ascribed to the removal of water. The TGA curves show very obvious mass losses (11.1%, 12.6% and 10.3% for PBA1-HST, PBA2-HST and PBA3-HST, respectively) between 125 °C and 500 °C, associated to clear exothermic events. This second mass loss is thus attributed to the removal of PBA. Finally the mass losses (*ca.* 3%) between 600°C and 700°C are believed to come from the loss of proton in the form of water (cf. paragraph **I.2.1.2**). Finally, the mass losses around 900 °C (1.6%, 1.2% and 1.0% for PBA1-HST, PBA2-HST and PBA3-HST, respectively) are proposed to be due to partial Bi removal and formation of the tungsten bronze phase (cf. paragraph **I.2.1.2**). According to the above analyses, the formulae of the three phases PBA1-HST, PBA2-HST and PBA3-HST can be estimated as follows: $(C_6H_5C_4H_8NH_2)_{0.5}H_{1.5}Bi_{0.1}Sr_{0.85}Ta_2O_7{\cdot}1.4\ H_2O$, $(C_6H_5C_4H_8NH_2)_{0.6}H_{1.4}Bi_{0.1}Sr_{0.85}Ta_2O_7{\cdot}1.6\ H_2O$ and $(C_6H_5C_4H_8NH_2)_{0.5}H_{1.5}Bi_{0.1}Sr_{0.85}Ta_2O_7{\cdot}1.0\ H_2O$, respectively. Since the three phases

have almost the same content of organic molecules, the various interlayer distances cannot be attributed to the difference of the content of PBA.

I.2.4.1.5. Solid state NMR study

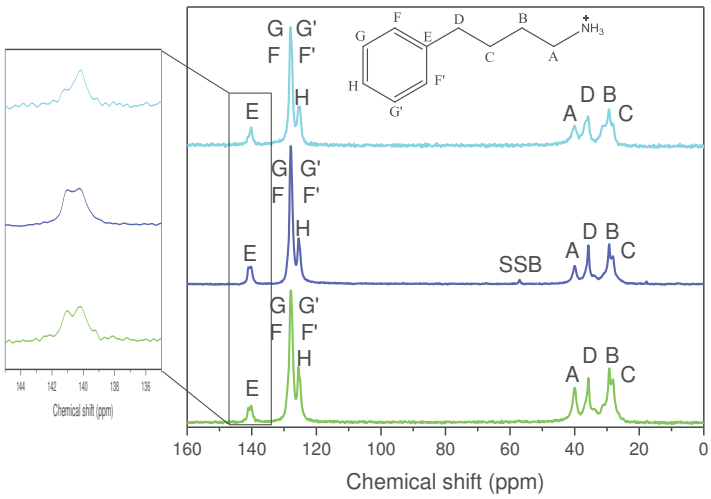

Figure I.19. *Solid-state ^{13}C CP/MAS NMR spectra of PBA1-HST (bottom), PBA2-HST (middle) and PBA3-HST (top).*

In order to further insight into the structure of hybrids, solid state NMR spectroscopy was employed (collaboration F. Leroux, Institut de Chimie de Clermont-Ferrand). The solid-state ^{13}C CP/MAS NMR spectra (***Figure I.19***) display a high degree of similarity between the three phases. According to the spectra, the signals of carbon A and carbon B appear at 40 ppm and 29 ppm, respectively, in all of three products. Yet, in the liquid-state ^{13}C NMR spectrum of PBA (in D_2O), the signals of carbon A and carbon B appear at 42.1 ppm and 33.4 ppm, respectively. As described before, the observed up-field shifts of A and B carbon indicate the conversion of $–NH_2$ groups to $–NH_3^+$ groups.[57-60] In addition, the signal of carbon E appears at 142.4 ppm in the liquid-state ^{13}C NMR spectrum. But in the solid-state ^{13}C CP/MAS NMR spectra of the three products, the signal of carbon E appears twinned at 141 ppm and 140 ppm. In the spectra of PBA3-HST, the signal at 140 ppm is much stronger than the one at 141 ppm whereas for PBA1-HST and PBA2-HST the two signals have about the same intensity. Until now, we have no explication for this phenomenon.

I.2.4.1.6. TEM observation

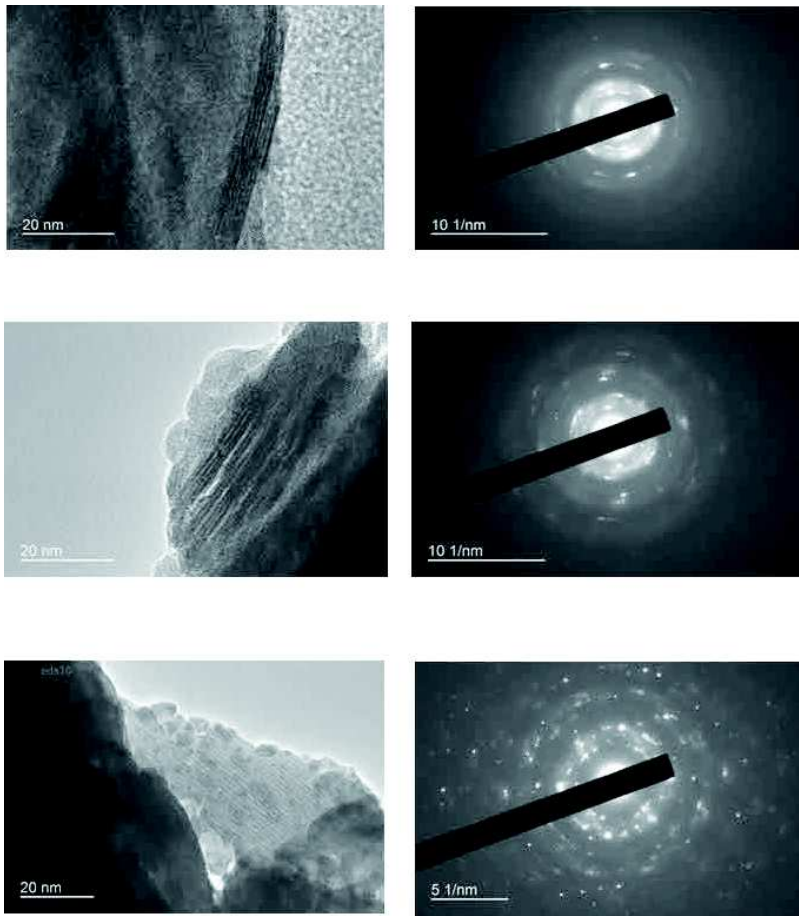

Figure I.20. *TEM images and the corresponding Electron Diffraction (ED) images of the three products PBA1-HST (top), PBA2-HST (middle) and PBA3-HST (bottom).*

Transmission Electron Microscopy (TEM) has also been employed to try to get new information on the three PBA-HST phases (***Figure I.20***). According to the TEM images, it is clear to observe the layered structures of the three products. Unfortunately, it was not possible to obtain useful information from the ED patterns.

As conclusion, up to now we have not been able to obtain information which could help to precise the arrangement of the PBA molecules within the interlayer space of HST and the reasons why different arrangements are obtained depending on the reaction conditions. 1D electron density maps are currently being extracted from the XRD patterns (collaboration C. Taviot-Guého, Institut de Chimie de Clermont-Ferrand) (high quality powder XRD patterns have been obtained, showing at least ten harmonics for the 00l diffraction lines). We hope that such analysis will allow to precise the intralayer arrangements.[61] In the following paragraph we report a more detailed study of the influence of the reaction conditions on the interlayer distance of PBA-HST intercalated compounds.

I.2.4.2. Study the effect of reaction conditions on the interlayer distance of PBA-HST intercalated products

I.2.4.2.1. Reaction temperature

First, the reaction temperature was taken as a variable (80 °C, 130 °C or 160 °C). The microwave assisted (1.5h) reactions were always performed using a large excess (*ca.* ×100) of PBA with respect to HST, in a THF/H_2O mixture (5:1 v:v). ***Figure I.21*** shows the XRD patterns of HST and its reaction products with PBA at 80 °C, 130 °C and 160 °C, respectively. The reflections at 80 °C are the same as the ones of HST indicating that the intercalation reaction does not take place at all. Instead, the interlayer distance increases from that of HST (0.98 nm) to 2.20 nm or to 2.65 nm, respectively, as the reaction temperature increase from 130 °C to 160 °C. Although there is some remaining starting material in the product of 160 °C, it appears that higher reaction temperature is advantageous for increasing the interlayer distance.

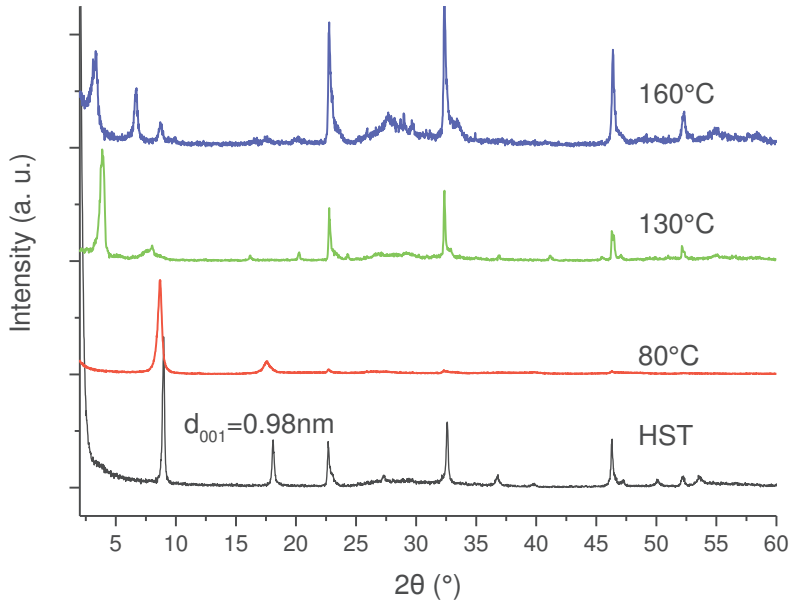

Figure I.21. *XRD patterns of HST and its reaction products with PBA at 80 °C, 130 °C and 160 °C, respectively.*

I.2.4.2.2. Reaction time

Secondly, the reaction time is selected as a variable (0.5 h, 1.5 h, 3h or 4.5 h). The microwave assisted (130 °C) reactions were always performed using a large excess (*ca.* ×100) of PBA with respect to HST, in a THF/H_2O mixture (5:1 v:v). ***Figure I.22*** shows the XRD patterns of HST and its reaction products with PBA at 130 °C by using 0.5 h, 1.5 h, 3 h and 4.5 h as reaction time, respectively. According to the XRD patterns, the interlayer distance of reaction products increase from 2.20 nm to 2.72 nm, as the corresponding reaction time increase from 0.5 h to 4.5 h. Even there is some remaining starting material in the reaction products, it also seems that longer reaction time is advantageous for increasing the interlayer distance.

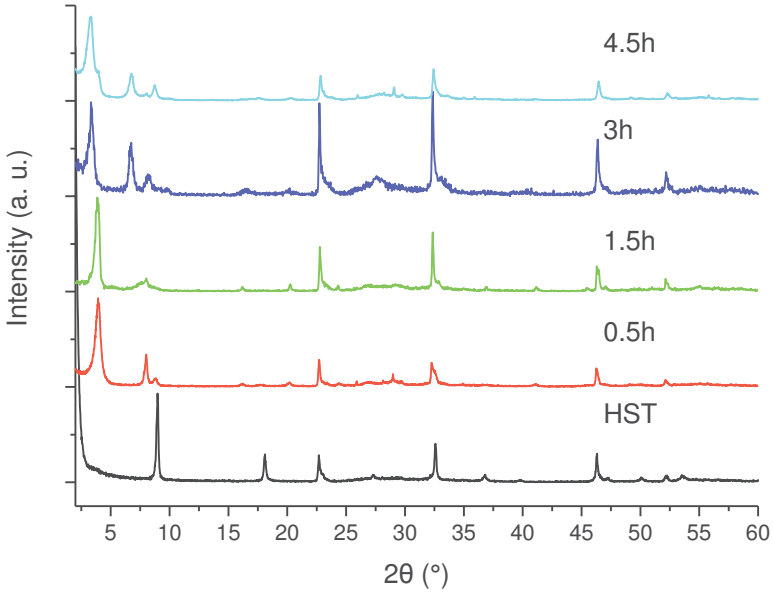

Figure I.22. *XRD pattern of HST and its reaction products with PBA at 130 °C by using 0.5 h, 1.5 h, 3 h and 4.5 h as reaction time, respectively.*

I.2.4.2.3. Molar ratio of PBA/HST

Finally, the molar ration between PBA and HST (PBA/HST) is taken as a variable (1, 2, 5, 10, 50, 100, and 200). The microwave assisted (130 °C, 1.5 h) reactions were always performed in a THF/H_2O mixture (5:1 v:v). ***Figure I.23*** shows the XRD patterns of HST and the reaction products at 130 °C with the value of PBA/HST as follows: 1, 2, 5, 10, 20, 50, 100 and 200. According to the XRD pattern, the interlayer distances of reaction products are almost always around 2.2 nm except for the very low PBA/HST ratio (1 and 2) for which new different phases were obtained (at 1.25 nm for the ratio PBA/HST = 1, and at around 3 nm for the ratio PBA/HST = 2, most probably corresponding to swelling). In conclusion, there is not an obvious effect of the molar ration between PBA and HST on the interlayer distance.

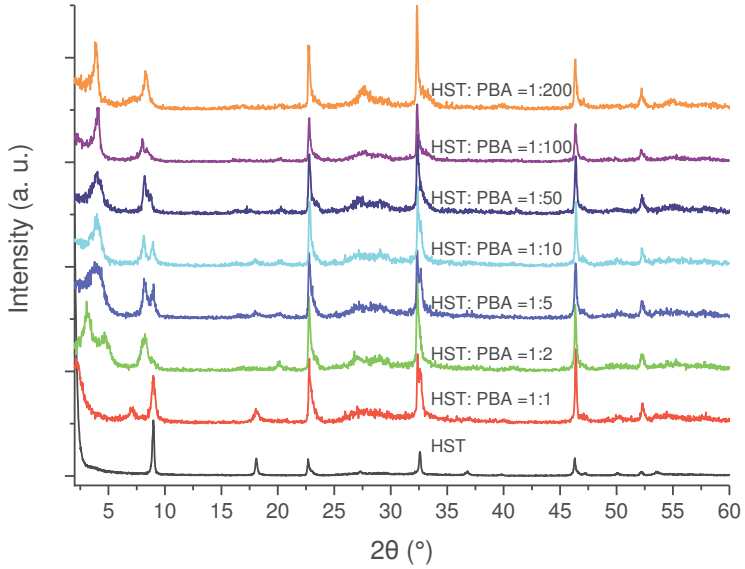

Figure I.23. *XRD pattern of HST and the reaction products at 130 °C with the value of PBA/HST as follows: 1, 2, 5, 10, 20, 50, 100 and 200. (The relatively low crystallinity of the compounds obtained here is due to a low crystallinity of the HST batch used for this set of experiments, due to a problem with the microwave oven during the synthesis of HST. Unfortunately up to now we did not have the time to reproduce this set of experiments.)*

I.2.4.3. Mutual conversion between PBA2-HST and PBA3-HST

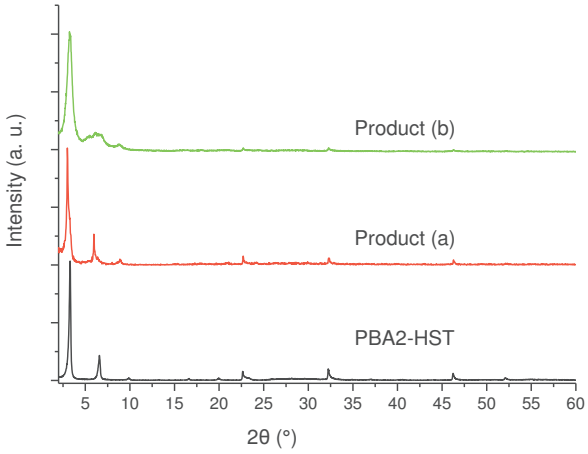

Figure I.24. *XRD patterns illustrating the mutual conversions between PBA2-HST and PBA3-HST. Product (a): PBA2-HST was stirred in acetone at room temperature overnight. Product (b): Product (a) was stirred in water at room temperature overnight.*

The possibility of mutual conversion between the three obtained products (PBA1-HST, PBA2-HST and PBA3-HST) has been tested by using solvent treatment. As shown in ***Figure I.24***, the interlayer distance increases from 2.67 nm to 2.95 nm when PBA2-HST (50 mg) was stirred in acetone (15 mL) at room temperature overnight. As the interlayer distance of the obtained solid (Product (a)) is almost as same as that of PBA3-HST, it seems that the conversion from PBA2-HST to PBA3-HST can be realized. In addition, according to

the XRD patterns, the interlayer distance decreases from 2.95 nm to 2.62 nm when Product (a) was then stirred in water (15 mL) at room temperature overnight. As a result, the conversion from PBA3-HST to PBA2-HST can also be realized, although there is hydrolysis behavior during the process. The above results indicate that the mutual conversion between PBA2-HST and PBA3-HST can be realized by simple solvent treatments. In addition, we have also studied the possibility of mutual conversion between PBA1-HST and PBA2-HST or the mutual conversion between PBA1-HST and PBA3-HST by similar operations. Yet, for the moment we have not find the proper conditions to realize these conversions.

I.3. Conclusion

In conclusion, the microwave-assisted acidification of the $Bi_2SrTa_2O_9$ Aurivillius phase, involving specific removal of the bismuth oxide layers, and its subsequent microwave-assisted functionalization by various amines has been described. Our results complete the recent studies on the use of the microwave approach to the hybridization of layered perovskites belonging to the Ruddlesden-Popper and Dion-Jacobson families. This approach appears to be really general and can be applied to a wide variety of amines and polyamines with a considerable gain in the duration of the reactions (a few hours, compared to several days for the classical strategy), without noticeable changes in the yields or crystallinity of the obtained hybrid compounds, compared to more classical routes. Even if thermodynamic limits remain (weakly basic amines, such as aniline or pyridine, seem impossible to insert), the fast heating provided by microwave and the pre-intercalation strategy described here allow to overcome some kinetic restrictions to the insertion of even bulky amines.
This opens the way for the insertion of new, more complex and functional amines in order to endow the obtained compounds with new properties, designed at will (luminescence, non-linear optics, magnetism) and possibly to microwave-assisted exfoliation.
We will see in the following chapters, that this strategy (microwave assisted reactions and prefunctionalization) can further be extended to the grafting of alcohols (chapter II) and to *in situ* reactions (chapters III and IV).

References

[1] R. Nedjar, M. M. Borel, B. Raveau, *Z. Anorg. Allg. Chem.* **1986**, *540/541*, 198-204.
[2] P. Clément, R. Marchand, *C. R. Acad. Sc. Paris* **1983**, *296*, 1161-1164.
[3] S. Kikkawa, M. Koizumi, *Mat. Res. Bull.* **1980**, *15*, 533-539.
[4] H. Rebbah, B. M. M., B. Raveau, *Mat. Res. Bull.* **1980**, *15*, 317-321.
[5] S. Uma, A. R. Raju, J. Gopalakrishnan, *J. Mater. Chem.* **1993**, *3*, 709-713.
[6] J. Gopalakrishnan, V. Bhat, *Mat. Res. Bull.* **1987**, *22*, 413-417.
[7] J. Gopalakrishnan, S. Uma, V. Bhat, *Chem. Mater.* **1993**, *5*, 132-136.
[8] Z. Liang, K. Tang, S. Zeng, D. Wang, T. Li, H. Zheng, *J. Sol. St. Chem.* **2008**, *181*, 2565-2571.
[9] M. Kudo, S. Tsuzuki, K.-i. Katsumata, A. Yasumori, Y. Sugahara, *Chem. Phys. Lett.* **2004**, *393*, 12-16.
[10] W. Sugimoto, M. Shirata, K. Kuroda, Y. Sugahara, *Chem. Mater.* **2002**, *14*, 2946-2952.
[11] W. Sugimoto, M. Shirata, Y. Sugahara, K. Kuroda, *J. Am. Chem. Soc.* **1999**, *121*, 11601-11602.
[12] Y. Tsunoda, M. Shirata, W. Sugimoto, Z. Liu, O. Terasaki, K. Kuroda, Y. Sugahara, *Inorg. Chem.* **2001**, *40*, 5768-5771.
[13] S. Tahara, A. Shimada, N. Kumada, Y. Sugahara, *J. Sol. St. Chem.* **2007**, *180*, 2517-2524.
[14] Y.-S. Hong, S.-J. Kim, *Bull. Korean Chem. Soc.* **1996**, *17*, 730-735.
[15] S. Tahara, T. Yamashita, G. Kajiwara, Y. Sugahara, *Chem. Lett.* **2006**, *35*, 1292-1293.
[16] Y. Tsunoda, W. Sugimoto, Y. Sugahara, *Chem. Mater.* **2003**, *15*, 632-635.
[17] C. Sun, P. Peng, L. Zhu, W. Zheng, Y. Zhao, *Eur. J. Inorg. Chem.* **2008**, *2008*, 3864-3870.
[18] Z. Peng, X. Xing, X. Chen, *J. Alloys Compd.* **2006**, *425*, 323-328.
[19] C. O. Kappe, *Chem. Soc. Rev.* **2008**, *37*, 1127-1139.
[20] M.-H. Zeng, Y.-L. Zhou, W.-X. Zhang, M. Du, H.-L. Sun, *Cryst. Growth Des.* **2009**, *10*, 20-24.
[21] A. Pons-Balague, N. Ioanidis, W. Wernsdorfer, A. Yamaguchi, E. C. Sanudo, *Dalton Trans.* **2011**, *40*, 11765-11769.
[22] S. H. Jhung, J. H. Lee, J.-S. Chang, *Micropor. Mesopor. Mater.* **2008**, *112*, 178-186.
[23] K. J. Rao, B. Vaidhyanathan, M. Ganguli, P. A. Ramakrishnan, *Chem. Mater.* **1999**, *11*, 882-895.
[24] A. N. Ergün, Z. Ö. Kocabaş, M. Baysal, A. Yürüm, Y. Yürüm, *Chem. Engineer. Commun* **2013**, *200*, 1057-1070.
[25] H. J. Kitchen, S. R. Vallance, J. L. Kennedy, N. Tapia-Ruiz, L. Carassiti, A. Harrison, A. G. Whittaker, T. D. Drysdale, S. W. Kingman, D. H. Gregory, *Chem. Rev.* **2014**, *114*, 1170-1206.
[26] D. Toulemon, B. P. Pichon, C. Leuvrey, S. Zafeiratos, V. Papaefthimiou, X. Cattoën, S. Bégin-Colin, *Chem. Mater.* **2013**, *25*, 2849-2854.
[27] Y. Yoo, V. Varela-Guerrero, H.-K. Jeong, *Langmuir* **2011**, *27*, 2652-2657.
[28] K. M. L. Taylor-Pashow, J. D. Rocca, Z. Xie, S. Tran, W. Lin, *J. Am. Chem. Soc.* **2009**, *131*, 14261-14263.
[29] M. Kim, S. J. Garibay, S. M. Cohen, *Inorg. Chem.* **2011**, *50*, 729-731.
[30] D. J. Lun, G. I. N. Waterhouse, S. G. Telfer, *J. Am. Chem. Soc.* **2011**, *133*, 5806-5809.
[31] S. M. Cohen, *Chem. Rev.* **2012**, *112*, 970-1000.
[32] O. Palamarciuc, E. Delahaye, P. Rabu, G. Rogez, *New J. Chem.* **2014**, *38*, 2016-2023.
[33] J. R. Boykin, L. J. Smith, *Inorg. Chem.* **2015**, *54*, 4177-4179.
[34] S. Akbarian-Tefaghi, E. Teixeira Veiga, G. Amand, J. B. Wiley, *Inorg. Chem.* **2016**, *55*, 1604-1612.
[35] S. Ida, C. Ogata, U. Unal, K. Izawa, T. Inoue, O. Altuntasoglu, Y. Matsumoto, *J. Am. Chem. Soc.* **2007**, *129*, 8956-8957.
[36] A. D. Rae, J. G. Thompson, R. L. Withers, *Acta Cryst. Sect. B* **1992**, *48*, 418-428.
[37] S. M. Blake, M. J. Falconer, M. McCreedy, P. Lightfoot, *J. Mater. Chem.* **1997**, *7*, 1609-1613.
[38] P. J. Ollivier, T. E. Mallouk, *Chem. Mater.* **1998**, *10*, 2585-2587.

[39] M.-P. Crosnier-Lopez, F. Le Berre, J.-L. Fourquet, *J. Mater. Chem.* **2001**, *11*, 1146-1151.
[40] F. Galasso, L. Katz, R. Ward, *J. Am. Chem. Soc.* **1959**, *81*, 5898-5899.
[41] A. Shimada, Y. Yoneyama, S. Tahara, P. H. Mutin, Y. Sugahara, *Chem. Mater.* **2009**, *21*, 4155-4162.
[42] S. Tahara, T. Ichikawa, G. Kajiwara, Y. Sugahara, *Chem. Mater.* **2007**, *19*, 2352-2358.
[43] H. Suzuki, K. Notsu, Y. Takeda, W. Sugimoto, Y. Sugahara, *Chem. Mater.* **2003**, *15*, 636-641.
[44] S. Takahashi, T. Nakato, S. Hayashi, Y. Sugahara, K. Kuroda, *Inorg. Chem.* **1995**, *34*, 5065-5069.
[45] K.-i. Shimizu, S. Itoh, T. Hatamachi, Y. Kitayama, T. Kodama, *J. Mater. Chem.* **2006**, *16*, 773-779.
[46] C. Rösner, G. Lagaly, *J. Sol. St. Chem.* **1984**, *53*, 92-100.
[47] R. A. Vaia, R. K. Teukolsky, E. P. Giannelis, *Chem. Mater.* **1994**, *6*, 1017-1022.
[48] K. Nakanishi, T. Goto, M. Ohashi, *Bull. Chem. Soc. Jap.* **1957**, *30*, 403-408.
[49] T. Coradin, R. Clément, P. G. Lacroix, K. Nakatani, *Chem. Mater.* **1996**, *8*, 2153-2158.
[50] P. G. Lacroix, R. Clément, K. Nakatani, J. Zyss, I. Ledoux, *Science* **1994**, *263*, 658-660.
[51] J. L. Colón, C.-Y. Yang, A. Clearfield, C. R. Martin, *J. Phys. Chem.* **1988**, *92*, 5777-5781.
[52] J. L. Colón, C.-Y. Yang, A. Clearfield, C. R. Martin, *J. Phys. Chem.* **1990**, *94*, 874-882.
[53] Q. Wang, D. Yu, Y. Wang, J. Sun, J. Shen, *Langmuir* **2008**, *24*, 11684-11690.
[54] G. Huang, S. Ma, X. Zhao, X. Yang, K. Ooi, *Chem. Commun.* **2009**, 331-333.
[55] E. Delahaye, S. Eyele-Mezui, J.-F. Bardeau, C. Leuvrey, L. Mager, P. Rabu, G. Rogez, *J. Mater. Chem.* **2009**, *19*, 6106-6115.
[56] E. Delahaye, S. Eyele-Mezui, M. Diop, C. Leuvrey, P. Rabu, G. Rogez, *Dalton Trans.* **2010**, *39*, 10577-10580.
[57] S. Tahara, T. Yamashita, G. Kajiwara, Y. Sugahara, *Chem. Lett.* **2006**, *35*, 1292-1293.
[58] B. Kamieński, W. Schilf, T. Dziembowska, Z. Rozwadowski, A. Szady-Chełmieniecka, *Solid State Nuclear Magnetic Resonance* **2000**, *16*, 285-289.
[59] Y. Komori, Y. Sugahara, K. Kuroda, *Applied Clay Science* **1999**, *15*, 241-252.
[60] M. Wallau, J. Patarin, I. Widmer, P. Caullet, J. L. Guth, L. Huve, *Zeolites* **1994**, *14*, 402-410.
[61] J. Demel, J. Hynek, P. Kovář, Y. Dai, C. Taviot-Guého, O. Demel, M. Pospíšil, K. Lang, *J. Phys. Chem. C* **2014**, *118*, 27131-27141.

Chapter II

Alcohol grafting *vs.* amine insertion

II.1. Introduction

Surface modification of layered compounds via grafting reactions to prepare various inorganic–organic hybrid materials has been widely studied.[1-7] The obtained hybrids possess strong iono-covalent bonds between organic molecules and the inorganic layer.[8] This strategy of surface modification *via* grafting reactions is suitable for the ion-exchangeable layered perovskites which include Dion-Jacobson phase and Ruddlesden-popper phase. For Dion-Jacobson phases, the grafting reactions of protonated phase $HLaNb_2O_7 \cdot xH_2O$ with alcohols,[9,10] with polyether,[11] with fluoro-alcohol,[12] or with organophosphonic acids[13] have been well described in literature. The grafting reactions of $HSr_2Nb_3O_{10}$[14] or $HCa_2Nb_3O_{10}$[15] with alcohols have also already been achieved. In addition, for Ruddlesden-popper phases, the grafting reactions between $H_2La_2Ti_3O_{10}$ and *n*-alcohols have also been reported.[16] However, the published methods are limited to reflux and autoclave, and they have the important drawback of being very long (typically several days).
The structure of perovskite-like slabs in Aurivillius phase $Bi_2SrTa_2O_9$ (BST) presented in the previous chapter is closely similar to those of ion-changeable layered perovskites. The protonated phase $H_{1.8}Bi_{0.2}Sr_{0.8}Ta_2O_7$ (HST) is very similar to Ruddlesden-Popper phase.[17] In addition, a very similar phase, protonated double-layered perovskite $H_2CaTa_2O_7$, has been reported to be grafted by *n*-alcohols by using an intermediate pre-reaction with an *n*-alkylamine.[18,19] The results described in the previous chapter gave us good reasons to believe that the interlayer surface modification via grafting reaction was also possible for HST. In addition, in view of its many advantages in the process of intercalation of HST with alkylamines, the microwave irradiation was among our first considerations.
In this chapter, we will present the rapid processes of successful preparation of various alkoxy derivatives of HST via microwave irradiation. Two different methods of preparation have been used and will be compared in this chapter: in the first one, we used as an intermediate HST functionalized by *n*-alkylamines, in the second one, we considered alcohol-exchange-type reactions. Besides linear aliphatic mono-alcohols, grafting HST with aliphatic diols and some bulky alcohols has also been carried out. The role of water and of the nature of the intermediate hybrid used will be discussed. Finally, the comparison of the reactivity of $-NH_2$ and $-OH$ groups towards HST has also been well investigated, either for an intermolecular competition (using butylamine and ethanol) or for an intramolecular competition (using 5-amino-pentan-1-ol).

II.2. Results and discussion

II.2.1. Attempts of direct interlayer surface modification of HST with EtOH

As described in literature, HST can directly react with *n*-alkylamines to form inorganic-organic hybrids[17] and some protonated forms of Dion-Jacobson phases, $HLaNb_2O_7 \cdot xH_2O$, $HCa_2Nb_3O_{10} \cdot xH_2O$ and $HSr_2Nb_3O_{10} \cdot xH_2O$, can directly react with *n*-alcohol to form grafted *n*-alkoxy derivatives.[10,14,15] Therefore, studying the possibility of directly modify the interlayer surface of HST seemed logical.

II.2.1.1. Synthesis

Attempts of direct modification of the interlayer surface of HST (50 mg) with EtOH (8 mL) by microwave irradiation (130 °C, 2h) or heating in oven (160 °C, 3 d) have been carried out in the presence of water (1 ml).

II.2.1.2. XRD analysis

Figure II.1 shows the powder XRD patterns of HST and its reaction products with EtOH. After reaction, the patterns of the reaction product *via* microwave irradiation (130°C, 2 h) (a) and of the reaction product *via* heating in oven (160°C, 3 d) (b) are almost identical to the one of HST. The interlamellar distances increase slightly with respect to the one of HST (1.00 nm compared to 0.98 nm). This difference is very small, and not compatible with a successful grafting of ethanol (an interlamellar distance of around 1.5 nm is expected). This tiny increase of the interlamellar distance may be ascribed to different water content.

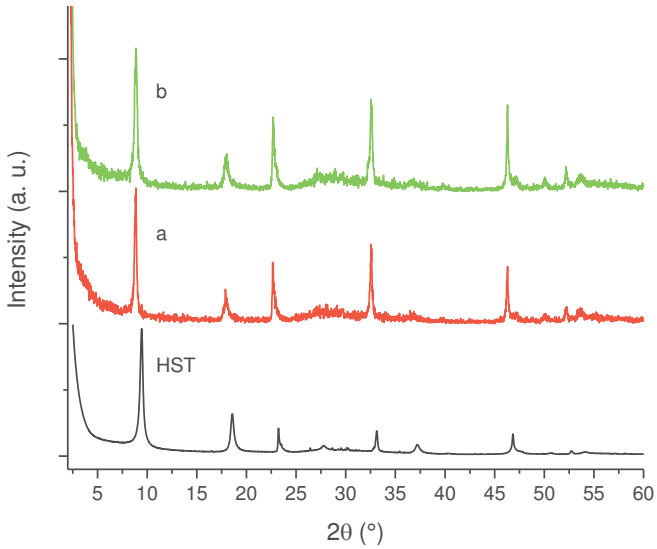

Figure II.1. *PXRD patterns of HST and its reaction product with EtOH. (a): the reaction product between HST and EtOH via microwave irradiation (130°C, 2 h); (b): the reaction product between HST and EtOH via heating in oven (160°C, 3 d).*

II.2.1.3. Infrared spectroscopy

The corresponding IR spectra (***Figure II.2***) do not display any signal coming from an organic phase, which confirms the failure of the direct grafting reactions and the conservation of the starting material HST.

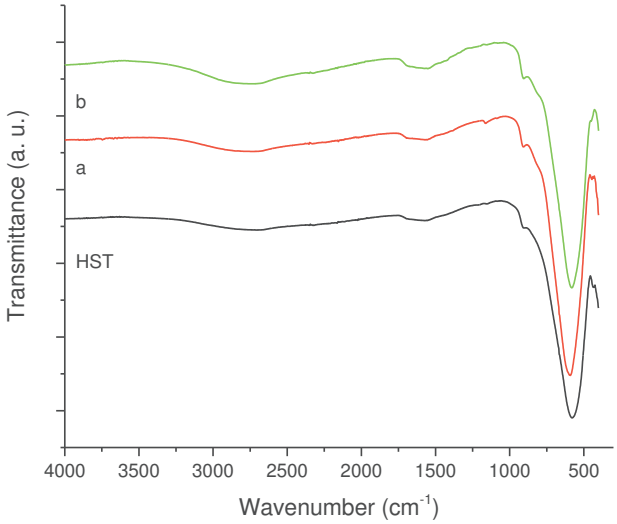

Figure II.2. *IR spectra of HST and its reaction product with EtOH. (a): the reaction product between HST and EtOH via microwave irradiation; (b): the reaction product between HST and EtOH via heating in oven.*

In conclusion, even if we have used relatively drastic conditions, both in terms of temperature and duration, the direct grafting of ethanol into HST failed. Considering our experience with amine insertion, it is very unlikely that any other condition would work. Therefore the direct insertion of ethanol into HST seems impossible, even using microwave. This result is identical to the ones reported for other Ruddlesden-Popper layered perovskites.[16,18,19]

II.2.2. Indirect interlayer surface modification of HST with *n*-alcohols.

II.2.2.1. Grafting reactions between amine pre-intercalated-HST and *n*-alcohols ($C_nH_{2n+1}OH$, n = 1, 2, 3, 4, 7, 12).

According to the work of P. Van Der Voort *et al.*, primary amines are known as catalysts to promote the silylation of silica surface and formation of Si-O-Si.[20] Furthermore, the very similar phase, protonated double-layered perovskite $H_2CaTa_2O_7$, has been reported to be grafted by *n*-alcohols by using an intermediate pre-intercalation of $H_2CaTa_2O_7$ with an *n*-alkylamine.[18,19] Therefore, the reactivity of HST with *n*-alkylamines, which has been described before (**cf. chapter I**), offers a possibility of indirect interlayer surface modification of this layered perovskite with *n*-alcohols.

II.2.2.1.1. General syntheses

Three different intermediates have been chosen as starting materials: NH_3-HST (HST intercalated by ammonium), C_2N-HST (HST intercalated by ethylamine) and C_4N-HST (HST intercalated by butylamine). The microwave-assisted (130 °C, 2h) grafting reactions were then performed using a large excess (more than ×200) of *n*-alcohols with respect to intermediates and a little of water (*ca.* 1.3 mass %, with respective to *n*-alcohols).

II.2.2.1.2. NH_3-HST as starting material

II.2.2.1.2.1. XRD analysis

First, the intermediate NH_3-HST has been used as a starting material to react with *n*-alcohols (C_nOH, n = 1, 2, 3). ***Figure II.3*** shows the XRD patterns of NH_3-HST and its reaction products with *n*-alcohols. The XRD patterns of compounds (e) (reaction with ethanol) and (f) (reaction with propanol) are almost identical to the one of NH_3-HST, indicating the failure of the grafting reactions. For compound (d) (reaction with the shortest alcohol, methanol), the XRD pattern shows clearly a mixture of the starting material NH_3-HST (interlamellar distance of 1.06 nm) and a new phase with an interlamellar distance of 1.23 nm, which corresponds to the effective grafting of methanol.

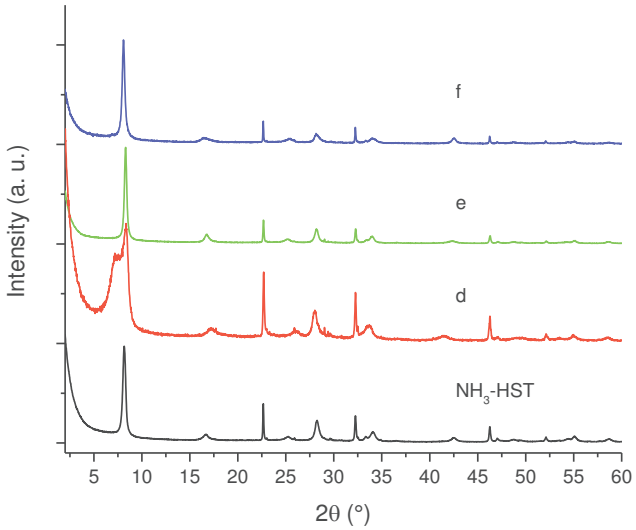

Figure II.3. *PXRD patterns of NH_3-HST and its reaction products with n-alcohols: (d): the reaction product between NH_3-HST and methanol; (e): the reaction product between NH_3-HST and ethanol; (f): the reaction product between NH_3-HST and propanol.*

II.2.2.1.2.2. Infrared spectroscopy

Figure II.4 shows the corresponding IR spectra. Comparing the IR spectra compounds (e) and (f) are very similar to the one of NH_3-HST, which confirms that the reaction with ethanol or propanol did not occur. Yet, comparing the IR spectra of the starting material with that of reaction product (d), it is clear that new signals appear : the CH_3 group (ν_{as} : 2919 cm^{-1}; ν_s : 2817 cm^{-1})[10,21] and the C-O elongation in the C-O-Ta motif (1171 cm^{-1}), which is blue shifted by about 140 cm^{-1} with respect to gaseous MeOH ($\nu_{(CO)}$ band at 1033.5 cm^{-1}).[21] This indicates the success of the grafting reaction between MeOH and NH_3-HST. However, the existence of signal at 1429 cm^{-1}, which comes from the starting material,[22] proves that the grafting reaction just partly works.

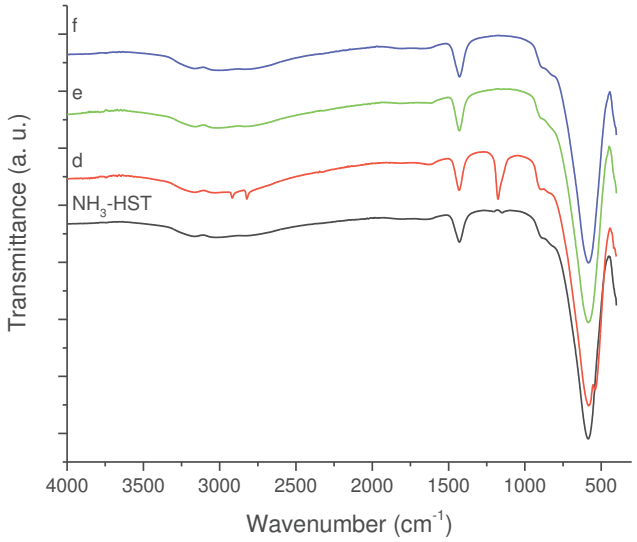

Figure II.4. *IR spectra of NH_3-HST and its reaction products with n-alcohols: (d): the reaction product between NH_3-HST and MeOH; (e): the reaction product between NH_3-HST and EtOH; (f): the reaction product between NH_3-HST and propanol.*

The above analyses prove that NH_3-HST is not an ideal intermediate to perform the grafting reactions with *n*-alcohols.

II.2.2.1.3. C_2N-HST as a starting material

II.2.2.1.3.1. XRD analysis

After the failure of grafting reactions using NH_3-HST as starting material, we turn to the second intermediate C_2N-HST as starting material. ***Figure II.5*** shows the XRD patterns of C_2N-HST and its reaction products with *n*-alcohols (C_nOH, n = 1, 2, 3, 4, 7, 12). The out-of-plane reflections, which are assigned to (100) and (110) in the XRD pattern of HST, are observed at the same positions (22.68° and 32.59°, respectively) in all the obtained products. This shows that the perovskite-like slab structure remains essentially unchanged upon insertion. For reaction with alcohols possessing relatively short carbon chains (C_nOH, n = 1, 2, 3, 4), the (00l) reflections of C_2N-HST are no longer present in the final compounds, and new sets of (00l) reflections appear. This is a positive signal to indicate the occurring of grafting reactions between *n*-alcohols (C_nOH, n = 1, 2, 3, 4) and HST. However, the compounds obtained after reactions with alcohols with longer carbon chains (C_nOH, n = 7, 12) are multiphasic and with a very bad crystallinity.

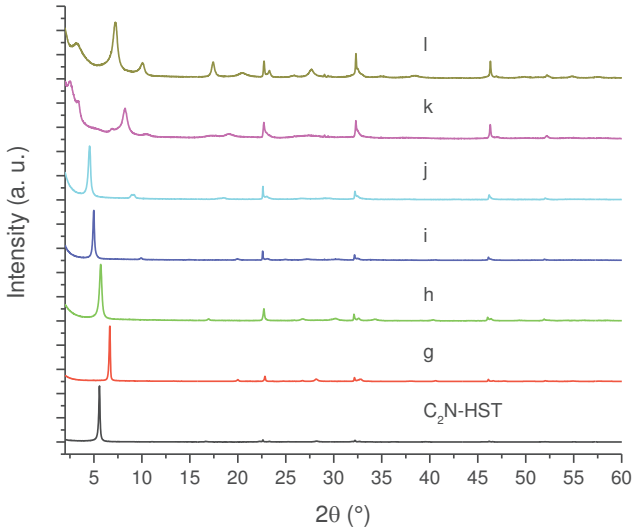

Figure II.5. *PXRD patterns of C_2N-HST and its reaction products ((g), (h), (i), (j), (k), (l)) with n-alcohols (C_nOH, n = 1, 2, 3, 4, 7, 12), respectively.*

II.2.2.1.3.2. Infrared spectroscopy

Infrared spectroscopy shows for all compounds the appearance of signals of asymmetric and symmetric stretching vibrations of CH_2 and CH_3 groups in the region 2800-3000 cm^{-1}. Yet, for the compounds obtained by reaction with C_7OH and $C_{12}OH$, these signals are particularly weaker than expected for such long alkyl chains. In addition, an intense absorption band in the region 1100-1150 cm^{-1}, is which is believed to come from the C-O stretching bond of the C-O-Ta motif. There again, this band is relatively weak for compound k, obtained with C_7OH, or even absent for compound l, obtained with $C_{12}OH$.

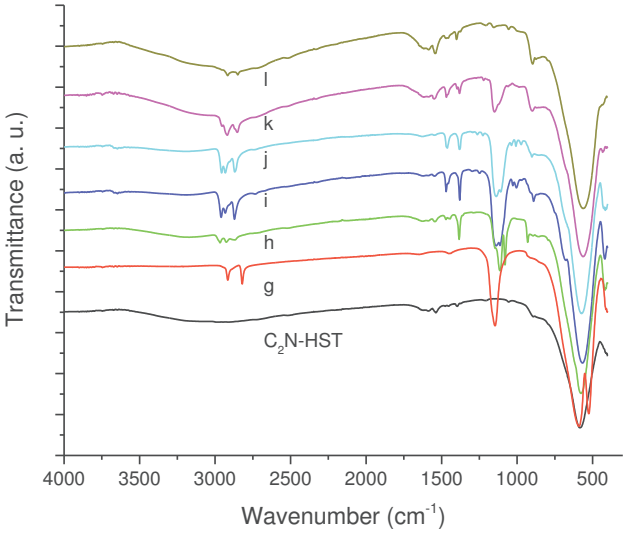

Figure II.6. *IR spectra of C_2N-HST and its reaction products ((g), (h), (i), (j), (k), (l)) with n-alcohols (C_nOH, n = 1, 2, 3, 4, 7, 12), respectively.*

Taking into account the above analyses (XRD and IR), it appears that the intermediate C_2N-HST can be used to graft alcohols with relatively short carbon chains (C_nOH, n = 1, 2, 3, 4), much better than the intermediate NH_3-HST. Yet, for alcohols bearing longer carbon chain (n = 7, 12), no mono-phasic grafted products can be obtained.

II.2.2.1.4. C_4N-HST as a starting material

II.2.2.1.4.1. XRD analysis

In order to achieve the grafting reactions between HST with n-alcohols possessing relatively long carbon chains, we logically turn to attempt the third intermediate C_4N-HST, for which the interlayer distance is larger. ***Figure II.7*** shows the XRD patterns of the starting material C_4N-HST and its reaction products with *n*-alcohols (C_nOH, n = 1, 2, 3, 4, 7, 12). The grafted products are denoted as C_nOH-HST (n represents the number of carbon atoms in n-alcohols). After reactions, the XRD patterns show that the (00l) reflections of C_4N-HST disappear, and new sets of (00l) reflections appear. In contrast, the reflections, which are assigned to (100) and (110) in the XRD pattern of HST, are observed at the same positions (22.68° and 32.59°, respectively) in all the obtained products, which indicates the retention of the inorganic perovskite-like slab structure.

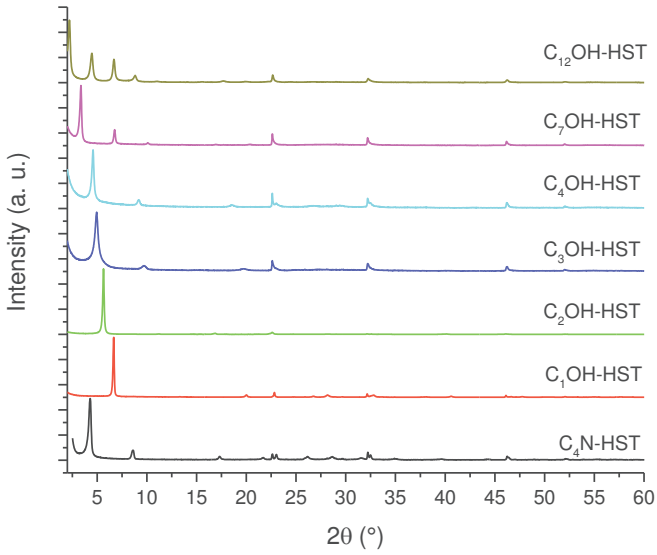

Figure II.7. *PXRD patterns of the starting material C_4N-HST and its reaction products with n-alcohols (C_nOH, n = 1, 2, 3, 4, 7, 12).*

Figure II.8 clearly reveals a linear relationship between the interlayer distance and the number of carbon atoms in *n*-alcohols. This relationship can be expressed as follows: d_{001} = 0.24n + 1.04. This linear relationship indicates that the conformation of *n*-alkyl chains within interlayer spaces of the reaction products is similar. In addition, the slope is 0.24, which is about twice the length of one CH_2 group in the case of an *all-trans* ordered n-alkyl chain (0.127 nm/carbon atom)[15] which indicates a bilayer arrangement. Similar results have been described for the intercalation of HST with n-alkylamines[17,23] and for the grafting reactions of Ruddlesden Popper phase $H_2CaTa_2O_7$[18,19] and of Dion-Jacobson phases $HLaNb_2O_7{\cdot}xH_2O$[10,19] and $HCa_2Nb_3O_{10}{\cdot}xH_2O$[15] with *n*-alcohols.

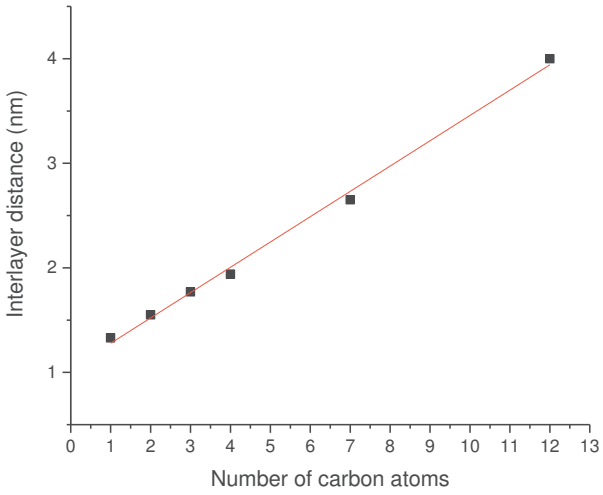

Figure II.8 *Relationship between the number of carbon atoms in the aliphatic chain of n-alcohols and the interlayer distance of the corresponding grafted products (full line corresponds to the best linear fit).*

Using the previous relationship, the tilt angle (with respect to the normal to the layers) can be estimated around 19° (***Scheme II.1***), which is the same as the one observed in for the alkoxy derivatives of $H_2CaTa_2O_7$.[18] This tilt angle is larger than that of C_nOH-$H_2La_2Ti_3O_{10}$ (15°)[16] which can be attributed to larger lattice parameters, which makes a larger *ab* plane for the extension of the n-alkyl chains.[18] Finally, there is a considerable difference between the tilt angle of alkoxy derivatives of HST (C_nOH-HST, 19°) and the one of the corresponding alkylamine intercalated HST (C_nN-HST, 40°, see **Chapter I**). This can only be attributed to the different bonding modes, electrostatic in the case of amines, covalent in the case of alcohols.

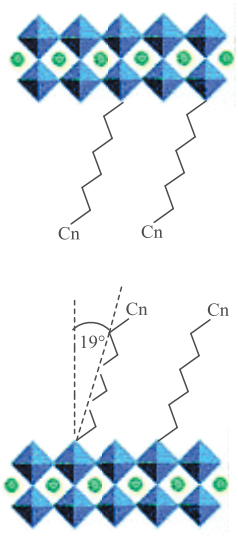

Scheme II.1. *Scheme of the bilayer arrangement of the mono-n-alkoxy derivatives.*

II.2.2.1.4.2. Infrared spectroscopy

Figure II.9 shows the IR spectra of the starting material C_4N-HST and its reaction products with *n*-alcohols (C_nOH, n = 1, 2, 3, 4, 7, 12). Comparing IR spectra of reaction products with that of the starting material, one notices the disappearance of the signals between 1530 and 1630 cm^{-1}, which belong to the intermediate C_4N-HST (see **chapter I**). The appearance of asymmetric and symmetric stretching bonds of CH_2 or the stretching bonds of CH_3 groups (2800-3000 cm^{-1}) is clearly observed, and one can also notice an intense absorption around 1145 cm^{-1} attributed to the C-O vibration in C-O-Ta. Comparing with the corresponding *n*-alcohols, there is an obvious blue shift (*ca.* 95 cm^{-1}) of the C-O band with respect to the corresponding free alcohol (*ca.*1050 cm^{-1}). This blue shift is attributed to the coordination of the alcohol.[24,25] In addition, the disappearance of stretching bonds of OH groups around 3312 cm^{-1} in the obtained products also indicates the grafting reactions. The above analyses strongly suggest the removal of butylamine and the formation of the covalent bond C-O-Ta. No clear attribution of the observed bands around 1110 cm^{-1} (for all compounds, hybrids and free alcohols) and 1085 cm^{-1} (for ethanol and propanol) could be found.

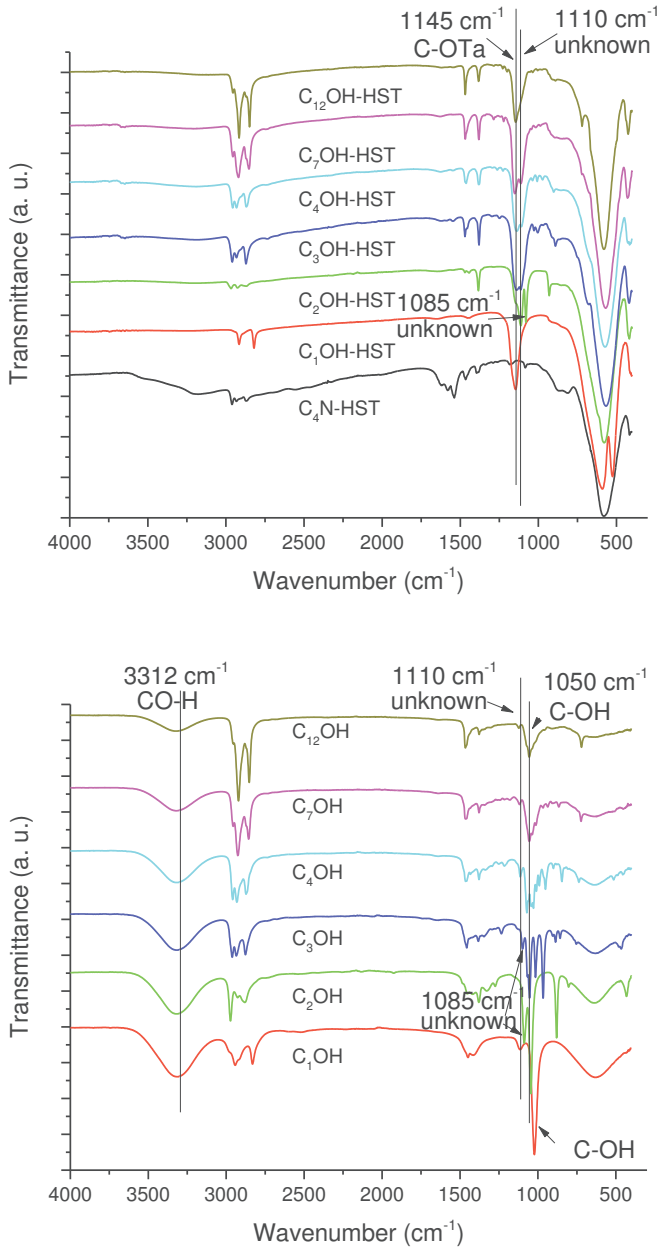

Figure II.9. *IR spectra of the starting material C_4N-HST and its reaction products with n-alcohols (C_nOH, n = 1, 2, 3, 4, 7, 12) (top) and the corresponding n-alcohols (bottom).*

The above important features are collected in ***Table II.1***. The asymmetric stretching bond of the CH_3 groups is visible between 2950 and 2970 cm^{-1} and hardly visible at around 2919 cm^{-1} (ν_{as}) for C_1OH-HST.[10,21] For the alcohols, except methanol being observed at 2817 cm^{-1}, the CH_3 ν_s band is masked by the more intense CH_2 stretching bond. The values of ν_{as} and ν_s for CH_2 group observed for C_7OH-HST and C_{12}OH-HST correspond to *all-trans* conformation.[26] When the length of the alkyl chains decreases, the frequencies of these bands increase as expected in the case of the presence of some *gauche* conformations,[26] yet, the ratio of gauche conformation is too low to have an influence on the basal spacing, as evidenced by the linear variation of the basal spacing (***Figure II.8***). The obvious signals at around 1470 cm^{-1} and 1350 cm^{-1} are proposed as C-H bend and C-H rock, respectively. In addition, Ta-O elongation vibration and C-O vibration are the dominant features at 580 cm^{-1} and 1145 cm^{-1},

respectively. These bands are slightly shifted depending on the samples, without any clear correlation with the functionalization. Finally, we have not managed to find an explanation for the presence of two signals (591 and 524 cm^{-1}) for the Ta-O elongation vibration in C_1OH-HST.

Product	ν_{as} (CH_2) (cm^{-1})	ν_s (CH_2) (cm^{-1})	ν_{as} (CH_3) (cm^{-1})	ν_s (C-O)	ν_s (Ta-O)
C_1OH-HST			2919	1147	591, 524
C_2OH-HST	2926	2869	2968	1143	576
C_3OH-HST	2933	2871	2960	1140	565
C_4OH-HST	2931	2869	2957	1139	573
C_7OH-HST	2919	2851	2955	1150	568
C_{12}OH-HST	2916	2848	2957	1144	579

Table II.1. *Positions of the IR absorption bands of the CH_2, CH_3, C-O and Ta-O groups in C_nOH-HST compounds.*

II.2.2.1.4.3. SEM observation

SEM observation for all compounds shows the same morphology of crystallites (see ***Figure II.10*** for representative examples), with stratification typical of lamellar compounds. Crystallites are not homogeneous in size. In addition, when the parent HST is functionalized by *n*-alcohol to form alkoxy derivatives, the fracturing becomes more obvious. This is attributed to reduce cohesion between crystallites. This may be useful for future delamination or even exfoliation.

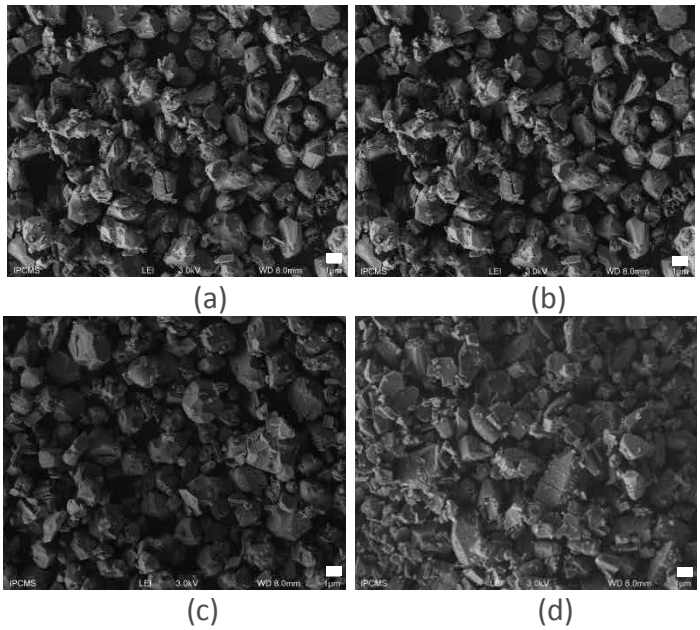

Figure II.10. *SEM images of (a) HST, (b) C_1OH-HST, (c) C_4OH-HST and (d) C_{12}OH-HST (The scale bars correspond to 1 µm).*

II.2.2.1.4.4. Solid state NMR

In order to further demonstrate the formation of covalent bond C-O-Ta in the reaction products, solid state NMR spectroscopy was employed (collaboration Fabrice Leroux, Institut

de Chimie de Clermont-Ferrand). As illustrations, the solid-state ^{13}C CP/MAS NMR spectra of C_1OH-HST and C_4OH-HST are presented (***Figure II.11***). The chemical shift of the α-carbon (-C-O-) signals of C_1OH-HST and C_4OH-HST are at 60 and 74 ppm, respectively. Comparing with the chemical shift of the α-carbon (-C-O-) signals of methanol and butanol in the liquid-state ^{13}C NMR spectra (50.0 and 61.4 ppm, respectively), there is a downfield shift of about 10 ppm. This downfield shift indicates unambiguously the formation of the covalent bond C-O-Ta in the reaction products. This observation by solid state ^{13}C CP/MAS NMR of the downfield shifts of α-carbon (-C-O-) has also been used previously to prove the formation of covalent bonds between alcohols and other inorganic perovskite-like slabs, $H_2CaTa_2O_7$,[18] $HLaNb_2O_7 \cdot xH_2O$,[9] and $H_2La_2Ti_3O_{10}$.[16]

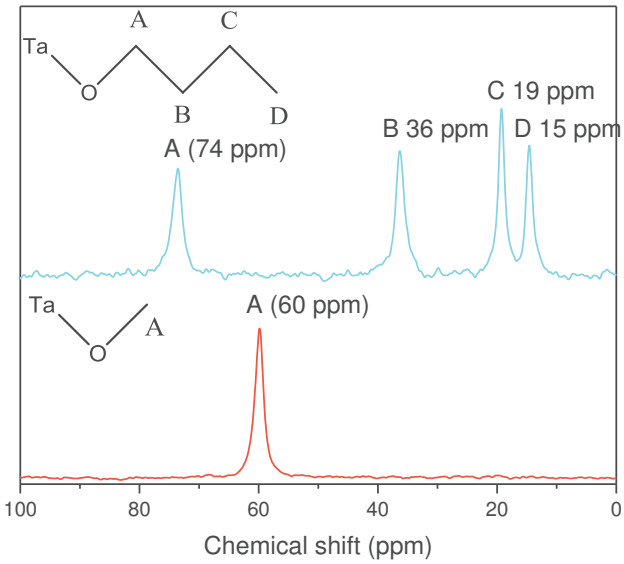

Figure II.11. *Solid-state ^{13}C CP/MAS NMR spectra of C_1OH-HST and C_4OH-HST.*

II.2.2.1.4.5. Thermal analyses

The thermal behaviors (***Figure II.12)*** of the grafted products have been studied with the help of Thermo Gravimetric and Thermo Differential Analyses (TGA-TDA) (under air stream). The TGA curves show small mass losses, of about 0.4 %-1.0 %, before 120°C, which are ascribed to the removal of water. It is worth noticing that there is no visible loss of free alcohol, which confirms the conclusions presented above and the effective grafting of the alcohol molecules. Between 200°C and 400°C, the obvious mass losses, associated to exothermic peaks are ascribed to the decomposition of the *n*-alkoxy groups within the interlayer space of the layered perovskite.

Concerning the thermal behaviour above 450°C, two hypotheses can be made. The first one is as follows: the mass losses and transformations before 450°C include the loss of water, the decomposition of organic phases, and the loss of proton of HST in the form of water. The weight losses, which occur between 600 °C and 700 °C, are thus ascribed to the combustion of residual organic groups.[18] This hypothesis is supported by the thermal behavior of HST, which loses protons in the form of water in the range 300-500 °C (see **Chapter I**).[27] The other hypothesis is as follows: HST is recovered at 450 °C and the mass losses before 450 °C only include the loss of water and the decomposition of organic phases. The weight increase

at around 600°C can be due to re-oxidation of the compound after the departure of the organic phase. The weight losses which occur between 600 °C and 700 °C are then ascribed to the loss of protons in the form of water. Considering that the grafting reactions may affect the thermal behavior of HST, the loss of protons in the form of water may require higher temperature.
Nevertheless, the formula of the product obtained at 800 °C can be proposed as being $Bi_{0.1}Sr_{0.85}Ta_2O_6$ (see **Chapter I**).[28,29]

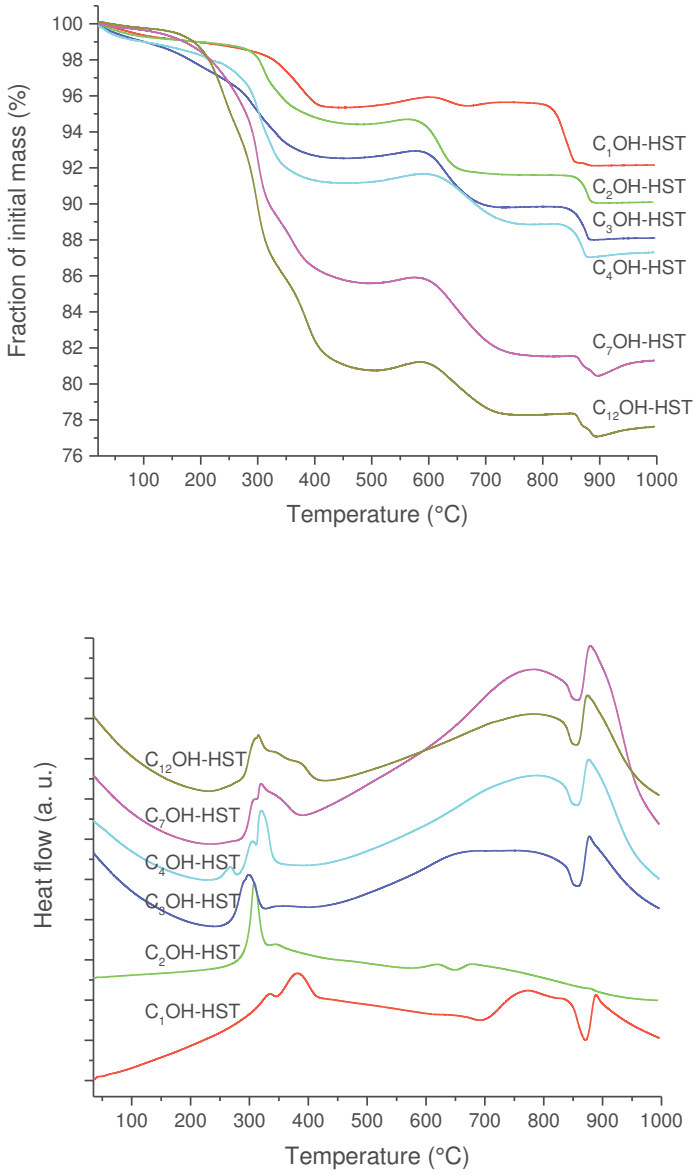

Figure II.12. *TGA (top) and TDA (bottom) curves of C_1OH-HST, C_2OH-HST, C_3OH-HST, C_4OH-HST, C_7OH-HST and C_{12}OH-HST.*

In order to discriminate between the two hypotheses, we have performed XRD analysis after heating at various temperatures. As an illustration, the case of C_2OH-HST is presented in ***Figure II.13***. The high degree of similarity between the diagram obtained after heating at 450°C and the one of HST is a strong indication in favor of the second hypothesis. By analogy with what has been described on $H_2SrTa_2O_7$ and re-explored in **Chapter I**, the XRD pattern at

800 °C indicate the formation of a three-dimensional perovskite of formula $Bi_{0.1}Sr_{0.85}Ta_2O_6$.[29] In conclusion, it appears that the layered perovskite structure of HST is more thermally stable when the perovskite has been grafted by alcohols.

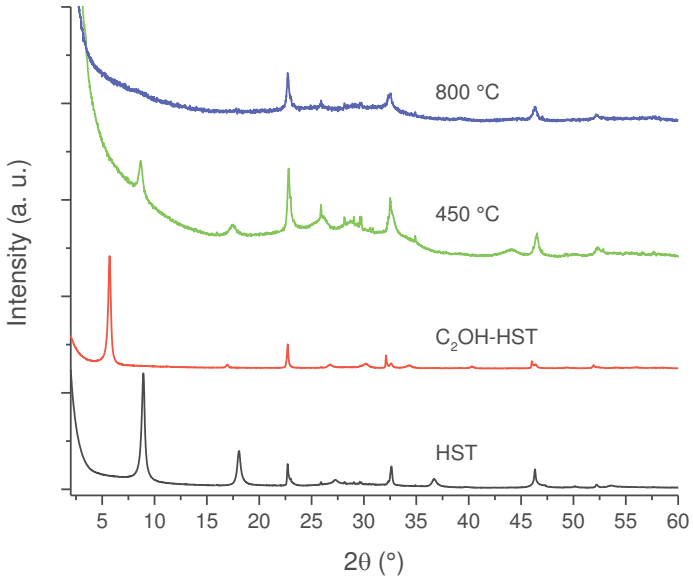

Figure II.13. *PXRD patterns of HST, C_2OH-HST and its heating treatment products at 450 °C and 800°C, respectively.*

II.2.2.1.4.6. Proposed formulae

Combining the above analyses and the results of elemental analyses (C, H, N, *cf.* **Annex**), the formulae of the grafted products are collected in ***Table II.2***.

Products	Formulae
C_1OH-HST	$(C_1O)_{1.5}H_{0.5}Bi_{0.1}Sr_{0.85}Ta_2O_{5.5}\cdot 0.4H_2O$
C_2OH-HST	$(C_2O)_{1.1}H_{0.9}Bi_{0.1}Sr_{0.85}Ta_2O_{5.9}\cdot 0.3H_2O$
C_3OH-HST	$(C_3O)_{1.1}H_{0.9}Bi_{0.1}Sr_{0.85}Ta_2O_{5.9}\cdot 0.3H_2O$
C_4OH-HST	$(C_4O)_{1.0}H_{1.0}Bi_{0.1}Sr_{0.85}Ta_2O_{6.0}\cdot 0.3H_2O$
C_7OH-HST	$(C_7O)_{0.9}H_{1.1}Bi_{0.1}Sr_{0.85}Ta_2O_{6.1}\cdot 0.3H_2O$
C_{12}OH-HST	$(C_{12}O)_{0.9}H_{1.1}Bi_{0.1}Sr_{0.85}Ta_2O_{6.1}\cdot 0.2H_2O$

Table II.2. *Proposed formulae of the grafted products.*

The amounts of *n*-alkoxyl groups (except C_1O-) per HST are about 1, which is obvious smaller than 2.0 (the theoretical value based on the chemical formula $H_{2.0}Bi_{0.1}Sr_{0.85}Ta_2O_7$). This phenomenon has been well explained by steric reasons in a previous report concerning the insertion, of amines into HST,[17] and in another report concerning the grafting of alcohols into the Ruddlesden-Popper phase $H_2La_2Ti_3O_{10}$.[16] As a result, only half of the reaction sites can be occupied. However, the amount of C_1O- group per HST in C_1O-HST is above this limit, around 1.5. It is noteworthy that this "excess" of methanol has already observed for the grafting of alcohols into the Ruddlesden-Popper phase $H_2CaTa_2O_7$.[18] This ultra-dense arrangements of C_1O- group on the interlayer surface of the perovskite-like slabs maybe

ascribed to the smaller cross-section area of methanol (0.126 nm^2)[30], compared to the one of alcohols with longer aliphatic chains, estimated to be 0.186 nm^2.[31]

II.2.2.1.5. Discussion on the role of the intermediates

Since the grafting reactions cannot take place at all between HST and *n*-alcohols, it is clear that the intermediate is necessary. We have shown above that HST functionalized by *n*-alkylamines are indeed efficient intermediates (provided the alkyl chain is long enough). According to the work of Van Der Voort *et al.*, primary amines are known as catalysts to promote the silylation of silica surface and formation of Si-O-Si linkage by acido-basic catalysis.[20] But the fact that the intermediate NH_3-HST cannot react with *n*-alcohols (except partially with methanol) proves that only the presence of NH_3^+ group is insufficient to promote the occurrence of grafting reactions in HST. However, the intermediate C_2N-HST can react with some relatively short n-alcohols (methanol, ethanol, propan-1-ol and butan-1-ol) and the intermediate C_4N-HST can react with more various *n*-alcohols (at least until dodecan-1-ol). This proves the importance of *n*-alkyl groups in the interlayer space of layered perovskite. And it appears that the longer *n*-alkyl groups are advantageous. As a result, we can infer that the increased hydrophobicity of the environment of the interlayer space of HST and/or the increased interlayer distance could account for the successful grafting reaction with *n*-alcohols. Here we cannot prove the necessity of the NH_3^+ group.

II.2.2.2. Grafting reactions between C_2OH-HST and *n*-alcohols ($C_nH_{2n+1}OH$, n = 3, 4, 7, 12): alcohol exchange reaction

As previously reported, the various alkoxy derivatives of $HLaNb_2O_7{\cdot}xH_2O$, $HCa_2Nb_3O_{10}{\cdot}xH_2O$ and $H_2La_2Ti_3O_{10}$ can be prepared by the alcohol-exchange-type reactions with an *n*-alkoxy derivative as starting material to react with various alcohols.[9,15,16] Here, it seems reasonable to try to prepare *n*-alkoxy derivatives of HST using alcohol-exchange-type reactions, since the similar *n*-alkoxy derivatives have been obtained by using C_2N-HST or C_4N-HST as intermediates.

II.2.2.2.1. Syntheses

Among the obtained n-alkoxy derivatives, C_2OH-HST was chosen as a starting material, in view of the cheap price and security of ethanol, to react with some *n*-alcohols (C_nOH, n = 3, 4, 7, 12) with the help of microwave irradiation (130 °C, 2 h). The grafting reactions were performed using a large excess (*more than* ×200) of n-alcohols with respect to the intermediate C_2OH-HST and litter water (ca. 1.3 mass % with respective to n-alcohols).

II.2.2.2.2. XRD analysis

Figure II.14 shows the XRD patterns of starting material C_2OH-HST and its reaction products with *n*-alcohols (C_nOH, n = 3, 4, 7, 12). After reactions, the (00l) reflections of C_2OH-HST disappear and new sets of (00l) reflections appear. The interlayer distances of the reaction products are, respectively, the same as the ones obtained by using C_4N-HST as an intermediate. Similarly, the infrared spectra are identical (not shown here). Therefore we can safely ascertain that the corresponding *n*-alkoxy derivatives of HST have been

successfully prepared by alcohol exchange from C_2OH-HST, and they were as same as the ones obtained by using C_4N-HST as an intermediate.

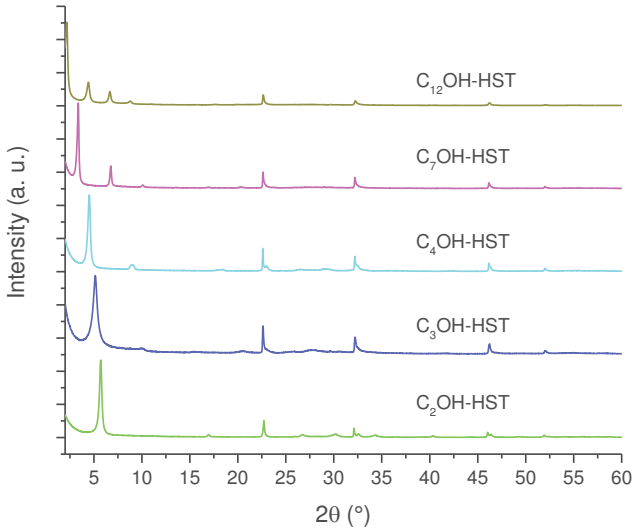

Figure II.14. *PXRD patterns of starting material C_2OH-HST and its reaction products with n-alcohols (C_nOH, n = 3, 4, 7, 12).*

II.2.2.2.3. Proposed mechanism

By analogy with what has been described in the literature for alcohol exchange in other layered perovskites,[9,13,15,16] we propose a hydrolysis-etherification mechanism :

$$C_2\text{OH-HST} + H_2O \xrightarrow{\text{-EtOH}} \text{HO-HST} \xrightarrow[\text{-}H_2O]{\text{ROH}} \text{ROH-HST}$$

II.2.3. Functionalization of HST by grafting α, ω-alkanediols, using C_4N-HST as an intermediate

The reactivity of HST with α, ω-alkyldiamines[32], which we have re-explored in **Chapter I,** gave us the idea to attempt to graft HST with α, ω-alkanediols. C_4N-HST was chosen as a starting material (since C_4N-HST can be easily prepared and its reactivity with *n*-alcohols has been proved to be good) to react with some α, ω-alkanediols ($C_n(OH)_2$, n = 2, 4, 8, 12) with the help of microwave irradiation. To the best of our knowledge, the reactivity of a layered perovskite towards diols has been explore only once, with the grafting of ethylene-glycol into a Dion-Jacobson phase $HLaNb_2O_7$.[9]

II.2.3.1. Syntheses

The microwave assisted (130 °C, 2 h) grafting reactions were performed using a large excess (*more than* ×200) of α, ω-alkanediols ($HOC_nH_{2n}OH$, n = 2, 4, 8, 12), with respect to the intermediate C_4N-HST, and some water (ca. 13 mass % with respective to diols).

II.2.3.2. Comparison between $C_2(OH)_2$-HST and $C_4(OH)_2$-HST

II.2.3.2.1. XRD analysis

Figure II.15 shows the XRD patterns of C_4N-HST and the reaction products. After reacting with $C_2(OH)_2$ (ethylene glycol) and $C_4(OH)_2$ (1,4-butanediol), the interlayer distances decrease from that of C_4N-HST (2.05 nm) to 1.52 nm and to 1.59 nm, respectively. In contrast, the reflections, which are assigned as (100) and (110) in the XRD pattern of HST, are observed at the same positions (22.68° and 32.59°, respectively) in all the obtained products, which indicate the retention of the inorganic perovskite-like slab structure. It is very interesting that the obtained $C_2(OH)_2$-HST has a interlayer distance similar to that C_2OH-HST (1.52 nm *vs.* 1.55 nm). On the contrary, the interlamellar distance of $C_4(OH)_2$-HST (1.59 nm) is significantly smaller than that C_4OH-HST (1.94 nm) and is similar to that of C_4N_2-HST (1.56 nm), , for which 1, 4-butanediamine has a pillaring arrangement, with both terminal –NH_2 groups protonated (see **Chapter I**).[23,32]

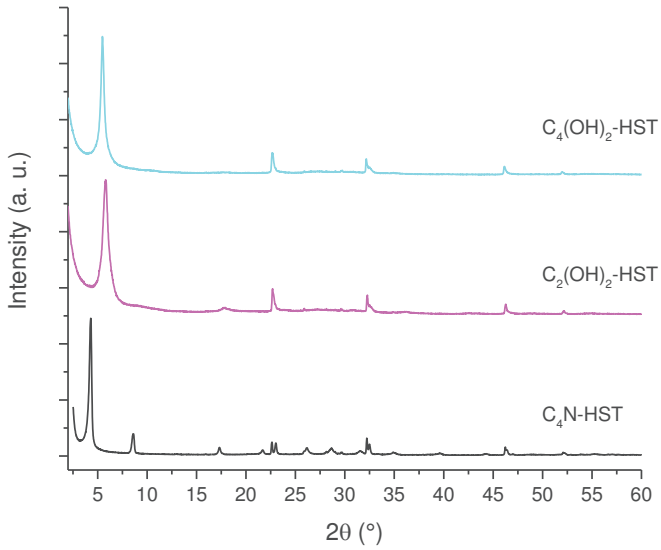

Figure II.15. *PXRD pattern of the starting product C_4N-HST and the reaction products with $C_2(OH)_2$ (ethylene glycol) and $C_4(OH)_2$ (1, 4-butadiol).*

II.2.3.2.2. Infrared spectroscopy

Figure II.16 shows IR spectra of ethylene glycol, 1, 4-butanediol, $C_2(OH)_2$-HST and $C_4(OH)_2$-HST. For both $C_2(OH)_2$-HST and $C_2(OH)_2$-HST, the disappearance of the signal of $–CH_3$ group, which belongs to starting material C_4N-HST, is clearly noticed. This means the butylamine in the intermediate is completely removed. Comparing with the spectrum of $C_2(OH)_2$-HST with that of ethylene glycol, we can notice that there are strong absorptions at the same positions : 3296 cm^{-1} which belongs to –OH group and 1086 cm^{-1} which belongs to C-O group, indicates the existence of free –OH groups in the obtained hybrid $C_2(OH)_2$-HST. In addition, the appearance of new signal at 1149 cm^{-1} which is believed to come from the blue shift of C-O group, indicates the formation of covalent bond C-O-Ta between ethylene glycol and layered perovskite. On the contrary, the spectrum of $C_4(OH)_2$-HST shows the disappearance of the signal of –OH group (3290 cm^{-1}) with respect to the spectrum of 1, 4-butanediol,

which strongly indicates the absence of –OH groups in the obtained hybrid. In addition, there is a blue shift of 100 cm^{-1} of the signal of the C-O group (1149 cm^{-1} for the hybrid and 1048 cm^{-1} for 1, 4-butandiol), which indicates the formation of covalent bond C-O-Ta between 1, 4-butanediol and layered perovskite.

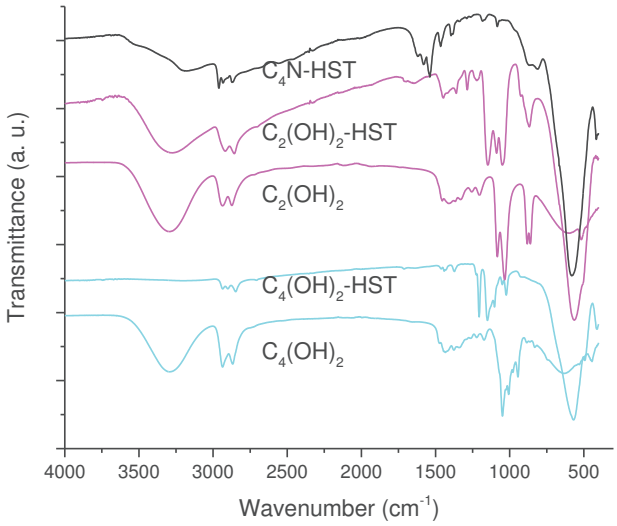

Figure II.16. *IR spectra of C_4N-HST, ethylene glycol, 1, 4-butanediol, $C_2(OH)_2$-HST and $C_4(OH)_2$-HST.*

The above analyses (XRD and IR spectroscopy) strongly suggest that $C_2(OH)_2$-HST presents a bilayer arrangement of the guest species, with only one side of ethylene glycol grafted to the perovskite-like slab, the other OH group remaining free. The $C_4(OH)_2$-HST, conversely, presents a pillaring arrangement of guest species with both sides of 1,4-butanediol grafted to the perovskite-like slab.

II.2.3.2.3. Solid state NMR

In order to prove the above hypothesis, solid state NMR spectroscopy was employed (collaboration Fabrice Leroux, Institut de Chimie de Clermont-Ferrand). For, $C_2(OH)_2$-HST two signals are observed at 75 and 64 ppm. The liquid state ^{13}C NMR spectrum of ethylene glycol shows only one signal at 63.8 ppm. Therefore, there is a downfield shift about 10 ppm for one α-carbo, while the other remains unchanged. This confirms that one alcohol group is coordinated to the perovskite layer, while the other remains free. The small signals at 36 and 14 ppm (marked with asterisks) are ascribed to residual C_2N (for this peculiar experiment, C_2N-HST was originally used as starting material instead of C_4N-HST). For $C_4(OH)_2$-HST, only one signal for the α-carbon (-C-O-) is observed, at 73 ppm (downfield shifted by about 10 ppm with respect to 1, 4-butanediol in the liquid-state ^{13}C NMR spectrum (62.4ppm). Therefore both O of butanediol are coordinated in $C_4(OH)_2$-HST. The small signal around 62 ppm (marked with asterisk) is proposed to come from free –OH groups of 1, 4-butanediol, probably coming from small defects, or residual solvent.

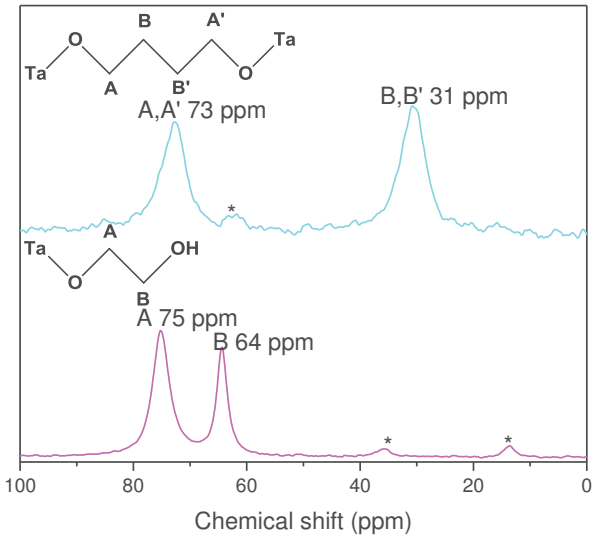

Figure II.17. *Solid-state ^{13}C CP/MAS NMR spectra of the chemical shift of $C_2(OH)_2$-HST and of $C_4(OH)_2$-HST.*

In conclusion, solid state ^{13}C NMR confirms the mono-grafting of ethylene-glycol, and the pillaring of 1, 4-butanediol.

II.2.3.2.4. Thermal analyses

The TGA and TDA curves of $C_2(OH)_2$-HST and $C_4(OH)_2$-HST have been carried out (***Figure II.18***). For $C_2(OH)_2$-HST, the 2.7 mass % losses between 20°C and 100°C can be ascribed to the removal of water in the hybrid. Between 100°C and 400°C the TGA curves show for both compounds, $C_2(OH)_2$-HST and $C_4(OH)_2$-HST, very obvious mass losses (about 4.9 mass % for $C_2(OH)_2$-HST and about 5.3 mass % for $C_4(OH)_2$-HST), associated to exothermic peaks in TDA. This can be ascribed to the combustion of organic molecules within the hybrid. As observed above for mono-alcohols, the small weight increase at 600°C is likely due to re-oxidation necessary after the loss of the grafted alcohols. Finally, the mass loss (about 2.5 mass % for $C_2(OH)_2$-HST and about 3.7 mass % for $C_4(OH)_2$-HST) between 600 °C and 700 °C is associated to the loss of proton in the form of water (see **Chapter I**).[28] Finally the mass loss between 850°C and 900°C is due to some structural transformations and bismuth removal (see **Chapter I**). According to the consistent formula for $C_2(OH)_2$-HST (see **Annex**), the molar ratio 0.7 is coherent with the fact that ethylene glygol is only mono-grafted here (so with a maximum expected ratio between organic molecule and Ta_2 motif of 1). For $C_4(OH)_2$-HST (see **Annex**), the molar ratio 0.5 is very consistent with the theoretical value (0.5), since both sides of 1,4-butanediol are coordinated to the perovskite-like slab.

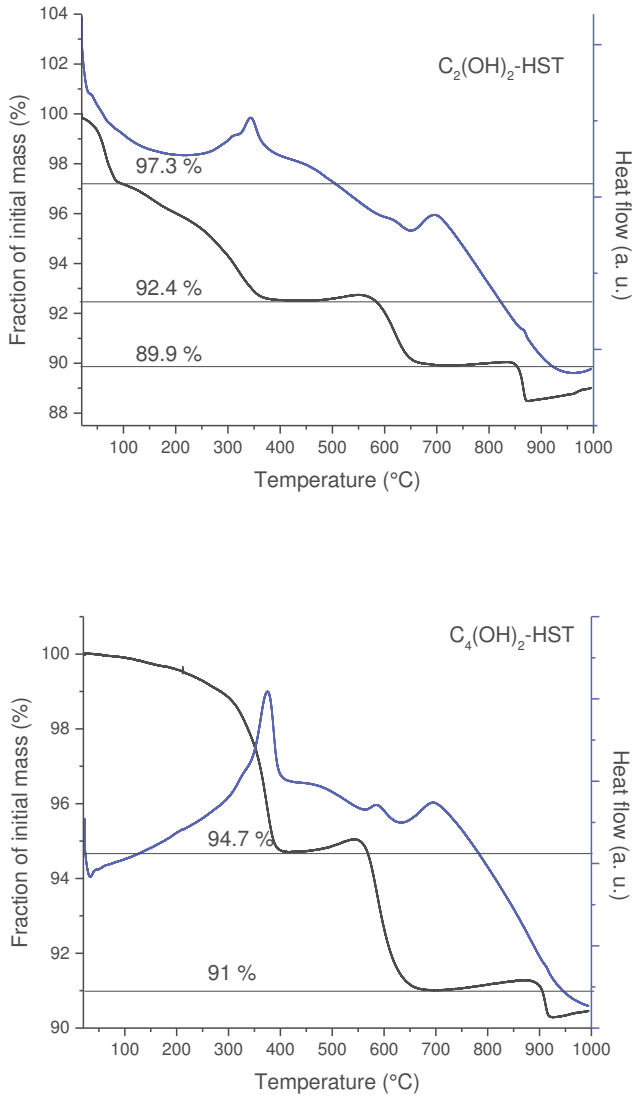

Figure II.18. *TGA and TDA curves of $C_2(OH)_2$-HST and of $C_4(OH)_2$-HST.*

II.2.3.3. Comparison between $C_4(OH)_2$-HST, $C_8(OH)_2$-HST and $C_{12}(OH)_2$-HST

II.2.3.3.1. XRD analysis

In order to further study the grafting state (mono or bi-grafting) in the interlayer space of HST, some diols possessing longer carbon chains, 1, 8-octanediol ($C_8(OH)_2$) and 1, 12-dodecanediol ($C_{12}(OH)_2$), have been employed. ***Figure II.19*** shows the XRD patterns of C_4N-HST and its reaction products with $C_8(OH)_2$ and $C_{12}(OH)_2$. The interlayer distances of the reaction products are different from that of starting material C_4N-HST, and obviously we can notice that the interlayer distances of the grafted products regularly increase with the increase of the number of carbon atoms in alkane-diols.

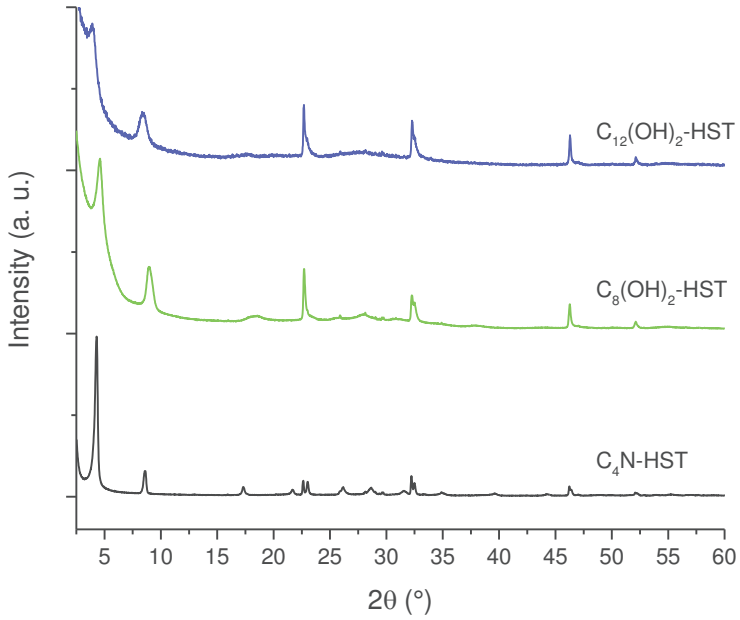

Figure II.19. *PXRD patterns of C_4N-HST and its reaction products with $C_8(OH)_2$ and $C_{12}(OH)_2$.*

Figure II.20 clearly shows a linear relationship between the interlayer distance and the number of carbon atoms in the aliphatic chain of α, ω-alkanediols. The relation can be expressed as follows: d_{001} = 0.08 n + 1.26. This linear relationship indicates that the conformation of *n*-alkyl chains in all the interlayer space of the reaction products is the same.

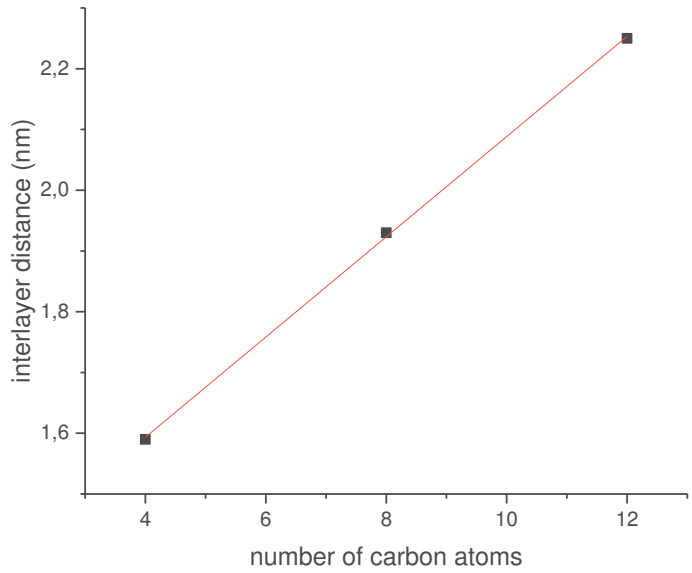

Figure II.20. *Relationship between the number of carbon atoms in the aliphatic chain of α, ω-alkanediols and the interlayer distance of the corresponding grafted products (full line corresponds to the best linear fit).*

In addition, the slope of the linear relationship is 0.08, which is smaller than the length of one CH_2 group in the case of an *all-trans* ordered *n*-alkyl chain (0.127 nm/carbon atom)[15] and of the same order of magnitude than α, ω-alkanediamines (see **Chapter I**). This is in agreement with a pillaring arrangement. The tilt angle (with respect to the normal to the layers) can be estimated around 51° (***Scheme II.2***). The above analyses strongly indicates that $C_8(OH)_2$ and $C_{12}(OH)_2$ have similar pillaring arrangement as $C_4(OH)_2$ in $C_4(OH)_2$-HST.

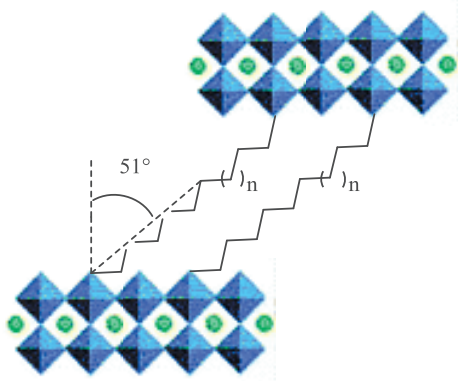

Scheme II.2. *Scheme of the pillaring arrangement of α, ω-alkanediols with long alkyl chains.*

II.2.3.3.2. Infrared spectroscopy

The corresponding IR spectra of octanediol, dodecanediol, $C_8(OH)_2$-HST and $C_{12}(OH)_2$-HST, displayed in ***Figure II.21***, further support the previous description. Comparing with the spectra of the two hybrids with that of the corresponding diols, the disappearance of the signal of –OH group (3397 and 3326 cm^{-1}) is noteworthy, and strongly indicates the absence of –OH groups in the obtained hybrid. In addition , there is a blue shift of 90 cm^{-1} for the signal of the C-O group (*ca.* 1140 cm^{-1} for the hybrid and *ca.* 1050 cm^{-1} for diols), which indicates the formation of covalent bond C-O-Ta between diols and the layered perovskite

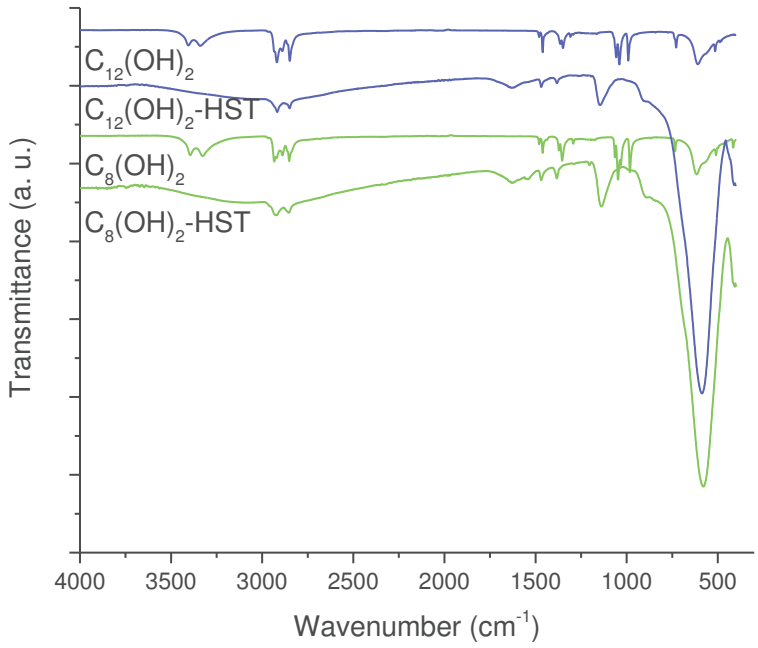

Figure II.21. *IR spectra of octanediol, dodecanediol, $C_8(OH)_2$-HST and $C_{12}(OH)_2$-HST.*

II.2.3.4. Discussion

The bilayer arrangement of $C_2(OH)_2$ in the interlayer space of HST is in good accordance with previous report about the Dion-Jacobson phase $HLaNb_2O_7 \cdot xH_2O$.[9] Yet, to the best of our knowledge, the pillaring arrangements of α, ω-alkanediols in the interlayer space of layered perovskite have never been described in literature. The modification of Kaolinite with propanediols has been reported.[33] Only one of the two –OH groups of 1, 2-and 1, 3-propanediols was bonded to the inorganic layers. When largely increasing the reaction time, 1, 3-propanediols partly forms a bridge type grafting where both OH groups were bonded to the same inorganic layer. The modification of Kaolinite with butanediols has also been reported and the pillaring arrangement was not obtained.[34] The grafting reactions between $HLaNb_2O_7 \cdot xH_2O$ and polyethylene glycols (PEGs) with various molecular masses were investigated and showed mono-grafting arrangements.[35] The functionalization of Dion-Jacobson phase $HLaNb_2O_7$ with D-glucopyranose has also been described as a mono-grafting arrangement.[25]

II.2.4. Functionalization of HST with bulky alcohols, using C_4N-HST as an intermediate

In order to further expand the scope of the grafting reactions between HST and alcohols, we have tested some more bulky alcohols, other than linear aliphatic alcohols.

II.2.4.1. Syntheses

As relatively bulky alcohols, 2-propanol, *tert*-butanol and benzyl alcohol have been employed. The microwave assisted (130 °C, 2 h) grafting reactions performed using a large excess (more than ×200) of bulky alcohols, with respect to the intermediate C_4N-HST, and litter water (ca. 1.3 mass % with respective to alcohols).

II.2.4.2. XRD analysis

Figure II.22 shows the XRD patterns of C_4N-HST and its reaction products with 2-propanol, *tert*-butanol and benzyl alcohol. After reacting with 2-propanol, *tert*-butanol and benzyl alcohol, the interlayer distances change from that of C_4N-HST (2.05 nm) to 1.57 nm, 1.72 nm and 2.06 nm, respectively. The reflections of (100) and (110) observed at the same positions (22.68° and 32.59°, respectively) in the XRD patterns always indicate the preservation of the structure of the inorganic perovskite-like slab.

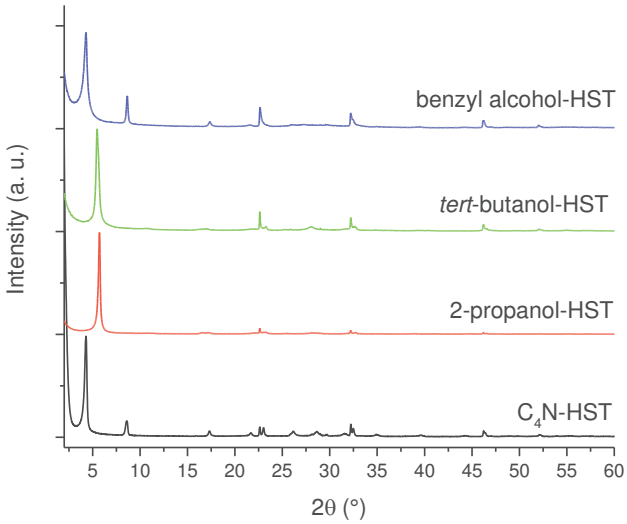

Figure II.22. *PXRD patterns of C_4N-HST and the reaction products with 2-propanol, tert-butanol and benzyl alcohol.*

II.2.4.3. Infrared spectroscopy

Comparing the IR spectra (***Figure II.23***) of the products with that of starting material, it's clear to notice the appearance of new signals at about 1130-1150 cm^{-1} which is proposed to come from the stretching bond of C-O-Ta. In addition, the absorption of the stretching OH vibration cannot be found. The above analyses strongly suggest the formation of the covalent bond C-O-Ta. For the reaction product with benzyl alcohol, the characteristic absorptions at 3026, 3059 and 1452 cm^{-1} are observed.

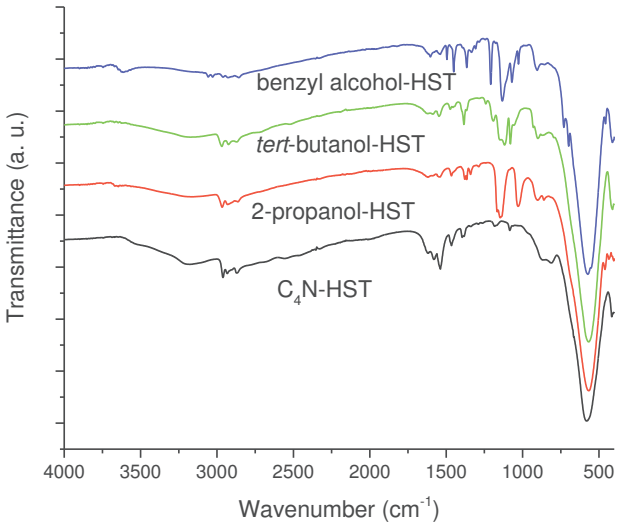

Figure II.23. *IR spectra of C_4N-HST and the reaction products with 2-probanol, tert-butanol and benzyl alcohol.*

II.2.4.4. Thermal analyses

The TGA and TDA curves for 2-propanol-HST and benzyl alcohol-HST are shown in ***Figure II.24***. The mass loss between 20°C and 100°C is ascribed to the removal of water in the hybrids. Between 100°C and 450°C, the mass loss, associated to exothermic peaks in TDA, is attributed to the removal of organic molecules within the hybrid. Around 600°C, there is a small mass increase due to reoxidation of the compound, followed by the formation of the $Bi_{0.1}Sr_{0.85}Ta_2O_6$ phase. Finally the mass around 850°C is attributed to the partial loss of bismuth. It is noteworthy that the organic contents are 0.6 and 0.7 alcohol per Ta_2 unit for 2-propanol-HST and benzyl alcohol-HST respectively, according to their corresponding estimated formulae (see **Annex**). This is smaller than the value of obtained for aliphatic linear *n*-alcohol-HST (ca. 1.0). This is likely due to the steric hindrance of these bulky alcohols.

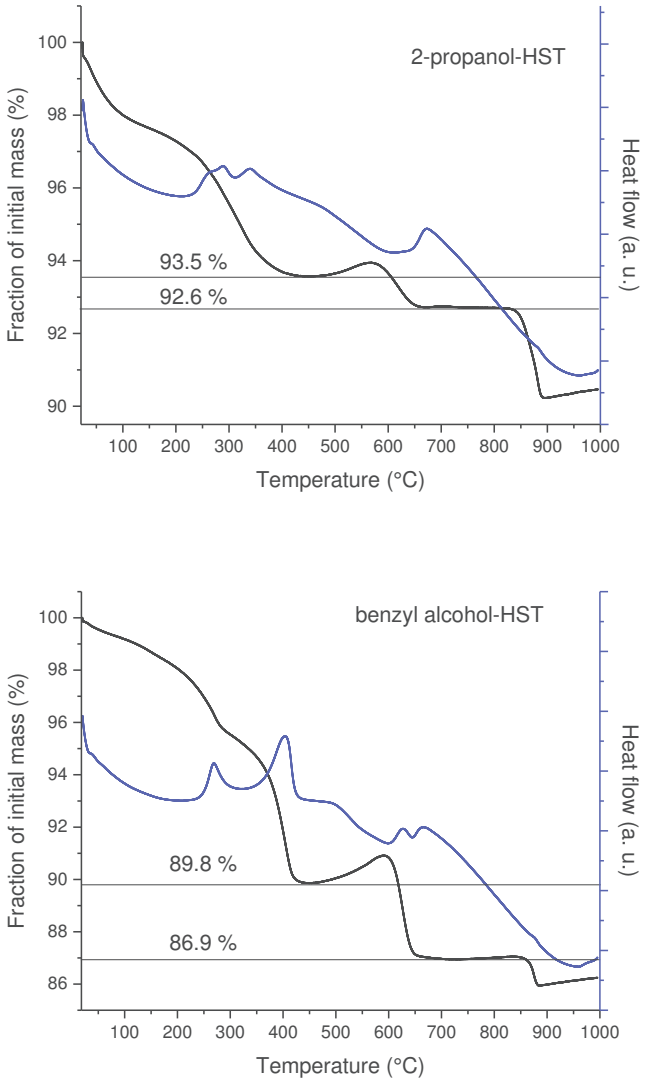

Figure II.24. *TGA and TDA curves of 2-probanol-HST and benzyl alcohol-HST.*

The thermal behavior of the last compound, *tert*-butanol-HST is not reported here, because the results of elemental analyses (see **Annex**) show the significant presence of nitrogen (which is not the case for the other two compounds). It proves that in this case, the grafting is not complete, even using more extreme conditions (130 °C, 48 h, oven; 160 °C, 2 h,

microwave). We attribute this difficulty to bulkiness of *tert*-butanol. On the contrary, elemental analyses for 2-propanol-HST and benzyl alcohol-HST show no trace of nitrogen, confirming the complete removal of C_4N.

II.2.5. Study of the role of water during the reaction process

During the process of exploring the reaction conditions for the grafting reactions, the crucial role of water is noticed, no matter using C_4N-HST or C_2OH-HST as starting materials. This importance of water was already evidenced in the previous chapter for the insertion of amines. Its importance for grafting reactions has been also reported in literature.[15,18,36]

II.2.5.1. Syntheses

In order to well study the role of water, a series of comparative reactions with water as the variable (0 mass %, 1 mass % and 20 mass %, with respect to the employed alcohols) has been carried out. The microwave assisted (130 °C, 2 h) reactions were performed using a large excess (8 mL, *more than* ×200) of propan-1-ol, with respect to the intermediate (100 mg) C_4N-HST or C_2OH-HST.

II.2.5.2. Using C_4N-HST as intermediate

II.2.5.2.1. XRD analysis

Figure II.25 shows the XRD patterns of C_4N-HST and the reaction products with propan-1-ol under the three different experimental conditions (0 mass %, 1 mass % and 20 mass % of water). When no water is added, the 00l reflexions of the resulting compound are exactely at the same position than in the starting compound. Therefore, it is clear that no reaction occurred in these conditions. On the contrary, the use of 1 mass % of water leads to decrease of the interlamellar distance, from that of C_4N-HST (2.05 nm) to 1.79 nm, in very good accordance with the one obtained for C_3OH-HST (1.77 nm) (see ***Figures II.7*** and ***II.8***). For higher water content (20 mass %), the interlayer distance increases from that of C_4N-HST (2.05 nm) to 2.80 nm along with a reduced crystallinity. This is reminiscent of the swelling phenomenon which has been described by T. Sasaki et al.[37] During the course of this PhD work, I did not have the time to investigate his phenomenon further. Nevertheless, it is very promising that a microwave-assisted swelling can be obtained, because it opens perspectives for microwave-assisted exfoliation, faster and with better yields that the existing procedures. Micro-analyses has been performed on the compound resulting from this reaction using 20 mass % of water. The result shows the coexistence of propan-1-ol 1-butylamine in the reaction product (the estimated formula is $(C_4N)_{0.1}(C_3OH)_{0.1}HST{\cdot}1.1H_2O$).

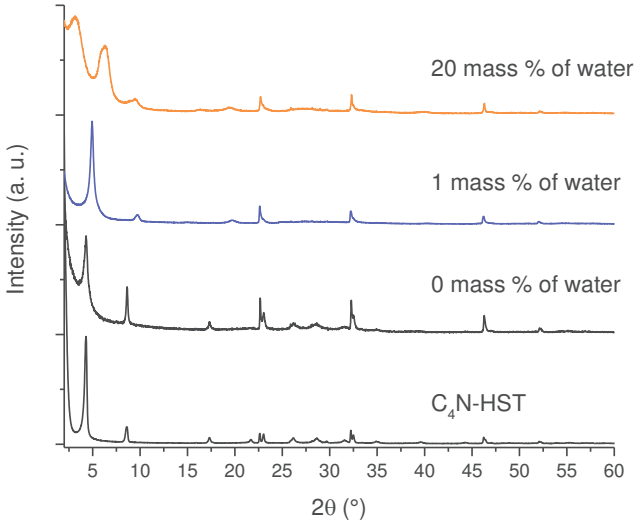

Figure II.25. *PXRD patterns of C_4N-HST and its reactions products with propan-1-ol by adding 0 mass %, 1 mass % and 20 mass % of distilled water to the reaction systems, respectively.*

II.2.5.2.2. Discussion

In summary, the addition of appropriate amount of water (*ca.* 1 mass %) to the reaction system is crucial for the occurrence of grafting reaction between propan-1-ol and C_4N-HST. Similar results have been obtained with longer alcohols (butan-1-ol). For smaller alcohols, methanol and ethanol, the grafting reactions with and C_4N-HST are not so sensitive to the amount of water in the reaction system. Even using 20 mass % of water in the reaction system, the grafting reactions work also well. For some α, ω-alkanediols, ethylene glycol and 1, 4-butanediol, the successful grafting reactions, with 13 mass % of water in reaction system, were also observed.

II.2.5.3. Using C_2OH-HST as intermediate

II.2.5.3.1. XRD analysis

The same procedure was followed for studying the reactions between C_2OH-HST and propan-1-ol. ***Figure II.26*** shows the XRD patterns of C_2OH-HST and the reaction products with propan-1-ol under the three different experimental conditions (0 mass %, 1 mass % and 20 mass % of water).There again, when no water is added, the grafting reaction does not take place. On the contrary, the use of 1 mass % of water leads to decrease of the interlamellar distance, from that of C_2OH-HST (1.55 nm) to 1.77 nm, which corresponds to the one obtained for C_3OH-HST (see ***Figures II.7*** and ***II.8***). When a higher water content is used (20 mass %), a multiphasic compound is obtained. Some target product C_3OH-HST is observed in the mixture. In addition another phase with an interlamellar dictance of 1.1 nm is obtained. This interlamellar distance is reminiscent to the one of HST (0.98 nm), which suggests the occurrence of a hydrolytic deintercalation of ethanol from C_2OH-HST when a high water content is used.

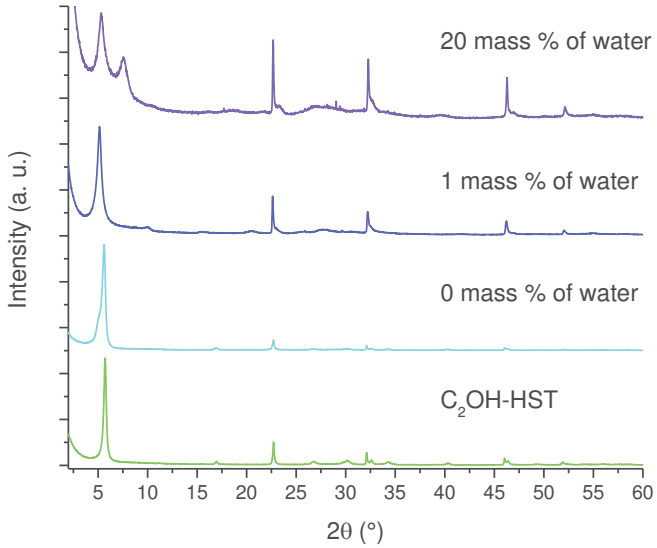

Figure II.26. *PXRD patterns of the reactions products between C_2OH-HST and propan-1-ol, by adding 0 mass %, 1 mass % and 20 mass % of distilled water to the reaction systems, respectively.*

II.2.5.3.2. Discussion

According to the above analysis, the conclusion is similar to the one which was obtained when using C_4N-HST as an intermediate. The addition of an appropriate amount of water (ca. 1 mass %) to the reaction system is crucial for the occurring of grafting reaction between propan-1-ol and C_2OH-HST. Similar results were obtained when longer alcohols (butan-1-ol, heptan-1-ol and dodecan-1-ol) were used.

II.2.6. Comparison of the reactivity of *n*-alkylamine and *n*-alcohol towards insertion/grafting into HST: role of water

The grafting reactions of alcohols thus appear to be relatively sensitive to the amount of water. For amines, water is necessary (**Chapter I**), but, contrary to alcohols, and even though we have not performed a complete study on this point, it appears from our experience that the amount of water is not so crucial. In addition, amine insertions were essentially performed in THF, whereas for the grafting of alcohols, alcohols are used as solvent. Therefore, it appeared interesting to investigate the compared reactivity of amines and alcohols, and how the reaction conditions (*i.e.* the amount of water) are able to change the preferential reactivity of HST towards $–NH_2$ group or –OH group. This study would be of great importance when times come for the insertion of very complicated molecules, bearing several functional groups.

II.2.6.1. Syntheses

In order to study the role of water for the preferential reactivity of HST towards $–NH_2$ group or –OH group, a series of reactions (microwave, 130 °C, 2 h) between an equimolar mixture of butylamine (5.1 mL, 3.7 g, 0.04 mol) and ethanol (2.9 mL, 2.3 g, 0.04 mol) to react with HST (50 mg), using water as the variable has been prepared. The amount of distilled water in

the reaction systems is 0 mass %, 0.1 mass % and 1.0 mass % with respect to the total mass of the reactive mixture.

II.2.6.2. XRD analysis

Figure II.27 shows the XRD patterns of HST and its reaction products depending on the reaction conditions. As expected, when no water is used, the reaction does not take place, neither with the amine, nor with ethanol. With a small amount of water (0.1 mass %), the interlamellar distance increases from 0.98 nm (HST) to 1.74 nm (which is slightly larger than that of C_2OH-HST (1.54 nm)). When the amount of water increases further (1 mass %), the interlamellar distance increases to 2.07 nm, which corresponds to the one of C_4N-HST).

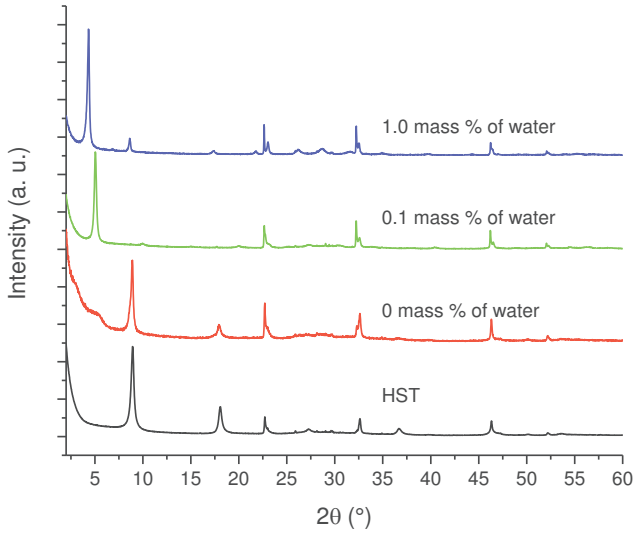

Figure II.27. *PXRD patterns of HST and its reaction products with an equimolar mixture of butylamine and ethanol, by adding 0 mass %, 0.1 mass % and 1 mass % of distilled water to the reaction systems, respectively*

II.2.6.3. Infrared spectroscopy

The corresponding IR spectra are shown in ***Figure II.28***. In the absence of water, the spectrum of HST is observed, as expected and in accordance with the corresponding XRD pattern. With 1 mass % of water, the spectrum shows the antisymmetric and symmetric stretching bands of the CH_2 group but also bands associated to the C-N group around 1500 cm^{-1}. This strongly suggests the co-insertion of 1-butylamine and ethanol, which would then explain the interlamellar distance larger than expected for C_2OH-HST. When a larger amount of water is used, only the signals of CH_2 group and the signals of C-N are observed and the signals of C-O band cannot be found. This means that in these conditions, there is only 1-butylamine in the interlayer space of HST.

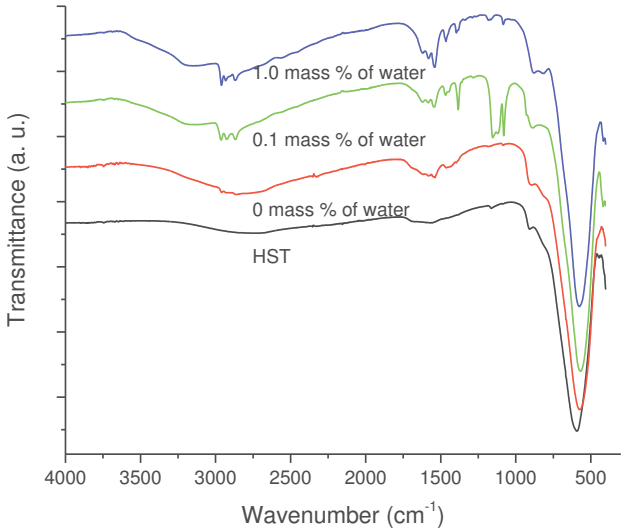

Figure II.28. *IR spectra of HST and its reaction products with an equimolar mixture of butylamine and ethanol, by adding 0 mass %, 0.1 mass % and 1 mass % of distilled water to the reaction systems, respectively*

II.2.6.4. Solid state NMR

The solid-state ^{13}C CP/MAS NMR spectra (***Figure II.29***, collaboration Fabrice Leroux, Institut de Chimie de Clermont-Ferrand) of the reaction products with 0.1 mass % and 1.0 mass % of water further confirm the above observations. When 1.0 mass % of water is used, only the signals of at 40, 30, 20 and 14 ppm were obtained, confirming the formation of C_4N-HST. When a smaller amount of water is used, 0.1 mass %, the solid-state ^{13}C CP/MAS NMR shows the signals which corresponds to the insertion of butylamine at 40, 30, 20 and 14 ppm, but also a signal at 68 ppm. This signal is attributed to the α-carbon (-C-O-) of ethanol, which is downfield shifted with respect to the corresponding signal for free ethanol in the liquid-state (58.3 ppm) This indicates the formation of the covalent bond C-O-Ta. In conclusion, this analysis confirms the co-insertion of ethanol and butylamine when only 0.1 mass% of water is used.

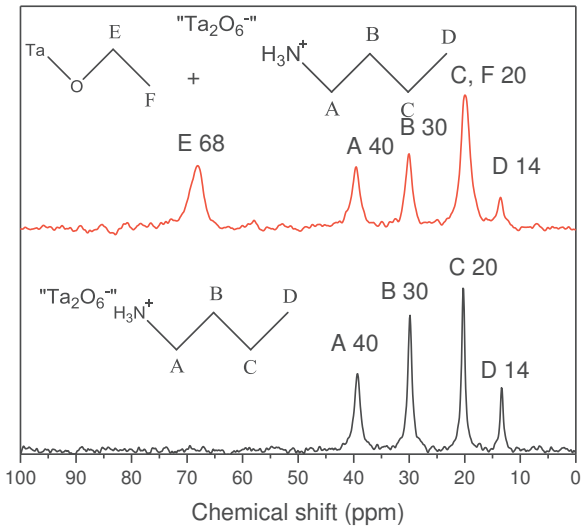

Figure II.29. *Solid-state ^{13}C CP/MAS NMR spectra of the products resulting from the reaction between HST and an equimolar mixture of butylamine and ethanol, 0.1 mass % (red) and 1 mass % (black) of distilled water to the reaction systems, respectively.*

We have shown in paragraph **II.2.1** that HST was not able to react with ethanol. Therefore, the fact that it is possible to graft ethanol into HST when a mixture of ethanol and amine is used indicates that butylamine serves as a catalyst. Depending on the conditions, C_4N-HST is formed first, and then the amine is replaced by ethanol as described in paragraphs **II.2.2.1.3** and **II.2.2.1.4** when C_2N-HST or C_4N-HST are used as starting compounds. The results presented here are complimentary the ones presented in paragraphs **II.2.2.1.3** and **II.2.2.1.4** and in paragraph **II.2.5.2**. Since they show that when the amine is present in excess (and not only in the form of C_nN-HST), the formation of a pure C_2OH-HST phase is not easy and requires notably the precise control of the water content. When the water content is too high, the preferential reactivity of HST towards amines leads to the formation of a C_nN-HST phase, or to mixture of phases.

II.2.7. Study the effect of water for the reactivity of 5-amino-1-pentanol

The previous study of the role of water for the preferential reactivity of HST towards $-NH_2$ group or –OH group, was further extended to the study of the reactivity of HST or various derivates (C_2N-HST, C_4N-HST and C_2OH-HST) towards a single molecule, bearing both a $-NH_2$ group and a –OH group : 5-amino-pentan-1-ol. A series of reactions (microwave, 130 °C, 1 h) were carried out using 5-amino-pentan-1-ol dissolved in THF (1/1 v:v) and using water as the variable (from ca. 1 mass % to 100 mass %, with respect to 5-amino-pentan-1-ol).

II.2.7.1. Using C_2N-HST or C_4N-HST as starting materials

II.2.7.1.1. XRD analysis

Figure II.30 shows the XRD patterns of C_2N-HST and its reaction products with 5-amino-1-pentanol by using different amount of water. The interlayer distance of the obtained product increases from 1.57 nm (C_2N-HST) to 1.61 nm, when the amount of water is

1 mass %. When the amount of water is 2 mass % or 3 mass %, the interlayer distance is around 1.75 nm. And when the amount of water is between 10 mass % and 100 mass %, the interlayer distance further increases to around 1.96 nm. The variable interlayer distances of the obtained products from around 1.6 nm to 2.0 nm is attributed to the change of the arrangement of 5-amino-1-pentanol in the interlayer space of HST, from pillaring arrangement to bilayer arrangement.

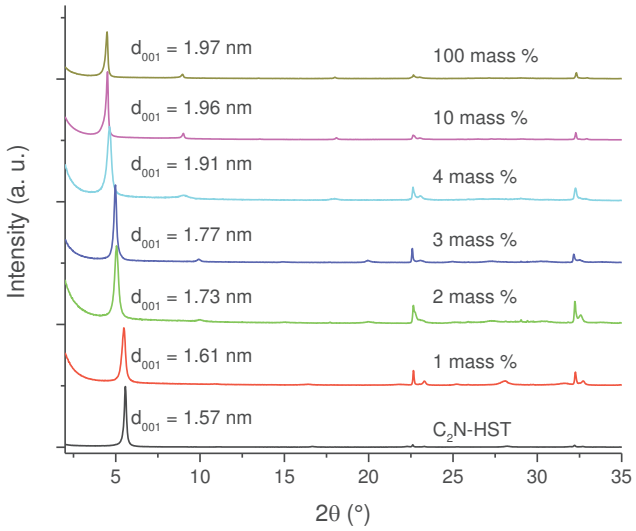

Figure II.30. *XRD patterns of C_2N-HST and its reaction products with 5-amino-1-pentanol by using different amount of water in the reaction mixtures.*

II.2.7.1.2. Infrared spectroscopy

The corresponding IR spectra are shown in ***Figure II.31***. The antisymmetric and symmetric stretching bands of the CH_2 group around 2935 and 2859 cm^{-1} are clearly visible in all of the obtained products. In addition, comparing with the spectra of 5-amino-1-pentanol, for all of the products, the sharp strong bands at 3332 cm^{-1} and 3286 cm^{-1} due to NH stretching of free $–NH_2$ group are greatly reduced in intensity and the new bands at 1578 cm^{-1} and 1545 cm^{-1} are attributed to $–NH_3^+$ groups deformation vibrations.[38,39] As noted several times in this chapter, the signal around 1130 cm^{-1} is attributed to the C-O stretching in C-OTa and the signal around 1060 cm^{-1} comes from the C-O stretching in C-OH. Therefore, when the amount of water is 1 mass %, both of –OH group and $–NH_2$ group react with the interlayer surface of HST, leading to a pillaring arrangement of 5-amino-pentan-1-ol. When the amount of water is more than 4 mass %, only $–NH_2$ group react, leading to a bilayer arrangement similar to the one previously described for *n*-alkylamines (cf. **Chapter I**). When the amount of water is between 2 and 4 mass %, the coexistence of signals around 1125 cm^{-1} and around 1060 cm^{-1} indicates the coexistence of the two arrangements. Unexpectedly, this coexistence of the two arrangements does not lead to a multiphasic compound, visible in XRD, but instead leads to the formation of compounds with an intermediate interlayer distance.

Finally, the same results are obtained when C_4N-HST is used instead of C_2N-HST. The important point here is that it is possible to finely control the interlayer spacing of the

hybrids and the arrangement 5-amino-pentan-1-ol by playing with the water content in the reaction mixture.

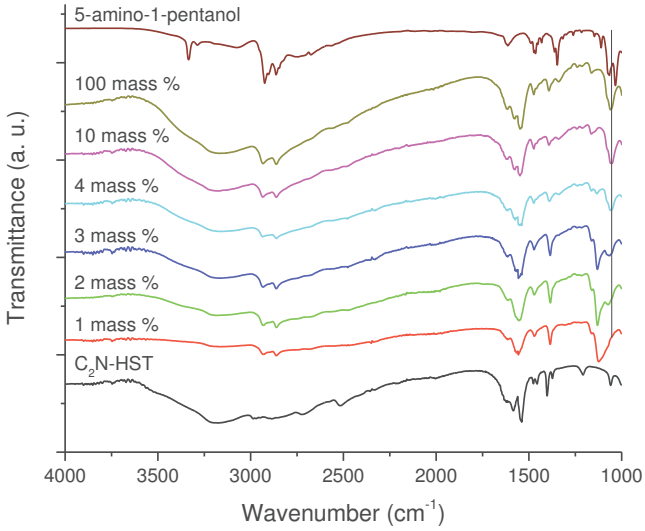

Figure II.31. *IR spectra of C_2N-HST and its reaction products with 5-amino-1-pentanol by using different amount of water (from ca. 0.5 mass % to 30 mass %).*

II.2.7.2. Using C_2OH-HST as starting material

II.2.7.2.1. XRD analysis

The XRD patterns of C_2OH-HST and its reaction products with 5-amino-pentan-1-ol by using different amount of water are displayed in ***Figure II.32***. It is obvious to notice that C_2OH-HST does not have reactivity until the amount of water is larger than 15 mass %. And the completeness of reactions cannot be realized until the amount of water increases to 20 mass %. It is noteworthy that the obtained products always have an interlayer distance around 1.96 nm, which indicates the bilayer arrangement as that of *n*-alkylamines. Apart from the completeness of reactions, the amount of water does not have a considerable effect on the reaction products when C_2OH-HST is employed as a starting material.

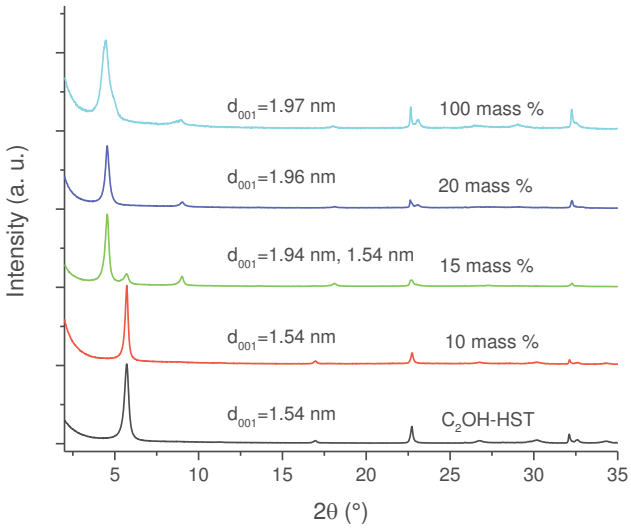

Figure II.32. *XRD patterns of C_2OH-HST and its reaction products with 5-amino-1-pentanol by using different amount of water.*

II.2.7.2.2. Infrared spectroscopy

The corresponding IR spectra are shown in ***Figure II.33***. When the amount of water is 10 mass %, the high similarity of IR spectra indicates the recovery of starting material. When the amount of water is more than 20 mass %, the spectra are as same as the ones of 10 mass % or 100 mass % in ***Figure II.31***, which indicates the bilayer arrangement of 5-amino-pentan-1-ol, possessing free –OH groups, in the interlayer space of HST. The IR spectra when the amount of water is 15 mass %, indicates the coexistence of C-OH (ca. 1060 cm^{-1}) and C-OTa (ca. 1130 cm^{-1}). Considering multiphasic character of the product obtained when the amount of water is 15 mass %, with the presence of the starting compound C_2OH-HST, (***Figure II.32***), 5-amino-1-pentanol is proposed to have free –OH groups in the interlayer space of HST to explain the signal around 1060 cm^{-1}.

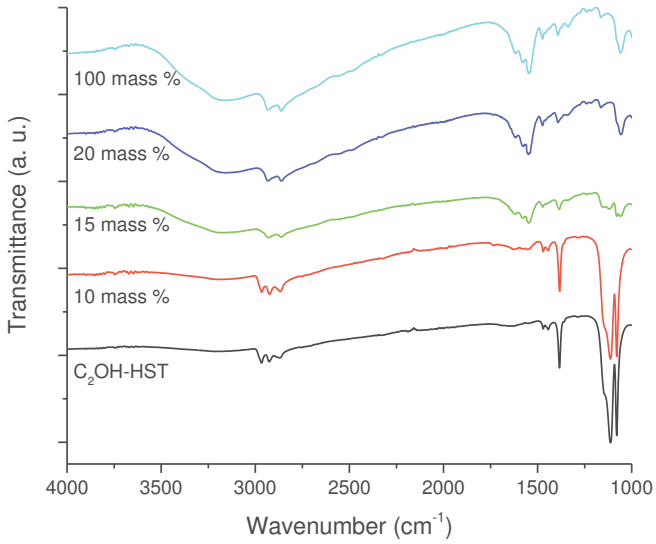

Figure II.33. *IR spectra of C_2OH-HST and its reaction products with 5-amino-pentan-1-ol by using different amount of water.*

II.2.7.3. Using HST as starting material

II.2.7.3.1. XRD analysis

The XRD patterns of HST and its reaction products with 5-amino-1-pentan-1-ol by using different amount of water are displayed in ***Figure II.34***. It is obvious that 5-amino-pentan-1-ol does not have reactivity with HST when the amount of water is 5 mass %. Yet, when the amount of water increases to 10 mass %, the reaction leads to a mono phasic product possessing an interlayer distance of 1.96 nm, which indicates a bilayer arrangement the same as that of *n*-alkylamines. When the amount of water continues to increase to 100 mass %, the reaction leads to the same phase with an interlayer distance of 1.94 nm and a residual starting material HST.

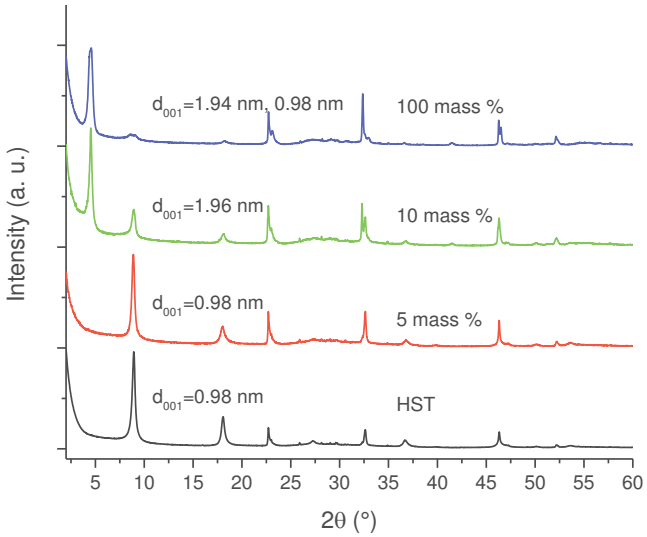

Figure II.34. *XRD patterns of HST and its reaction products with 5-amino-1-pentanol by using different amount of water.*

II.2.7.3.2. Infrared spectroscopy

The corresponding IR spectra are shown in ***Figure II.35***. When the amount of water is 5 mass %, the high similarity of IR spectra indicates the recovery of starting material. When the amount of water is more than 10 mass %, the spectra are the same as the ones of 10 mass % or 100 mass % in ***Figure II.31***, which indicates the bilayer arrangement of 5-amino-pentan-1-ol, possessing free –OH groups in the interlayer space of HST.

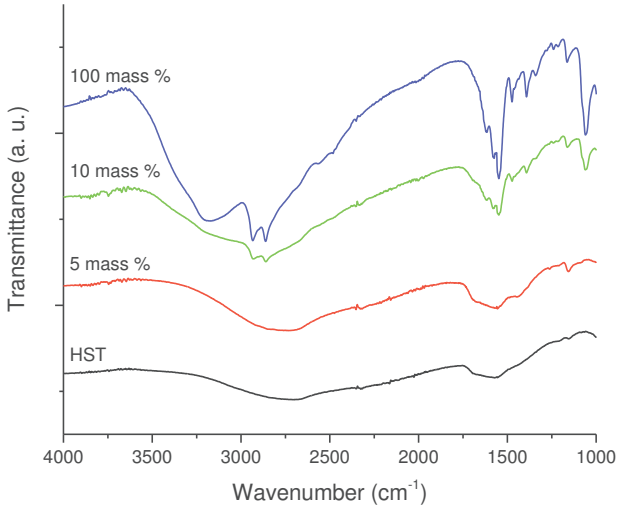

Figure II.35. *IR spectra of HST and its reaction products with 5-amino-pentan-1-ol by using different amount of water.*

Considering the above experiments, it appears that 5-amino-pentan-1-ol usually forms bilayer arrangement, presenting a free alcohol group in the interlamellar space. The only possibility to obtain a pillaring arrangement is to use C_2N-HST or C_4N-HST as starting material,

with a very tiny amount of water (1 mass %). In the following paragraph, we report our investigations on the possibility to post-treat the obtain compounds and to go from a bilayer to a pillaring arrangement.

II.2.7.4. Post treatment: from bilayer to pillaring arrangement

The bilayer arrangement of 5-amino-pentan-1-ol within the interlayer space of HST, present free –OH groups. These groups have the potential to undergo further grafting reaction to lead to pillaring arrangement.

II.2.7.4.1. Synthesis

The hybrid possessing bilayer arrangement of 5-amino-pentan-1-ol underwent several heating treatment at 70 °C in oven for 1 day, 2 days and 3 days, respectively. The stability of this hybrid has also been tested through a 10 day standing at room temperature.

II.2.7.4.2. XRD analysis

The XRD patterns of the starting hybrid and the products obtained after heating treatment are shown in ***Figure II.36***. After 10 days, the XRD pattern of the hybrid remains unchanged which indicates its stability at room temperature. When the hybrid is heated at 70 °C during one day, the interlayer distance decreased from 1.98 nm to 1.70 nm and further decreased to 1.62 nm when the heating time is prolonged to two days. Longer heating times do not lead to any further change of the interlamellar distance. It is noteworthy that the distance which is obtained after heating (1.62 nm) is the same as the one obtained by the reaction between C_2N-HST and 5-amino-pentan-1-ol using 1 mass % of water (***Figure II.30***) which corresponds to a pillaring arrangement of 5-amino-pentan-1-ol.

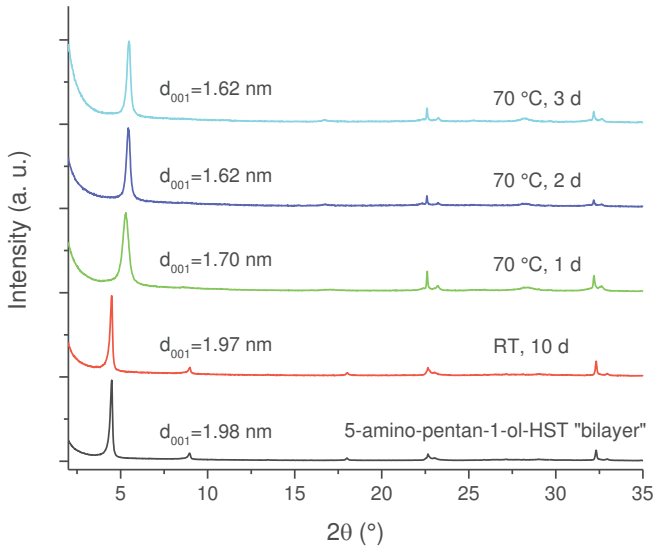

Figure II.36. *XRD patterns of 5-amino-pentan-1-ol-HST "bilayer" and the products obtained after heating treatment.*

II.2.7.4.3. Infrared spectroscopy

The corresponding IR spectra (***Figure II.37***) further support the above hypothesis, based on the results of DRX (***Figure II.36***). The unchanged IR spectrum after 10 days at room temperature confirms the stability of the initial bilayer hybrid. An indicate the stability of this hybrid at room temperature, even after 10 days. Upon heating, the spectra show important reduction of the intensity of signals around 3170 cm^{-1} (coming from water or –OH groups). In addition, the C-O stretching vibration undergoes a clear blue shift from 1058 cm^{-1} (C-OH) to 1120 cm^{-1} (C-OTa). These results indicate the grafting of the alcohol moiety of 5-amino-pentan-1-ol, and thus confirm the transformation from bilayer arrangement to pillaring arrangement within the interlayer space of HST. These results will be (hopefully) confirmed by solid state NMR spectroscopy.

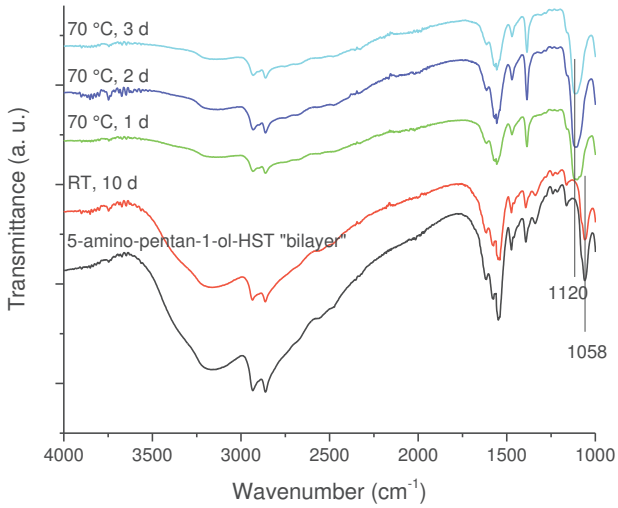

Figure II.36. *IR spectra of 5-amino-pentan-1-ol-HST "bilayer" and the products obtained after heating treatment.*

II.3. Conclusions

In conclusion, we have described the successful rapid microwave-assisted interlayer surface modification of a protonated form of a layered perovskite tantalite, HST, via grafting reactions with various alcohols (*n*-alcohols, linear diols and bulky alcohols). This approach appears to be rather general. This enriches the means of modification of HST not only *via* acid-base insertion but also *via* grafting reactions.

We have particularly investigated the role of water in the reaction processes. It appears that water has a key role not only to allow grafting of alcohols, but also to drive the preferential reactivity of HST with amines or alcohols.

In addition, we have underlined the importance of the starting product for the preparation of alkoxy derivatives of HST. Nice results were obtained using intermediates possessing *n*-alkylamine in the interlayer space, but we cannot prove the necessity of $-NH_3^+$ group, since the alcohol exchange reaction also works well when using C_nOH-HST as intermediate with $n \geq 4$. These results will be most useful when times come for the insertion of very complicated molecules, bearing several functional groups.

Finally, we have observed an interesting swelling behavior during the reaction processes between C_4N-HST and propan-1-ol, depending on the amount of water. This might be an

interesting strategy to obtain rapidly exfoliated 2D materials, nanosheets of functionalized HST.

In the next two chapters, we will investigate other strategies to functionalize layered perovskite, no longer by insertion/grafting reaction but using post-synthesis modification, either organic or inorganic.

References

[1] I. Fujita, K. Kuroda, M. Ogawa, *Chem. Mater.* **2003**, *15*, 3134-3141.
[2] J. J. Tunney, C. Detellier, *J. Mater. Chem.* **1996**, *6*, 1679-1685.
[3] J.-H. Choy, J.-B. Yoon, D.-K. Kim, S.-H. Hwang, *Inorg. Chem.* **1995**, *34*, 6524-6531.
[4] S. Bruzaud, G. Levesque, *Chem. Mater.* **2002**, *14*, 2421-2426.
[5] P. M. Forster, M. M. Tafoya, A. K. Cheetham, *J. Phys. Chem. Solids* **2004**, *65*, 11-16.
[6] S. Si, A. Taubert, A. Mantion, G. Rogez, P. Rabu, *Chem. Sci.* **2012**, *3*, 1945-1957.
[7] S. Eyele-Mezui, E. Delahaye, G. Rogez, P. Rabu, *Eur. J. Inorg. Chem.* **2012**, *2012*, 5225-5238.
[8] E. Ruiz-Hitzky, *Chem. Record* **2003**, *3*, 88-100.
[9] H. Suzuki, K. Notsu, Y. Takeda, W. Sugimoto, Y. Sugahara, *Chem. Mater.* **2003**, *15*, 636-641.
[10] S. Takahashi, T. Nakato, S. Hayashi, Y. Sugahara, K. Kuroda, *Inorg. Chem.* **1995**, *34*, 5065-5069.
[11] Y. Takeda, T. Momma, T. Osaka, K. Kuroda, Y. Sugahara, *J. Mater. Chem.* **2008**, *18*, 3581-3587.
[12] Y. Asai, Y. Ariake, H. Saito, N. Idota, K. Matsukawa, T. Nishino, Y. Sugahara, *RSC Adv.* **2014**, *4*, 26932-26939.
[13] A. Shimada, Y. Yoneyama, S. Tahara, P. H. Mutin, Y. Sugahara, *Chem. Mater.* **2009**, *21*, 4155-4162.
[14] J. R. Boykin, L. J. Smith, *Inorg. Chem.* **2015**, *54*, 4177-4179.
[15] S. Tahara, Y. Sugahara, *Langmuir* **2003**, *19*, 9473-9478.
[16] S. Tahara, T. Ichikawa, G. Kajiwara, Y. Sugahara, *Chem. Mater.* **2007**, *19*, 2352-2358.
[17] Y. Tsunoda, W. Sugimoto, Y. Sugahara, *Chem. Mater.* **2003**, *15*, 632-635.
[18] Y. Wang, C. Wang, L. Wang, Q. Hao, X. zhu, X. Chen, K. Tang, *RSC Adv.* **2014**, *4*, 4047-4054.
[19] S. Akbarian-Tefaghi, E. Teixeira Veiga, G. Amand, J. B. Wiley, *Inorg. Chem.* **2016**, *55*, 1604-1612.
[20] P. V. Der Voort, E. F. Vansant, *J. Liq. Chromatogr.Relat. Technol.* **1996**, *19*, 2723-2752.
[21] F. C. Cruz, A. Scalabrin, D. Pereira, P. A. M. Vazquez, Y. Hase, F. Strumia, *J. Mol. Spectrosc.* **1992**, *156*, 22-38.
[22] E. G. Robertson, C. Medcraft, L. Puskar, R. Tuckermann, C. D. Thompson, S. Bauerecker, D. McNaughton, *Phys. Chem. Chem. Phys.* **2009**, *11*, 7853-7860.
[23] Y. Wang, E. Delahaye, C. Leuvrey, F. Leroux, P. Rabu, G. Rogez, *Inorg. Chem.* **2016**, *55*, 4039-4046.
[24] M. V. Korolevich, R. G. Zhbankov, V. V. Sivchik, *J. Mol. Struct.* **1990**, *220*, 301-313.
[25] C. Wang, K. Tang, D. Wang, Z. Liu, L. Wang, Y. Zhu, Y. Qian, *J. Mater. Chem.* **2012**, *22*, 11086-11092.
[26] R. A. Vaia, R. K. Teukolsky, E. P. Giannelis, *Chem. Mater.* **1994**, *6*, 1017-1022.
[27] Y. Tsunoda, M. Shirata, W. Sugimoto, Z. Liu, O. Terasaki, K. Kuroda, Y. Sugahara, *Inorg. Chem.* **2001**, *40*, 5768-5771.
[28] M.-P. Crosnier-Lopez, F. Le Berre, J.-L. Fourquet, *J. Mater. Chem.* **2001**, *11*, 1146-1151.
[29] P. J. Ollivier, T. E. Mallouk, *Chem. Mater.* **1998**, *10*, 2585-2587.
[30] Y. Marcus, *The properties of solvents*; John Wiley & Sons Ltd: Chichester, **1998**.
[31] A. Goñi, J. Rius, M. Insausti, L. M. Lezama, J. L. Pizarro, M. I. Arriortua, T. Rojo, *Chem. Mater.* **1996**, *8*, 1052-1060.
[32] S. Tahara, T. Yamashita, G. Kajiwara, Y. Sugahara, *Chem. Lett.* **2006**, *35*, 1292-1293.
[33] T. Itagaki, K. Kuroda, *J. Mater. Chem.* **2003**, *13*, 1064-1068.
[34] J. Murakami, T. Itagaki, K. Kuroda, *Solid State Ionics* **2004**, *172*, 279-282.
[35] S. Hotta, N. Idota, Y. Sugahara, *Key Engineering Materials* **2014**, *616*, 82-86.
[36] N. Toihara, Y. Yoneyama, A. Shimada, S. Tahara, Y. Sugahara, *Dalton Trans.* **2015**, *44*, 3002-3008.
[37] F. Geng, R. Ma, Y. Ebina, Y. Yamauchi, N. Miyamoto, T. Sasaki, *J. Am. Chem. Soc.* **2014**, *136*, 5491-5500.

[38] K. Nakanishi, T. Goto, M. Ohashi, *Bull. Chem. Soc. Jap.* **1957**, *30*, 403-408.
[39] R. A. Heacock, L. Marion, *Can. J. Chem.* **1956**, *34*, 1782-1795.

Chapter III

Post modification of layered perovskite phases via microwave-assisted Copper (I) catalyzed Alkyne-Azide Cycloaddition (CuAAC)

III.1. Introduction

As presented in the two previous chapters, the use of microwave irradiation allows reducing considerably the reaction timescales for the functionalization of ion-exchangeable layered perovskites.[1-3] Yet, the molecules that have been inserted or grafted using this approach remain very simple, even though some more elaborated amines have been successfully inserted (chiral amines or amines bearing an aromatic group for instance as described at the end of **Chapter I**).[3] This intrinsic limitation of the mere insertion/grafting strategy thus narrows the range of functionalization and hence of applications of these layered hybrid perovskites.

Post-synthesis modification (PSM) can then be proposed to overcome the difficulty to insert directly complex or little reactive molecular guests. Following this approach, the desired molecule would be synthesized *in situ*, within the interlamellar space. Indeed post-synthesis modification has been proposed at the beginning of the 90's,[4] and really developed for Metal Organic Frameworks ten years later.[5] The use of PSM for MOFs has been thoroughly reviewed.[6-8] PSM has also been employed for microporous materials[9] or for meso-porous silicates.[10,11]

In the field of layered systems, PSM has been relatively seldom used: in clay,[12,13] layered silicates,[14] Layered Double Hydroxides[15,16] and more recently in Layered Simple Hydroxides.[17] To the best of our knowledge, the post-modification strategy has been used so far only once in the field of layered perovskites, for the *in situ* hydrosilylation of a Dion-Jacobson phase.[18]

In this chapter, we report the efficient microwave-assisted post-synthesis modification of a layered perovskite via Copper(I) Catalyzed Alkyne-Azide Cycloaddition ("click reaction" or CuAAC reaction, which was firstly reported by Sharpless[19]) (***Scheme III.1***). Click reactions have proved to be particularly useful in molecular chemistry in that they are particularly efficient, with high yield and few side-products and compatible with most functional groups.[20] As for other reactions,[21,22] microwave assisted CuAAC reactions for molecular synthesis have been widely used recently.[21-26] In the past few years, CuAAC reactions have been applied for the PSM of a large number of MOFs, either for selective surface modification,[27] or for internal functionalization.[28-33]

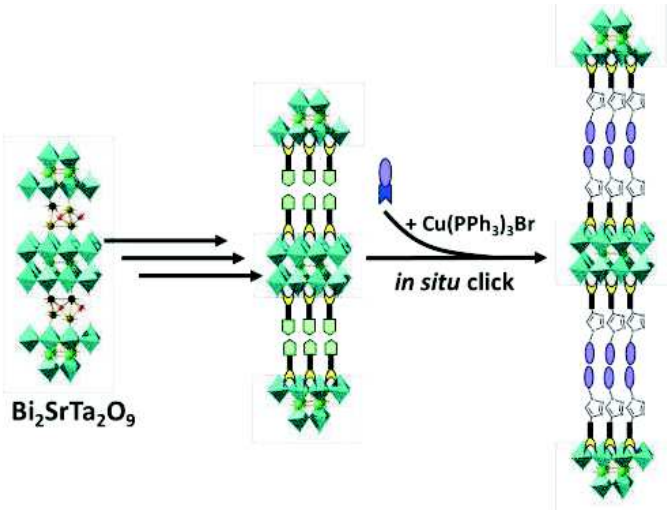

Scheme III.1. *Microwave-assisted post-synthetic modification of the Aurivillius* ***$Bi_2SrTa_2O_9$*** *phase by in situ Copper(I) Catalyzed Alkyne-Azide Cycloaddition.*

In order to achieve the *in situ* post modification objective, the first step is to immobilize some functionalized precursor, bearing a terminal alkyne or azide group, into the layered oxide. Following our results on the microwave-assisted insertion of various amines (**Chapter I**),[3] we first tried to functionalize HST by amines bearing a terminal alkyne group (4-pentyn-1-amine[34]). Unfortunately, these reactions failed, because of the instability of the inserted molecules. Therefore, we took advantage of the possibility to graft alcohols into the interlamellar spacing of such layered perovskites described in **Chapter II**.[35-37] In the present chapter, we will first present the rapid immobilization of 4-pentyn-1-ol and 3-azidopropan-1-ol, respectively, on the interlayer surface of the layered perovskite HST (***Scheme III.2***). Unfortunately, we will see that the modification of HST with 3-azidopropan-1-ol is incomplete.

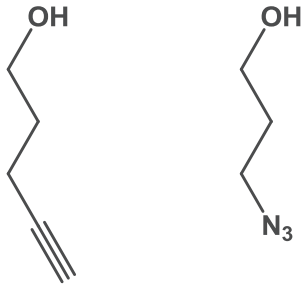

Scheme III.2. *4-pentyn-1-ol (left) and 3-azidopropan-1-ol (right).*

We will after present the subsequent microwave-assisted CuAAC reactions between alkyne-terminated precursor and azidohexane or azidobenzene respectively (***Scheme III.3***), to achieve the in situ post modification of HST from alkyne functionalized HST.

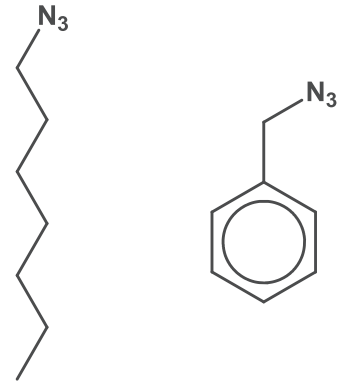

Scheme III.3. *azidohexane (left) and azidobenzene (right).*

Several catalysts, commonly used in organic chemistry, such as Cu metal,[38] Cu metal/$CuSO_4$,[39] CuI,[40,41] CuI/$(i\text{-}Pr)_2EtN$,[42-44] and $CuBr/CH_3SCH_3$,[45,46] have been tried unsuccessfully in various solvent and temperature conditions. For the famous $CuSO_4$/sodium ascorbate, the click reaction using the conditions described below worked only partly, with the presence of the starting material and of **HST** in the final product. This is likely due to the use of water, necessary with this catalyst, which leads to hydrolysis of the alcohol-Ta bonds.[35] Indeed the precursor can be regarded as macromolecular heterometallic oxoalkoxide,[47] which is therefore sensitive to hydrolysis, especially at high temperatures.[35,47] Therefore our choice went to $CuBr(PPh_3)_3$ which could be used non-aqueous, aprotic solvents, typically dry THF.[48-50] We will particular detail in the optimization of the catalyst quantity, as an excess of residual catalyst in the final product can be a great obstacle for the characterization of reaction product (by solid state NMR for instance).

We will also describe the de-intercalation of the molecules synthesized *in situ* to further prove the success of this strategy.
Finally, we will present preliminary results concerning the extension of this approach to the post-synthesis modification of the layered Dion-Jacobson phase $HLaNb_2O_7 \cdot xH_2O$.

III.2. Results and discussion

III.2.1. Preparation of precursors based on HST

III.2.1.1. Preparation of alkyne-terminated precursor (alkyne-HST)

III.2.1.1.1. Synthesis

We first attempted to prepare the alkyne-terminated precursor (hereafter noted alkyne-HST) through the reaction between C_4N-HST (or C_2N-HST) and 4-pentyn-1-ol, by analogy with what has been described for the preparing of *n*-alcohol-HST (cf. **Chapter II**). Yet this procedure led to incomplete transformation.
Therefore, we chose to proceed *via* alcohol exchange from C_2OH-HST as an intermediate, using microwave assisted exchange reaction (110°C, 2 h) (cf. **Chapter II**). 4-pentyn-1-ol is used in large excess (*ca.* ×100) with respect to the intermediate.

III.2.1.1.2. XRD analysis

The XRD patterns of HST, C_2OH-HST and its reaction product with 4-pentyn-1-ol are shown in ***Figure III.1***. After reaction, the (00l) reflections of C_2OH-HST disappear, and new sets of (00l) reflections appear. The interlayer distance increases from that of C_2OH-HST (1.55 nm) to 1.87 nm, which indicates the occurring of exchange reaction. which is compatible with a bilayer arrangement of the alkyne molecules in the interlamellar space with a tilt angle of 60° with respect to the normal to the layers (considering the size of the molecules around 0.7 nm, the thickness of the inorganic layers around 1 nm[51,52] and 0.3 nm between the terminal alkyne groups[53]). Assuming a bilayer arrangement, the tilt angle is about twice those previously reported for the grafting of aliphatic alcohols into Ta-based Ruddlesden-Popper perovskites,[2,54] which may suggest partial interdigitation of the inserted molecules. The alcohol-exchange reaction is topotactic, as suggested by the preservation of unshifted characteristic out-of-plane reflections of **HST** (for instance (100) at 22.68°, (110) at 32.59°, and (200) at 46.32° (Cu Kα1)).

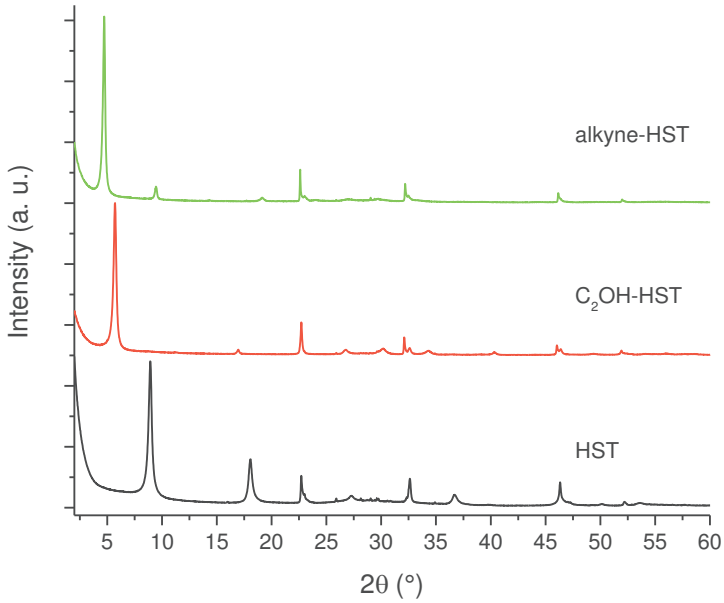

Figure III.1. *PXRD patterns of HST, C_2OH-HST and its reaction product with 4-pentyn-1-ol (alkyne-HST).*

III.2.1.1.3. Infrared spectroscopy

Their corresponding infrared spectra and that of 4-pentyn-1-ol are shown in ***Figure III.2***. The Ta-O elongation vibration is the dominant feature at 580 cm^{-1} for the hybrids. This band is slightly shifted depending on the sample (HST, C_2OH-HST and alkyne-HST), without any clear correlation with the functionalization. Comparing the IR spectra of the reaction product with that of C_2OH-HST, it's clear to notice not only the appearance of new signals (the stretching C-H vibration of the terminal alkyne group at 3285 cm^{-1} and the stretching C≡C vibration at 2114 cm^{-1}) but also the disappearance of the signals of CH_3 group (2967 cm^{-1}), which belongs to starting material C_2OH-HST. In addition, comparing the IR spectra of the reaction product with that of 4-pentyn-1-ol, an obvious blue shift of about 90 cm^{-1} of the stretching vibration of C-O between the reaction product (1132 cm^{-1}) and 4-pentyn-1-ol (1046 cm^{-1}) is observed. Finally, there is no evidence of O-H stretching vibration at 3360 cm^{-1} as would be the case for a mere alcohol insertion. All these features indicate the complete replacement of grafted ethanol by 4-pentyn-1-ol and the formation of a covalent bond C-O-Ta between HST and 4-pentyn-1-ol.

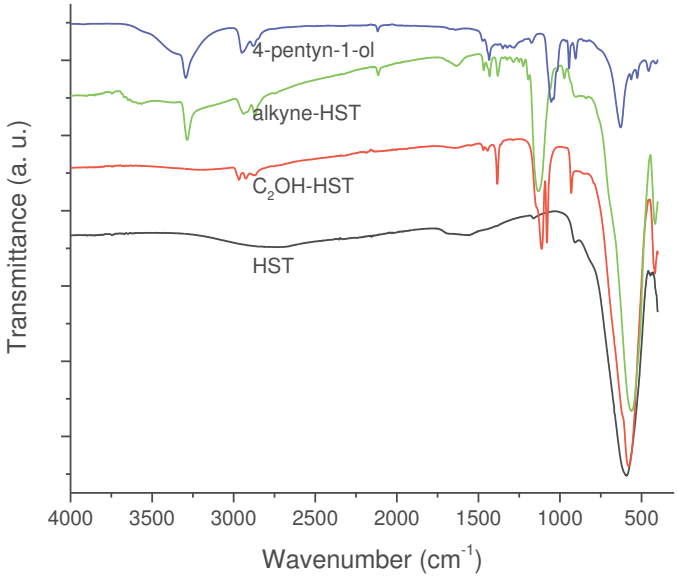

Figure III.2. *Infrared spectra of HST, C_2OH-HST, alkyne-HST and 4-pentyn-1-ol.*

III.2.1.1.4. Thermal analyses

The TGA and TDA curves of alkyne-HST have also been done (***Figure III.3***). The behaviour is very similar to the one encountered in the previous chapter for HST functionnalized by alcohols. Based on this thermal behaviour and along with elemental analysis, a consistent formula for alkyne-HST: $H_{1.3}Bi_{0.1}Sr_{0.85}Ta_2O_{6.3}(OC_3H_6C{\equiv}CH)_{0.7}{\cdot}0.5H_2O$ (see **Annex**). This organic loading of 0.7 alcohol per Ta_2 unit is within the range of reported alcohol loading in other layered perovskites, either by classical functionalization[35-37,54-56] or by microwave assisted functionalization.[1,2]

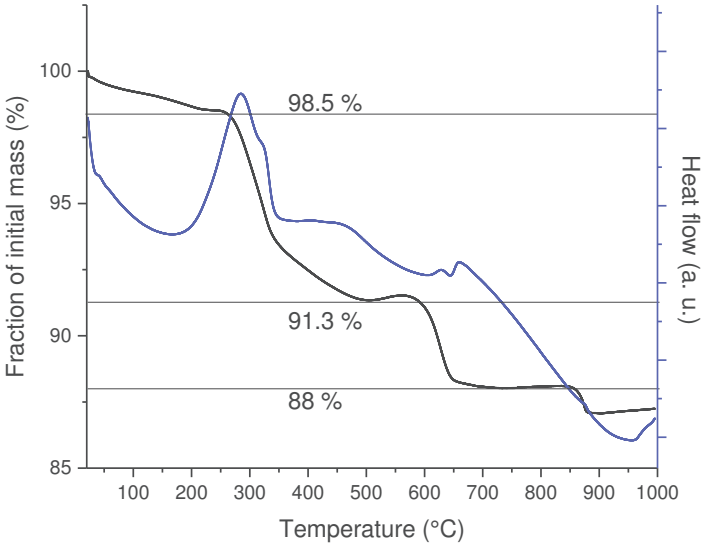

Figure III.3. *TGA and TDA curves for alkyne-HST.*

III.2.1.1.5. Solid state NMR

In order to further demonstrate the successful preparation of alkyne-HST, solid state NMR spectroscopy (collaboration Fabrice Leroux, Institut de Chimie de Clermont-Ferrand) was employed. ***Figure III.4*** shows the solid-state ^{13}C CP/MAS NMR spectrum of alkyne-HST. The chemical shift of the α-carbon (-C-O-, A) signal of alkyne-HST is 73 ppm. Comparing with the chemical shift of the α-carbon (-C-O-) signal of 4-pentyn-1-ol in the liquid-state ^{13}C NMR spectrum (61.4 ppm), there is a downfield shift of about 12 ppm, which indicates the formation of the covalent bond C-O-Ta.[57] On the contrary, the other signals, B, C, D and E do not move upon grafting (32, 15, 85 and 70 ppm respectively in the hybrid **HC≡C⊂HST**, and 31, 15, 84 and 69 ppm respectively for the free molecule).Finally, the signal marked with asterisk at 62 ppm may indicate the existence of a tiny amount of ungrafted 4-pentyn-1-ol in the precursor.

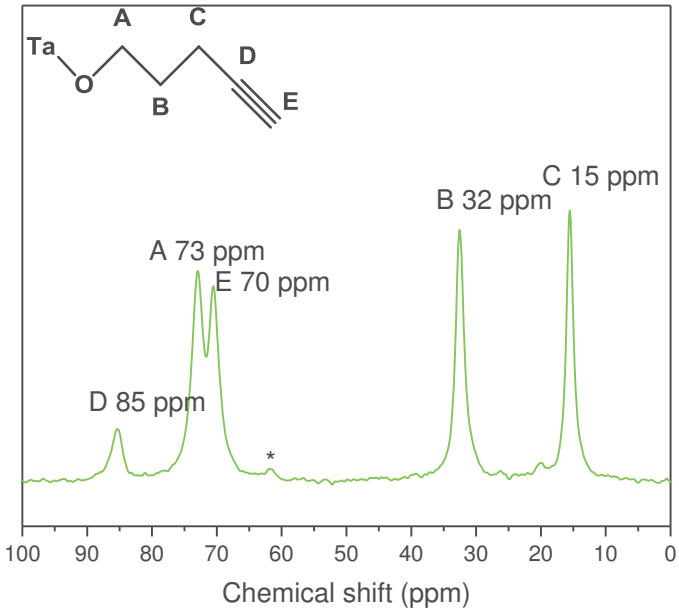

Figure III.4. *Solid-state ^{13}C CP/MAS NMR spectra of alkyne-HST.*

III.2.1.2. Preparation of azide-terminated precursor (azide-HST)

We have also tried to immobilize another precursor for a further *in situ* click chemistry reaction, this time an azide-bearing molecule (3-azidopropan-1-ol).

III.2.1.2.1. Synthesis

Immobilization of 3-azidopropan-1-ol on the interlayer surface of HST to prepare azide-terminated precursor (hereafter noted azide-HST) is quite complicated, and three different compounds (C_2OH-HST, C_{12}OH-HST and C_4N-HST) have been employed as intermediates. The microwave assisted (90°C, 2h) reactions were performed by using large excess (*ca.* ×100) of 3-azidopropan-1-ol with respect to intermediates.

III.2.1.2.2. XRD analysis

Figure III.5 shows the XRD patterns of HST, the three intermediates (C_2OH-HST, C_{12}OH-HST and C_4N-HST) and their respective reaction products with 3-azidopropan-1-ol. For all compounds, the reflections assigned to (100) and (110) in the XRD pattern of HST, are observed at the same positions (22.68° and 32.59°, respectively), which indicates the preservation of the perovskite-like slab structure.

Comparing C_2OH-HST with its reaction product, after reaction, the interlayer distance increases from 1.54 nm for C_2OH-HST to 1.72 nm. For C_{12}OH-HST, the interlayer distance decreases from that of C_{12}OH-HST (4.0 nm) to 1.95 nm. Finally, when using C_4N-HST as intermediate, the PXRD pattern of its reaction product with 3-azidopropan-1-ol reveals a multiphasic compound, with very bad crystallinity. As a result, C_4N-HST is not an ideal intermediate to prepare the target precursor.

For the other two intermediates, after reacting with 3-azidopropan-1-ol, both present a drastic change in the interlayer distances, but the two obtained products have different interlayer distances (1.72 nm and 1.95 nm, respectively).

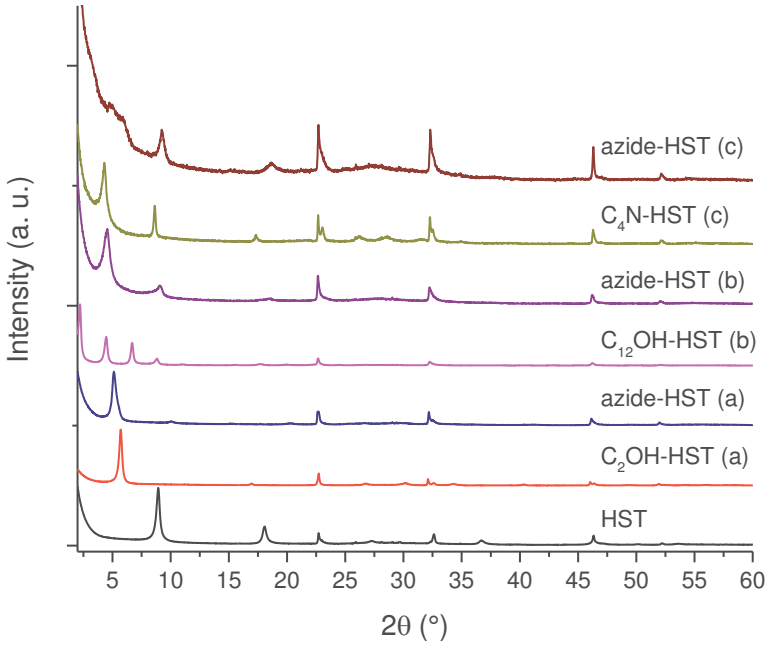

Figure III.5. *PXRD patterns of HST, C_2OH-HST, C_{12}OH-HST, C_4N-HST and their reaction products with 3-azidopropan-1-ol, respectively.*

III.2.1.2.3. Infrared spectroscopy

In order to further understand the nature of the two obtained products, their infrared spectra have been recorded (***Figure III.6***). Comparing the IR spectrum of C_2OH-HST with that of its reaction product, the new signal of the stretching bond of azide (2095 cm^{-1}) appears, which indicates the successful immobilization of 3-azidopropan-1-ol on the interlayer surface of HST. Unfortunately, the existence of CH_3 group (2968 cm^{-1}), which comes from C_2OH-HST, strongly indicates the unfinished alcohol-exchange-type reaction. Comparing the IR spectrum of C_{12}OH-HST with that of its reaction product, the signal of the stretching bond of

azide (2095 cm^{-1}) is also observed. Considering the relative weakness of CH_3 group signal (2955 cm^{-1}) in the spectrum of C_{12}OH-HST, it is difficult to confirm the complete disappearance of this signal in the reaction product. In addition, comparing the IR spectrum of the reaction product with that of 3-azidopropan-1-ol, an obvious blue shift of 95 cm^{-1} of the stretching bond of C-O is observed. Considering also the missing of the absorption of OH bond (3337 cm^{-1}), the formation of covalent bond C-O-Ta between HST and 3-azidopropan-1-ol is proposed. Finally the intermediate C_{12}OH-HST appears to be the best intermediate to prepare the azide-terminated precursor.

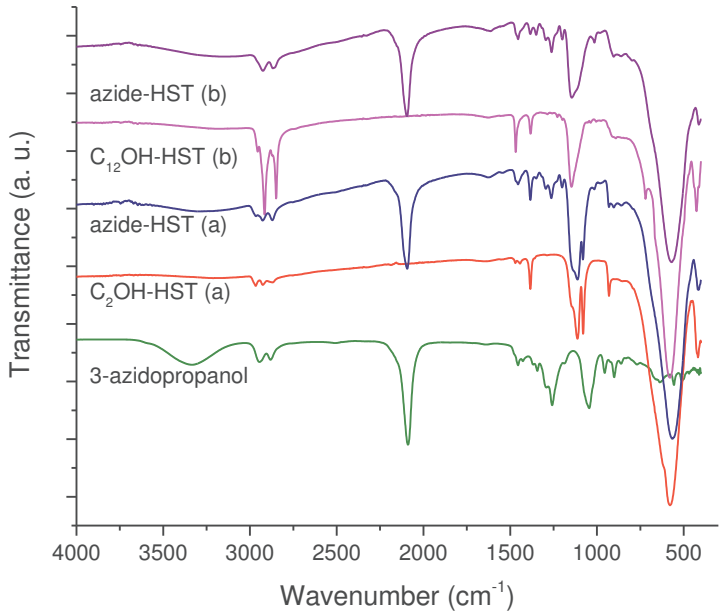

Figure III.6. *IR spectra of 3-azidopropan-1-ol, C_2OH-HST, C_{12}OH-HST and their reaction products with 3-azidopropan-1-ol.*

III.2.1.2.4. Solid state NMR

In order to further study the azide-terminated precursor obtained using C_{12}OH-HST as intermediate, solid state NMR spectroscopy was used (collaboration Fabrice Leroux, Institut de Chimie de Clermont-Ferrand). The solid-state ^{13}C CP/MAS NMR spectrum is shown ***Figure III.7***. The chemical shift of the α-carbon (-C-O-, A) signal of azide-HST is 71 ppm. Comparing with the chemical shift of the α-carbon (-C-O-) signal of 3-azidopropan-1-ol in the liquid-state ^{13}C NMR spectra (59.9 ppm), there is a downfield shift of about 11 ppm, which indicates the formation of covalent bond C-O-Ta between HST and 3-azidopropan-1-ol.[57] The two signals at 49 ppm and at 33 ppm are believed to come from the other two CH_2 groups. In addition, some signals, marked with asterisks, are believed to come from *n*-dodecanoxy of the starting material. This means that the alcohol-exchange-type reaction is unfinished.

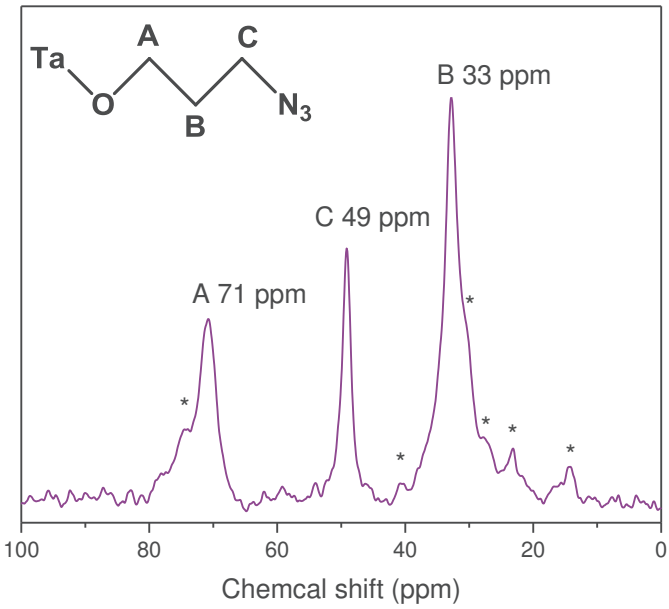

Figure III.7. *Solid-state ^{13}C CP/MAS NMR spectra of azide-HST prepared from C_{12}OH-HST.*

According to the above results of characterizations, there are sufficient evidences to prove the successful immobilization of 3-azidopropan-1-ol on the interlayer surface of HST. Unfortunately, the alcohol-exchange-type reaction is unfinished and the pure precursor, until now, could not be obtained.

Attempts have further been carried out to immobilize 3-azidopropyl-1-amine[58] on the interlayer surface of HST, in view of the reactivity of HST with amines (**Chapter I**). The direct intercalation between HST and 3-azidopropyl-1-amine does not lead to a monophasic product. The use of the pre-intercalation strategy (cf. **chapter I**) allows obtaining a monophasic product. Yet, according to the results of micro-analyses (C, H, N), the ratio between carbon and nitrogen is much higher than the theoretical value, which indicates the incompleteness of exchange reaction. Finally, attempts to form *in situ* the terminal azide group, by reacting 3-chloropropyl-1-amine-HST with NaN_3, did not succeed. Until now, we could not find a good way to prepare a proper azide-terminated precursor.

III.2.2. Post-synthesis modification of alkyne-HST

III.2.2.1. Post-synthesis modification *via* 1, 3-dipolar cycloaddition reaction without using copper (I) catalyst

Since the possibility of thermal reactions between terminal or internal alkynes and organic azides has been demonstrated for long,[59] it seemed reasonable to attempt direct the post-synthesis modification of alkyne-HST via thermal 1,3-dipolar cycloaddition reaction without using copper (I) catalyst.

III.2.2.1.1. Synthesis

The microwave assisted (80°C, 2h) reactions were performed by using large excess (*ca.* ×100) of azidohexane (1 g (7.9 mmol) dissolved in 1 mL of dry THF) with respect to alkyne-HST (50 mg, 0.08 mmol).

III.2.2.1.2. XRD analysis

Figure III.8 shows the XRD patterns of HST, alkyne-HST and its reaction product using the conditions presented above. After reaction, the interlayer distance slightly decreases from that of alkyne-HST (1.87 nm) to 1.75 nm, which indicates the failure of the expected post-synthesis modification (since the obvious increasing of interlayer distance of the reaction product is foreseeable). The slight decrease of the interlayer distance is ascribed to rearrangement of the alkyne molecules within the interlamellar spacing (more interdigitation for instance) likely induced by the partial loss of organic phase during the process of thermal reaction.

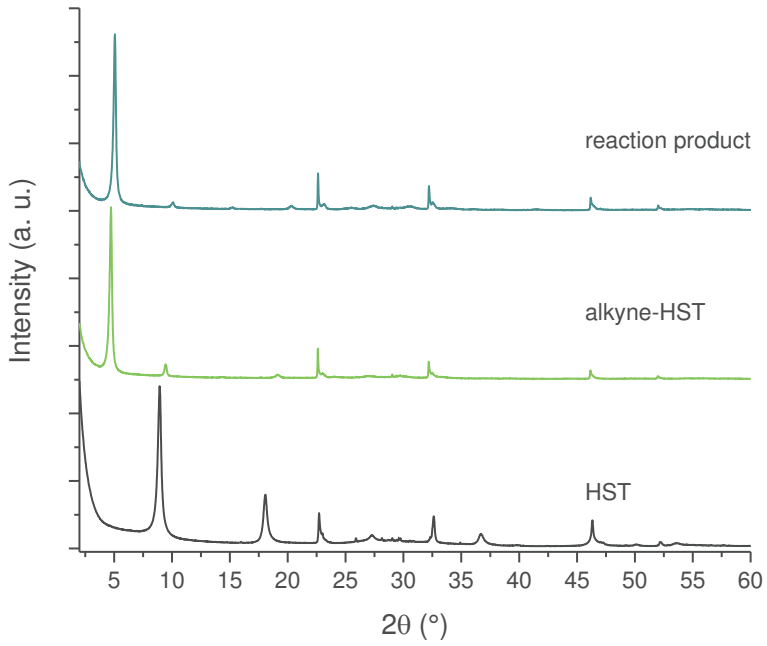

Figure III.8. *PXRD patterns of HST, alkyne-HST and its reaction product.*

III.2.2.1.3. Infrared spectroscopy

Figure III.9 shows the corresponding IR spectra. The existence of signals of the stretching bond of C≡C-H (3285 cm^{-1}) and of C≡C (2114 cm^{-1}) in the final product, and the missing of foreseeable signal of CH_3 group strongly demonstrate the failure of the post-modification. Comparing the IR spectrum of the reaction product with the one of the starting material alkyne-HST, we can notice that there is a high degree of similarity between them. As a result, it is believed that, after reaction, the starting material is obtained instead of our target product. Taking into account the slight decreasing of the interlayer distance and the high

degree of similarity of IR spectra, there are sufficient evidences to prove the failure of the post-synthesis modification without using catalyst.

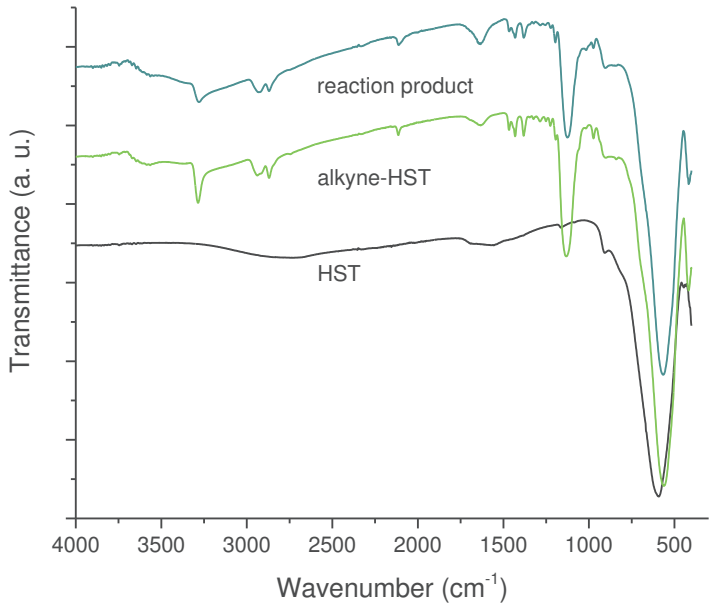

Figure III.9. *IR spectra of HST, alkyne-HST and its reaction product.*

III.2.2.2. Post-synthesis modification of alkyne-HST via microwave-assisted Copper (I) catalyzed Alkyne-Azide Cycloaddition (CuAAC) reaction

After the failure of direct post-synthesis modification of alkyne-HST *via* thermal 1, 3-dipolar cycloaddition reaction, we attempted to use the microwave-assisted CuAAC reaction to realize our objective. Two different azide reactants, one bearing an aliphatic group (1-azidohexane), the other bearing a more bulky and rigid aromatic group (1-azidobenzene) have been employed. We will describe first the optimization of the reaction conditions, considering the reaction with 1-azidohexane.

III.2.2.2.1. Optimization of the reaction conditions, especially the amount of catalyst, using 1-azidohexane

III.2.2.2.1.1. Synthesis

The microwave-assisted (80°C, 2 h) CuAAC reactions between alkyne-HST and 1-azidohexane (large excess, *ca.* ×100) have been performed, using different molar amount of $CuBr(PPh_3)_3$ catalyst (0.5, 1.0, 10 mol % with respect to alkyne-HST, respectively). The whole manipulations and reactions are performed under a protective argon atmosphere. The obtained compounds were named hexyl-click-HST.

III.2.2.2.1.2. XRD analysis

Figure III.10 shows the PXRD patterns of HST, alkyne-HST and its reaction products with 1-azidohexane by using different molar amount of $CuBr(PPh_3)_3$catalyst. After reactions, the (00l) reflections of alkyne-HST disappear, and new sets of (00l) reflections appear. In contrast, the reflections, which are assigned to (100) and (110) in the XRD pattern of HST, are observed at the same positions (22.68° and 32.59°, respectively) in all the obtained products, which indicates the preservation of the structure of the inorganic perovskite-like slab. For the reaction using 0.5 mol % of $CuBr(PPh_3)_3$, after reaction, the interlayer distance increases from that of alkyne-HST (1.87 nm) to 2.00 nm. When the quantity of $CuBr(PPh_3)_3$ increased from 0.5 mol % to 1.0 mol %, the interlayer distance of reaction product further increases to 2.72 nm. However, when the quantity of the catalyst continues to increase from 1.0 mol % to 10 mol %, a reaction product with the same interlayer distance (2.68 nm) as that of the one obtained by using 1.0 mol % catalyst is obtained. In conclusion, the increase of the interlayer distance of reaction products is a very positive signal to indicate the occurring of CuAAC click reaction and it seems that 1.0 mol % of catalyst is enough for this type of reaction.

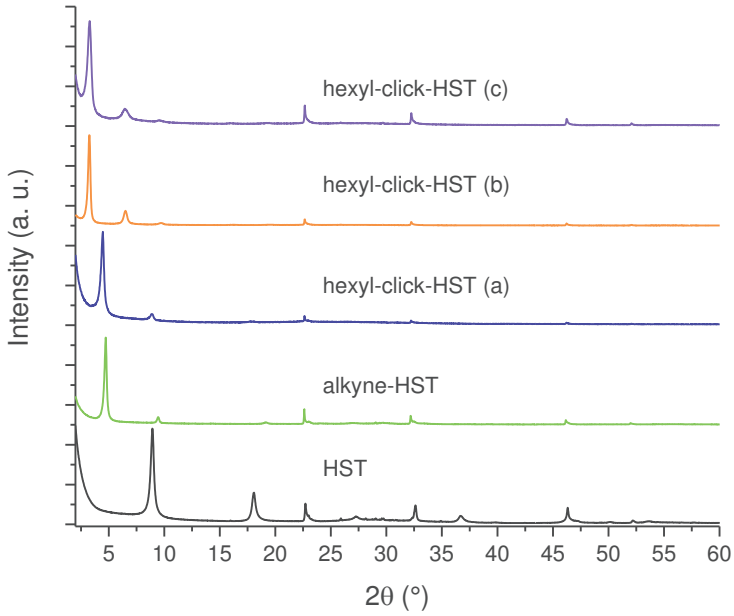

Figure III.10. *PXRD patterns of HST, alkyne-HST and its reaction products with 1-azidohexane by using different molar amount of $CuBr(PPh_3)_3$ catalyst : (a): 0.5 mol %; (b): 1.0 mol %; (c): 10 mol % of catalyst.*

III.2.2.2.1.3. Infrared spectroscopy

Further information about the products is obtained from the corresponding IR spectra (***Figure III.11***). Comparing the IR spectra of the reaction product (a, 0.5 mol %) with that of alkyne-HST, the appearance of the weak signal of CH_3 group (2955 cm^{-1}) and of N=N bond (1551 cm^{-1}), indicates the occurrence of CuAAC click reaction. However, the existence of signals of the stretching bond of C≡C-H (3285 cm^{-1}) and C≡C (2114 cm^{-1}) proves that the CuAAC reaction is unfinished. Comparing the IR spectra of the reaction product (b, 1 mol %) with that of alkyne-HST, it is clear to observe the complete disappearance of signals of the

stretching bond of C≡C-H (3285 cm^{-1}) and C≡C (2114 cm^{-1}). The appearance of the signals of CH_3 group (2955 cm^{-1}) and N=N bond (1551 cm^{-1}) is also noticed. The signals at 1632 cm^{-1} and 1457 cm^{-1} are believed to come from the triazole bonds,[60] and the weak signal at 3132 cm^{-1} is proposed to come from C=C-H group in pentaheterocyclic structure. In addition, the enhanced absorption intensity of CH_2 group indirectly reflects the presence of long alkyl chain. Incidentally, the remaining intense absorption at 1137 cm^{-1} in the spectra of reaction product, indicates the retention of the C-O-Ta bond during the reaction process. Finally, comparing the IR spectrum of reaction product (c) with that of the reaction product (b), it is clear to observe that the two spectra are exactly the same.
According to the above analysis, the occurrence of click reaction between the precursor and the organic azide is very positive. In addition, 1.0 mol % of catalyst is enough for this type of reaction.

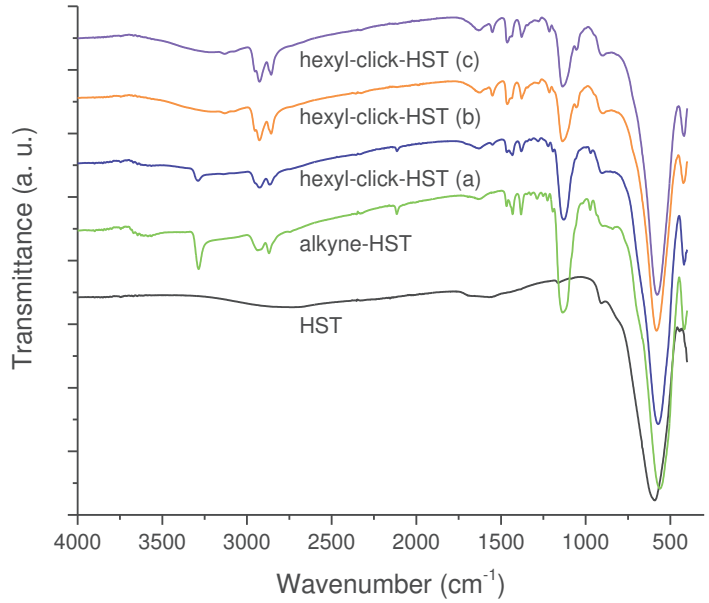

Figure III.11. *IR spectra of HST, alkyne-HST and its reaction products with 1-azidohexane by using different molar amount of $CuBr(PPh_3)_3$ catalyst : (a): 0.5 mol %; (b): 1.0 mol %; (c): 10 mol % of catalyst.*

III.2.2.2.2. Generalization of the above optimal conditions using 1-azidobenzene

In order to further expand the application scope of the CuAAC reactions of alkyne-HST, we tested a different azide, more rigid and bearing an aromatic group. We chose benzyl azide.

III.2.2.2.2.1. Synthesis

The reaction conditions established in the previous paragraphs (microwave-assisted, 80°C, 2h and 1.0 mol % of $CuBr(PPh_3)_3$) are employed for the reaction between alkyne-HST and 1-azidobenzene (large excess, *ca.* ×100). The whole manipulations and reactions are performed under a protective argon atmosphere. The obtained compound was named benzyl-click-HST.

III.2.2.2.2.2. XRD analysis

Figure III.12 shows the PXRD patterns of HST, alkyne-HST and its reaction product with 1-azidobenzene. After reaction, we can observe that the (00l) reflections of alkyne-HST disappear, and new sets of (00l) reflections appear. The interlayer distance increases from that of alkyne-HST (1.87 nm) to 2.60 nm. In contrast, the reflections, which are assigned to (100) and (110) in the XRD pattern of HST, are observed at the same position (22.68° and 32.59°, respectively) in the obtained product. According to the above analyses, the increasing of interlayer distance of reaction product is a very positive signal to indicate the occurrence of CuAAC click reaction between alkyne-HST with 1-azidobenzene and it seems that 1.0 mol % of catalyst is also enough for this type of reaction, even when the organic reactant is changed.

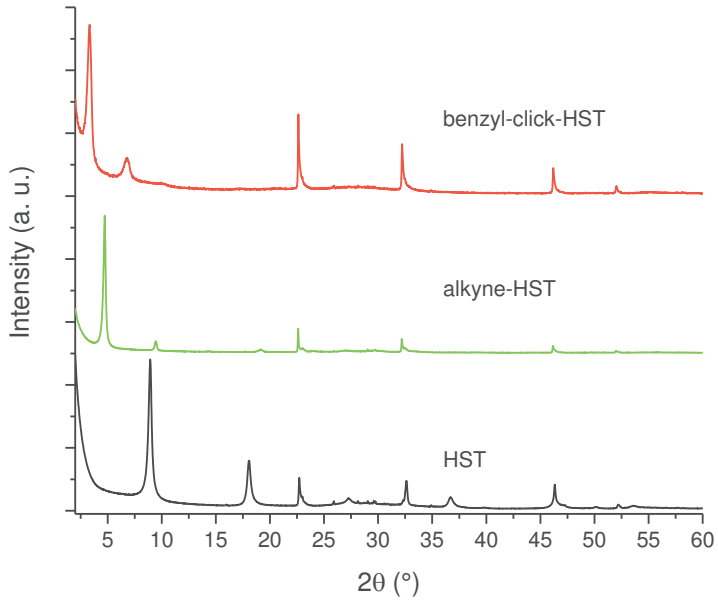

Figure III.12 *PXRD patterns of HST, alkyne-HST and its reaction product with 1-azidobenzene.*

III.2.2.2.2.3. Infrared spectroscopy

The corresponding IR spectra are presented in ***Figure III.13***. Comparing the IR spectrum of the reaction product with that of alkyne-HST, it is clear to notice the disappearance of signals of the stretching bond of C≡C-H (3285 cm^{-1}) and of C≡C (2114 cm^{-1}). In addition, the appearance of characteristic signals of aromatic (weak signals of C-H stretch (3064, 3029 cm^{-1}) and the signal of C-C stretch (1497 cm^{-1})) strongly indicate the introduction of the benzene ring. The signals at 1632 cm^{-1} and 1461 cm^{-1} are believed to come from the triazole bonds,[60] and the weak signal at 3132 cm^{-1} is assigned to the C=C-H group in the pentaheterocyclic structure. By the way, the remaining intense absorption at 1128 cm^{-1} in the spectrum of the reaction product indicates that the bond C-O-Ta remains intact during the reaction process. The above analyses are good indication of the occurrence of click reaction between alkyne-HST and 1-azidobenzene.

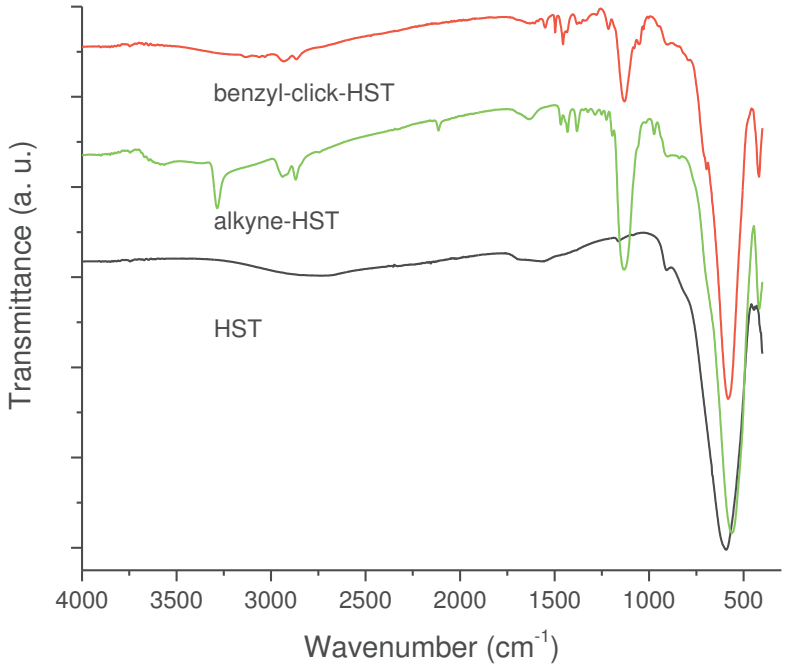

Figure III.13. *IR spectra of HST, alkyne-HST and its reaction product with 1-azidobenzene.*

As a result, the established reaction conditions are also applicable for 1-azidobenzene, which illustrates the general application of this method.

III.2.2.2.3. Further characterizations of hexyl-click-HST and benzyl-click-HST

III.2.2.2.3.1. Solid-state NMR

In order to further confirm the occurring of click reactions in the interlayer space of the precursor alkyne-HST with azidohexane or azidobenzene, solid state ^{13}C CP/MAS NMR spectroscopy (collaboration Fabrice Leroux, Institut de Chimie de Clermont-Ferrand) was performed (***Figure III.14***). The signal of the carbon bearing the anchoring oxygen (A) remains unshifted at 73 ppm in all compounds, confirming the grafting of the molecules. Yet, a small signal at 62 ppm (marked with an asterisk) may indicate that a tiny amount of molecules have been ungrafted during the reaction. Looking carefully at the IR spectra (***Figures III.11*** and ***III.13***), a small shoulder around 1050 cm^{-1} may be attributed to the presence of a small amount of alcohol which has been ungrafted during the *in situ* reaction. Despite several attempts, this ungrafting seems unavoidable.
Finally, in addition to the presence of the signals coming from the aliphatic or aromatic moieties of the azido reactants, the obvious downfield shift of the signals D and E of the terminal alkyne group from 85 and 70 ppm to *ca.* 150 and 120 ppm is a clear indication of the formation of triazole moiety.[61] The position of the signal E, around 120 ppm, indicates the formation of a unique regio-isomer of the 1*H*-1,2,3-triazole, the 1,4-disubstituted, and not the 1,5-disubstituted for which the signal E would be expected around 133 ppm, as expected for a copper(I) catalyzed 1,3-dipolar cycloaddition.[61]

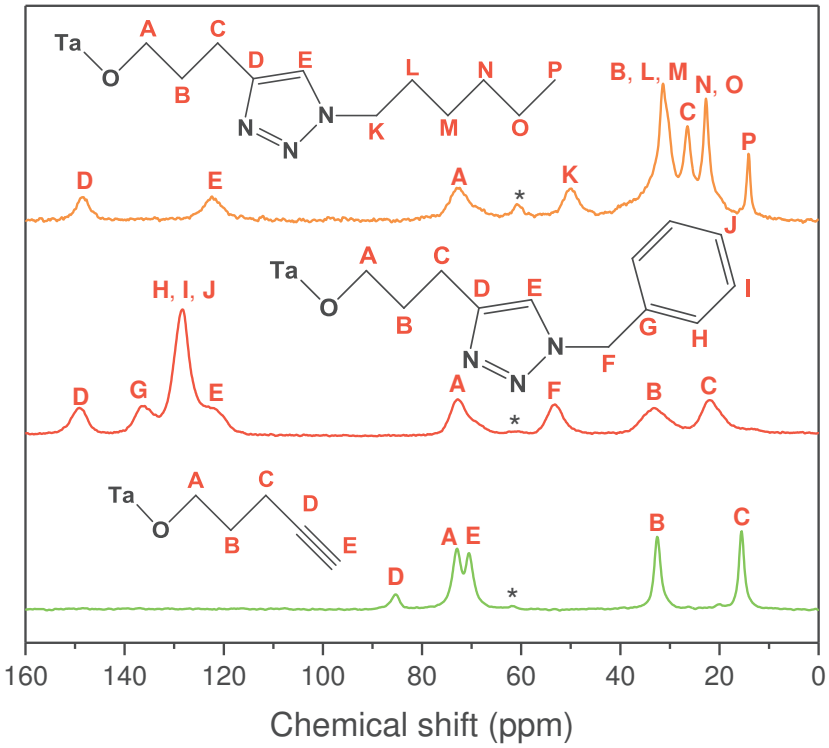

Figure III.14. *Solid-state ^{13}C CP/MAS NMR spectra of alkyne-HST and its click reaction products with 1-azidohexane or benzyl azide.*

III.2.2.2.3.2. Thermal analysis and proposed formulae

The C/N ratios, determined from elemental analyses, are in accordance with the expected values for an *in-situ* triazole formation by click-reaction (exp: 3.8 and 4.2, expected: 3.7 and 4.0 for hexyl-click-HST and benzyl-click-HST respectively). The organic content can be determined from thermogravimetric analysis (***Figure III.15***), and, along with elemental analysis, the formulae deduces for hexyl-click-HST and benzyl-click-HST are: $H_{1.5}Bi_{0.1}Sr_{0.85}Ta_2O_{6.5}(OC_{11}N_3H_{20})_{0.5}\cdot 0.3H_2O$ and $H_{1.4}Bi_{0.1}Sr_{0.85}Ta_2O_{6.4}(OC_{12}N_3H_{14})_{0.6}\cdot 0.6H_2O$ respectively. The leaching of the grafted alkyne-alcohol precursor is thus relatively moderate. The organic content decreases from 0.7 alcohol per Ta_2 unit in alkyne-HST to 0.5 and 0.6 for hexyl-click-HST and benzyl-click-HST respectively. This partial leaching may be due to traces of water present during the *in situ* click reaction.

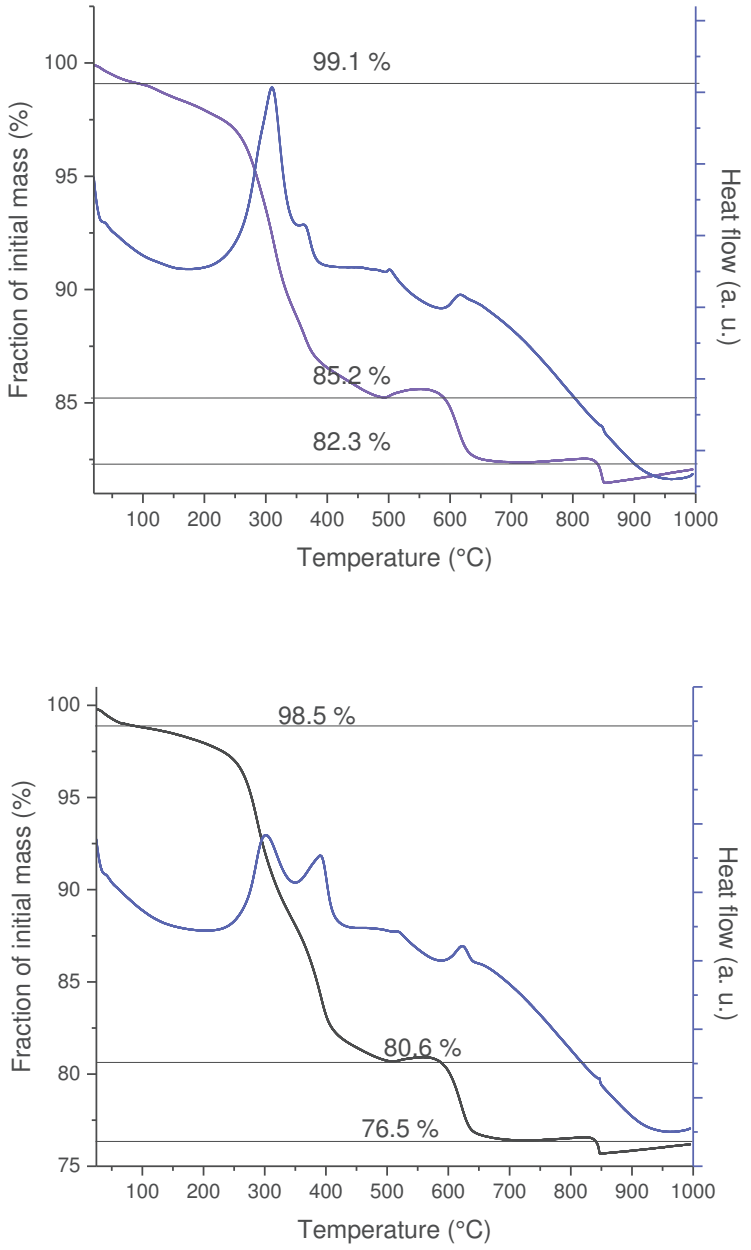

Figure III.15. *TGA and DTA curves for hexyl-click-HST (top) and benzyl-click-HST (bottom).*

III.2.2.2.3.3. SEM observation

The SEM images of alkyne-HST, hexyl-click-HST and benzyl-click-HST are displayed in ***Figure III.16***. The shape, morphology and size of the crystallites are preserved during the intercalation of 4-pentyn-1-ol and the further click reactions.

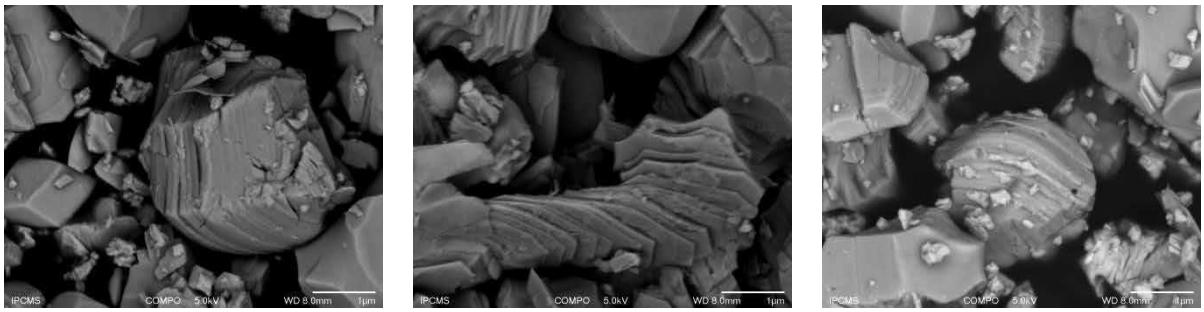

***Figure III.16**. SEM images of alkyne-HST (left), hexyl-click-HST (middle) and benzyl-click-HST (right).*

III.2.2.2.4. Deintercalation behaviors of hexyl-click-HST and benzyl-click-HST

As described in literature, the organic derivatives of a layered perovskite compound, $HLaNb_2O_7 \cdot xH_2O$ (HLN) with interlayer surface functionalized by *n*-dodecanoxy groups, can be removed via hydrolysis of the R-O-Nb bond by using base treatment.[35] Therefore, the *in-situ* formed molecules in the obtained click reaction products are likely to be further deintercalated by alkaline treatment.

III.2.2.2.4.1. Synthesis

The click reaction products hexyl-click-HST and benzyl-click-HST were stirred in NaOH aqueous solution (6 M) at 80 °C for 48 h (see **Annex**)

III.2.2.2.4.2. Obtained solids

III.2.2.2.4.2.1. Collection

After reaction, the obtained solid and solution were separated via centrifugation and the obtained solid was washed with water and acetone and air-dried.

III.2.2.2.4.2.2. XRD analysis

Figure III.17 shows the XRD patterns the corresponding base treated products. After alkaline treatment, the interlayer distance decreases from that of click reaction products (2.72 nm, 2.60 nm, respectively) to *ca.* 1.30 nm, which is slightly larger than that of HST (0.98 nm). The crystallinity of the obtained products is rather poor. The obvious decrease of the interlayer distance is a good signal to indicate the removal of the organic phase from the interlayer space of hybrid. The reflections, which are assigned as (100) and (110) in the XRD pattern of HST, are observed at the same positions (22.68° and 32.59°, respectively) in the base treated products, indicating that the structure of the inorganic perovskite-like slab is retained.

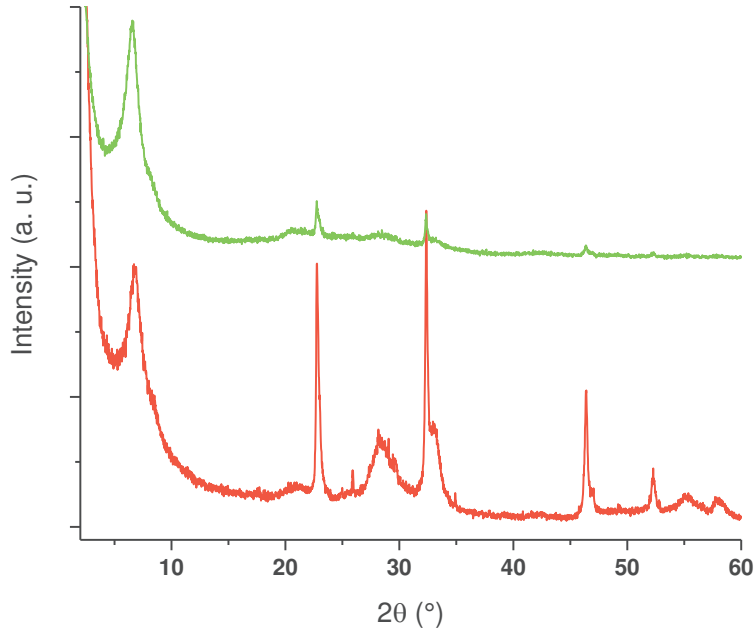

Figure III.17. *PXRD patterns of the solids resulting from the alkaline treatment of hexyl-click-HST (red) and benzyl-click-HST (green).*

III.2.2.2.4.2.3. Energy-dispersive X-ray spectroscopy (EDX)

As HST is a weak acid (cf. **Chapter I**) the alkaline treated products should be "salts" (proton is replaced by sodium ion), which can be described as NaST. This assumption was confirmed by the results of energy-dispersive X-ray spectroscopy (EDX) of the obtained solid from the base treatment of hexyl-click-HST. EDX analysis reveals the presence of a large amount of Na, with a ratio Na/Ta close to 1/3, suggesting that this phase may be the protonated HST phase where protons have been partially replaced by Na^+ cations.

III.2.2.2.4.2.4. Infrared spectroscopy

The corresponding IR spectra provide further evidence of the hydrolysis reaction (***Figure III.18***). After reaction, comparing the spectra of hexyl-click-HST and benzyl-click-HST reaction product with that of the corresponding base treated product, the complete disappearance of signals of organic phase is observed.

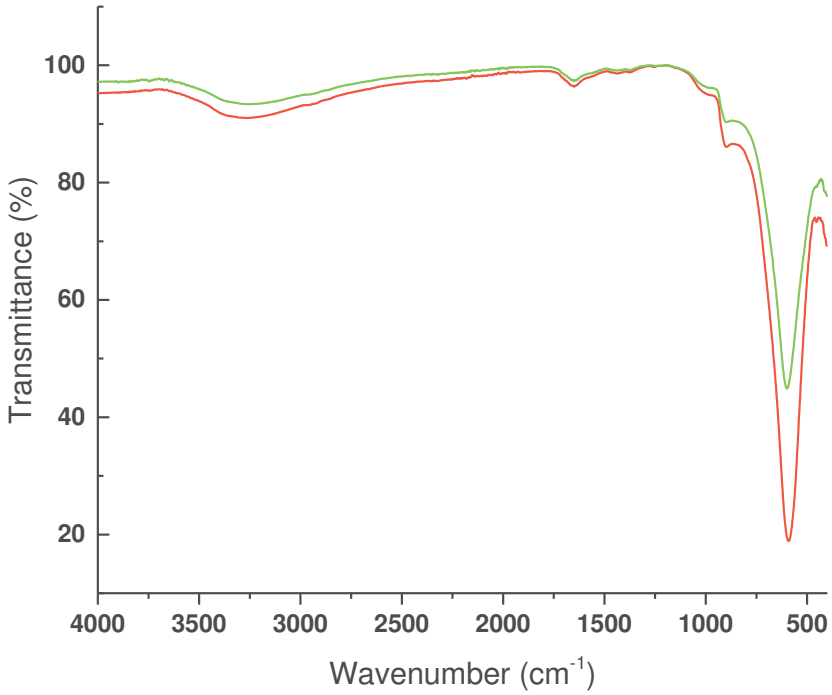

Figure III.18. *Infrared spectra of the insoluble phases resulting from the alkaline treatment of hexyl-click-HST (red) and benzyl-click-HST (green).*

III.2.2.2.4.3. Obtained organic phases

III.2.2.2.4.3.1. Collection

In order to collect the organic phase, diethyl ether and CH_2Cl_2 were employed to extract the obtained solution of the base treatment reaction of hexyl-click-HST and benzyl-click-HST, respectively. After being dried over Na_2SO_4 and concentrated at reduced pressure, organic phases are obtained in the form of light yellow oil and light yellow crystal respectively.

III.2.2.2.4.3.2. NMR spectroscopy in solution

The ^{13}C NMR spectra in solution ($CDCl_3$) of the organic phases (***Figure III.19***) are very similar to the one of the corresponding hybrids in the solid state (***Figure III.14***).The only difference concerns the position of the signal of the carbon bearing the anchoring oxygen (A) which is shifted upfield (by about 11 ppm), as expected for free alcohol α-carbon.

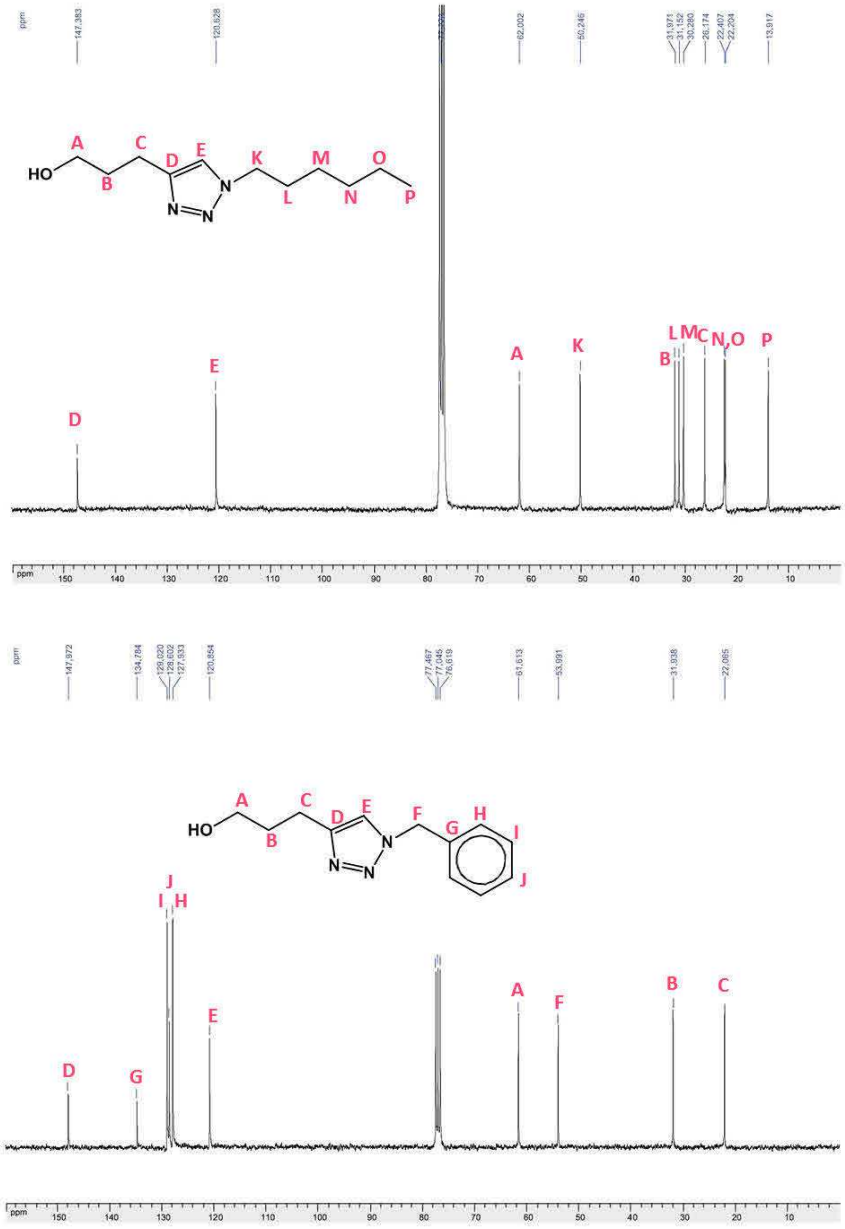

Figure III.19. *^{13}C NMR spectrum of the molecule deintercalated from hexyl-click-HST (top) and benzyl-click-HST (bottom) in $CDCl_3$ (300 MHz).*

III.2.2.2.5. Discussion

The above analyses prove the success of the post-synthesis functionalization method for the functionalization of HST. To the best of our knowledge, this is the first time such an approach is used in ion-exchangeable layered perovskites. We have shown that $CuBr(PPh_3)_3$ is the most suitable catalyst, because it is efficient in no-aqueous solvent. 1 mol % of catalyst has been proved to be enough to realize the complete *in situ* reaction. This is in the lower limit of the range commonly used in the literature (1 mol % -20 mol %).[48,62,63] In our case, the problem of the quantity of the catalyst is particularly important, because the catalyst is likely to remain trapped in the layered perovskite and so difficult to remove if used in too large quantity. Furthermore, its total removal is absolutely necessary for solid state NMR

characterization. It is noteworthy that the use of a base, for example triethylamine (TEA) or N, N-diisopropylethylamine (DIPEA), was not necessary in our case, although a lot of examples in literature employ the above organic bases for organic reactions.[24,49,62,63] The reason for this unnecessity of base is still unknown.
The microwave assisted CuAAC *in situ* reaction which has been used here is fast and particularly efficient. It is worth underlining that the reaction takes place on the whole interlamellar spacing, without noticeable reactivity limitations due to potential difficulties for the azide reactant (even if bulky) and the Cu(I) complex catalyst to diffuse. This strategy completes the ones used up to now to functionalize layered perovskite oxides (amine insertion, alcohol grafting) described in the previous chapters. This post-synthesis modification approach allows to consider the functionalization of layered perovskites by a much broader range of molecules, and hence to expend the properties and functionalities of the obtained hybrids. In the following paragraphs we will investigate variations of this strategy (change of HST precursor, and change of inorganic layered perovskite)

III.2.3. Post-synthesis modification of azide-HST via CuAAC reaction

In order to expand the application scope of the CuAAC reactions for the post-modification of layered perovskite, we tested the reactivity towards hexyne of azide-terminated precursor (azide-HST described in paragraph **III.2.1.b** (even if it is not totally pure).

III.2.3.1. Synthesis

The microwave-assisted (80°C, 2 h) CuAAC reactions have been carried out by using different molar amount of $CuBr(PPh_3)_3$ catalyst (1.0, 20, and 100 mol % respectively, with respect to azide-HST). 1-hexyne is used in large excess (*ca.* $\times$30) with respect to azide-HST. The whole manipulations and reactions are performed under a protective argon atmosphere. The obtained products were named click-azide-HST. For the reactions with 20 and 100 mol % of catalyst, the solids obtained are yellow, and no longer white as the ones which are obtained using alkyne-HST as precursor. This is likely due to the remaining excess of catalyst, which cannot be entirely removed.

III.2.3.2. XRD analysis

Figure III.20 shows the XRD patterns of HST, azide-HST and its reaction products with 1-hexyne by using different molar amount of $CuBr(PPh_3)_3$ catalyst. After reactions, one notes that the (00l) reflections of azide-HST disappear while a new set of (00l) reflections appears. In contrast, the reflections which are assigned to (100) and (110) in the XRD pattern of HST, are observed at the same positions (22.68° and 32.59°, respectively) in all the obtained products which indicate the preservation of the inorganic perovskite-like slab. For the reaction using 1.0 mol % of $CuBr(PPh_3)_3$, the interlayer distance of product (a) slightly increases from that of azide-HST (1.95 nm) to 2.05 nm. When the quantity of $CuBr(PPh_3)_3$ was increased to 20 mol %, the interlayer distance of product (b) further increased to 2.26 nm. When the quantity of the catalyst became 100 mol %, the interlayer distance of product (c) further increased to 2.42 nm. According to the above analysis, the increase of the interlayer distance of reaction products is a very positive signal to indicate the occurrence of CuAAC click reaction and it seems that much more catalyst is needed for this type of

reactions, comparing with the CuAAC reactions between alkyne-HST and 1-azidohexane or azidobenzene.

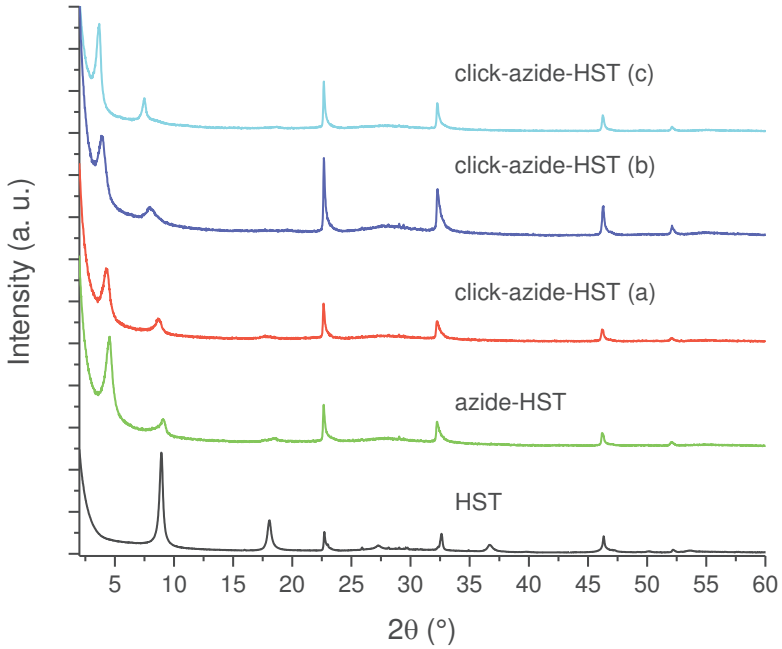

Figure III.20. *PXRD patterns of HST, azide-HST and its reaction product with 1-hexyne by using different molar amount of $CuBr(PPh_3)_3$ catalyst : (a): 1.0 mol %; (b): 20 mol %; (c): 100 mol % of catalyst.*

III.2.3.3. Infrared spectroscopy

Figure III.21 shows the corresponding IR spectra.
Comparing the IR spectrum of azide-HST with that of the reaction product (a) (1.0 mol % of $CuBr(PPh_3)_3$), the existence of the stretching bond of azide (2095 cm^{-1}) and the missing of the foreseeable signal of CH_3 group, strongly demonstrate the failure of the post-modification. And there is a high degree of similarity between the IR spectra of the starting material and that of reaction product (a), which signifies the recovery of starting material.
Comparing the IR spectrum of azide-HST with that of the reaction product (b) (20 mol % of $CuBr(PPh_3)_3$), the appearance of the weak signal of CH_3 group (2960 cm^{-1}) and the weak signal of N=N bond (1527 cm^{-1}) is noticed, which indicates the occurrence of CuAAC click reaction. However, the existence of the stretching bond of azide (2095 cm^{-1}) shows that the CuAAC reaction is unfinished.
Comparing the IR spectrum of azide-HST with that of the reaction product (c) (100 mol % of $CuBr(PPh_3)_3$) the complete disappearance of signal of the stretching bond of azide (2095 cm^{-1}) and the appearance of the signal of CH_3 group (2960 cm^{-1}) and the signal of N=N band (1527 cm^{-1}) are noteworthy. The signals at 1623 cm^{-1} and at 1460 cm^{-1} are attributed to the triazole vibrations.[60] The remaining intense absorption at 1139 cm^{-1} in the spectrum of the reaction products indicates the preservation of the C-O-Ta bond during the reaction process. According to the above analyses, the click reaction between our precursor azide-HST and 1-hexyne seems to occur. In addition, 100 mol % of catalyst seems to be necessary for this

reaction, which is much more than the necessary quantity for CuAAC reaction between alkyne-HST and 1-azidohexane or azido benzene.

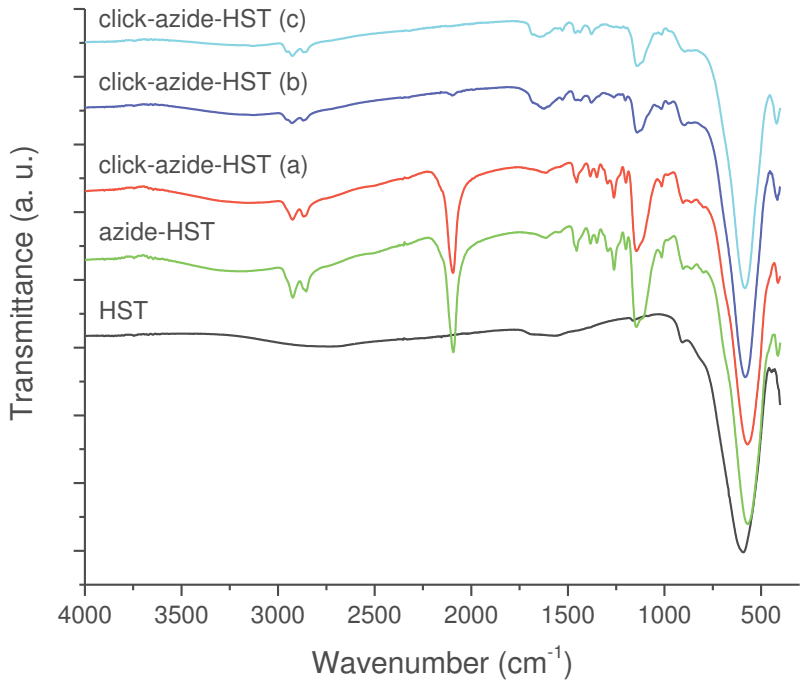

Figure III.21. *IR spectra of HST, azide-HST and its reaction product with 1-hexyne by using different molar amount of $CuBr(PPh_3)_3$ catalyst : (a): 1.0 mol %; (b): 20 mol %; (c): 100 mol % of catalyst.*

III.2.3.4. SEM observation

SEM images (***Figure III.22***) of HST, azide-HST and its reaction products with 1-hexyne by using different molar amount of $CuBr(PPh_3)_3$: (b): 20 mol % of catalyst; (c): 100 mol % of catalyst show the sheet-like shapes in all the products, with similar size of the crystallites.

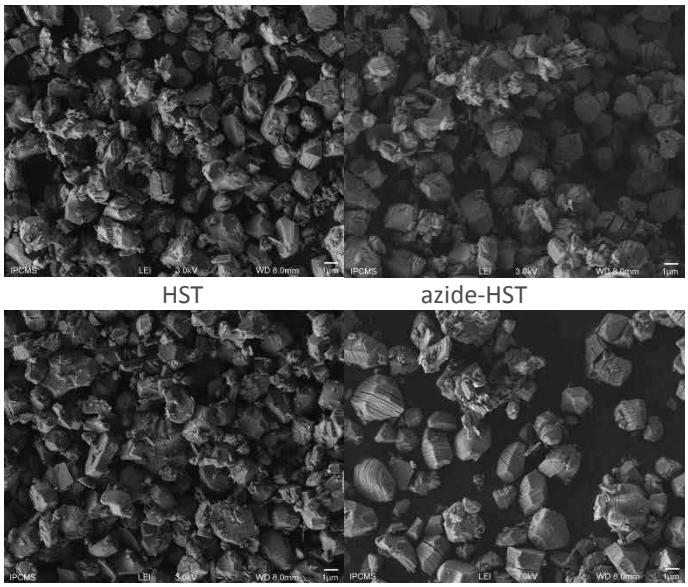

Figure III.22. *SEM images of HST, azide-HST and its reaction product with 1-hexyne by using different molar amount of $CuBr(PPh_3)_3$ catalyst : (b): 20 mol %; (c): 100 mol % of catalyst (the scale bars represent 1 µm).*

III.2.3.5. EDX analysis

As expected the energy-dispersive X-ray spectroscopy (EDX) confirms the visual observation (yellow color due to unremoved catalyst), and shows the noticeable presence of Cu (about 0.02 Cu per Ta_2 unit for click-azide-HST (b) and about 0.17 Cu per Ta_2 unit for click-azide-HST (c)).

As described above, the azide-terminated precursor needs 100 mol % of catalyst to promote click reactions, which is much more than for alkyne-terminated precursor (1 mol %). The modification of azides immobilized on the surface of cellulose using 20 mol % of $CuBr(PPh_3)_3$ has been reported in the presence of organic base DIPEA.[62] Therefore, in the present case, the addition of organic base maybe helpful for the CuAAC reactions between immobilized azides in azide-HST and free alkynes. This has not been tested yet.

III.2.4. Preparation of precursors based on $HLaNb_2O_7{\cdot}xH_2O$ (HLN)

In order to further expand the scope of CuAAC reaction for the post-modification of layered perovskite, another different type of layered perovskite, Dion-Jacobson phase $HLaNb_2O_7{\cdot}xH_2O$ (HLN), which has been thoroughly investigated in the past decades years, has been selected. The phase HLN was obtained via acid treatment of a precursor $KLaNb_2O_7$, which is prepared through solid-state sintering of a stoichiometric mixture of K_2CO_3, La_2O_3 and Nb_2O_5 by following published procedures.[64].

III.2.4.1. Preparation of alkyne-terminated precursor (alkyne-HLN)

III.2.4.1.1. Synthesis

In order to immobilize 4-pentyn-1-ol on the interlayer surface of HLN to prepare an alkyne-terminated precursor alkyne-HLN, the microwave assisted (110°C, 2 h) alcohol-exchange-

type reaction by using C_3OH-HLN as an intermediate was employed. 4-pentyn-1-ol was used in large excess (*ca.* ×130) with respect to C_3OH-HLN. The organic derivative of HLN with interlayer surface possessing n-propoxyl groups (C_3OH-HLN) can be prepared via direct grafting reaction between 1-propanol and HLN with the help of microwave irradiation (130°C, 2 h).

III.2.4.1.2. XRD analysis

The XRD patterns of HLN and C_3OH-HLN are shown in ***Figure III.23***. They are identical to the ones described in literature.[35,64]After reaction with 4-pentyn-1-ol, the interlayer distance increases from that of C_3OH-HLN (1.54 nm) to 1.76 nm, which is a good signal to indicate the occurring of exchange reaction. However, the typical characteristic in-plane reflection assigned to (110) (32.56 °) in the XRD pattern of HLN, cannot be observed in the reaction product.

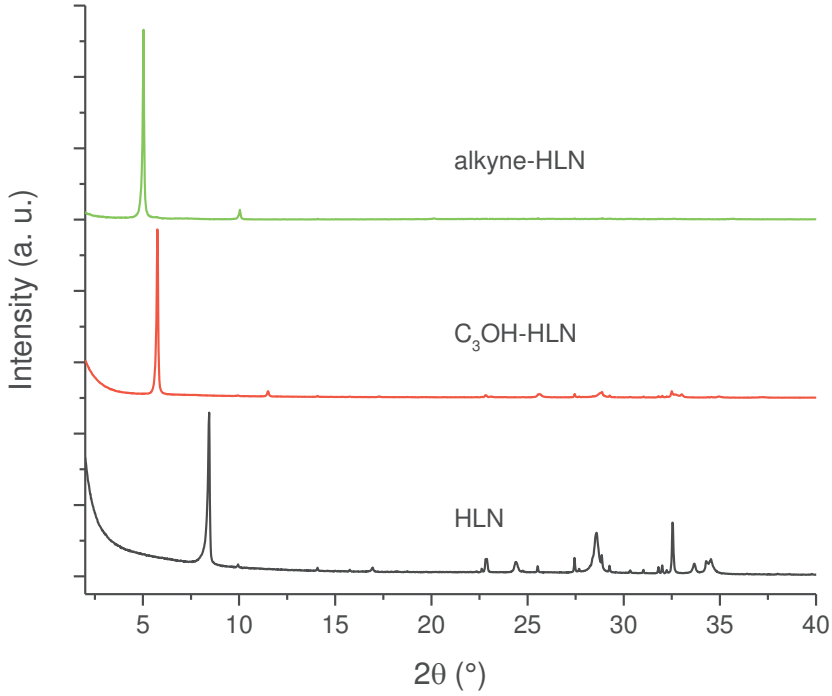

Figure III.23. *PXRD patterns of HLN, C_3OH-HLN and its reaction product with 4-pentyn-1-ol.*

III.2.4.1.3. Infrared spectroscopy

The corresponding IR spectra and that of 4-pentyn-1-ol are collected in ***Figure III.24***. The Nb-O elongation vibration is the dominant feature at 570 cm^{-1} for the hybrids. This bond is slightly shifted depending on the sample, without any clear correlation with the functionalization. Comparing the IR spectrum of C_3OH-HLN and that of the reaction product, one clearly observes new signals at 3280 cm^{-1}, attributed to stretching C-H vibration of the terminal alkyne group, and at 2114 cm^{-1} due the C≡C stretching vibration. In addition, the signal of the CH_3 group (2970 cm^{-1}) disappears. Comparing the stretching bond of C-O between the reaction product (1096 cm^{-1}) and 4-pentyn-1-ol (1039 cm^{-1}, 1053 cm^{-1}), there is

an obvious blue shift of about 40 cm^{-1}. Finally, there is no signal coming from a free alcohol group at 3360 cm^{-1}. The above analyses thus support the complete removal of propanol, and the formation of covalent bond C-O-Nb between HLN and 4-pentyn-1-ol.

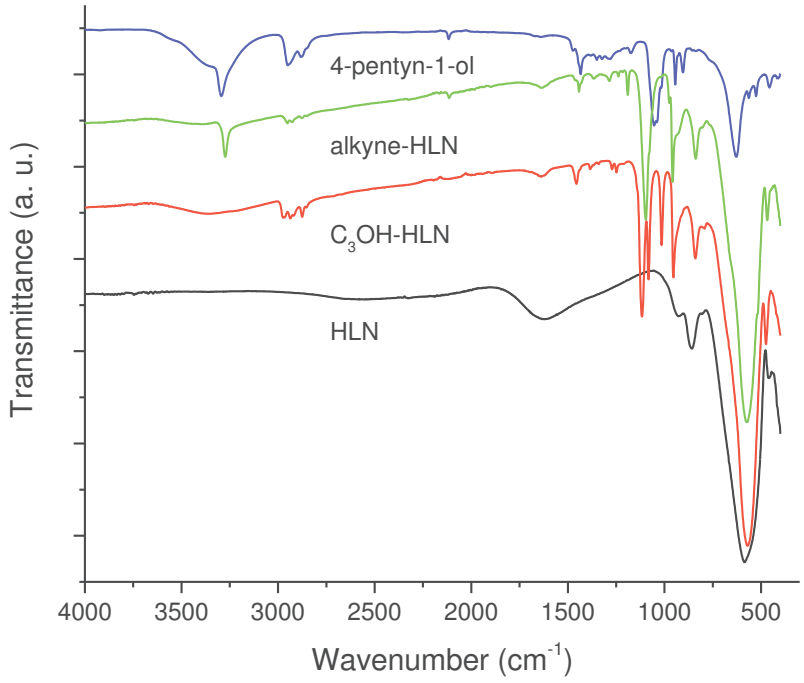

Figure III.24. *IR spectra of 4-pentyn-1-ol, HLN, C_3OH-HLN and its reaction product with 4-pentyn-1-ol.*

III.2.4.1.4. Thermal analyses and proposed formula

Figure III.25 shows the TGA and TDA curves of HLN, for reference, and of alkyne-HLN.
The TGA curve of alkyne-HLN shows first mass loss between 20 °C and 200 °C, attributed to the water removal (about 1.5 mass %). The other mass loss (about 10.9 mass %) occurs between 200 °C and 500 °C (associated to exothermic peaks), and is attributed to the removal of organic molecules within the hybrid and the loss of proton in the form of water from the perovskite itself.[65] According to the obtained results, the estimated formula of alkyne-HLN is: $(C_5H_7O)_{0.6}H_{0.4}LaNb_2O_{6.4}{\cdot}0.4H_2O$ (M = 470 g/mol).

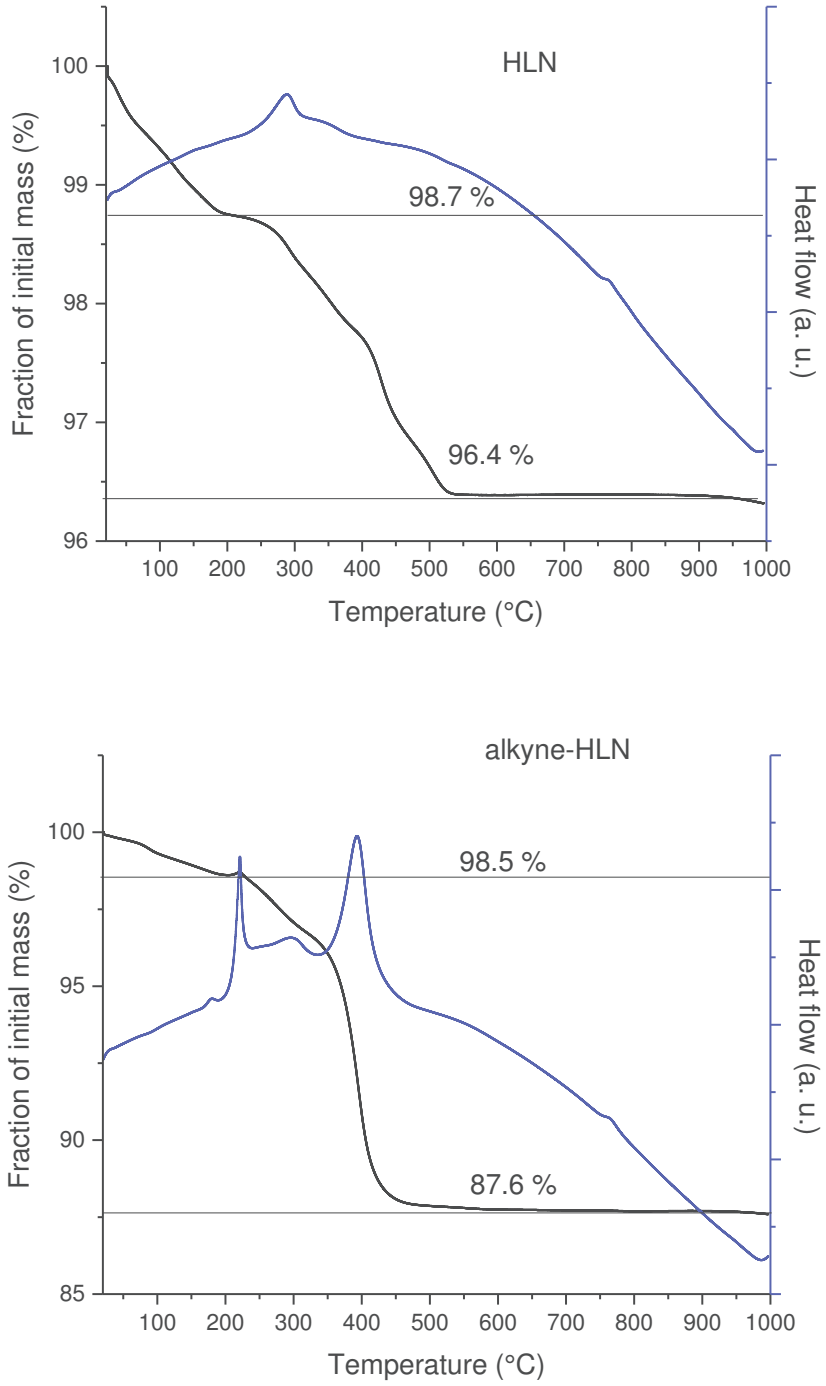

Figure III.25. *TGA and DTA curves for HLN (top) and alkyne-HLN (bottom).*

The above characterizations support the effective immobilization of 4-pentyn-1-ol on the interlayer surface of HLN (alkyne-HLN). The solid state ^{13}C CP/MAS NMR spectrum has not been obtained yet. Furthermore, the reactivity of alkyne-HLN toward an azide *via* CuAAC reaction could not be tested during the course of this PhD. action.

III.2.4.2. Preparation of azide-terminated precursor (azide-HLN)

III.2.4.2.1. Synthesis

In order to immobilize 3-azidopropan-1-ol on the interlayer surface of HLN to prepare an azide-terminated precursor (azide-HLN), the microwave-assisted (90°C, 2 h) alcohol-exchange-type reaction was employed by using C_3OH-HLN as an intermediate. 3-azidopropan-1-ol was used in large excess (*ca.* ×100) with respect to C_3OH-HLN.

III.2.4.2.2. XRD analysis

Figure III.26 shows the XRD patterns of HLN, C_3OH-HLN and its reaction product with 3-azidopropan-1-ol. After reaction, the interlayer distance increases from that of C_3OH-HLN (1.54 nm) to 1.68 nm. The characteristic reflection which are assigned to (110) in the XRD pattern of HLN, is observed at the same position (32.56°) in the obtained product. Yet, the other characteristic reflection around 28.62° assigned to (100) in the XRD pattern of HLN, cannot be observed in the grafted products.

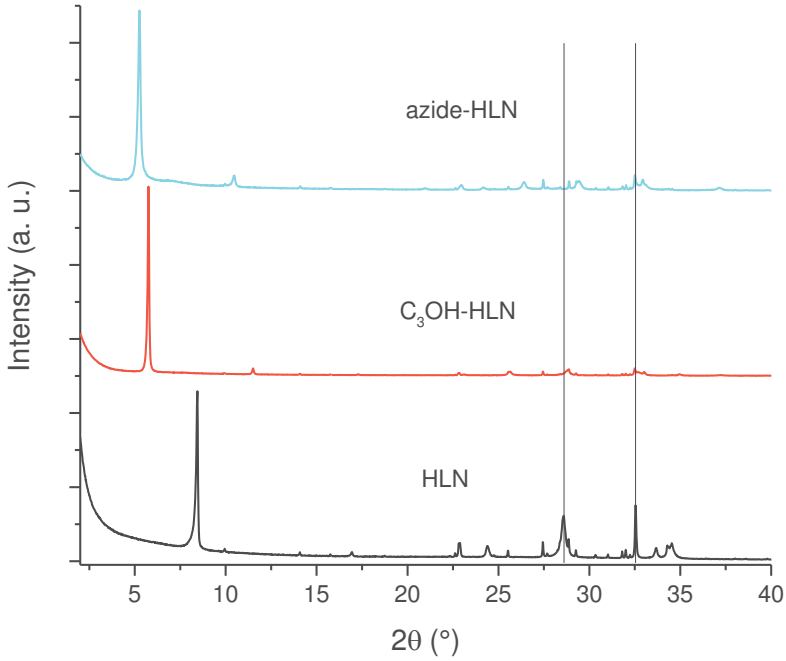

Figure III.26. *PXRD patterns of HLN, C_3OH-HLN and its reaction product with 3-azidopropan-1-ol.*

III.2.4.2.3. Infrared spectroscopy

Figure III.27 shows the IR spectra of 3-azidopropan-1-ol, HLN, C_3OH-HLN and its reaction product with 3-azidopropan-1-ol. Comparing the IR spectrum of the reaction product with that of C_3OH-HLN, the appearance of the stretching bond of azide (2095 cm^{-1}) and the disappearance of the signals of CH_3 group (2970 cm^{-1}) indicate the successful immobilization of 3-azidopropan-1-ol on the interlayer surface of HLN. In addition, comparing the IR spectra of reaction product with that of 3-azidopropan-1-ol, there is an obvious blue shift of 60 cm^{-1}

of the stretching bond of C-O between the reaction product (1104 cm^{-1}) and 3-azidopropan-1-ol (1044 cm^{-1}). Finally, there is no signal coming from a free alcohol group at 3360 cm^{-1}. The above analyses thus support the complete removal of propanol, and the formation of covalent bond C-O-Nb between HLN and 3-azidopropan-1-ol.

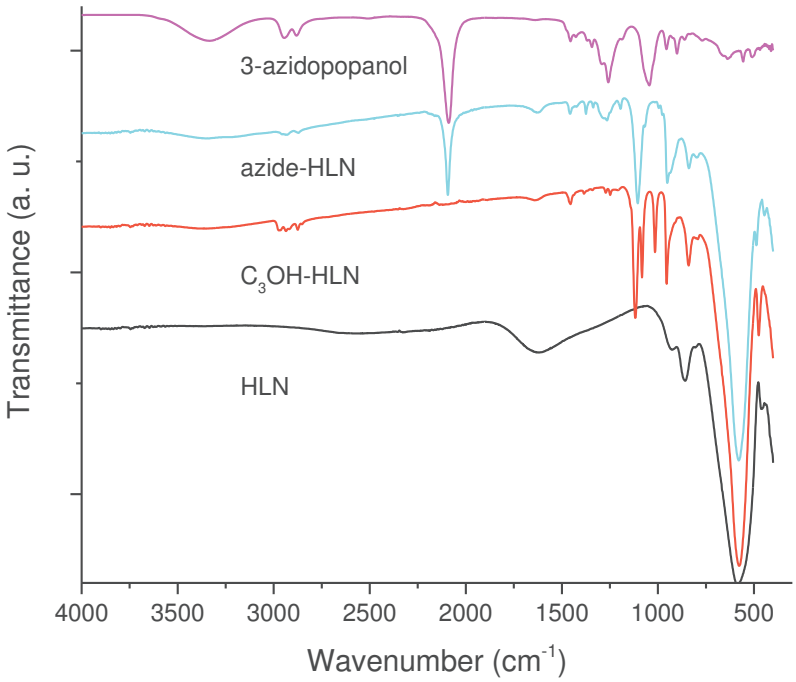

Figure III.27. *IR spectra of 3-azidopopanol, HLN, C_3OH-HLN and its reaction product with 3-azidopropan-1-ol.*

III.2.4.2.4. Thermal analyses and proposed formula

The TGA and TDA curves for azide-HLN are shown in ***Figure III.28***.
The TGA curve shows mass loss of about 1.3 % between 20°C and 200°C, which is ascribed to the removal of water in the hybrid. Between 150°C and 500°C, there is a 11.2% mass loss, associated to exothermic peaks. This is attributed to the decomposition of the organic molecules within the hybrid and the loss of proton in the form of water from the perovskite itself.
In addition, the elemental analysis (**Annex**) shows that the molar ratio between carbon and nitrogen is 1.1. This is consistent with the theoretical value (1.0).
According to the obtained results, the formula of the precursor can be estimated as follows: $(C_3H_6N_3O)_{0.5}\ H_{0.5}LaNb_2O_{6.5}{\cdot}0.3H_2O$ (M = 470 g/mol).

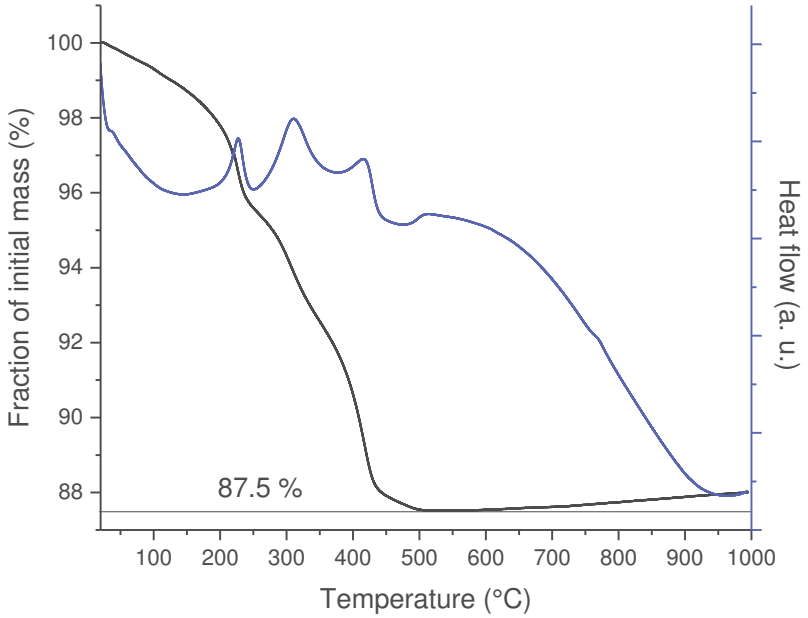

Figure III.28. *TGA and DTA curves for azide-HLN.*

The above characterizations support the effective immobilization of 3-azidopropan-1-ol on the interlayer surface of HLN (azide-HLN). The solid state ^{13}C CP/MAS NMR spectrum has not been obtained yet. The first results concerning the reactivity of azide-HLN towards a terminal free alkyne are reported in the following paragraphs.

III.2.5. Post-modification of azide-HLN via microwave-assisted CuAAC with 1-hexyne.

III.2.5.1. Synthesis

The post-modification of azide-HLN via microwave-assisted (80°C, 2 h) CuAAC has been done by using different molar amount of $CuBr(PPh_3)_3$ catalyst (100, 200 or 400 mol %, respectively, with respect to azide-HLN). 1-hexyne was used in large excess (*ca.* ×100) with respect to azide-HLN. The whole manipulations and reactions are performed under a protective argon atmosphere. The obtained product is named click-azide-HLN.

III.2.5.2. XRD analysis

Figure III.29 shows the XRD patterns of azide-HLN and its reaction products with 1-hexyne by using different amounts of $CuBr(PPh_3)_3$. When using 100 mol % of $CuBr(PPh_3)_3$, a compound presenting several interlayer distance of 2.10, 1.70 and 1.30 nm is obtained. The phase with interlayer distance of 1.70 nm can be ascribed to the unreacted starting material and the phase with 1.30 nm is thought to come from the decomposition of starting material. The presence of a phase with an interlayer distance larger than that of the starting material is a positive indication of the occurrence of CuAAC click reaction (even partial).
When the quantity of $CuBr(PPh_3)_3$ is increased from 100 mol % to 200 mol %, the obtained compound is still a multiphasic, but with only two with interlayer distances of 2.10 nm and

1.70 nm. It is noteworthy that the signal intensity of the phase with interlayer distance of 2.10 nm is largely enhanced.
When the quantity of $CuBr(PPh_3)_3$ is increased to 400 mol %, the signal intensity of the phase with interlayer distance of 2.10 nm is further enhanced, but there is always residual starting material at 1.70 nm.
According to the above analyses, the increase of interlayer distance of reaction products is a very positive signal to indicate the occurrence of CuAAC click reaction. But the click reaction cannot be completely finished even when a large excess of catalyst (400 mol %) is used.

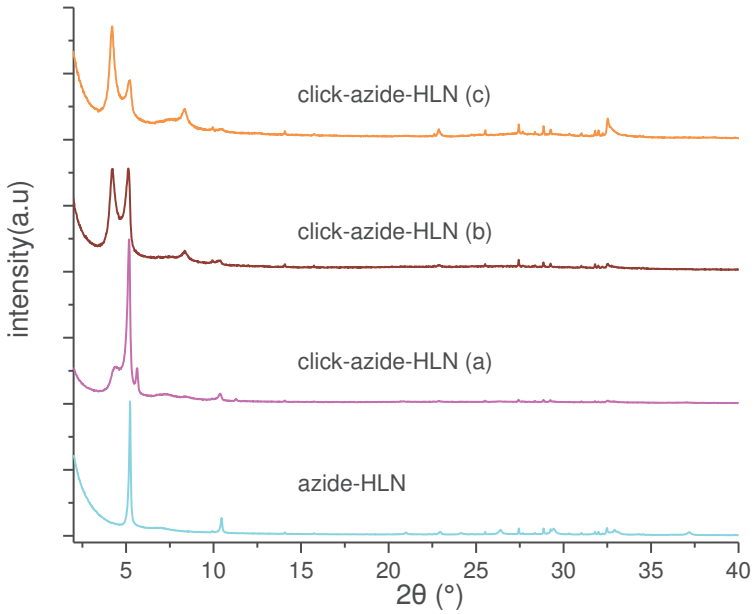

Figure III.29. *PXRD pattern of azide-HLN and its reaction product with 1-hexyne by using different molar amount of $CuBr(PPh_3)_3$ catalyst : (a) : 100 mol %; (b) : 200 mol %; (c) : 400 mol % of catalyst.*

III.2.6.3. Infrared spectroscopy

Figure III.30 shows the corresponding IR spectra. In all spectra, the presence of the signal of the stretching bond of azide (2095 cm^{-1}) is obvious and confirms that the reaction is not finished. But along with the increase of the amount of catalyst, the signal intensity of the stretching bond of azide gradually decreases and the appearance of the signature of the CH_3 group can be observed at 2970 cm^{-1}, which indicates the occurrence of CuAAC click reaction. Therefore azide-HLN is not an ideal precursor to do CuAAC click reaction under the used reaction conditions. There again, like with azide-HST, addition of an organic base may favor there action.

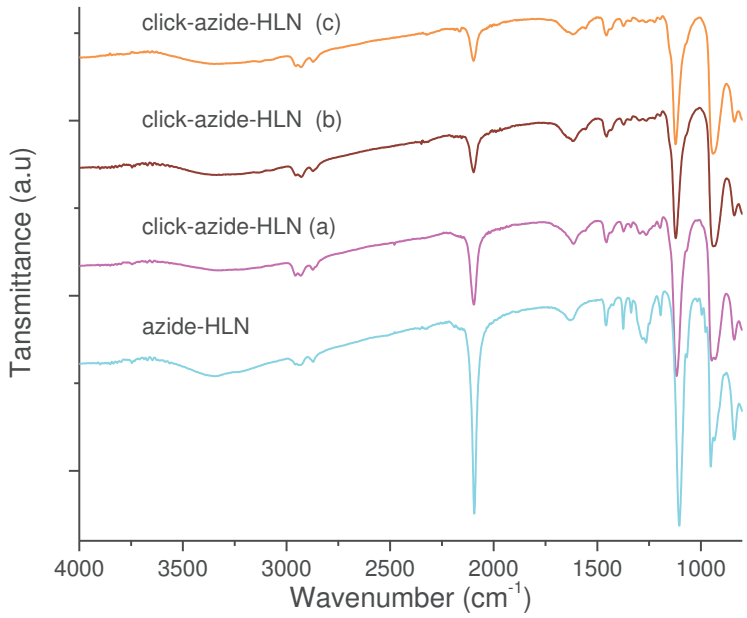

Figure III.30. *IR spectra of azide-HLN and its reaction product with 1-hexyne by using different molar amount of $CuBr(PPh_3)_3$ catalyst : (a) : 100 mol %; (b) : 200 mol %; (c) : 400 mol % of catalyst.*

III.3. Conclusion

In conclusion, the microwave-assisted grafting of alcohols bearing a reactive terminal alkyne group or a reactive terminal azide group into a protonated Aurivillius phase $H_2Bi_{0.1}Sr_{0.85}Ta_2O_7$ or a protonated Dion-Jacobson phase $HLaNb_2O_7{\cdot}xH_2O$ have been described. The efficient post-synthesis modification of these phases by means of *in situ* microwave-assisted Copper (I) Catalyzed Alkyne-Azide Cycloaddition has further been carried out.

It is noteworthy that alkyne-terminated precursor is more suitable than azide-terminated precursors to perform the post-synthesis modification of HST. In the same way, azide-HLN also seems to be less efficient for *in situ* CuAAC (even though we have not performed yet the experiment with alkyne-HLN to compare). We do not have explanation for this difference of reactivity. Yet, the reactivity of azide precursors has to be tested by adding an organic base for the CuAAC reaction.

The microwave assisted Cu-AAC in situ reaction which has been used here is fast and particularly efficient. It is worth underlining that, when using the appropriate amount of catalyst, the reaction takes place on the whole interlamellar spacing, without noticeable reactivity limitations due to potential difficulties for the azide reactant (even if bulky) and the Cu(I) complex catalyst to diffuse.

This strategy completes the ones used up to-now to functionalize layered perovskite oxides (amine insertion, alcohol or phosphonic acid grafting). This post-synthesis modification approach allows to consider the functionalization of layered perovskites by a much broader range of molecules, and hence to expend the properties and functionalities of the obtained hybrids. To the best of our knowledge, this is the first time to report the application of microwave-assisted CuAAC reactions in the interlayer space of layered perovskite. This not

only enriches the post-modification means of layered perovskite but also expands the scope of application of CuAAC reactions.

References

[1] J. R. Boykin, L. J. Smith, *Inorg. Chem.* **2015**, *54*, 4177-4179.
[2] S. Akbarian-Tefaghi, E. Teixeira Veiga, G. Amand, J. B. Wiley, *Inorg. Chem.* **2016**, *55*, 1604-1612.
[3] Y. Wang, E. Delahaye, C. Leuvrey, F. Leroux, P. Rabu, G. Rogez, *Inorg. Chem.* **2016**, *55*, 4039-4046.
[4] B. F. Hoskins, R. Robson, *J. Am. Chem. Soc.* **1990**, *112*, 1546-1554.
[5] J. S. Seo, D. Whang, H. Lee, S. I. Jun, J. Oh, Y. J. Jeon, K. Kim, *Nature* **2000**, *404*, 982-986.
[6] S. M. Cohen, *Chem. Rev.* **2012**, *112*, 970-1000.
[7] K. K. Tanabe, S. M. Cohen, *Chem. Soc. Rev.* **2011**, *40*, 498-519.
[8] Z. Wang, S. M. Cohen, *Chem. Soc. Rev.* **2009**, *38*, 1315-1329.
[9] V. Valtchev, G. Majano, S. Mintova, J. Perez-Ramirez, *Chem. Soc. Rev.* **2013**, *42*, 263-290.
[10] D. Bruhwiler, *Nanoscale* **2010**, *2*, 887-892.
[11] A. Mehdi, C. Reye, R. Corriu, *Chem. Soc. Rev.* **2011**, *40*, 563-574.
[12] J. Zhu, A. B. Morgan, F. J. Lamelas, C. A. Wilkie, *Chem. Mater.* **2001**, *13*, 3774-3780.
[13] D. R. Robello, N. Yamaguchi, T. Blanton, C. Barnes, *J. Am. Chem. Soc.* **2004**, *126*, 8118-8119.
[14] M. W. Weimer, H. Chen, E. P. Giannelis, D. Y. Sogah, *J. Am. Chem. Soc.* **1999**, *121*, 1615-1616.
[15] E. Coronado, C. Martí-Gastaldo, E. Navarro-Moratalla, A. Ribera, *Inorg. Chem.* **2010**, *49*, 1313-1315.
[16] G. Layrac, D. Tichit, J. Larionova, Y. Guari, C. Guérin, *J. Phys. Chem. C* **2011**, *115*, 3263-3271.
[17] O. Palamarciuc, E. Delahaye, P. Rabu, G. Rogez, *New J. Chem.* **2014**, *38*, 2016-2023.
[18] S. Yoshioka, Y. Takeda, Y. Uchimaru, Y. Sugahara, *J. Organomet. Chem.* **2003**, *686*, 145-150.
[19] H. C. Kolb, M. G. Finn, K. B. Sharpless, *Angew. Chem. Int. Ed.* **2001**, *40*, 2004-2021.
[20] *Chem. Soc. Rev.* **2010**, *39*, Applications of click chemistry themed issue.
[21] C. O. Kappe, *Chem. Soc. Rev.* **2008**, *37*, 1127-1139.
[22] C. O. Kappe, A. Stadler, D. Dallinger, *Microwaves in Organic and Medicinal Chemistry, 2nd edition*; Wiley-VCH, **2012**.
[23] W. J. Sommer, M. Weck, *Langmuir* **2007**, *23*, 11991-11995.
[24] F. Amblard, J. H. Cho, R. F. Schinazi, *Chem. Rev.* **2009**, *109*, 4207-4220.
[25] K. Bürglová, N. Moitra, J. Hodačová, X. Cattoën, M. Wong Chi Man, *J. Org. Chem.* **2011**, *76*, 7326-7333.
[26] R. Guezguez, K. Bougrin, K. El Akri, R. Benhida, *Tetrahedron Lett.* **2006**, *47*, 4807-4811.
[27] T. Gadzikwa, G. Lu, C. L. Stern, S. R. Wilson, J. T. Hupp, S. T. Nguyen, *Chem. Commun.* **2008**, 5493-5495.
[28] C. Liu, T. Li, N. L. Rosi, *J. Am. Chem. Soc.* **2012**, *134*, 18886-18888.
[29] F.-G. Xi, H. Liu, N.-N. Yang, E.-Q. Gao, *Inorg. Chem.* **2016**, *55*, 4701-4703.
[30] P.-Z. Li, X.-J. Wang, J. Liu, J. S. Lim, R. Zou, Y. Zhao, *J. Am. Chem. Soc.* **2016**, *138*, 2142-2145.
[31] S. Castellanos, K. B. Sai Sankar Gupta, A. Pustovarenko, A. Dikhtiarenko, M. Nasalevich, P. Atienzar, H. García, J. Gascon, F. Kapteijn, *Eur. J. Inorg. Chem.* **2015**, *2015*, 4648-4652.
[32] S. Wu, L. Chen, B. Yin, Y. Li, *Chem. Commun.* **2015**, *51*, 9884-9887.
[33] X.-C. Yi, F.-G. Xi, Y. Qi, E.-Q. Gao, *RSC Adv.* **2015**, *5*, 893-900.
[34] G. Chouhan, K. James, *Org. Lett.* **2013**, *15*, 1206-1209.
[35] H. Suzuki, K. Notsu, Y. Takeda, W. Sugimoto, Y. Sugahara, *Chem. Mater.* **2003**, *15*, 636-641.
[36] A. Shimada, Y. Yoneyama, S. Tahara, P. H. Mutin, Y. Sugahara, *Chem. Mater.* **2009**, *21*, 4155-4162.
[37] S. Tahara, T. Ichikawa, G. Kajiwara, Y. Sugahara, *Chem. Mater.* **2007**, *19*, 2352-2358.
[38] F. Himo, T. Lovell, R. Hilgraf, V. V. Rostovtsev, L. Noodleman, K. B. Sharpless, V. V. Fokin, *J. Am. Chem. Soc.* **2005**, *127*, 210-216.

[39] P. Appukkuttan, W. Dehaen, V. V. Fokin, E. Van der Eycken, *Org. Lett.* **2004**, *6*, 4223-4225.
[40] G. A. Molander, J. Ham, *Org. Lett.* **2006**, *8*, 2767-2770.
[41] Z. Li, R. Bittman, *J. Org. Chem.* **2007**, *72*, 8376-8382.
[42] C. W. Tornøe, C. Christensen, M. Meldal, *J. Org. Chem.* **2002**, *67*, 3057-3064.
[43] D. Giguere, R. Patnam, M.-A. Bellefleur, C. St-Pierre, S. Sato, R. Roy, *Chem. Commun.* **2006**, 2379-2381.
[44] D. Font, C. Jimeno, M. A. Pericàs, *Org. Lett.* **2006**, *8*, 4653-4655.
[45] P. G. Andersson, H. E. Schink, K. Österlund, *J. Org. Chem.* **1998**, *63*, 8067-8070.
[46] Y. Liu, D. D. Díaz, A. A. Accurso, K. B. Sharpless, V. V. Fokin, M. G. Finn, *J. Polym. Sci.* **2007**, *45*, 5182-5189.
[47] S. Tahara, Y. Sugahara, *Langmuir* **2003**, *19*, 9473-9478.
[48] J. E. Hein, V. V. Fokin, *Chem Soc Rev.* **2010**, *39*, 1302-1315.
[49] D. Toulemon, B. P. Pichon, C. Leuvrey, S. Zafeiratos, V. Papaefthimiou, X. Cattoën, S. Bégin-Colin, *Chem. Mater.* **2013**, *25*, 2849-2854.
[50] J. E. Hein, V. V. Fokin, *Chem. Soc. Rev.* **2010**, *39*, 1302-1315.
[51] S. Ida, C. Ogata, U. Unal, K. Izawa, T. Inoue, O. Altuntasoglu, Y. Matsumoto, *J. Am. Chem. Soc.* **2007**, *129*, 8956-8957.
[52] A. D. Rae, J. G. Thompson, R. L. Withers, *Acta Cryst. Sect. B* **1992**, *48*, 418-428.
[53] C. Rösner, G. Lagaly, *J. Sol. St. Chem.* **1984**, *53*, 92-100.
[54] Y. Wang, C. Wang, L. Wang, Q. Hao, X. Zhu, X. Chen, K. Tang, *RSC Adv.* **2014**, *4*, 4047-4054.
[55] S. Takahashi, T. Nakato, S. Hayashi, Y. Sugahara, K. Kuroda, *Inorg. Chem.* **1995**, *34*, 5065-5069.
[56] Y. Takeda, H. Suzuki, K. Notsu, W. Sugimoto, Y. Sugahara, *Mater. Res. Bull.* **2006**, *41*, 834-841.
[57] Y. Wang, C. Wang, L. Wang, Q. Hao, X. zhu, X. Chen, K. Tang, *RSC Adv.* **2014**, *4*, 4047-4054.
[58] F. Landi, C. M. Johansson, D. J. Campopiano, A. N. Hulme, *Org. Biomol. Chem.* **2010**, *8*, 56-59.
[59] R. Huisgen, *Angew. Chem. Int. Ed.* **1963**, *2*, 565-598.
[60] H. Li, Q. Zheng, C. Han, *Analyst* **2010**, *135*, 1360-1364.
[61] X. Creary, A. Anderson, C. Brophy, F. Crowell, Z. Funk, *J. Org. Chem.* **2012**, *77*, 8756-8761.
[62] M. I. Montañez, Y. Hed, S. Utsel, J. Ropponen, E. Malmström, L. Wågberg, A. Hult, M. Malkoch, *Biomacromolecules* **2011**, *12*, 2114-2125.
[63] M. Meldal, C. W. Tornøe, *Chem. Rev.* **2008**, *108*, 2952-3015.
[64] S. Takahashi, T. Nakato, S. Hayashi, Y. Sugahara, K. Kuroda, *Inorg. Chem.* **1995**, *34*, 5065-5069.
[65] J. Wu, Y. Cheng, J. Lin, Y. Huang, M. Huang, S. Hao, *J. Phys. Chem. C* **2007**, *111*, 3624-3628.

Chapter IV

Soft-chemistry route for insertion of paramagnetic metals into layered perovskites

IV.1. Introduction

As well known, the Aurivillius phase $Bi_2SrTa_2O_9$ is a ferroelectric material.[1] Considering that its protonated phase (HST) is particularly tailored for being easily functionalized by various kinds of molecules with the help of microwave irradiation (cf. **Chapter I**, **II** and **III**), it may be a promising candidate to be converted into a multiferroic material (*i.e.* materials presenting at least two coexisting electric, magnetic or elastic orders) via soft chemistry approach.[2,3] In the present case, we are particularly interested in obtaining by this approach a compound associating ferroelectricity and ferromagnetism.

Even though we have no proof yet that HST is ferroelectric (measurement of dielectric properties on powders are particularly tricky), we have shown that it presents a strong non-linear optical activity (**Annex**). Since the symmetry requirements for Second Harmonic Generation (SHG) are less restrictive than those for ferroelectricity, observation of SHG is a necessary condition for a compound to be ferroelectric.[4] Observation of SHG is thus a positive indication that HST may be ferroelectric just like the parent compound BST. Our plan here consists in synthesizing new multiferroic hybrid materials, by functionalizing the potentially ferroelectric HST. The first step in this strategy, which is presented in this chapter, is to convey HST with magnetic properties, even only paramagnetic. In a second step, not attempted during my PhD, the work will concern the *in situ* formation of a ferromagnetic network.

In order to realize the above plan, we decided first to prepare a precursor HST functionalized by a polydentate ligand, which can further coordinate paramagnetic transition metal ions (Cu (II), Ni (II)…). Therefore, we intercalated HST with a commercial polyamine, bis-(3-aminopropyl) (hereafter designated as N3), using the tools developed in **Chapter I**. The obtained hybrid precursor N3-HST was then fully characterized.

The subsequent *in situ* coordination reactions were carried out between the obtained precursor and aqueous solution of $Cu(NO_3)_2{\cdot}2.5H_2O$ or a preformed $Cu(N3)(NO_3)_2$ complex via microwave irradiation. Depending on the reaction conditions, two different products were obtained, one blue and the other green. These compounds were characterized by ancillary techniques (XRD, IR and UV spectroscopies, SEM and TEM) but also by squid and EPR measurements.

Finally, the influence of the nature of the precursor N3-HST or C_2N-HST (described in **Chapter I**) was studied, and a mechanism for the insertion of Cu(II) ions and for the formation of the blue or the green hybrids is proposed.

IV.2. Results and discussion

IV.2.1. Direct reaction between HST and $Cu^{II}(X)_2{\cdot}yH_2O$

As described in the literature, Dion-Jacobson phases and Ruddlesden-Popper phases can undergo ion-exchange reactions (Li^+, NH_4^+, Na^+),[5-8] even divalent ion exchange (Pb^{2+}, Sr^{2+}, Ba^{2+}, Co^{2+}, Cu^{2+} and Zn^{2+})[9-11] using molten salts (molten nitrate salt, or mixture between the chloride salt and potassium chloride) as the ion-exchange medium. Formation of a $(CuX)LaNb_2O_7$ layered phase was also reported by solid state "low" temperature (350°C) reaction between the Dion-Jacobson $RbLaNb_2O_7$ phase and anhydrous CuX_2 (X = Cl or Br).[12]

Finally, it is noteworthy that aqueous divalent ion exchange of Ruddlesden-Popper phases has also been realized (Ni^{2+}, Cu^{2+}, Zn^{2+}, Mg^{2+}, Ca^{2+} and VO^{2+})[8,10,13], but the reaction times are very important (around 5 days, between 45°C and 100°C).
Since HST, which is very similar as a Ruddlesden-Popper phase, can be seen as a weak acid (cf. **Chapter I**), the cationic exchange reaction between copper ions and protons of HST may be possible even though the resulting formation of a strong acid (for instance HNO_3 by reaction between HST and $Cu(NO_3)_2$), is thermodynamically unfavorable.

IV.2.1.1. Synthesis

Attempts to perform direct exchange between HST and Cu^{2+} were performed, using various Cu(II) salts ($Cu(NO_3)_2$, $CuCl_2$, $Cu(OAc)_2$ and $CuSO_4$), using microwave irradiation (equimolar mixture of HST (50 mg) and Cu(II) salt, in 6 mL of H_2O, 80 °C, 2h).

IV.2.1.2. XRD analysis, infrared spectroscopy and EDX analysis

As an representative illustration, the powder XRD patterns of HST and its reaction product with $Cu(NO_3)_2 \cdot 2.5H_2O$ (a) are shown in ***Figure IV.1***. After reaction, the interlayer distance of reaction product (a) is the same as that of HST (0.98 nm). No obvious difference between the starting material and reaction product (a) could be observed, except the wider (002) peak of reaction product (a).

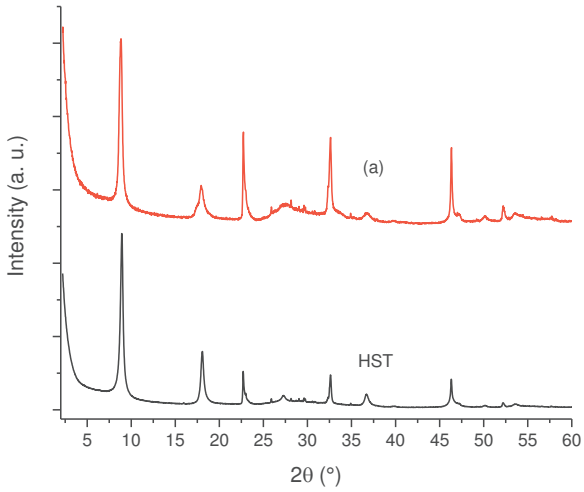

Figure IV.1. *Powder XRD patterns of HST and its reaction product with $Cu(NO_3)_2 \cdot 2.5H_2O$ (a).*

Accordingly, the IR spectrum of the reaction product is also very similar to the one of HST (***Figure IV.2***).

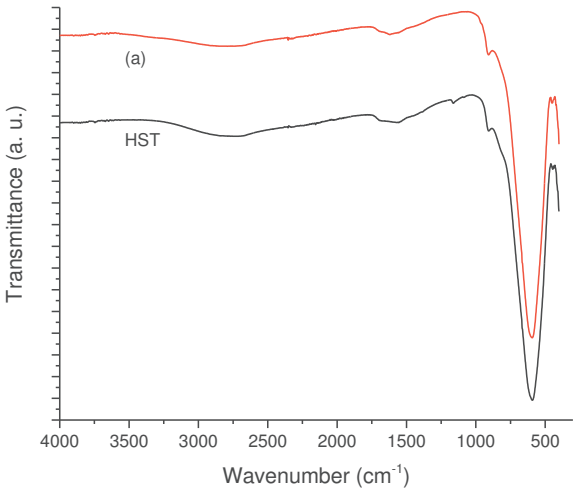

Figure IV.2. *IR spectra of HST and its reaction product with $Cu(NO_3)_2 \cdot 2.5H_2O$ (a).*

The failure of the cationic exchange reaction between copper ions and protons of HST was further confirmed by energy-dispersive X-ray spectroscopy (EDX), which shows the absence of copper in the reaction product.

Here, a pre-conversion of the proton form of Aurivillius phase (HST) into its alkali form (MST, M = Na^+, K^+…) may have been helpful for the subsequent divalent ion exchange reaction with Cu(II) or Ni (II).[11,13] We chose a somehow different strategy, using the tools of coordination chemistry.

IV.2.2. Indirect insertion of copper ions into HST via a precursor N3-HST

After the failure of direct ion exchange reactions between HST and Cu(II) salts, we have followed an organic-inorganic hybrid approach.[14,15] We first functionalized HST with a polyamine, bis-(3-aminopropyl)amine (N3) (***Scheme IV.1***). The idea is that the two terminal NH_2 groups act as pillars between the inorganic layers, leaving the central secondary amine free for coordinating metal ions or complexes.

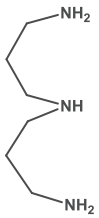

Scheme IV.1. *Bis-(3-aminopropyl)amine (N3).*

IV.2.2.1. Preparation of the precursor N3-HST

IV.2.2.1.1. Synthesis

The microwave assisted (130 °C, 1.5 h) insertion reaction was performed using a large excess (*ca.* ×100) of polyamine with respect to HST, in a THF/H_2O mixture (4:1 v:v).

IV.2.2.1.2. XRD analysis

Figure IV.3 shows the XRD patterns of HST and its reaction product with N3. After reaction, the (00l) reflections are shifted to lower angles with respect to the ones of HST. The increased interlayer distance (1.82 nm) of the reaction product strongly indicates the occurring of intercalation reaction. The interlayer distance of the obtained hybrid is in accordance with the calculated value (1.86 nm) using the relationship established for *α,ω*-diaminoalkanes d (nm) = 1.09 + 0.11 n_C (cf. **Chapter I**) (considering the central nitrogen atom in N3 as a carbon). This indicates a pillaring arrangement of N3. The out of plane reflections, which are assigned as (100) and (110) in the XRD pattern of HST, are observed at the same positions (22.68° and 32.59°, respectively) in the obtained product. This shows that the perovskite-like slab structure has remained essentially unchanged upon the insertion.

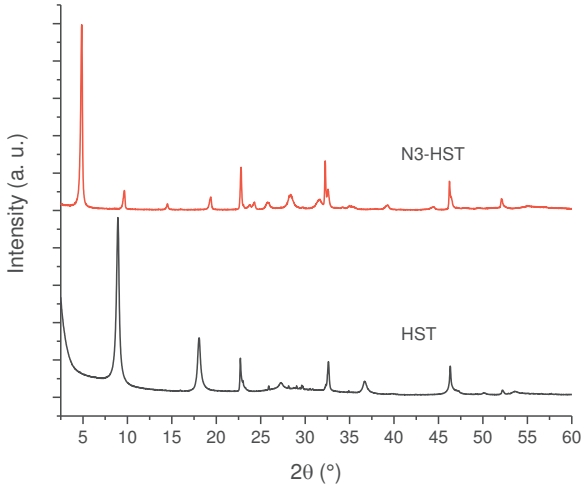

Figure IV.3. *Powder XRD patterns of HST and its reaction product with bis-(3-aminopropyl)amine (N3).*

IV.2.2.1.3. Infrared spectroscopy

The infrared spectra of polyamine N3, HST and its reaction product with N3 are shown in ***Figure IV.4***. Comparing the spectra of N3-HST with that of N3, the sharp strong bands at 3356 cm^{-1} and 3278 cm^{-1} due to NH stretching of free $–NH_2$ groups are greatly reduced in intensity and a new NH stretching band appears at 2518 cm^{-1}. Similar results have been obtained by Depas and Khaladji on the investigation of the infrared spectra of aliphatic primary amines and their protonated salts,[16] or by Larsson on the study of the IR spectra of butylamine and its hydrochloride salt.[17] This analysis confirms the conversion from $–NH_2$ groups to $–NH_3^+$ groups The new bands which appear at 1567 cm^{-1} and 1543 cm^{-1} in the spectrum of N3-HST are ascribed to $–NH_3^+$ deformation vibrations.[18] The protonated form of the ended $–NH_2$ groups of N3 within the hybrid are thus clear. Unfortunately, no clear evidence of the protonation state of the central secondary amine in N3-HST could be obtained.

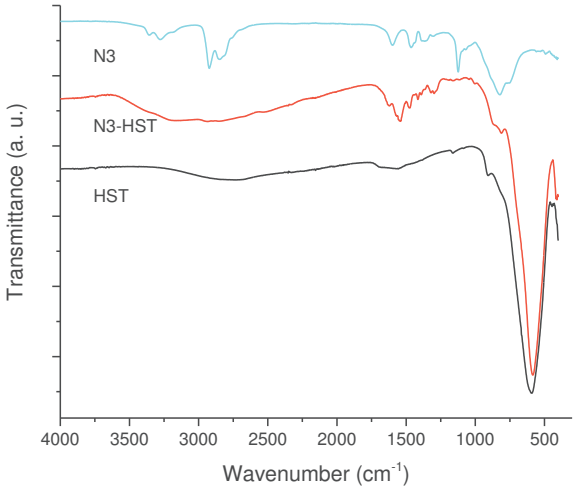

Figure IV.4. *Infrared spectra of polyamine N3, HST and its reaction product with N3.*

IV.2.2.1.4. Thermal analyses

The TGA and TDA curves for N3-HST are shown in ***Figure IV.5***. The 5.4 % mass loss which occurs before 130 °C and associated to endothermic peaks is ascribed to the removal of water. The following very gradual mass loss (about 7.6 %) between 110 °C and 540 °C is associated to exothermic peaks. It is ascribed to the decomposition of the organic part of the hybrid. In accordance with what has been described in **Chapter II**, the mass loss (2.3 %) between 600 °C and 800 °C is ascribed to the loss of proton in the form of water (*ca.* 3 %), which simultaneously leads to a metastable phase.[19] The final mass loss around 850°C can be ascribed to the partial bismuth removal (cf. **Chapter I**).

According to the above analyses, a consistent formula can be proposed for N3-HST: $((NH_3(CH_2)_3)_2NH)_{0.4}H_{1.2}Bi_{0.1}Sr_{0.85}Ta_2O_7 \cdot 2H_2O$ (M = 658 g/mol). The molar ratio between N3 and HST is similar to the one obtained for *α*, *ω*-diaminoalkanes and HST (ca. 0.5) (**Chapter I**).

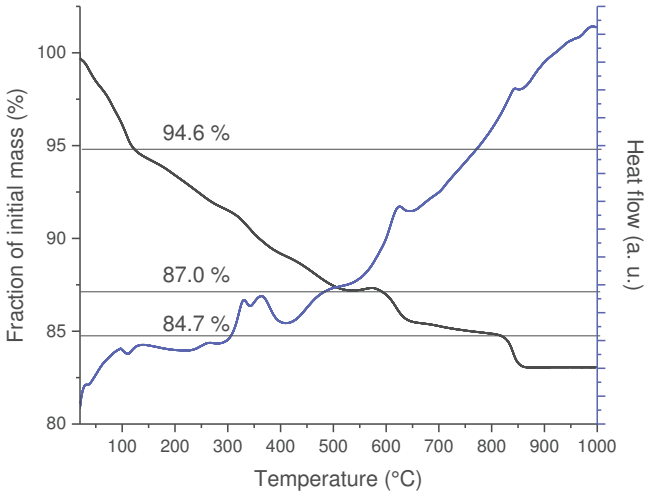

Figure IV.5. *TGA and TDA curves for N3-HST.*

IV.2.2.1.5. Solid state NMR

Further investigation of the structure of N3-HST was performed using solid state NMR spectroscopy (collaboration Fabrice Leroux, Institut de Chimie de Clermont-Ferrand). ***Figure IV.6*** shows the solid-state ^{13}C CP/MAS NMR spectra of N3-HST. According to the spectra of N3-HST, there are at least five signals: 47, 44, 38, 29 and 24 ppm, and according to the signals intensities, they can be divided into two groups (I: 47, 38, 29 ppm; II: 44, 24 ppm). In the liquid-state ^{13}C NMR spectrum of N3 (solvent, deuterium oxide), the signals are as follows: 46.3 ppm, 38.7 ppm and 31.6 ppm, with no other set of signals.
Comparing the signal of carbon B of group I (29 ppm) in N3-HST with the corresponding one in N3 (31.6 ppm), there is an upfield shift of 2.6 ppm, which is attributable to the protonation of N3.[20-24] In addition, there is an upfield shift of about 1 ppm of carbon A and a downfield shift of 1 ppm of carbon C. The above analyses tend to indicate that the –NH– group, which is at the center of N3, is its amine state, the two $–NH_2$ groups at both ends of N3 are in their ammonium state, *i.e.* protonated.
The liquid-state ^{13}C NMR spectrum (solvent, deuterium oxide) of protonated N3 (being protonated by 3 equivalents of HCl) presents three signals at 45, 37 and 24 ppm. Taking into account the possibility that the signal at 37 ppm might be masked, the signals of group II (44, 24 ppm) in native N3-HST are believed to come from a completely protonated N3. As a result, there are probably two forms of N3 in the interlayer space of HST, both of them with protonated terminal $–NH_2$ groups: the major one with a free amine group at the center and a minor fraction with a protonated secondary amine instead.

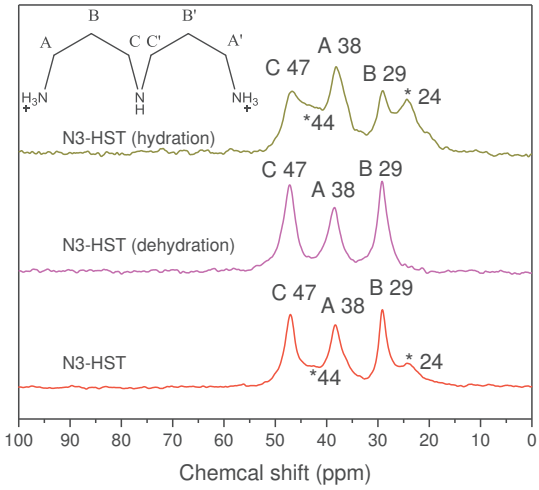

Figure IV.6. *Solid-state ^{13}C CP/MAS NMR spectra of native N3-HST, N3-HST after dehydration and overhydrated N3-HST.*

In order to further study the protonation state of polyamine in N3-HST, the dehydration and hydration treatments of this precursor have been performed. The dehydrated N3-HST was obtained by vacuum drying for two weeks at room temperature, and overhydrated N3-HST was obtained by stirring native N3-HST in water for 0.5 h at room temperature followed by simple centrifugation. The solid-state ^{13}C CP/MAS NMR spectra of these two compounds are presented in ***Figure IV.6*** along with the one of native N3-HST. Comparing the spectra of the dehydrated N3-HST with that of native N3-HST, we can clearly observe the disappearance of the signals at 24 and 44 ppm. On the contrary, comparing the spectrum of the overhydrated

N3-HST with that of native N3-HST, the enhanced intensity of the signal at 24 ppm and of a shoulder around 44 ppm is observed. This behavior may be due to the cross-polarization technique[25,26] involved in ^{13}C solid state NMR, for which the polarization transfer between proton and carbon atoms is more efficient when the proton density around the carbon atom is larger. The water molecules present in native N3-HST and even more present in overhydrated N3-HST, are likely to be preferentially around tri-protonated N3 molecules rather than around di-protonated ones, thus increasing the ^{13}C signal coming from tri-protonated N3 molecules.

IV.2.2.2. Reactions between N3-HST and $Cu(NO_3)_2{\cdot}2.5H_2O$ or $Cu(N3)(NO_3)_2$.

IV.2.2.2.1. Synthesis

In order to immobilize copper ions in the interlayer space of HST, two different reactions using N3-HST were performed, one with $Cu(NO_3)_2{\cdot}2.5H_2O$, the other with the complex $CuN3(NO_3)_2$. The complex $CuN3(NO_3)_2$ is made by adding drop by drop one equivalent of an aqueous solution of N3 to an aqueous solution of $Cu(NO_3)_2{\cdot}2.5H_2O$ at room temperature. The obtained mixture is stirred during 10 minutes and used without further purification. N3-HST was reacted with a small excess (115 mol % with respect to N3-HST) of aqueous solution of $Cu(NO_3)_2{\cdot}2.5H_2O$ or of the complex $CuN3(NO_3)_2$ via microwave irradiation (80°C, 0.5 h). After reactions, a green solid and a blue solid were obtained respectively.

IV.2.2.2.2. XRD analysis

The powder XRD patterns of HST, N3-HST, green solid and blue solid are displayed in ***Figure IV.7***. Comparing the diffractogram of green solid with that of N3-HST, the interlayer distance decreases from 1.82 nm to 1.25 nm. In addition, there is an obvious reduction of the crystallinity. Comparing the diffractogram of the blue solid and that of N3-HST, the interlayer distance only slightly decreases from 1.82 nm to 1.76 nm, and the crystallinity is rather preserved. In both solids, the green one and the blue one, the reflections, which are assigned as (100) and (110) in the XRD pattern of HST, are observed at the same positions (22.68° and 32.59°, respectively) in the obtained products. This proves that the structure of the inorganic perovskite-like slab is retained.

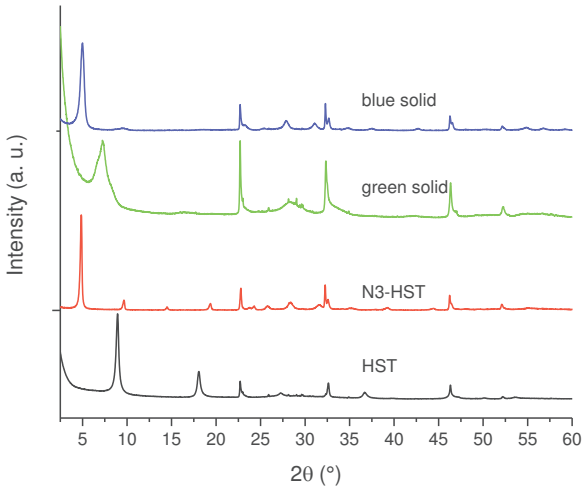

Figure IV.7. *Powder XRD patterns of HST, N3-HST, green solid and blue solid.*

IV.2.2.2.3. Infrared spectroscopy

The corresponding infrared spectra are displayed in ***Figure IV.8***. In order to well study the relatively weak characteristic vibration bands of guest phases, the wavelength range presented in ***Figure IV.8*** is intentionally reduced to 800-4000 cm^{-1}, which results in the missing of Ta-O elongation vibration.

Comparing the spectrum of the green solid with that of N3-HST, it is clear to observe the disappearance of the bands at 1567 cm^{-1}, 1543 cm^{-1} and 1466 cm^{-1}, which correspond the protonated N3 in the interlayer space of HST. This indicates the removal of N3 during the reaction leading to the formation of the green solid. The remaining band at 1621 cm^{-1} is attributed to water bending, or to traces of remaining N3 molecules.

Comparing the spectrum of the blue solid with that of N3-HST, the disappearance of bands at 1567 cm^{-1} and 1543 cm^{-1} (which were attributed to $–NH_3^+$ group deformation vibrations) is observed. In addition, new bands appear at 3241 cm^{-1} and 3155 cm^{-1} (attributed to N-H stretching of $–NH_2$ group), at 2930 cm^{-1} and 2867 cm^{-1} (masked in N3-HST, and attributed to antisymmetric and symmetric stretching vibrations of CH_2 groups) and at 1153 cm^{-1} (attributed to the stretching vibration of $C\text{-}NH_2$). Finally, the band at 1620 cm^{-1} in N3-HST (attributed to NH deformation vibration) is redshifted (1610 cm^{-1}) in the blue solid. These observations suggest the retention and deprotonation of the polyamine N3 in the blue solid.

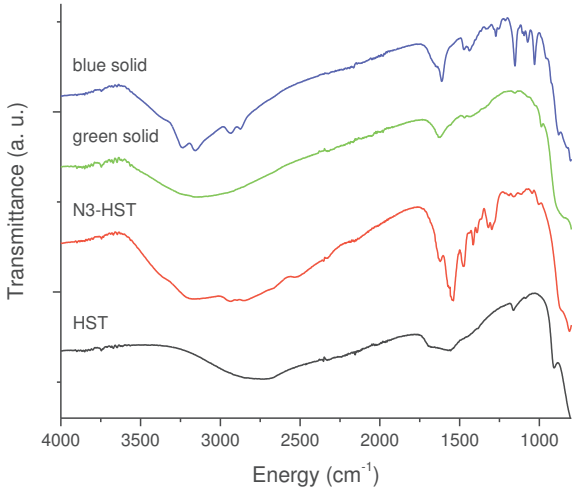

Figure IV.8. *Infrared spectra of HST, N3-HST, green solid and blue solid.*

Figure IV.9 presents a comparison between the infrared spectra of green and blue solids and the spectrum of the complex $CuN3(NO_3)_2$ (which is obtained by drying the corresponding aqueous solution under reduced pressure). The first marking observation is the disappearance of the band due to nitrate elongation (around 1308 cm^{-1}), which is very intense in $CuN3(NO_3)_2$.

Taking into account the charge balance, the above observation indicates that there is a cation exchange reaction between Cu(II) and the protons on the interlayer surface of HST during both reactions (leading to green and blue solid respectively). Further studies presented in the rest of this chapter will allow to precise the reaction mechanism.

In addition, more detailed comparison between the spectrum of the blue solid and the one of the $CuN3(NO_3)_2$ complex shows very similar signals : $CuN3(NO_3)_2$ (blue solid): 3250 cm^{-1} (3241 cm^{-1}) , 3167 cm^{-1} (3155 cm^{-1}), 1600 cm^{-1} (1610 cm^{-1}), 1150 cm^{-1} (1153 cm^{-1}) and 1133 cm^{-1} (1130 cm^{-1}). The above analysis strongly not only indicates that there are not nitrates in blue solid just like in the green solid, but also that the guest species in the interlayer space of the blue solid looks very similar to complex $CuN3^{2+}$.

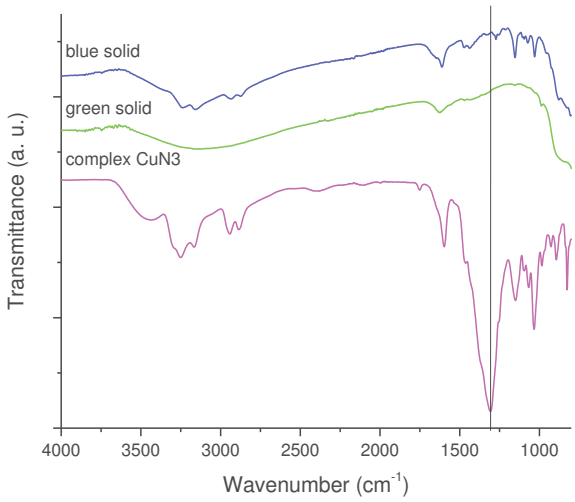

Figure IV.9. *Infrared spectra of green solid, blue solid and the complex $CuN3(NO_3)_2$.*

IV.2.2.2.4. UV-Visible absorption spectroscopy

The solid-state UV-Vis. spectra of the products are presented in ***Figure IV.10***. The green solid presents an absorption signal at 779 nm, blue shifted by about 25 nm with respect to the one of $Cu(NO_3)_2 \cdot 2.5H_2O$ (in water solution). The blue solid presents an absorption signal at 643 nm red shifted of about 25 nm with respect to the one of $CuN3(NO_3)_2$ (in water solution). The confirms that the inserted species in the green solid is close to "free" Cu^{II} ions, whereas the inserted species in the blue solid is close to $CuN3^{2+}$.

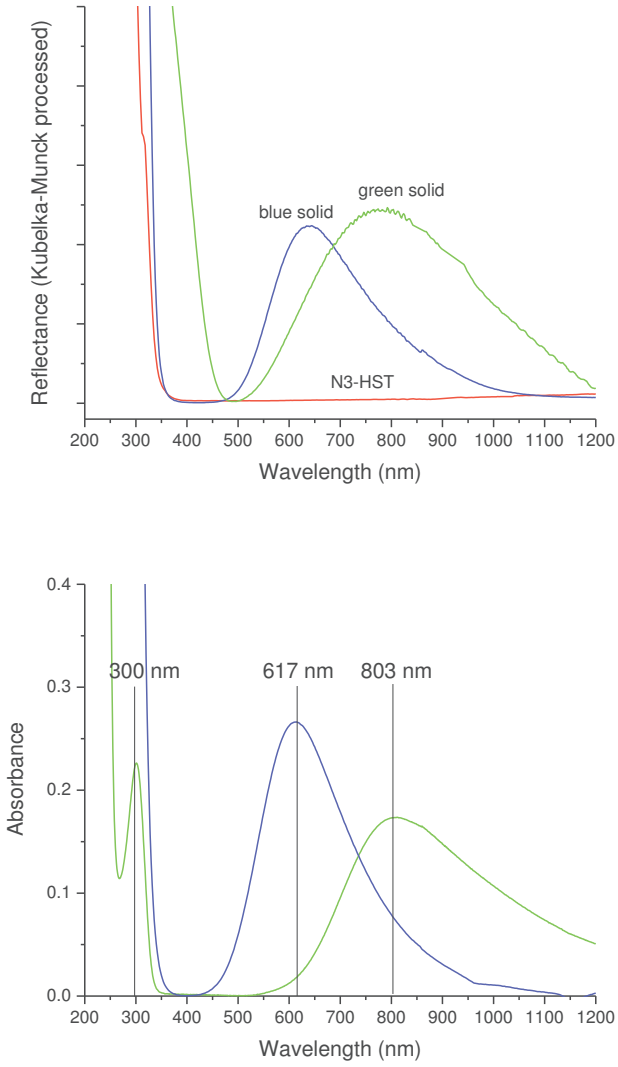

Figure IV.10. *Top) Solid-state UV spectra of N3-HST, green solid and blue solid, Bottom) Liquid-state UV-Vis. spectra of $Cu(NO_3)_2$ (15 mM) (green) and $CuN3(NO_3)_2$ (3 mM) (blue) in water.*

IV.2.2.2.5. SEM observation and EDX analysis

As seen on the SEM images (***Figure IV.11***), HST, N3-HST, green solid and blue solid present very similar platelet-like morphology. In addition the crystallites have similar size for all the compounds. The intercalation of polyamine N3 and the following coordination reactions do not change the morphology of HST. No clear difference can be seen at this stage between

the green solid and the blue solid. In addition, energy-dispersive X-ray spectroscopy (EDX) shows that the Cu/Ta_2 ratio is about 0.4 for the green solid and about 0.3 for the blue solid.

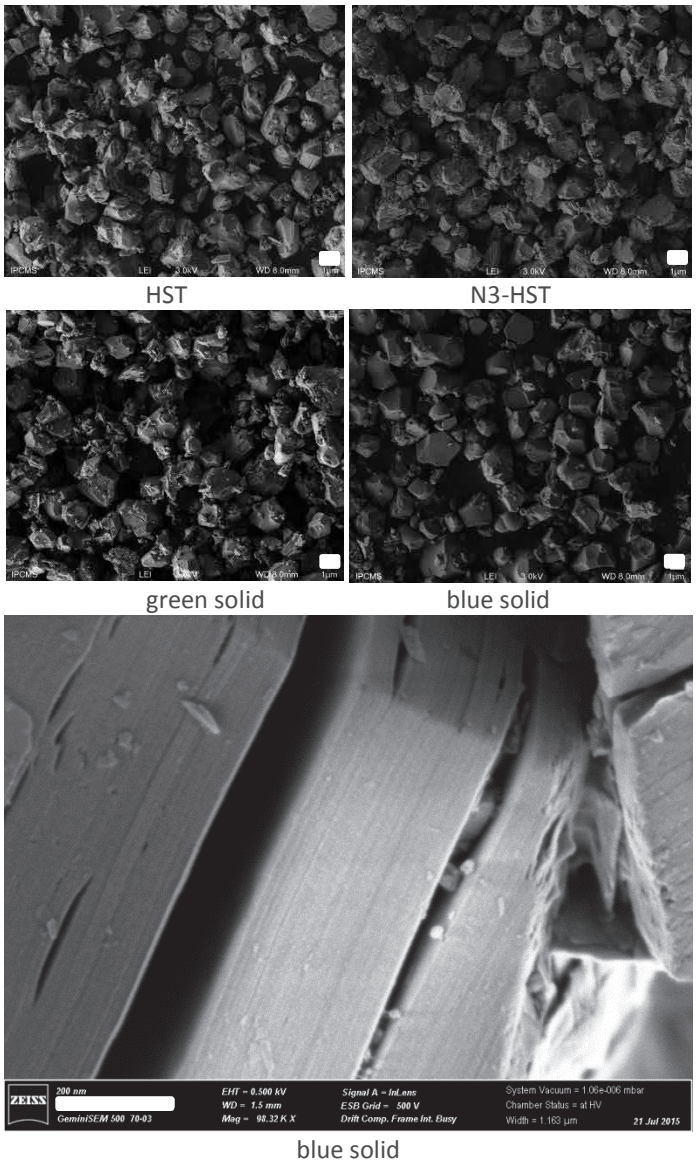

Figure IV.11. *SEM images of HST, N3-HST, green solid and blue solid (the scale bars represent 1 µm for the four images at top, and 200 nm for the image at bottom).*

IV.2.2.2.6. Elemental analysis and proposed formulae

The results of elemental analyses (**Annex**) for green solid and blue solid as well as the previous observations above allow to propose consistent formulae : $Cu_{0.60}(C_6N_3H_{17})_{0.08}H_{0.80}Bi_{0.1}Sr_{0.85}Ta_2O_7{\cdot}4H_2O$ for the green solid and $Cu_{0.35}(C_6N_3H_{17})_{0.35}H_{1.30}Bi_{0.1}Sr_{0.85}Ta_2O_7{\cdot}2H_2O$ for the blue solid. Elemental analyses confirm the almost complete removal of N3 in the green solid whereas the polyamine is still present in the blue solid. In addition, the proposed formulae established from elemental analyses do not show the presence of nitrate ions. This is in complete accordance with what was inferred from IR spectroscopy (***Figure IV.8***). Finally for the blue solid, the molar ratio between copper ion and N3 is 1, which corresponds to the formula of the complex $CuN3^{2+}$.[27,28]

IV.2.2.2.7. STEM characterization

IV.2.2.2.7.1. STEM view of the cross section

Further investigation of the structure of the products was performed using STEM spectroscopy. As an illustration, ***Figure IV.12*** shows the scanning TEM (STEM) view of the cross section of blue solid. The dark bands, visible in the top right image, are attributed to the inorganic perovskite-like slabs, since the tetragonal structures can be clearly observed in the bottom right image. However, because of the limited resolution of our equipment, the intermittent black spots in the inter-lamellar space could not be unambiguously identified.

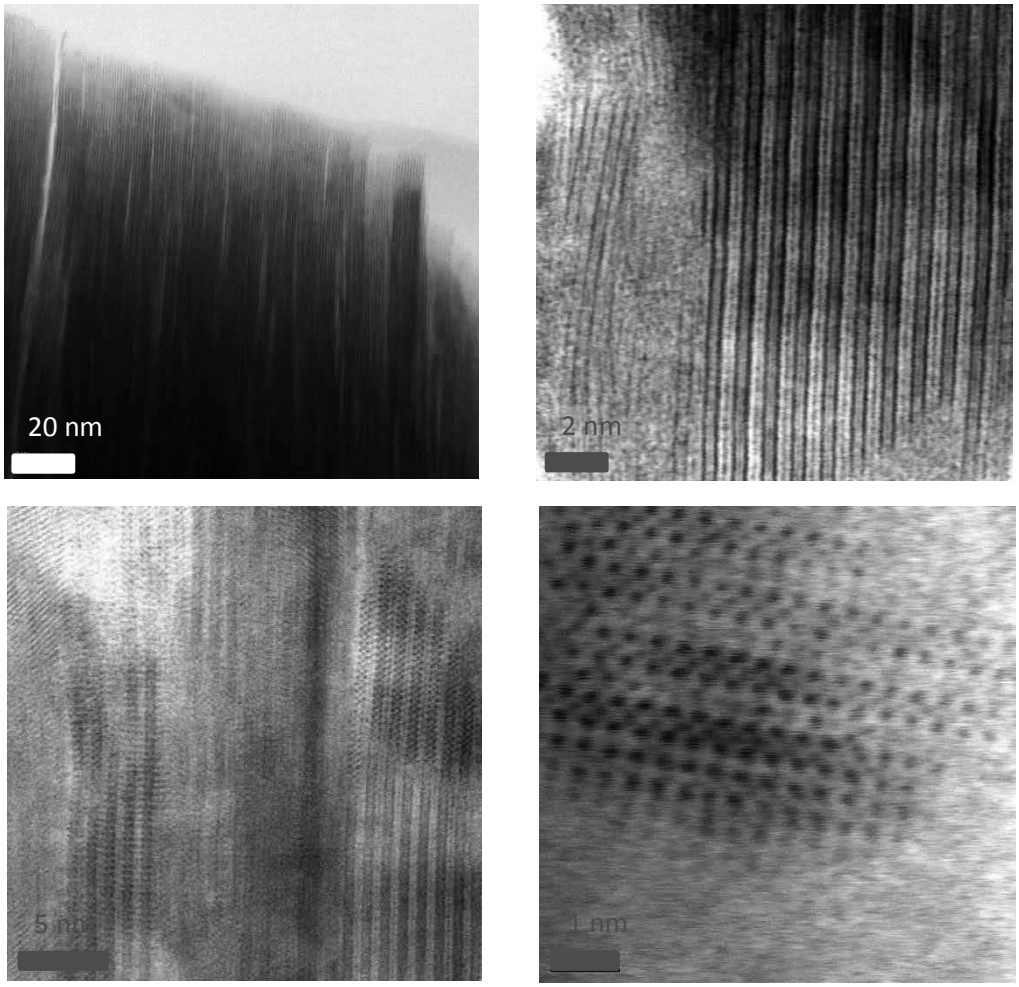

Figure IV.12. *STEM view of the cross section of the blue solid.*

IV.2.2.2.7.2. STEM-EDX profile analyses

The STEM-EDX profile analyses (***Figure IV.13***) have also been carried out. The objective was to obtain an accurate map in order to obtain the composition of the different layers. Unfotunately, in our case, the sensitivity and resolution of the EDX do not allow for satisfactory results. All elements are observed and one can see a small difference in the intensity profile but not precise enough to make conclusions. A microscope with a new generation of EDX, with a higher resolution should be employed.[29,30] Experiments are in progress.

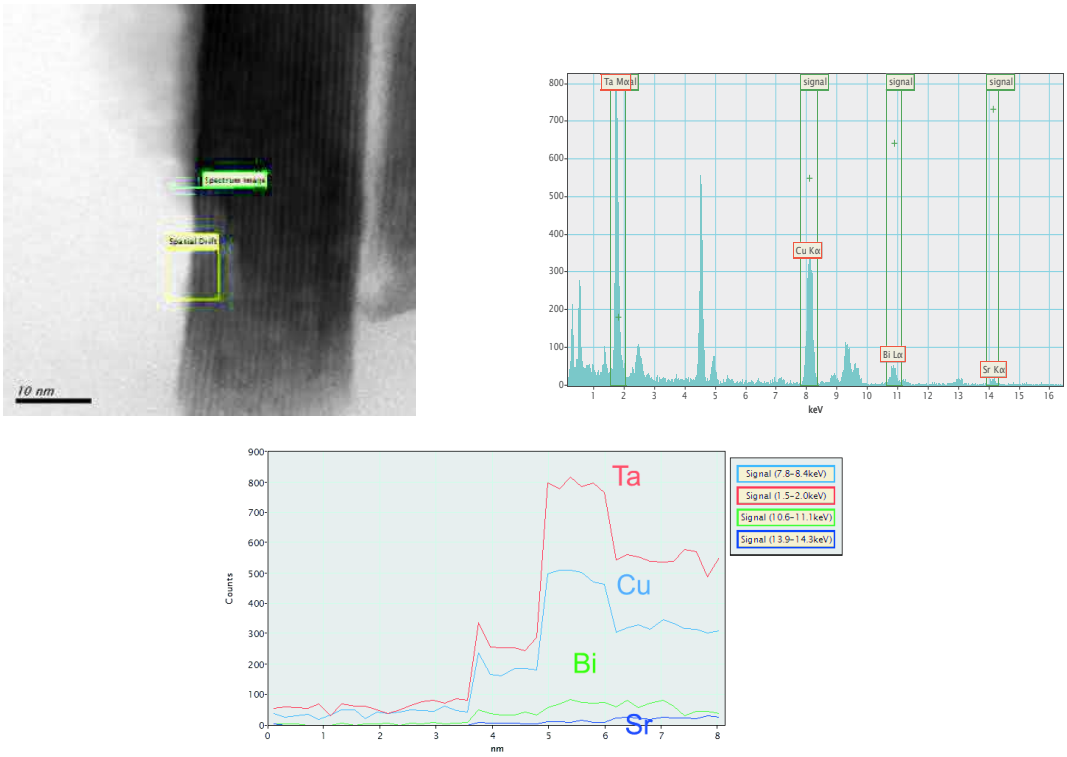

Figure IV.13. *STEM-EDX profile analyses of the blue solid.*

IV.2.2.2.8. Squid magnetometry

The magnetic behaviors of the green and blue solids were investigated by squid magnetometry. Temperature-dependent measurements were carried out under a 5000 G dc field. Data were corrected for the sample holder, and diamagnetism was estimated using the formula χ_{dia} = - M/2 × 10^{-6} using the formulae established in paragraph **IV.2.2.2.6**.

Figure IV.14 shows the χT = f(T) curves for the green and blue solids. These curves have been scaled to 1 Cu ion using the formulae established in paragraph **IV.2.2.2.6**.

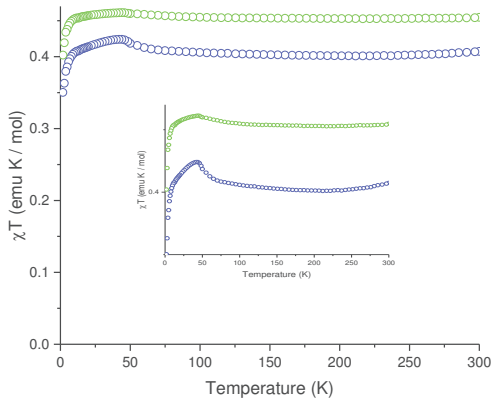

Figure IV.14. *χT = f(T) curves for the green and blue solids under a static field of 5000 G. Insert shows a zoom.*

The fit of the 1/χ = f(T) curves using the Curie-Weiss law provides Curie constants of 0.45 emu·K·mol^{-1} and 0.40 emu·K·mol^{-1} for green and blue solids respectively, in very good agreement with the expected values for one Cu(II) ion. The high temperature magnetic properties are thus in remarkable agreement with the formulae proposed in paragraph **IV.2.2.2.6**.

Blue and green solids have a very similar behavior. The χT product increases slightly from room temperature to about 50 K. Then when the temperature decreases further, the χT product decreases first slightly, then more steeply below 10 K. At this stage, we did not manage to rationalize this behavior. The small initial decrease of χT from 300 K to about 200 K for the blue solid is likely due to an excessive correction of diamagnetism.

The M = f(H) curves are presented in ***Figure IV.15*** (scaled to 1 Cu ion according to the formulae established in paragraph **IV.2.2.2.6**). They can be fitted using a Brillouin function, which provides g factors of 2.11(5) and 1.95(5) for green and blue solids respectively. Obviously the g factor obtained for the solid is slightly too small. This is likely due to the unavoidable error in the formula of the solids. The fact that these M = f(H) curves can be fitted with a Brillouin with a reasonable agreement with the established formulae confirms the paramagnetic (with very weak coupling) behavior of the green and blue solid.

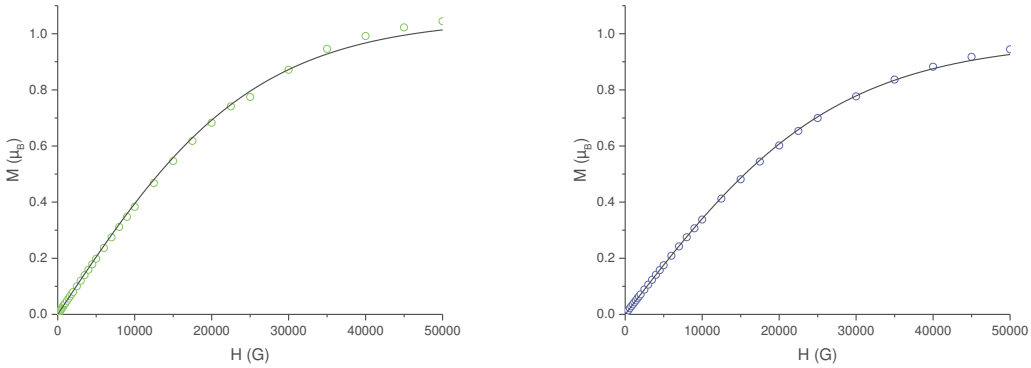

Figure IV.15. *M = f(H) curves for the green and blue solids at 1.8 K. Full lines represent best fits using a Brillouin function.*

IV.2.2.2.9. EPR spectroscopy

In order to further characterize the environment of the copper ions in the green solid and in the blue solid, continuous-wave EPR spectroscopy and pulsed EPR (ESEEM-2P) spectroscopy was performed (collaboration with Nathalie Parizel and Philippe Turek, Institut de Chimie de Strasbourg).
The X band (ν ≈ 9.8 GHz) EPR spectra of both compounds have been registered as a function of temperature, from room temperature to 10 K.
Concerning the blue solid, the spectrum does not change much when the temperature decreases (***Figure IV.16***). It presents a single symmetric and narrow signal centered around g = 2 with a peak to peak width of about 100 G.

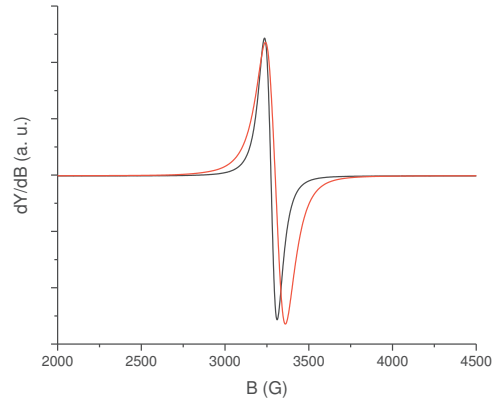

Figure IV.16. *X-band EPR spectrum of the blue solid at room temperature (black, ν = 9.546 GHz) (g = 2.083, ΔB_{pp} = 70 G) and at 10 K (red, ν = 9.727 GHz) (g = 2.105, ΔB_{pp} = 112 G).*

The spectra for the blue solid are very narrow, not characteristic of isolated Cu(II) species. It thus shows that the copper ions are interacting relatively strongly with each other (likely *via* dipolar interactions).
As for the green solid, the X band spectra at room temperature and at 10 K are clearly axial (***Figure IV.17***). The hyperfine interaction cannot be extracted from the spectra, which are modelled using B_{strain} (residual linewidth in the Gaussian simulation) different for the parallel and perpendicular parts respectively in order to account for the non-resolution of the hyperfine interaction.

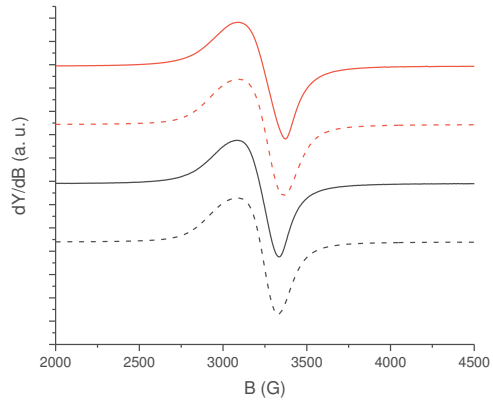

Figure IV.17. *X-band EPR spectrum of the green solid at room temperature (black, ν = 9.596 GHz) and at 10 K (red, ν = 9.744 GHz). Full lines correspond to the experimental spectra, dashed lines correspond to the best fit (at room temperature: $g_{//}$ = 2.283, $g_{\perp}$ = 2.092, $Bstrain_{//}$ = 671 MHz, $Bstrain_{\perp}$ = 348 MHz, line width = 95 G and at 10 K: $g_{//}$ = 2.311, $g_{\perp}$ = 2.105, $Bstrain_{//}$ = 706 MHz, $Bstrain_{\perp}$ = 431 MHz, line width = 95 G).*

In order to characterize the environment of the unpaired electrons of the Cu(II) ions detected by continuous wave EPR, we have performed pulsed EPR (ESEEM-2P) (Electron Spin Echo Envelope Modulation-2 Pulses) at 10 K. The Hahn echo modulations are registered as a function of the delay between the two pulses (at 90° and 180°). The Fourier transformation of the signal after subtraction of the decay due to transverse relaxation gives the frequencies of the nuclei on which the electron is delocalized (***Figure IV.18***).

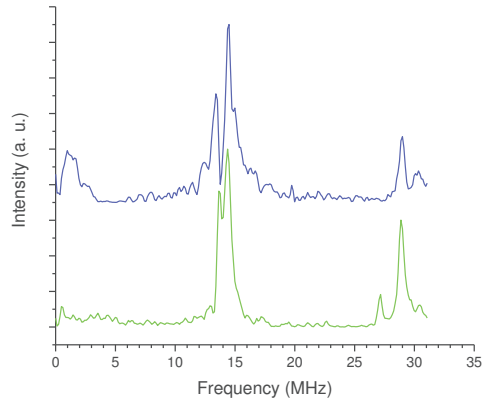

Figure IV.18. *ESEEM-2P spectra of the green solid (green) and the blue solid (blue) at 10 K.*

For the blue solid, the ESEEM-2P spectrum shows a signal due to ^{14}N around ν = 1.1 MHz, with the double resonance around 2.2 MHz. In addition, one sees the signal of ^{1}H around ν = 14.5 MHz, with the double resonance around 29 MHz.
In comparison, the ESEEM-2P spectrum of the green solid only present the signal of ^{1}H and its double resonance, in addition the ^{1}H is less large than for the blue solid, which indicates a less important interaction between the Cu(II) ions and protons. Moreover, the signal of ^{14}N is clearly absent.
Continuous wave EPR and pulsed EPR thus indicate that for the blue solid, the Cu(II) ions are surrounded by N and H atoms (as expected for a coordination by N3 ligand) and that they interact with each other (probably *via* dipolar interactions). For the green solid, the Cu(II) ions are more isolated (in agreement with what has been observed in squid measurements),

and their environment do not contain N atoms. Additional experiments should be performed on compounds with a lower copper content.

IV.2.2.3. Study of the mechanism: influence of the quantity of $Cu(NO_3)_2 \cdot 2.5H_2O$

IV.2.2.3.1. Synthesis

In order to study the effect of the quantity of copper nitrate on the reaction products, we have prepared a series of comparative experiments by using the quantity of copper nitrate as a variable, using N3-HST as precursor and under same reaction conditions (microwave irradiation, 80 °C and 0.5 h). The reaction conditions and first experimental observations are summarized in ***Table IV.1***.

Precursor	N3-HST (50 mg; 0.076 mmol) ($(N3)_{0.4}$-HST *i. e.* 0.03 mmol of N3)					
Reactant	Solution of $Cu(NO_3)_2 \cdot 2.5H_2O$ in water					
Mixture	**a**	**b**	**c**	**d**	**e**	**f**
[Cu(II)] (mol/L)	0.001	0.003	0.004	0.006	0.009	0.015
Vol. (mL)	6					
$n_{Cu(II)}$ (mmol)	0.006	0.018	0.024	0.036	0.054	0.090
pH (before)	5.4	5.4	5.4	5.2	5.1	4.9
Color (before)	Light green					
pH (after)	9.3	7.8	7.8	6.3	5.3	5.0
Color (after)	Colorless		Light blue		Light green	
Color of the obtained solid	Blue			Green		

Table IV.1. *Reaction conditions and first experimental observations ("before": the solution before the addition of N3-HST; "after": the filtrate after reaction with N3-HST and centrifugation of the solid).*

According to the above table, the pH of copper nitrate solutions before reaction with N3-HST is around 5, yet the pH of the filtrates after reaction with N3-HST depend on the quantity of copper nitrate. When the quantity of copper nitrate is much smaller than the quantity of N3 involved in the precursor (0.032 mmol), the filtrates are colorless and their pH are around 8. The solids obtained in these conditions are blue. When the quantity of copper nitrate is roughly the same as the quantity of N3 in the precursor, the filtrates are light blue and their pH are around 7. The solids obtained in these conditions are green. Finally, when the quantity of copper nitrate is much larger than the quantity of N3 in the precursor, the filtrates are light green and their pH are around 5. The solids obtained in these conditions are green.
These initial observations suggest a complex mechanism in solution and in the hybrid in suspension. The further more precise characterizations of the solids and filtrates described in the next paragraphs will allow to precise this mechanism.

IV.2.2.3.2. XRD analysis

The powder XRD patterns of the solids obtained following the various conditions presented above are presented ***Figure IV.19***. After reactions, the interlayer distance decreases from that of N3-HST (1.82 nm) to about 1.5 nm and further to about 1.3 nm and finally to about 1.2 nm along with the increasing the copper solution concentration. In addition, the crystallinity is obviously reduced along the series. It is noteworthy that when the quantity of

copper nitrate is between 0.024 mmol and 0.054 mmol, we obtain a mixture of products, one with an interlayer distance around 1.3 nm and the other one around 1.2 nm.
According to what has been described above for the blue and green solids (with interlamellar distances of 1.76 nm and 1.25 nm respectively), we attribute the gradual decrease of the interlamellar distance in this series of compounds to the gradual removal of polyamine N3. In addition, for all the reaction products, the reflections, which are assigned to (100) and (110) in the XRD pattern of HST, are observed at the same positions (22.68° and 32.59°, respectively), indicated the persistence of the perovskite-slab structure.

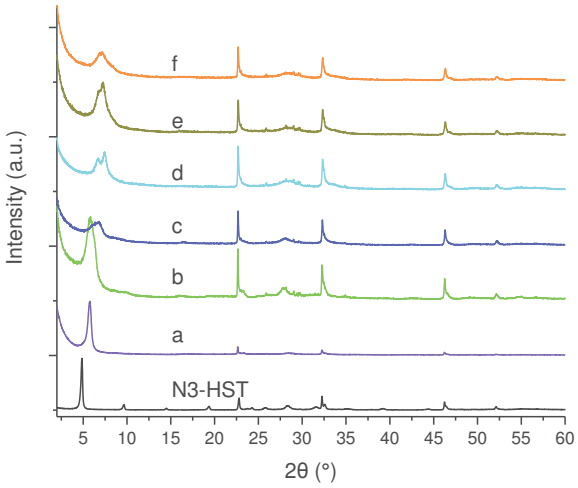

Figure IV.19. *PXRD patterns of N3-HST and its reaction products with different quantities of copper nitrate (a: 0.006 mmol; b: 0.018 mmol; c: 0.024 mmol; d: 0.036 mmol; e: 0.054 mmol; f: 0.090 mmol) according to the conditions presented in* ***Table IV.1****.*

IV.2.2.3.3. Infrared spectroscopy

Figure IV.20 shows the corresponding IR spectra of the products. When the quantity of copper nitrate is between 0.006 mmol (a) and 0.024 mmol (c), the bands at 3241 cm^{-1}, 3155 cm^{-1} (which are due to NH stretching of $–NH_2$ group) and 2930 cm^{-1} and 2867 cm^{-1} (which are due to antisymmetric and symmetric stretching vibrations of CH_2 groups), which have been described in the spectra of blue solid (***Figure IV.8***) are present. On the contrary, when the quantity of copper nitrate is larger, the obtained spectra are the same as that of green solid (***Figure IV.8***). The disappearance of bands at 1567 cm^{-1}, 1543 cm^{-1} and 1466 cm^{-1}, which are ascribed to protonated N3 in the interlayer space of HST, is clearly observed. The above analyses are in good accordance with the information from XRD and coherent with the experimental observations reported in ***Table IV.1***.

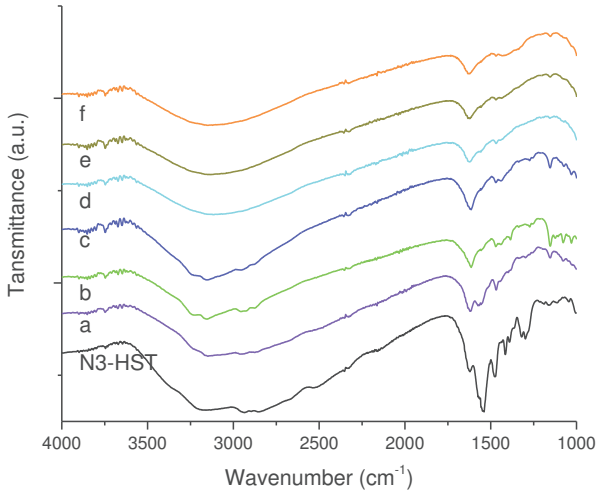

Figure IV.20. *Infrared spectra of N3-HST and its reaction products with different quantities of copper nitrate (a: 0.006 mmol; b: 0.018 mmol; c: 0.024 mmol; d: 0.036 mmol; e: 0.054 mmol; f: 0.090 mmol) according to the conditions presented in* ***Table IV.1****.*

IV.2.2.3.4. UV-Vis. absorption spectroscopy and elemental analysis

In order to precise the trivial observation of the color reported in ***Table IV.1***, the solid-state UV-Vis. spectra of the obtained solids have been also recorded (***Figure IV.21***). Upon the increase of the quantity of copper nitrate, the absorbance of the obtained solids shifts from 640 nm (which is as same as that of blue solid) and 780 nm (which is as same as that of green solid). For "medium" quantity of copper nitrate (compound c, 0.024 mmol) the spectrum shows clearly two signals, indicating a mixture of green solid and blue solid. This result confirms the conclusions of the XRD.

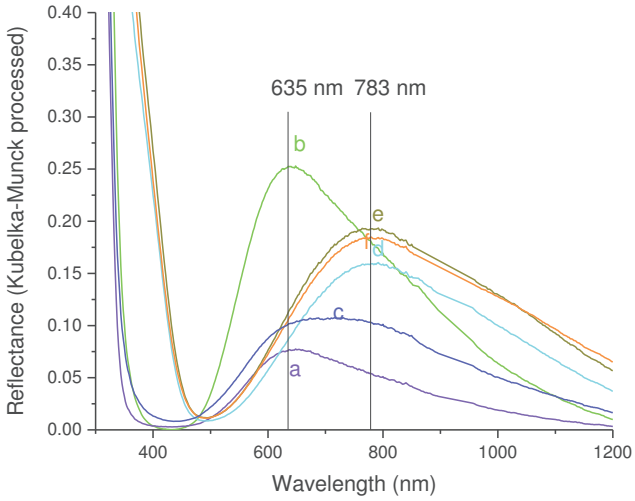

Figure IV.21. *The solid-state UV spectra of the obtained solids after the reactions between N3-HST and different quantities of copper nitrate (a: 0.006 mmol; b: 0.018 mmol; c: 0.024 mmol; d: 0.036 mmol; e: 0.054 mmol; f: 0.090 mmol) according to the conditions presented in* ***Table IV.1****.*

In addition, the corresponding liquid-state UV-Vis. absorption spectra of the filtrates obtained after reactions were recorded and compared to the spectra of the starting $Cu(NO_3)_2$ solutions, and of equivalent solutions of the complex $CuN3(NO_3)_2$ (***Figures IV.22***, ***IV.23*** and ***IV.24***). In the present case, the absorption of the N3 amine masks the absorption of the nitrate group at 300 nm in $CuN3(NO_3)_2$ and in the spectra of the filtrates. Due to distortions from the pure octahedral geometry, the visible part of the spectra of $Cu(H_2O)_6(NO_3)_2$ and of $CuN3(NO_3)_2$ cannot be fitted by a single Gaussian peak (after having changed the abscise axis from wavelength scale into energy scale). Therefore, the spectra of the filtrates were simply fitted by a linear combination of the spectra of $Cu(H_2O)_6(NO_3)_2$ and of $CuN3(NO_3)_2$ which allows to determine the concentration of both species in the filtrates (***Table IV.2***).

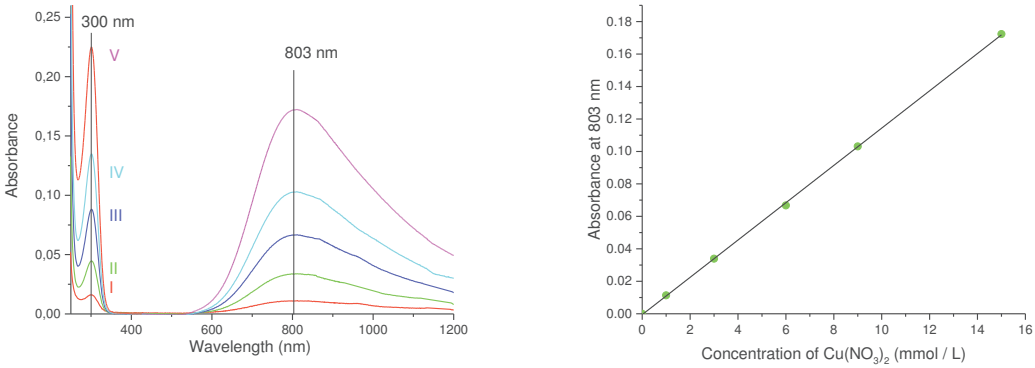

Figure IV.22. *Left) Liquid-state UV-Vis. spectra of $Cu(NO_3)_2$ in water (I: 1 mM; II: 3 mM; III: 6 mM; IV: 9 mM; V: 15 mM), Right) Plot of the absorbance at 803 nm as a function of concentration and best linear fit.*

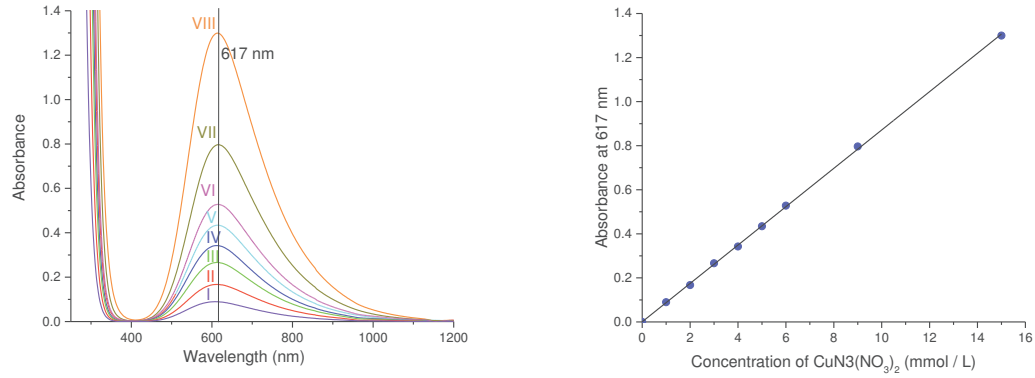

Figure IV.23. *Left) Liquid-state UV-Vis. spectra of $CuN3(NO_3)_2$ in water (I: 1 mM; II: 2 mM; III: 3 mM; IV: 4 mM; V: 5 mM; VI: 6 mM; VII: 9 mM; VIII: 15 mM), Right) Plot of the absorbance at 617 nm as a function of concentration and best linear fit.*

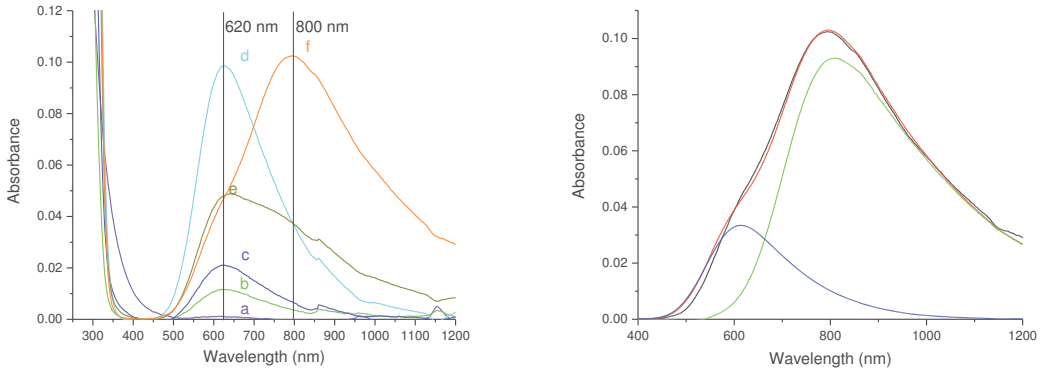

Figure IV.24. *Left) Liquid-state UV-Vis. spectra of the filtrates obtained after the reactions between N3-HST and different quantities of copper nitrate (a: 0.006 mmol; b: 0.018 mmol; c: 0.024 mmol; d: 0.036 mmol; e: 0.054 mmol; f: 0.090 mmol) according to the conditions presented in* ***Table IV.1****. Right) Example of linear combination of spectra of CuN3(NO$_3$)$_2$ and Cu(NO$_3$)$_2$ to reproduce spectrum f (black : experimental spectrum; blue : CuN3(NO$_3$)$_2$, 0.39 mM; green : Cu(NO$_3$)$_2$, 8.1 mM; red : sum).*

Unfortunately, this study cannot provide the total N3 concentration in the filtrate (free and coordinated to Cu(II)), because the free N3 absorbs at a too high energy and the complexation constant of Cu(II) by N3 in water is unknown (and more important, is likely to change upon pH variation, which occurs during the reaction as observed in ***Table IV.1***). Therefore, only the Cu(II) concentration in the filtrate (in the form of free Cu(II) and complexed by N3 ligand) could be determined. This allows to estimate the quantity of Cu(II) trapped by N3-HST as a function of initial Cu(II) concentration (***Figure IV.25***). The relative error on the Cu(II) content can be estimated around 15%.

Precursor	N3-HST (50 mg; 0.076 mmol) ((N3)$_{0.4}$-HST *i. e.* 0.03 mmol of N3)					
Reactant	Solution of Cu(NO$_3$)$_2$·2.5H$_2$O in water (6 mL)					
Mixture	**a**	**b**	**c**	**d**	**e**	**f**
[Cu(II)] (mmol/L)	1	3	4	6	9	15
n$_{Cu(II)}$ (mmol)	0.006	0.018	0.024	0.036	0.054	0.090
Number of equivalents of Cu(II) with respect to N3-HST / N3	0.079 0.20	0.24 0.60	0.32 0.80	0.47 1.18	0.71 1.78	1.18 2.95
[CuN3(NO$_3$)$_2$] in the filtrate (mmol/L) / n (mmol)	0.01 5.8×10^{-5}	0.13 7.8×10^{-4}	0.22 1.3×10^{-3}	1.08 6.5×10^{-3}	0.49 3.0×10^{-3}	0.39 2.3×10^{-3}
[Cu(H$_2$O)$_6$(NO$_3$)$_2$] in the filtrate (mmol/L) / n (mmol)	0* 0*	0* 0*	0.09 5.4×10^{-4}	0.67 4.0×10^{-3}	2.14 1.3×10^{-2}	8.10 4.8×10^{-2}
Color of the hybrid solid	Blue	Blue	Blue	Green	Green	Green
Estimated Cu content in the obtained solids per HST unit	Cu$_{0.08}$	Cu$_{0.23}$	Cu$_{0.29}$	Cu$_{0.34}$	Cu$_{0.50}$	Cu$_{0.52}$

Table IV.2. *Analysis of the filtrates of the reactions between N3-HST and various concentrations of Cu(NO$_3$)$_2$·2.5H$_2$O (*: given the imprecision of the fit at these low concentration of complex, these values have not been fitted, and were fixed to 0). The copper content of the solids is estimated considering the element conservation.*

Elemental micro-analyses (C, H, N) and energy-dispersive X-ray spectroscopy have been performed on the obtained solids. The estimated formulae of the obtained products are estimated and collected in ***Table IV.3***.

Reaction	EDX	Micro-analysis			Formula
	n_{Cu} / n_{Ta}	C (mass %) Exp (calcd)	H (mass %) Exp	N (mass %) Exp (calcd)	
a	0.00	2.73 (2.76)	1.30	1.66 (1.61)	$Cu_{0.00}$-$(N3)_{0.23}$-HST
b	0.05	2.85 (2.51)	1.21	1.41 (1.46)	$Cu_{0.10}$-$(N3)_{0.21}$-HST
c	0.07	1.42 (1.69)	0.95	0.93 (0.99)	$Cu_{0.14}$-$(N3)_{0.14}$-HST
d	0.11	0.70 (0.85)	0.70	0.52 (0.50)	$Cu_{0.22}$-$(N3)_{0.07}$-HST
e	0.20	0.59 (0.60)	0.72	0.50 (0.35)	$Cu_{0.40}$-$(N3)_{0.05}$-HST
f	0.20	0.51 (0.60)	0.66	0.49 (0.35)	$Cu_{0.40}$-$(N3)_{0.05}$-HST

Table IV.3. *Results of micro-analysis (C, H, N) and EDX spectroscopy of the reaction products between N3-HST and different quantities of copper nitrate (a: 0.006 mmol; b: 0.018 mmol; c: 0.024 mmol; d: 0.036 mmol; e: 0.054 mmol; f: 0.090 mmol) according to the conditions presented in* ***Table IV.1****. Considering the unknown water content parameter, and the very low quantity of H, this H content was not taken into account. The proposed formulae are only based on Cu, C and N analyses.*

According to the above table, the content of copper gradually increases while the content of polyamine (N3) gradually decreases along with the increase of the initial copper nitrate quantity (***Figure IV.25***). When the initial quantity of copper nitrate is between 0.006 mmol and 0.024 mmol, the final quantity of N3 in the residual solid is larger than that of copper, which indicates the coexistence of the complex $CuN3^{2+}$ and N3 in the interlayer space. However, when the molar quantity of copper nitrate is between 0.054 mmol and 0.090 mmol, the content of copper reaches a plateau. In addition, the polyamine is almost completely removed; the quantities observed in elemental analysis are indeed traces. This is in good agreement with the results obtained for the composition of the green solid (paragraph **IV.2.2.2.6**, $Cu_{0.60}(C_6N_3H_{17})_{0.08}H_{0.80}Bi_{0.1}Sr_{0.85}Ta_2O_7{\cdot}4H_2O$)

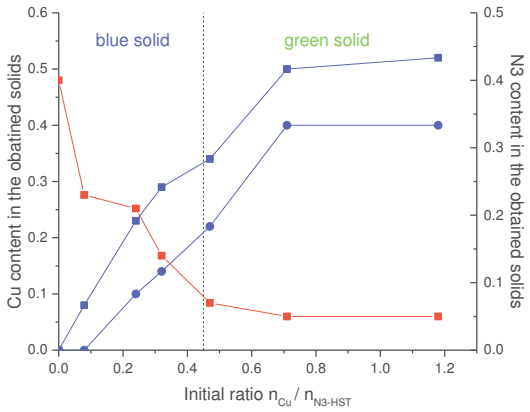

Figure IV.25. *Estimated composition of the solids obtained after the reactions between N3-HST and different quantities of copper nitrate according to the conditions presented in* ***Table IV.1*** *(red squares: quantity of N3 (from elemental analysis); blue squares: quantity of Cu (from UV-Vis. spectroscopy of the filtrates); blue circles: quantity of Cu (from EDX analysis)) (full lines are just guide for the eye).*

IV.2.2.3.5. Proposed mechanism

Considering the above observations, and taking into account the necessary charge balance, we can propose a mechanism for the formation of the blue and green solids from the reaction between N3-HST and copper nitrate. For the sake of clarity, the nomenclature is slightly modified to precise the protonation state of HST and of N3.

For low copper concentrations :

$Cu(NO_3)_2 + N_3H_2\text{-ST} \rightarrow CuN3\text{-ST} + 2\ H^+ + 2\ NO_3^-$

In the blue solid which forms, CuN3-ST, N3 is in the form of amine and not ammonium. The Cu(II) ions are thus tri-coordinated by N3 in the interlamellar spacing. The Cu(II) ions bring two positive unbalanced charges (the NO_3^- ions are not intercalated, as proved by the absence of their signature in the IR spectra). Therefore, two protons leave the interlamellar spacing.

The other hypothesis $Cu(NO_3)_2 + N_3H_2\text{-ST} \rightarrow CuN3(NO_3)_2\text{-}H_2ST$ can be rejected, because NO_3^- should then be observed in IR spectroscopy.

For high copper concentrations :

$Cu(NO_3)_2 + N_3H_2\text{-ST} \rightarrow Cu\text{-ST} + N3H_2^{2+} + 2\ NO_3^-$

In the green solid which forms, Cu-ST, the amine N3 is no longer intercalated. The Cu(II) ions are thus "free" (likely surrounded by the oxygen atoms of the perovskite layers). The Cu(II) ions bring two positive unbalanced charges (the NO_3^- ions are not intercalated, as proved by the absence of their signature in the IR spectra). Therefore, two protons leave the interlamellar spacing along with amine (which likely explains the lower association constant between N3 and Cu(II) in the filtrate).

The other hypothesis $Cu(NO_3)_2 + N_3H_2\text{-ST} \rightarrow Cu(NO_3)_2\text{-}H_2ST + N3$ can be rejected, because NO_3^- should then be observed in IR spectroscopy and the pH of the filtrate should increase.

IV.2.2.4. Study of the mechanism: influence of the quantity of $CuN3(NO_3)_2$

IV.2.2.4.1. Synthesis

The same analysis as before with Cu nitrate was performed, but using the preformed $CuN3(NO_3)_2$ complex instead of $Cu(NO_3)_2$. We have prepared a series of comparative experiments by using the quantity of $CuN3(NO_3)_2$ as a variable, using N3-HST as precursor and under same reaction conditions (microwave irradiation, 80 °C and 0.5 h). The reaction conditions and first experimental observations are summarized in ***Table IV.4***.

Precursor	N3-HST (50 mg; 0.076 mmol) ($(N3)_{0.4}$-HST *i. e.* 0.03 mmol of N3)							
Reactant	Solution of $CuN3(NO_3)_2$ in water							
Mixture	**g**	**h**	**i**	**j**	**k**	**l**	**m**	**n**
[Cu(II)N3] (mol/L)	0.001	0.002	0.003	0.004	0.005	0.006	0.009	0.015
Vol. (mL)	6							
$n_{Cu(II)}$ (mmol)	0.006	0.012	0.018	0.024	0.030	0.036	0.054	0.090
pH (before)	9.5	9.4	9.3	9.4	9.4	9.3	9.3	9.6
Color (before)	Blue							
pH (after)	10.0	9.7	9.7	9.7	9.4	9.5	9.4	9.6
Color (after)	Colorless				Blue			
Color of the obtained solid	Blue							

Table IV.4. *Reaction conditions and first experimental observations ("before": the solution before the addition of N3-HST; "after": the filtrate after reaction with N3-HST and centrifugation of the solid).*

According to the table, the pH of $CuN3(NO_3)_2$ solutions before reaction with N3-HST are around 9.5 and the pH of the filtrates after reaction with N3-HST are almost identical and do not change upon reaction. It is noteworthy that when the quantity of $CuN3(NO_3)_2$ complex is less than the quantity of N3 in the precursor N3-HST (0.03 mmol), the filtrates are colorless, whereas the solids obtained are blue. This strongly indicates the transfer of $CuN3^{2+}$ complex or copper ions from solution to the precursor N3-HST. When the quantity of $CuN3(NO_3)_2$ is larger than the quantity of N3 in the precursor, the filtrates are logically blue and as products we also obtain blue solids.
There again, the following experiments and characterizations will allow to precise and understand these initial observations.

IV.2.2.4.2. XRD analysis

In order to further investigate the obtained products, their powder XRD patterns have been recorded (***Figure IV.26***).

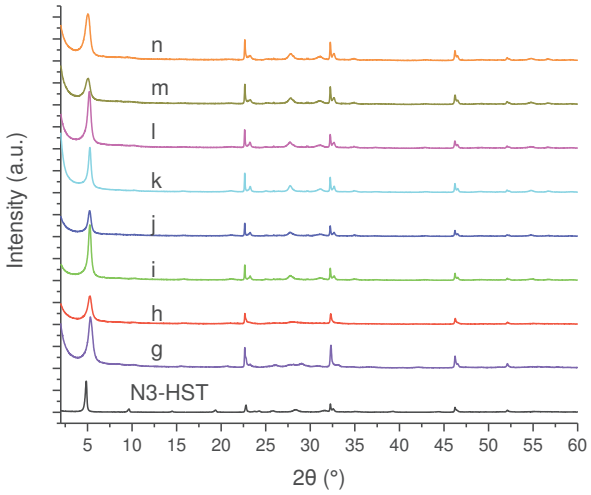

Figure IV.26. *PXRD patterns of N3-HST and its reaction products with different quantity of $CuN3(NO_3)_2$ (g: 0.006 mmol; h: 0.012 mmol; i: 0.018 mmol; j: 0.024 mmol; k: 0.030 mmol; l: 0.036 mmol; m: 0.054 mmol; n: 0.090 mmol) according to the conditions presented in* ***Table IV.4****.*

After reactions, the interlayer distance slightly decreases from that of N3-HST (1.82 nm) to about 1.70 nm when the quantity of $CuN3(NO_3)_2$ is between 0.006 mmol (g) and 0.036 mmol

(l), or to about 1.75 nm when the molar quantity of $CuN3(NO_3)_2$ is between 0.054 mmol (m) and 0.090 mmol (n). In addition, for all the reaction products, the reflections, which are assigned to (100) and (110) in the XRD pattern of HST, are observed at the same positions (22.68° and 32.59°, respectively), indicated the persistence of the perovskite-slab structure.

IV.2.2.4.3. Infrared spectroscopy

The infrared spectra of corresponding products are presented in ***Figure IV.27***. When the quantity of $CuN3(NO_3)_2$ is between 0.006 mmol (g) and 0.030 mmol (k), we can observe the conversion from N3-HST to blue solid by observing the decrease of the intensity of the signals belonging to N3-HST (1620 cm^{-1} and 1543 cm^{-1}) and the increase of the intensity of the signals belonging to blue solid (3241 cm^{-1}, 3155 cm^{-1}, 1610 cm^{-1}, 1153 cm^{-1} and 1133 cm^{-1} *cf.* ***Figure IV.8***) upon increasing the quantity of $CuN3(NO_3)_2$. When the molar quantity of $CuN3(NO_3)_2$ is between 0.036 mmol (l) and 0.090 mmol (n), the infrared spectra of the obtained products are the same as that of the blue solid. The above analyses clearly present the gradual conversion process from N3-HST to blue solid.

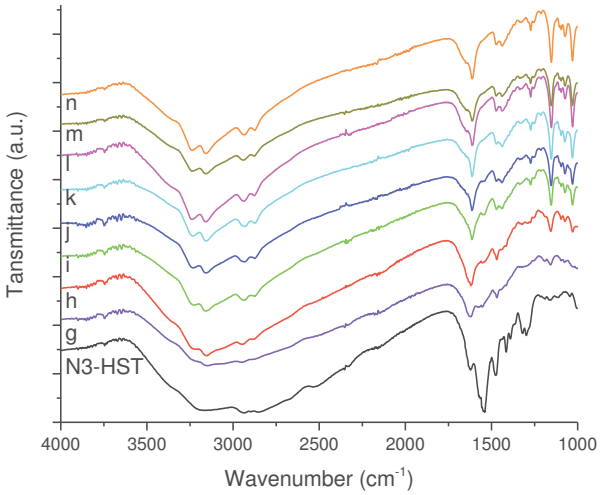

Figure IV.27. *Infrared spectra of N3-HST and its reaction products with different quantity of $CuN3(NO_3)_2$ (g: 0.006 mmol; h: 0.012 mmol; i: 0.018 mmol; j: 0.024 mmol; k: 0.030 mmol; l: 0.036 mmol; m: 0.054 mmol; n: 0.090 mmol) according to the conditions presented in* ***Table IV.4****.*

IV.2.2.4.4. UV-Vis. absorption spectroscopy and elemental analysis

Figure IV.28 shows the solid-state UV spectra of the obtained reaction products. A signal at 640 nm (the same as that of blue solid) is always observed whatever the quantity of $CuN3(NO_3)_2$.

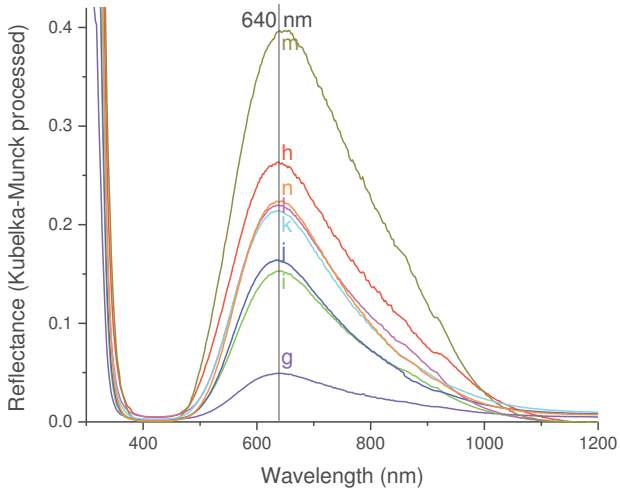

Figure IV.28. *Solid-state UV spectra of the reactions products between and different quantity of CuN3 (g: 0.006 mmol; h: 0.012 mmol; i: 0.018 mmol; j: 0.024 mmol; k: 0.030 mmol; l: 0.036 mmol; m: 0.054 mmol; n: 0.090 mmol) according to the conditions presented in* ***Table IV.4****.*

Figure IV.29 shows the liquid-state UV-Vis. spectra of the filtrates obtained after reactions. They can be quantitatively compared to the spectra of the starting $CuN3(NO_3)_2$ solution (***Figure IV.22***). When the initial quantity of $CuN3(NO_3)_2$ is between 0.006 mmol (1 mM) and 0.024 mmol (4 mM), there are not absorption signals of CuN3 in the corresponding filtrates. That means the concentration of the complex $CuN3(NO_3)_2$ in the filtrates is zero, or at least negligible. This is a strong evidence to prove the transfer of copper ions or $CuN3^{2+}$ complex from solution to the interlayer space of HST. When the initial quantity of $CuN3(NO_3)_2$ is more than 0.024 mmol (4 mM), we can observe in the spectra of the obtained filtrates the signal at 615 nm, the intensity of which increases along with the increase of the initial quantity of $CuN3(NO_3)_2$. This indicates that the transfer has reached a state of saturation.

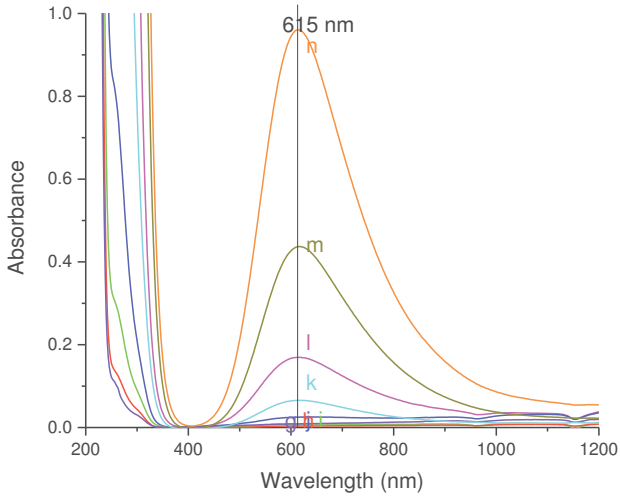

Figure IV.29. *Liquid-state UV-Vis. spectra of the filtrates obtained after the reactions between N3-HST and different quantities of $CuN3(NO_3)_2$ (g: 0.006 mmol; h: 0.012 mmol; i: 0.018 mmol; j: 0.024 mmol; k: 0.030 mmol; l: 0.036 mmol; m: 0.054 mmol; n: 0.090 mmol) according to the conditions presented in* ***Table IV.4****.*

The quantitative analysis is summarized in ***Table IV.5***.

Precursor	N3-HST (50 mg; 0.076 mmol) ($(N3)_{0.4}$-HST *i. e.* 0.03 mmol of N3)							
Reactant	Solution of $CuN3(NO_3)_2$ in water (6 mL)							
Mixture	**g**	**h**	**i**	**j**	**k**	**l**	**m**	**n**
[Cu(II)] (mmol/L)	1	2	3	4	5	6	9	15
$n_{Cu(II)}$ (mmol)	0.006	0.012	0.018	0.024	0.030	0.036	0.054	0.090
Number of equivalents of Cu(II) with respect to N3-HST / N3	0.079 0.20	0.16 0.39	0.24 0.59	0.32 0.79	0.39 0.99	0.47 1.18	0.71 1.78	1.18 2.96
[$CuN3(NO_3)_2$] in the filtrate (mmol/L) / n (mmol)	0 0	0 0	0 0	0.29 1.7×10^{-3}	0.76 4.5×10^{-3}	1.95 1.17×10^{-2}	5.02 3.01×10^{-2}	11.0 6.62×10^{-2}
Color of the hybrid solid	Blue							
Estimated Cu content in the obtained solids per HST unit	$Cu_{0.08}$	$Cu_{0.16}$	$Cu_{0.24}$	$Cu_{0.29}$	$Cu_{0.34}$	$Cu_{0.32}$	$Cu_{0.31}$	$Cu_{0.31}$

Table IV.5. *Analysis of the filtrates of the reactions between N3-HST and various concentrations of $CuN3(NO_3)_2$.*

The results presented in ***Table IV.5*** show that the content of copper gradually increases along with the increase of the initial quantity of CuN3 complex until around 0.024 mmol. When the initial quantity of $CuN3(NO_3)_2$ complex is higher than 0.030 mmol (0.39 eq with respect to N3-HST), we observe that the copper content in the final solid reaches a plateau, around 0.3 Cu per HST unit.

Finally, elemental micro-analyses (C, H, N) and energy-dispersive X-ray spectroscopy have been performed on the obtained solids. The estimated formulae of the obtained products are estimated and collected in ***Table IV.6***.

Reaction	**EDX**	**Micro-analysis**			**Formula**
	n_{Cu} / n_{Ta}	**C (mass %) Exp (calcd)**	**H (mass %) Exp**	**N (mass %) Exp (calcd)**	
g	0.00	2.76 (3.10)	1.44	2.07 (1.81)	$Cu_{0.00}$-$(N3)_{0.26}$-HST
h	0.04	2.96 (3.18)	1.41	1.85 (1.86)	$Cu_{0.08}$-$(N3)_{0.27}$-HST
i	0.08	3.30 (3.38)	1.43	2.04 (1.97)	$Cu_{0.16}$-$(N3)_{0.29}$-HST
j	0.11	3.41 (3.57)	1.44	2.07 (2.08)	$Cu_{0.22}$-$(N3)_{0.31}$-HST
k	0.13	3.36 (3.45)	1.36	2.17 (2.01)	$Cu_{0.26}$-$(N3)_{0.30}$-HST
l	0.14	3.34 (3.45)	1.41	2.11(2.01)	$Cu_{0.28}$-$(N3)_{0.30}$-HST
m	0.15	3.37 (3.44)	1.43	2.12 (2.01)	$Cu_{0.30}$-$(N3)_{0.30}$-HST
n	0.15	3.52 (3.65)	1.36	2.18 (2.13)	$Cu_{0.30}$-$(N3)_{0.32}$-HST

Table IV.6. *Results of micro-analysis (C, H, N) and EDX spectroscopy of the reaction products between N3-HST and different quantities of $CuN3(NO_3)_2$ (g: 0.006 mmol; h: 0.012 mmol; i: 0.018 mmol; j: 0.024 mmol; k: 0.030 mmol; l: 0.036 mmol; m: 0.054 mmol; n: 0.090 mmol) according to the conditions presented in* ***Table IV.4****. Considering the unknown water content parameter, and the very low quantity of H, this H content was not taken into account. The proposed formulae are only based on Cu, C and N analyses.*

According to the above table, the content of copper gradually increases along with the increase of the initial $CuN3(NO_3)_2$ quantity (***Figure IV.30***) until a plateau after 0.036 mmol (0.47 eq with respect to N3-HST). On the contrary, the content of polyamine remains constant (the ratio between N3 and HST is about 0.3) whatever the quantity of $CuN3(NO_3)_2$. Yet it is noteworthy that the N3 content has decreased by about 25 % with respect to the starting N3-HST. Finally, when the copper content in the obtained solids has reached the

plateau, the ratio between copper and N3 in the final product is about 1, which is very consistent with the composition of the complex $CuN3^{2+}$.[27,28] These results are in very good agreement with the results obtained for the composition of the blue solid (paragraph **IV.2.2.2.6**, $Cu_{0.35}(C_6N_3H_{17})_{0.35}H_{1.30}Bi_{0.1}Sr_{0.85}Ta_2O_7{\cdot}2H_2O$)

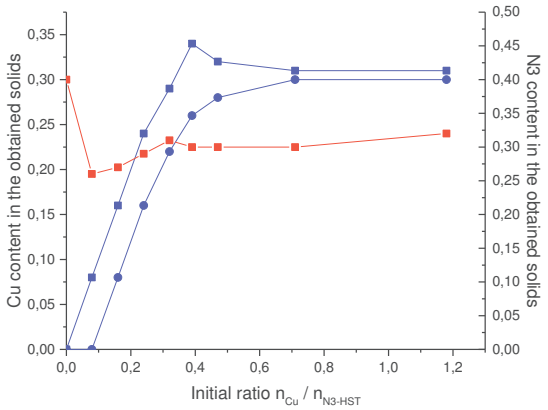

Figure IV.30. *Estimated composition of the solids obtained after the reactions between N3-HST and different quantities of $CuN3(NO_3)_2$ according to the conditions presented in* ***Table IV.4*** *(red squares : quantity of N3 (from elemental analysis); blue squares : quantity of Cu (from UV-Vis. spectroscopy of the filtrates); blue circles : quantity of Cu (from EDX analysis)) (full lines are just guide for the eye).*

IV.2.2.4.5. Proposed mechanism

Similarly to what has been done when using copper nitrate as the source of copper, we can propose a mechanism for the formation of the blue solid from the reaction between N3-HST and $CuN3(NO_3)_2$. For the sake of clarity, the nomenclature is slightly modified to precise the protonation state of HST and of N3. Moreover, when necessary, we differentiate using colors the origin of the polyamine N3, from the $CuN3(NO_3)_2$ complex or from N3-HST. Several hypotheses must be considered:

$CuN3(NO_3)_2 + N_3H_2\text{-ST} \rightarrow CuN3(NO_3)_2\text{-}H_2ST + N3$

This hypothesis can be rejected, because NO_3^- should then be observed in IR spectroscopy.

$CuN3(NO_3)_2 + N_3H_2\text{-ST} \rightarrow Cu(N3)_2(NO_3)_2\text{-}H_2ST$

or $CuN3(NO_3)_2 + N_3H_2\text{-ST} \rightarrow Cu(N3)_2\text{-ST} + 2\ NO_3^- + 2\ H^+$

These two hypotheses can be rejected in view of the analyses which all point to a Cu/N3 ratio of 1 in the blue solid.

Finally the two remaining similar propositions are:

(1) $CuN3(NO_3)_2 + N_3H_2\text{-ST} \rightarrow CuN3\text{-ST} + N3 + 2\ H^+ + 2\ NO_3^-$

(2) $CuN3(NO_3)_2 + N_3H_2\text{-ST} \rightarrow CuN3\text{-ST} + N3 + 2\ H^+ + 2\ NO_3^-$

In order to know if the mechanism proceeds by $CuN3^{2+}$ complex exchange with $N3H_2^{2+}$ (reaction 1) or by transfer of Cu^{II} ion (reaction 2), we have performed similar studies, but using C_2N-HST (cf. **Chapter I**) instead of N3-HST as starting compound.

IV.2.3. Indirect insertion of copper ions into HST via a simpler precursor C_2N-HST

IV.2.3.1. Reactions between C_2N-HST and $Cu(NO_3)_2{\cdot}2.5H_2O$ or $Cu(N3)(NO_3)_2$

IV.2.3.1.1. Synthesis

The reaction conditions were similar to the ones used before (paragraph **IV.2.2.2.1**). C_2N-HST was reacted with a small excess (110 mol % with respect to C_2N-HST) aqueous solution of $Cu(NO_3)_2{\cdot}2.5H_2O$ or of the complex $CuN3(NO_3)_2$ via microwave irradiation (80 °C, 0.5 h). After reactions, a green solid (green solid-2) and a blue solid (blue solid-2) were obtained respectively.

IV.2.3.1.2. XRD analysis

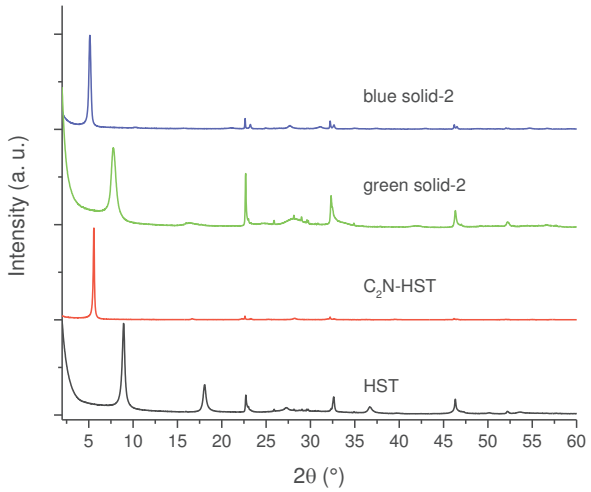

Figure IV.31. *Powder XRD patterns of HST, C_2N-HST, green solid-2 and blue solid-2.*

Figure IV.31 shows the XRD patterns of HST, C_2N-HST, green solid-2 and blue solid-2. Comparing the pattern of green solid-2 with that of C_2N-HST, the interlayer distance decreases from 1.58 nm to 1.15 nm (close to the interlayer distance of the green solid obtained from N3-HST (1.25 nm)) and there is an obvious reduced crystallinity (but better than the one of the green solid obtained from N3-HST (***Figure IV.7***)). Comparing the diffractogram of blue solid-2 with that of C_2N-HST, the interlayer distance increases from 1.58 nm to 1.74 nm (very close to the interlayer distance of the blue solid obtained from N3-HST (1.76 nm)). In both solids, the reflections, which are assigned to (100) and (110) in the XRD pattern of HST, are observed at the same positions (22.68° and 32.59°, respectively), in the obtained products. As a result, after reactions, the structure of the inorganic perovskite-like slab is retained. According to above analysis, we can see that the reaction products of C_2N-HST with copper nitrate or complex $CuN3(NO_3)_2$ are very similar to the ones obtained from N3-HST.

IV.2.3.1.3. Infrared spectroscopy

The corresponding infrared spectra of C_2N-HST, green solid-2 and blue solid-2 are shown in ***Figure IV.32***.

Comparing the spectrum of green solid-2 with that of C_2N-HST, the disappearance of the bands at 1584 cm^{-1}, 1543 cm^{-1} and 1400 cm^{-1}, which come from protonated C_2N in the interlayer space of HST, is observed. This suggests the removal of C_2N during the generation process of green solid-2, just like the ligand N3 was removed when using N3-HST. The remaining band at 1621 cm^{-1} may come from water or come from partly remaining C_2N and the band at 1380 cm^{-1} is still unidentified.

Comparing the spectrum of blue solid-2 with that of C_2N-HST, we can observe the disappearance of bands at 1584 cm^{-1}, 1543 cm^{-1} and 1400 cm^{-1}, which are believed to come from protonated C_2N in the interlayer space of HST and the appearance of bands at 3241 cm^{-1}, 3155 cm^{-1}, 2930 cm^{-1}, 2867 cm^{-1} and 1153 cm^{-1}, which have been described in the spectrum of blue solid (cf. ***Figure IV.8***). As a result, during the reaction process, ethylamine in interlayer space of HST has been replaced by the complex $CuN3^{2+}$.

According to the above analyses, C_2N-HST can also be used as precursor to immobilize copper ions.

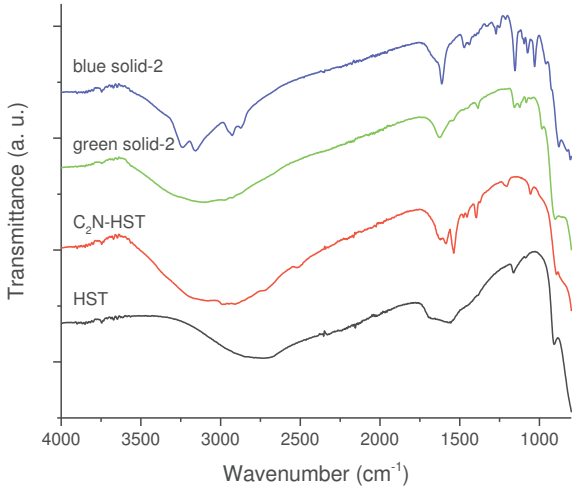

Figure IV.32. *Infrared spectra of HST, C_2N-HST, green solid-2 and blue solid-2.*

The absence of the signal of nitrate, which presents a very intense absorption at 1308 cm^{-1}, in both infrared spectra of green solid-2 and blue solid-2, is noteworthy. Taking into account the charge balance, the above fact indicates that there is a cation exchange reaction between Cu (II) and the proton on the interlayer surface of HST during both reactions.

IV.2.3.1.4. UV-Visible absorption spectroscopy

Figure IV.33 shows the solid-state UV-Vis. spectra of C_2N-HST, green solid-2 and blue solid-2. There is an absorption signal at 779 nm in the spectra of green solid-2 and an absorption signal at 643 nm in that of blue solid-2. This provides a new evidence to prove the high degree of similarity of the reaction products obtained by using the two different precursors C_2N-HST and N3-HST.

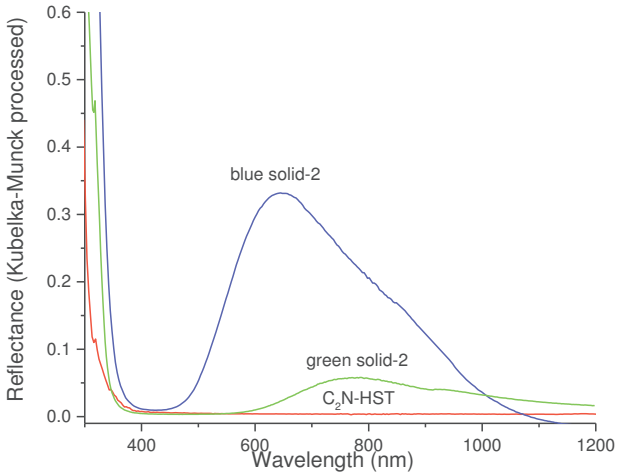

Figure IV.33. *Solid-state UV-Vis. spectra of C_2N-HST, green solid-2 and blue solid-2.*

IV.2.3.1.5. Elemental analysis and proposed formulae

The results of elemental analyses (**Annex**) for green solid-2 and blue solid-2 as well as the previous observations above allow to propose consistent formulae: $Cu_{0.30}H_{1.40}Bi_{0.1}Sr_{0.85}Ta_2O_7{\cdot}4H_2O$ for green solid-2 and $Cu_{0.38}(C_6N_3H_{17})_{0.37}H_{1.24}Bi_{0.1}Sr_{0.85}Ta_2O_7{\cdot}2H_2O$ for blue solid-2.

According to the elemental analysis obtained for green solid-2, all the ethylamine in the interlayer space has been removed .The molar ratio between copper ion and HST is 0.30 which is much smaller than that of green solid obtained by using N3-HST as a precursor (0.60). We do not have any explanation at this stage for this difference.

According to the elemental analysis obtained for blue solid-2, a formula without ethylamine can be proposed. The molar ratio between copper ion and N3 is 1, which is very accordable to the formula of the complex $CuN3(NO_3)_2$. And the molar ratio between copper ion and HST is 0.38 which is almost as same as that of blue solid obtained by using N3-HST as a precursor (0.35).

IV.2.3.2. Study of the mechanism: influence of the quantity of $Cu(NO_3)_2{\cdot}2.5H_2O$

IV.2.3.2.1. Synthesis

In order to study the effect of the quantity of copper nitrate on the reaction products, we have prepared a series of comparative experiments by using the quantity of copper nitrate as a variable, using C_2N-HST as precursor and under same reaction conditions (microwave irradiation, 80 °C and 0.5 h). The reaction conditions and first experimental observations are summarized in ***Table IV.7***.

Precursor	C_2N-HST (50 mg; 0.077 mmol) ($(C_2N)_{0.8}$-HST *i. e.* 0.061 mmol of C_2N)				
Reactant	Solution of $Cu(NO_3)_2 \cdot 2.5H_2O$ in water				
Mixture	**I**	**II**	**III**	**IV**	**V**
[Cu(II)] (mol/L)	0.001	0.003	0.006	0.009	0.015
Vol. (mL)	6				
$n_{Cu(II)}$ (mmol)	0.006	0.018	0.036	0.054	0.090
pH (before)	5.3	5.2	5.2	5.0	5.0
Color (before)	Light green				
pH (after)	6.5	6.3	3.9	3.5	3.2
Color (after)	Colorless		Light green		
Color of the obtained solid	Green				

Table IV.7. *Reaction conditions and first experimental observations ("before": the solution before the addition of C_2N-HST; "after": the filtrate after reaction with C_2N-HST and centrifugation of the solid).*

According to the above table, the pH of copper nitrate solutions before reaction with C_2N-HST is around 5 and the pH of the corresponding filtrates after reaction with C_2N-HST decreases from about 6 to about 3 along with the increase of the quantity of copper nitrate. When the molar amount of copper nitrate is less than 0.018 mmol, the filtrates are colorless. When the molar amount of copper nitrate is more than 0.036 mmol, the filtrates are light green, which indicates the occurrence of a plateau in the insertion phenomenon. Finally, we always obtain green solids whatever the quantity of copper nitrate involved.

IV.2.3.2.2. XRD analysis

The obtained products have been characterized by powder XRD (***Figure IV.34***). The interlayer distance of reaction products decreases from that of C_2N-HST (1.58 nm) to about 1.4 nm and finally to about 1.1 nm along with the increase of the solution concentration. For very low quantity of copper nitrate (0.006 mmol), a biphasic compound is obtained, with interlayer distances of about 1.4 nm and 1.1 nm. When the molar quantity of copper nitrate is between 0.018 mmol and 0.090 mmol, we always obtain products with interlayer distance about 1.1 nm. In addition, in the XRD pattern of all the reaction products, the reflections, which are assigned to (100) and (110) in the XRD pattern of HST, are observed at the same positions in the obtained products, indicating the preservation of the structure of the inorganic perovskite-like layers.

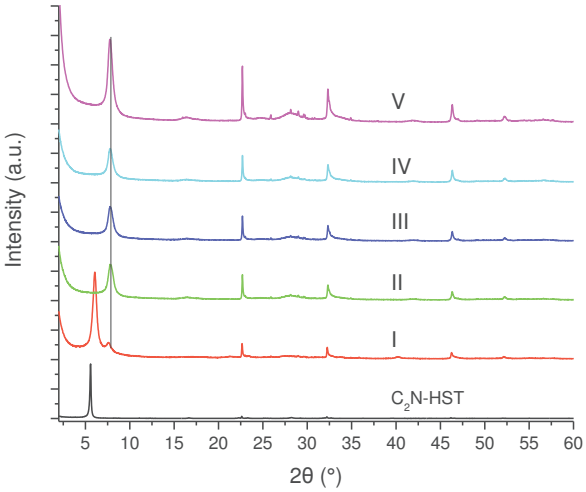

Figure IV.34. *PXRD pattern of C_2N-HST and its reaction products with different quantities of copper nitrate (I: 0.006 mmol; II: 0.018 mmol; III: 0.036 mmol; IV: 0.054 mmol; V: 0.090 mmol) according to the conditions presented in* ***Table IV.7****.*

IV.2.3.2.3. Infrared spectroscopy

Figure IV.35 shows the corresponding IR spectra. Comparing the spectra of the reaction products with that of C_2N-HST, the disappearance of the bands at 1584 cm^{-1}, 1543 cm^{-1} and 1400 cm^{-1}, which come from protonated C_2N in the interlayer space of HST, is clearly observed. When the quantity of copper nitrate is 0.006 mmol, we can clearly observe the signals of protonated C_2N but with reduced intensities. The above fact indicates the removal of C_2N from precursor C_2N-HST during the reaction processes. The remaining band at 1621 cm^{-1} may come from water or come from partly remaining C_2N and the band at 1380 cm^{-1} is unindentified. In addition, the absence of the signal of nitrate, which presents a very intense absorption at 1308 cm^{-1}, indicates that there is a cation exchange reaction between Cu (II) and the proton on the interlayer surface of HST during the insertion reaction.

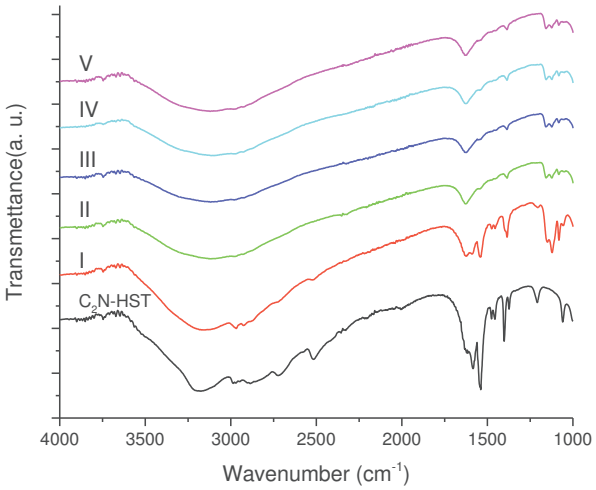

Figure IV.35. *Infrared spectra of C_2N-HST and its reaction products with different quantities of copper nitrate (I: 0.006 mmol; II: 0.018 mmol; III: 0.036 mmol; IV: 0.054 mmol; V: 0.090 mmol) according to the conditions presented in* ***Table IV.7****.*

IV.2.3.2.4. UV-Vis. absorption spectroscopy and elemental analysis

The corresponding solid-state UV-Vis. spectra of the reaction products are displayed in ***Figure IV.36***. They show an absorption signal at about 778 nm, whatever the initial amount of copper nitrate.

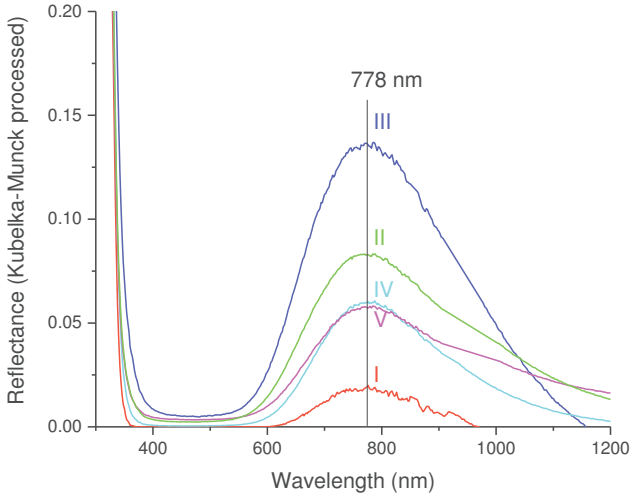

Figure IV.36. *Solid-state UV-Vis. spectra of the reaction products between C_2N-HST and different quantities of copper nitrate (I: 0.006 mmol; II: 0.018 mmol; III: 0.036 mmol; IV: 0.054 mmol; V: 0.090 mmol) according to the conditions presented in* ***Table IV.7****.*

In addition, the corresponding liquid-state UV-Vis. absorption spectra of the filtrates obtained after reactions were recorded (***Figure IV.37***) and compared to the spectra of the starting $Cu(NO_3)_2$ solutions (***Figure IV.22***). When the initial quantity of copper nitrate is

between 0.006 mmol (1 mM) and 0.018 mmol (3 mM), there is not absorption at 812 nm in the corresponding filtrates. That means the concentration of copper in the filtrates is zero or at least negligible. This is a strong evidence to prove the transfer of copper ions from solution to the interlayer space of HST. When the initial quantity of copper nitrate is more than 0.018 mmol (3 mM), the intensity of the signal at 812 nm increases along with the increase of the initial quantity of copper nitrate. This indicates that the transfer has reached a state of saturation.

In the present case, the absorption band of nitrate at 300 nm is not masked by the released C_2N amine. And it is noteworthy that the intensity of this band is identical before and after the reaction, whatever the initial quantity of copper nitrate. This proves that there is not transfer of nitrate ion from solution to the solid hybrid products. This further indicates the hypothesis of cation exchange reaction.

Finally, there is no evidence in the filtrates of the formation of a complex between released C_2N amine and unreacted Cu(II) ions. This is due to the low pH at the end of the reaction (***Table IV.7***).

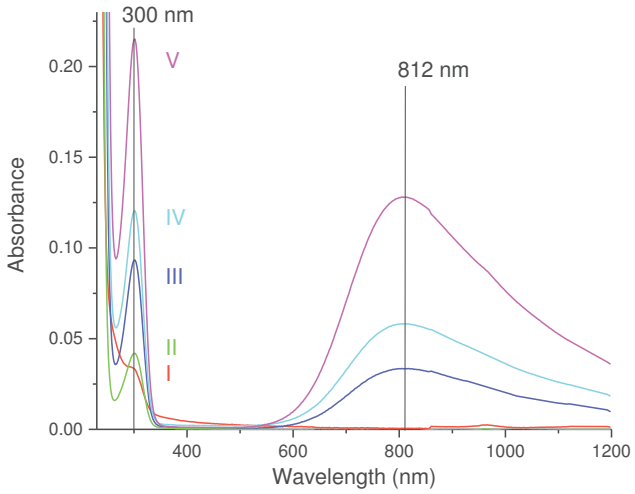

Figure IV.37. *Liquid-state UV-Vis. spectra of the filtrates obtained after the reactions between C_2N-HST and different quantities of copper nitrate (I: 0.006 mmol; II: 0.018 mmol; III: 0.036 mmol; IV: 0.054 mmol; V: 0.090 mmol) according to the conditions presented in* ***Table IV.7****.*

Combining ***Figure IV.37*** and ***Figure IV.22***, quantitative calculations have been made to analyze the composition of the obtained solids (***Table IV.8*** and ***Figure IV.37***).

Precursor	C_2N-HST (50 mg; 0.077 mmol) ($(C_2N)_{0.8}$-HST *i. e.* 0.061 mmol of C_2N)				
Reactant	Solution of $Cu(NO_3)_2{\cdot}2.5H_2O$ in water				
Mixture	**I**	**II**	**III**	**IV**	**V**
[Cu(II)] (mmol/L)	1	3	6	9	15
$n_{Cu(II)}$ (mmol)	0.006	0.018	0.036	0.054	0.090
Number of equivalents of Cu(II) with respect to C_2N-HST	0.078	0.23	0.47	0.70	1.17
$[Cu^{2+}]$ in the filtrate (mmol/L) / n (mmol)	0 0	0 0	2.9 1.7×10^{-2}	5.1 3.0×10^{-2}	11.1 6.7×10^{-2}
Ratio n_{NO3-} in the filtrate / n_{NO3-} initial	220 %*	93 %	100 %	89 %	96 %
Color of the hybrid solid	Green				
Estimated Cu content in the obtained solids per HST unit	$Cu_{0.08}$	$Cu_{0.23}$	$Cu_{0.25}$	$Cu_{0.31}$	$Cu_{0.30}$

Table IV.8. *Analysis of the filtrates of the reactions between C_2N-HST and various concentrations of $Cu(NO_3)_2{\cdot}2.5H_2O$. The copper content of the solids is estimated considering the element conservation. *This value is obviously overestimated because of the large error induced by the overlap of the nitrate band with the ammonium absorption band at higher energy.*

The results presented in ***Table IV.8*** show that the content of copper gradually increases along with the increase of the initial quantity of copper nitrate until 0.054 mmol. When the initial quantity of copper nitrate is higher than 0.054 mmol (0.7 eq with respect to C_2N-HST), we observe that the copper content in the final solid reaches a plateau, around 0.3 Cu per HST unit.

It is noteworthy that the nitrate ions essentially remain in solution, confirming the process of insertion of a cationic species by cation exchange between copper and ammonium.

Finally, elemental micro-analyses (C, H, N) and energy-dispersive X-ray spectroscopy have been performed on the obtained solids. The estimated formulae of the obtained products are estimated and collected in ***Table IV.9***.

Reaction	**EDX**	**Micro-analysis**			**Formula**
	n_{Cu} / n_{Ta}	**C (mass %) Exp (calcd)**	**H (mass %) Exp**	**N (mass %) Exp (calcd)**	
I	0.02	1.14 (0.90)	0.94	0.53 (0.53)	$Cu_{0.04}$-$(C_2N)_{0.22}$-HST
II	0.08	0.25 (0)	0.68	0.00 (0)	$Cu_{0.16}$-$(C_2N)_0$-HST
III	0.08	0.40 (0)	0.63	0.00 (0)	$Cu_{0.16}$-$(C_2N)_0$-HST
IV	0.09	0.40 (0)	0.63	0.00 (0)	$Cu_{0.18}$-$(C_2N)_0$-HST
V	0.10	0.23 (0)	0.68	0.00 (0)	$Cu_{0.20}$-$(C_2N)_0$-HST

Table IV.9. *Results of micro-analysis (C, H, N) and EDX spectroscopy of the reaction products between C_2N-HST and different quantities of copper nitrate (I: 0.006 mmol; II: 0.018 mmol; III: 0.036 mmol; IV: 0.054 mmol; V: 0.090 mmol) according to the conditions presented in **Table IV.7**. Considering the unknown water content parameter, and the very low quantity of H, this H content was not taken into account. The proposed formulae are only based on Cu, C and N analyses.*

According to the above table, the content of copper gradually increases along with the increase of the initial copper nitrate quantity (***Figure IV.38***) until a plateau after about 0.018 mmol (0.47 eq with respect to C_2N-HST). Ethylamine has been totally removed from the interlayer spacing upon insertion of copper cations. In the case of reaction I, elemental

analysis shows the residual presence of ethylamine, which is in accordance with the multiphasic character of the compound (***Figure IV.34***).

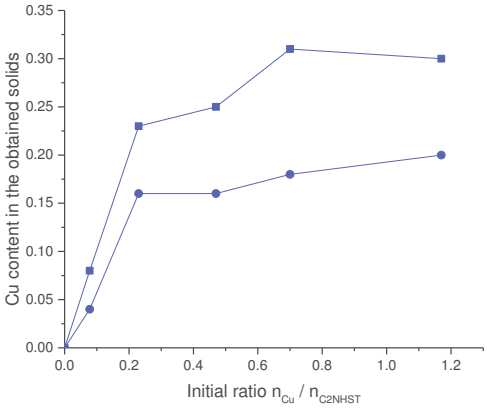

Figure IV.38. *Estimated composition of the solids obtained after the reactions between C_2N-HST and different quantities of copper nitrate according to the conditions presented in* ***Table IV.7*** *(blue squares: quantity of Cu from UV-Vis. spectroscopy of the filtrates; blue circles: quantity of Cu from EDX analysis) (full lines are just guide for the eye).*

IV.2.3.2.5. Proposed mechanism

The mechanism which can be proposed here is very similar to the one leading to the formation of the green solid from N3-HST and copper nitrate. The experiments realized here confirm the cation exchange between Cu^{II} and ethylammonium, without insertion of nitrate. For the sake of clarity, the nomenclature is slightly modified to precise the protonation state of HST and of C_2N.

$Cu(NO_3)_2 + (C_2NH)_2$-ST → Cu-ST + 2 C_2NH^+ + 2 NO_3^-

A similar method to introduce copper into a Dion-Jacobson phase $HLaNb_2O_7$ has been reported by means of the reaction between copper nitrate solution and a precursor ($HLaNb_2O_7$ intercalated by n-octylamine).[31] This reaction was taken as a monovalent ion exchange reaction since the Cu^{2+} was introduced in the form of $Cu(NO_3)^+$ or $Cu(OH)^+$.

IV.2.3.3. Study of the mechanism: influence of the quantity of CuN3

IV.2.3.3.1. Synthesis

The same series of experiments was performed using the preformed $CuN3(NO_3)_2$ complex, C_2N-HST as precursor and under same reaction conditions (microwave irradiation, 80 °C and 0.5 h). The reaction conditions and first experimental observations are summarized in ***Table IV.10***.

Precursor	C_2N-HST (50 mg; 0.077 mmol) ($(C_2N)_{0.8}$-HST *i. e.* 0.061 mmol of C_2N)					
Reactant	Solution of $CuN3(NO_3)_2$ in water					
Mixture	**VI**	**VII**	**VIII**	**IX**	**X**	**XI**
[Cu(II)] (mol/L)	0.001	0.003	0.004	0.006	0.009	0.015
Vol. (mL)	6					
$n_{Cu(II)}$ (mmol)	0.006	0.018	0.024	0.036	0.054	0.090
pH (before)	9.0	9.1	9.3	9.4	9.3	9.4
Color (before)	Blue					
pH (after)	9.0	9.0	8.6	8.9	8.5	9.1
Color (after)	Colorless			Blue		
Color of the obtained solid	Green	Blue				

Table IV.10. *Reaction conditions and first experimental observations ("before": the solution before the addition of C_2N-HST; "after": the filtrate after reaction with C_2N-HST and centrifugation of the solid).*

Like when using copper nitrate, the filtrates at the end of the reaction are colorless when the quantity of copper is low (below 0.024 mmol). This indicates the transfer of $CuN3^{2+}$ complex or of copper ions from the solution to the precursor N3-HST. Interestingly, when the $CuN3(NO_3)_2$ quantity is very small (0.006 mmol), the obtained solid is green, suggesting a decomplexation of the inserted copper ions.

IV.2.3.3.2. XRD analysis

Figure IV.39 shows the XRD pattern of C_2N-HST and its reaction products with quantities of $CuN3(NO_3)_2$. After reactions, the interlayer distance increases from that of C_2N-HST (1.58 nm) to about 1.6 nm and finally to about 1.74 nm along with the increase of the solution concentration.

As seen from the first observations in ***Table IV.10***, the compound **VI** (obtained when the quantity of $CuN3(NO_3)_2$ is only 0.006 mmol) is peculiar since its interlayer distance is smaller than that C_2N-HST (about 1.5 nm). Yet, and even if compound **VI** is green, its interlayer distance is still much larger than that of the green-solid.

Finally, for all compounds, the structure of the inorganic perovskite-like slab is retained.

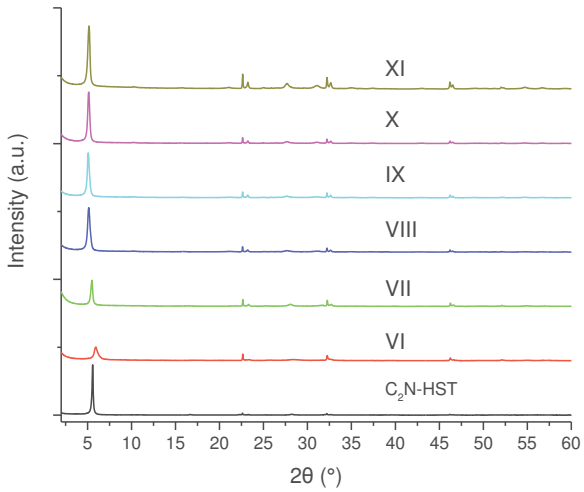

Figure IV.39. *PXRD patterns of C_2N-HST and its reaction products with quantities of $CuN3(NO_3)_2$ (VI: 0.006 mmol; VII: 0.018 mmol; VIII: 0.024 mmol; IX: 0.036 mmol; X: 0.054 mmol; XI: 0.090 mmol) according to the conditions presented in* ***Table IV.10****.*

IV.2.3.3.3. Infrared spectroscopy

The corresponding infrared spectra are presented in ***Figure IV.40***. Comparing the spectra of products with that of C_2N-HST, the gradual disappearance of bands at 1584 cm^{-1}, 1543 cm^{-1} and 1400 cm^{-1}, which come from protonated C_2N in the interlayer space of C_2N-HST is observed. New bands ascribed to the polyamine N3 appear at 3241 cm^{-1}, 3155 cm^{-1}, 2930 cm^{-1} and 2867 cm^{-1} when the quantity of $CuN3(NO_3)_2$ increases.

Therefore, during the reaction process, ethylamine in the interlayer space of C_2N-HST appears to have been replaced by the complex $CuN3^{2+}$.

For compound **VI** (when the quantity of $CuN3(NO_3)_2$ is only 0.006 mmol), we cannot find the signals of the polyamine N3, but the signals of precursor C_2N-HST with reduced intensities. This indicates that compound **VI** is an intermediate compound, in which ethylamine has not been completely removed, and $CuN3^{2+}$ has not been intercalated, only free Cu ions have been intercalated.

Finally, for all compounds, no bands coming from the nitrate ions can be observed. According to the above analyses, the behavior of C_2N-HST with complex $CuN3(NO_3)_2$ is very similar to the one of N3-HST as a precursor.

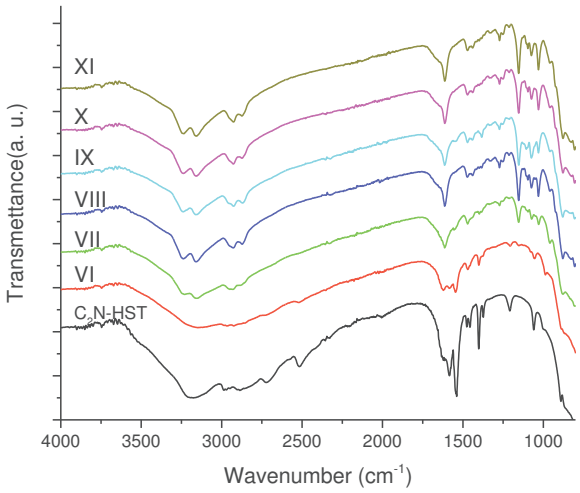

Figure IV.40. *Infrared spectra of C_2N-HST and its reaction products with different quantities of $CuN3(NO_3)_2$ (VI: 0.006 mmol; VII: 0.018 mmol; VIII: 0.024 mmol; IX: 0.036 mmol; X: 0.054 mmol; XI: 0.090 mmol) according to the conditions presented in* ***Table IV.10****.*

IV.2.3.3.4. UV-Vis. absorption spectroscopy and elemental analysis

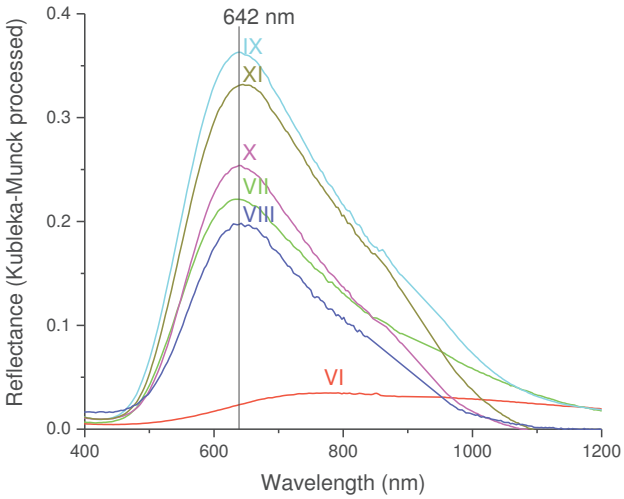

Figure IV.41. *Solid-state UV spectra of the reaction products between C_2N-HST with different quantities of $CuN3(NO_3)_2$ (VI: 0.006 mmol; VII: 0.018 mmol; VIII: 0.024 mmol; IX: 0.036 mmol; X: 0.054 mmol; XI: 0.090 mmol) according to the conditions presented in* ***Table IV.10****.*

Figure IV.41 shows the solid-state UV spectra of the reaction products. There is always an absorption signal at 640 nm when the quantity of $CuN3(NO_3)_2$ is larger than 0.006 mmol, which indicates the presence of a $CuN3^{2+}$complex within the hybrid solid. Compound **VI** presents clearly absorption around 800 nm. Yet, all the other compounds present a small shoulder around 800 nm, difficult to quantify, which likely indicates the presence of uncoordinated Cu(II) ions.

Figure IV.42 shows the liquid-state UV-Vis. spectra of the filtrates obtained after the reactions. When the initial quantity of $CuN3(NO_3)_2$ in solution is below 0.024 mmol (4 mM) there is no absorption of $CuN3(NO_3)_2$ in the corresponding filtrates which indicates the transfer of copper ions or $CuN3^{2+}$ complex from the solution to the interlayer space of HST. When the initial quantity of $CuN3(NO_3)_2$ is larger than 0.036 mmol, the intensity of the signal at 619 nm increases along with the increase of the initial quantity of $CuN3(NO_3)_2$. This indicates that the transfer has reached a state of saturation.

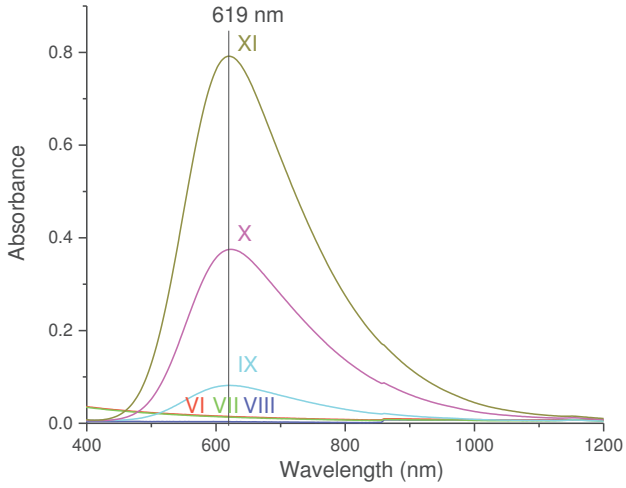

Figure IV.42. *Liquid-state UV spectra of the filtrates obtained after the reactions between C_2N-HST with different quantities of $CuN3(NO_3)_2$ (VI: 0.006 mmol; VII: 0.018 mmol; VIII: 0.024 mmol; IX: 0.036 mmol; X: 0.054 mmol; XI: 0.090 mmol) according to the conditions presented in* ***Table IV.10****.*

Combining ***Figure IV.42*** and ***Figure IV.23***, quantitative calculations have been made to analyze the composition of the obtained solids (***Table IV.11*** and ***Figure IV.43***).

Precursor	C_2N-HST (50 mg; 0.077 mmol) ($(C_2N)_{0.8}$-HST *i. e.* 0.061 mmol of C_2N)					
Reactant	S Solution of $CuN3(NO_3)_2$ in water (6 mL)					
Mixture	**VI**	**VII**	**VIII**	**IX**	**X**	**XI**
[Cu(II)] (mmol/L)	1	3	4	6	9	15
$n_{Cu(II)}$ (mmol)	0.006	0.018	0.024	0.036	0.054	0.090
Number of equivalents of Cu(II) with respect to C_2N-HST	0.078	0.23	0.31	0.47	0.70	1.17
[Cu^{2+}] in the filtrate (mmol/L) / n (mmol)	0 0	0 0	0 0	0.94 5.6×10^{-3}	4.31 2.6×10^{-2}	9.09 5.5×10^{-2}
Color of the hybrid solid	Green	Blue				
Estimated Cu content in the obtained solids per HST unit	$Cu_{0.08}$	$Cu_{0.23}$	$Cu_{0.31}$	$Cu_{0.39}$	$Cu_{0.36}$	$Cu_{0.45}$

Table IV.11. *Analysis of the filtrates of the reactions between C_2N-HST and various concentrations of $CuN3(NO_3)_2 \cdot 2.5H_2O$. The copper content of the solids is estimated considering the element conservation.*

The results presented in ***Table IV.11*** show that the content of copper gradually increases along with the increase of the initial quantity of $CuN3(NO_3)_2$ until 0.036 mmol. When the initial quantity of copper nitrate complex is higher than 0.036 mmol (0.47 eq with respect to C_2N-HST), we observe that the copper content in the final solid reaches a plateau, around 0.4 Cu per HST unit.

Finally, elemental micro-analyses (C, H, N) and energy-dispersive X-ray spectroscopy have been performed on the obtained solids. The estimated formulae of the obtained products are estimated and collected in ***Table IV.12***.

Reaction	EDX	Micro-analysis			Formula
	n_{Cu} / n_{Ta}	C (mass %) Exp (calcd)	H (mass %) Exp	N (mass %) Exp (calcd)	
VI	0.04	2.19 (2.01)	1.32	1.29 (1.17)	$Cu_{0.08}$-$(C_2N)_{0.50}$ -HST
VII	0.10	3.22 (3.36)	1.45	1.79 (1.96)	$Cu_{0.20}$-$(N3)_{0.29}$-HST
VIII	0.13	3.95 (3.99)	1.56	2.05 (2.32)	$Cu_{0.26}$-$(N3)_{0.35}$-HST
IX	0.18	3.98 (3.95)	1.58	2.19 (2.30)	$Cu_{0.36}$-$(N3)_{0.35}$-HST
X	0.19	4.14 (4.15)	1.54	2.23 (2.42)	$Cu_{0.38}$-$(N3)_{0.37}$-HST
XI	0.19	4.16 (4.15)	1.56	2.31 (2.42)	$Cu_{0.38}$-$(N3)_{0.37}$-HST

Table IV.12. *Results of micro-analysis (C, H, N) and EDX spectroscopy of the reaction products between C_2N-HST and different quantities of $CuN3(NO_3)_2$ (VI: 0.006 mmol; VII: 0.018 mmol; VIII: 0.024 mmol; IX: 0.036 mmol; X: 0.054 mmol; XI: 0.090 mmol) according to the conditions presented in* ***Table IV.10****. Considering the unknown water content parameter, and the very low quantity of H, this H content was not taken into account. The proposed formulae are only based on Cu, C and N analyses.*

According to the above table, we can clearly observe that the content of copper gradually increase along with the increasing of molar amount of $CuN3(NO_3)_2$ until 0.036 mmol. On the contrary, the content of polyamine is a constant (the molar ratio between N3 and HST is about 0.3) whatever the initial quantity of $CuN3(NO_3)_2$. One noticeable exception concerns compound **VI** for which shows only very reduced Cu insertion, and no polyamine N3. The amount of C_2N amine is about 0.5, compared to 0.8 in the starting C_2N-HST.

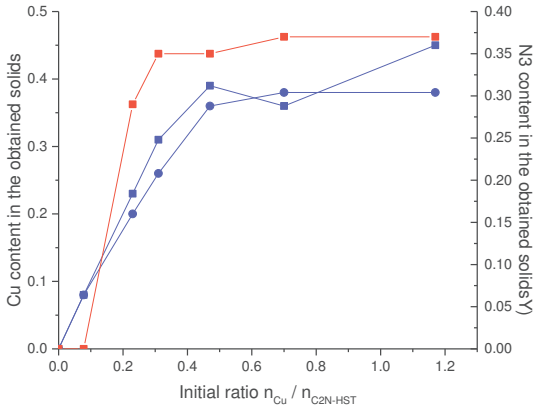

Figure IV.43. *Estimated composition of the solids obtained after the reactions between C_2N-HST and different quantities of $CuN3(NO_3)_2$ according to the conditions presented in* ***Table IV.10*** *(red squares : quantity of N3 (from elemental analysis); blue squares : quantity of Cu (from UV-Vis. spectroscopy of the filtrates); blue circles : quantity of Cu (from EDX analysis)) (full lines are just guide for the eye).*

IV.2.3.3.5. Proposed mechanism

The mechanism which can be proposed here is very similar to the one leading to the formation of the blue solid from N3-HST and $CuN3(NO_3)_2$ complex, for which two hypothesis were proposed (paragraph **IV.2.2.4.5**)

(1) $CuN3(NO_3)_2$ + N_3H_2-ST → CuN3-ST + N3 + 2 H^+ + 2 NO_3^-

(2) $CuN3(NO_3)_2$ + N_3H_2-ST → CuN3-ST + N3 + 2 H^+ + 2 NO_3^-

Here the mechanism is simpler:

$CuN3(NO_3)_2$ + $(C_2NH)_2$-ST → CuN3-ST + 2 C_2NH^+ + 2 NO_3^-

The fact that it is possible to insert $CuN3^{2+}$ complex even when using C_2N-HST as precursor is a good indication in favor of hypothesis (1) when N3-HST is used. The whole $CuN3^{2+}$ complex

is inserted, not a Cu^{2+} transfer. Yet the fact that we have observed (compound VI) the insertion of only Cu^{2+} into C_2N-HST, with partial removal of C_2NH^+ and no insertion of N3 ligand suggests that the problem is probably more complex, and that the two hypotheses may coexist. Only labelling of the ligand may solve the question.
Finally, the last part of this chapter will deal with preliminary experiments that have been done using Ni(II) instead of Cu(II) and with the synthesis and characterization of HST functionalized with other ligands designed to coordinate transition metal ions.

IV.2.4. Indirect insertion of nickel ions into HST via a precursor N3-HST

IV.2.4.1. Synthesis

As previously with copper, two different reactions using N3-HST were performed, one with $Ni(NO_3)_2{\cdot}6H_2O$, the other with the complex $NiN3(NO_3)_2$. The complex $NiN3(NO_3)_2$ is made by adding drop by drop one equivalent of an aqueous solution of N3 to an aqueous solution of $Ni(NO_3)_2{\cdot}6H_2O$ at room temperature. The obtained mixture is stirred during 10 minutes and used without further purification. N3-HST was reacted with a small excess (115 mol % with respect to N3-HST) of aqueous solution of $Ni(NO_3)_2{\cdot}6H_2O$ or of the complex $NiN3(NO_3)_2$ via microwave irradiation (80 °C, 0.5 h). After reactions, two products, solid I (light green) and solid II (light blue), were obtained, respectively.

IV.2.4.2. XRD analysis

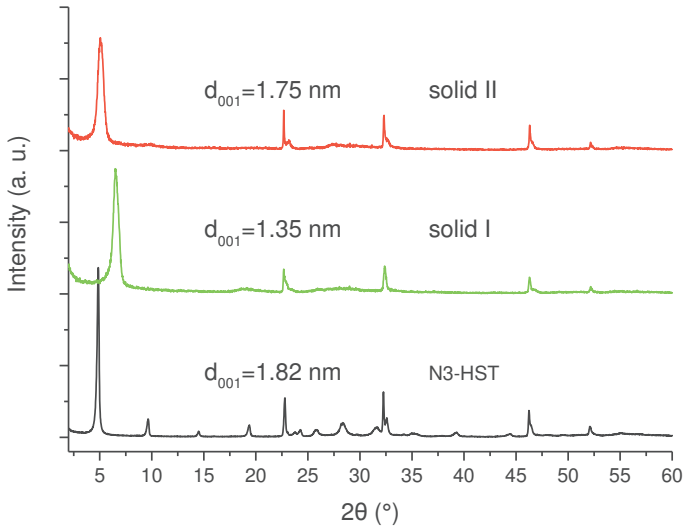

Figure IV.44. *Powder XRD patterns of N3-HST, solid I (reaction between N3-HST and aqueous solution of $Ni(NO_3)_2{\cdot}6H_2O$) and solid II (reaction between N3-HST and aqueous solution of the complex $NiN3(NO_3)_2$).*

The powder XRD patterns of N3-HST, solid I and solid II are shown in ***Figure IV.44***. Comparing the diagram of solid I with that of N3-HST, the interlayer distance decreases from 1.82 nm to 1.35 nm, and the crystallinity is slightly reduced. Comparing the diagram of solid II and that of N3-HST, the interlayer distance only slightly decreases from 1.82 nm to 1.75 nm. In both solids, the reflections, which are assigned to (100) and (110) in the XRD pattern of HST, are observed at the same positions (22.68° and 32.59°, respectively) in the obtained products,

indicating the preservation of the structure of the inorganic perovskite-like slab is retained. Finally, the XRD patterns of solid I and solid II are very similar to those of the green and blue solids respectively. This suggests similar behaviors for copper and nickel ions (free or complexed) towards insertion into N3-HST.

IV.2.4.3. Infrared spectroscopy

The corresponding infrared spectra are displayed in ***Figure IV.45***. Comparing the spectra of solid I with that of N3-HST, it is clear to observe the reduced intensity of bands at 1567 cm^{-1}, 1543 cm^{-1} and 1466 cm^{-1}, which correspond the protonated N3 in the interlayer space of HST. This indicates the removal of N3 during the generation process of solid I.
Comparing the spectra of solid II with that of N3-HST, the disappearance of bands at 1567 cm^{-1} and 1543 cm^{-1} (which were attributed to $-NH_3^+$ group deformation vibrations) is observed. In addition, new bands appear at 3241 cm^{-1} and 3155 cm^{-1} (which are due to N-H stretching of $-NH_2$ group) and 2930 cm^{-1} and 2867 cm^{-1} (masked in N3-HST, and attributed to antisymmetric and symmetric stretching vibrations of CH_2 groups). By analogy with the blue solid in the case of copper, and according to the above analyses, the deprotonation and the retention of polyamine N3 in solid II is proposed.
Finally, no signal coming from nitrate is observed in solid I or in solid II, indicating a similar process of cation exchange between Ni^{2+} or $NiN3^{2+}$ and the $N3H_2^{2+}$ in N3-HST.

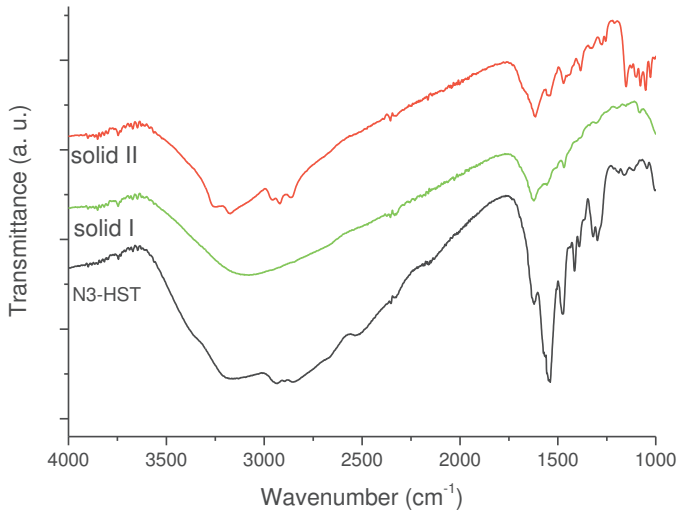

Figure IV.45. *Infrared spectra of N3-HST, solid I (reaction between N3-HST and aqueous solution of* $Ni(NO_3)_2{\cdot}6H_2O$ *) and solid II (reaction between N3-HST and aqueous solution of the complex* $NiN3(NO_3)_2$*).*

IV.2.4.4. SEM observations and EDX analysis

The SEM images of solid I and solid II are shown on ***Figure IV.46***. Solid I and solid II present very similar platelet-like morphology. In addition the crystallites have similar size for all the compounds. Finally, energy-dispersive X-ray spectroscopy (EDX) shows that the Ni/Ta_2 ratio is about 0.2 for solid I and about 0.3 for solid II.

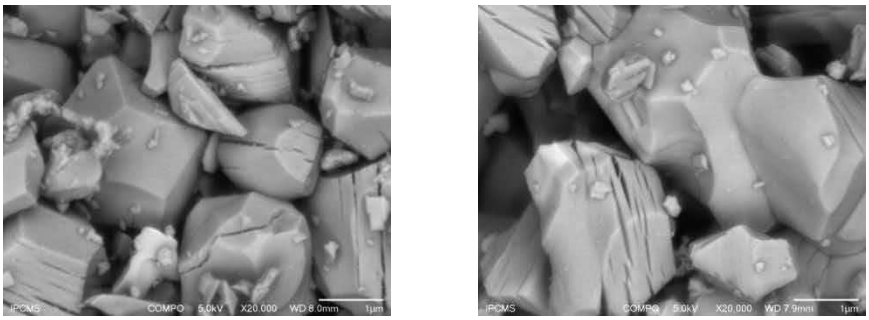

Solid I *Solid II*

Figure IV.46. *SEM images of solid I and solid II (the scale bars represent 1 µm).*

IV.2.5. Preparation of other precursors

In order to expand the application scope of the above simple approach to other metal ions, several different precursors have been synthesized. The selected molecules are as follows: N,N'-bis(3-aminopropyl)-ethylenediamine (N4), 4-(2-aminoethyl)pyridine (PA) (synthetized according to a published procedure[32]) and N,N',N'',N'''-tetra(3-aminopropyl)-1,4,8,11-tetra-azacyclotetradecane (cyclam$(NH_2)_4$)(prepared according to literature protocol[33-36]) (***Scheme IV.2***).

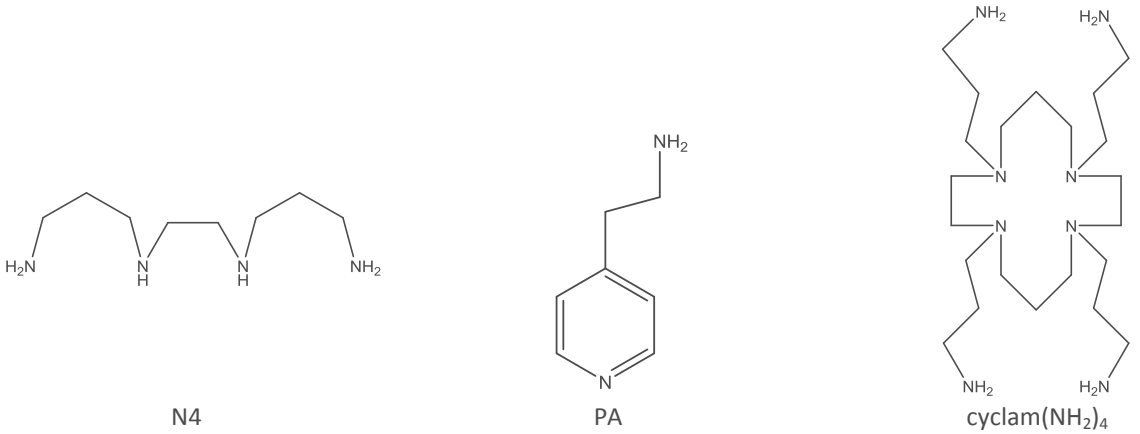

N4 PA cyclam$(NH_2)_4$

Scheme IV.2. *N,N'-bis(3-aminopropyl)-ethylenediamine (N4), 4-(2-aminoethyl)-pyridine (PA) and N,N',N'',N'''-tetra(3-aminopropyl)-1,4,8,11-tetra-azacyclotetradecane (cyclam$(NH_2)_4$).*

IV.2.5.1. Synthesis

The microwave assisted (130°C, 1 h) insertion reaction was performed using a large excess of amines with respect to C_2N-HST (*ca.* ×200 for N4 or PA and *ca.* ×10 for cyclam$(NH_2)_4$), in a THF/H_2O mixture (5:1 for N4, 1:5 for PA and 4:5 for cyclam, v:v).

IV.2.5.2. XRD analyses

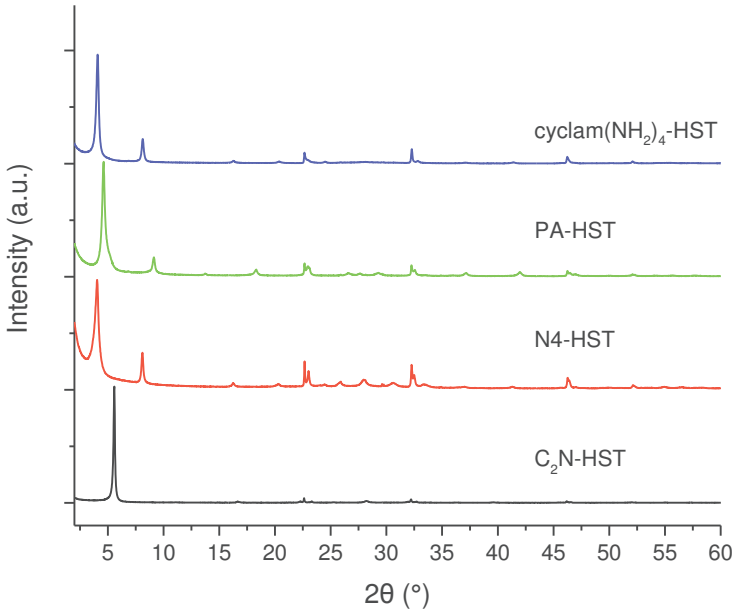

Figure IV.47. *Powder XRD patterns of C_2N-HST and its reaction products with N4, PA and cyclam$(NH_2)_4$, respectively.*

Figure IV.47 shows the XRD patterns of C_2N-HST and its reaction products with amines N4, PA and cyclam$(NH_2)_4$, respectively. After reaction, the (00l) reflections are shifted to lower angles with respect to the ones of C_2N-HST. The increased interlayer distances (2.18 nm, 1.91 nm and 2.16 nm for N4-HST, PA-HST and cyclam$(NH_2)_4$-HST, respectively) of the reaction products strongly indicates the occurrence of intercalation reaction. The interlayer distances of the obtained hybrids N4-HST and cyclam$(NH_2)_4$-HST are in accordance with the calculated value (2.19 nm) using the relationship established for α,ω-diaminoalkanes d (nm) = 1.09 + 0.11 n_C (cf. **Chapter I**) (considering the central nitrogen atoms in N4 and cyclam as carbons). This indicates a pillaring arrangement of N4 and cyclam$(NH_2)_4$. Considering the inertia of pyridine towards HST (cf. **Chapter I**), PA is logically considered as a monoamine with consequently bilayer arrangement. The out of plane reflections, which are assigned to (100) and (110) in the XRD pattern of HST, are observed at the same positions (22.68° and 32.59°, respectively) in the obtained product. This shows that the perovskite-like slab structure has remained essentially unchanged upon insertion.

IV.2.5.3. Infrared spectroscopy

The corresponding infrared spectra are displayed in ***Figure IV.48***. The sharp strong bands between 3400 cm^{-1} and 3200 cm^{-1} due to NH stretching of free $–NH_2$ group are greatly reduced in intensity with respect to the free amines. This analysis confirms the conversion from $–NH_2$ groups to $–NH_3^+$ groups. The bands which appear at around 1560 cm^{-1} in the spectra are ascribed to $–NH_3^+$ deformation vibrations. Unfortunately, no clear evidence of the protonation state of the central amine in N4-HST and cyclam$(NH_2)_4$-HST could be obtained. The absorption around 1600 cm^{-1} clearly observed in the spectrum of PA-HST is attributed to the C-C and C-H vibration of the pyridine moiety.

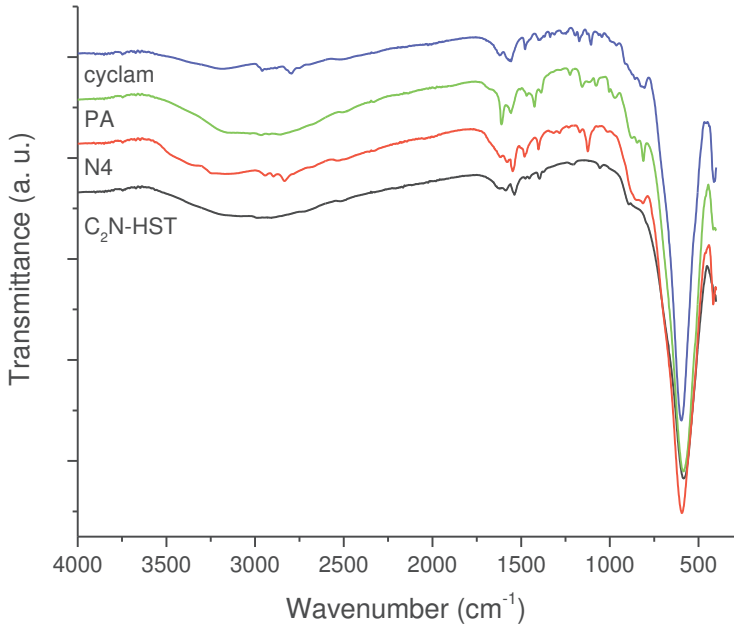

Figure IV.48. *Infrared spectra of C_2N-HST and its reaction products with amines N4, PA and cyclam$(NH_2)_4$, respectively.*

IV.2.5.4. Proposed formulae

According to the results of elemental analyses (C, H, N, *cf.* **Annex**), the formulae of the grafted products are collected in ***Table IV.13***.

Products	Formulae
N4-HST	$(C_8N_4H_{24})_{0.3}H_{1.4}Bi_{0.1}Sr_{0.85}Ta_2O_7{\cdot}1.0H_2O$
PA-HST	$(C_7N_2H_{11})_{0.4}H_{1.6}Bi_{0.1}Sr_{0.85}Ta_2O_7{\cdot}0.9H_2O$
cyclam$(NH_2)_4$-HST	$(C_{20}N_8H_{52})_{0.2}H_{1.2}Bi_{0.1}Sr_{0.85}Ta_2O_7{\cdot}0.5H_2O$

Table IV.13. *Proposed formulae.*

IV.3. Conclusion

A soft-chemistry route for the insertion of paramagnetic metals (Cu(II) and Ni(II)) into layered perovskite HST has been established using organic amines intercalated HST as intermediates. The application scope of this simple approach is being expanded to other metal ions (Co, Mn, Fe, etc.) and to other precursors.

The failure of directly functionalizing HST with copper ions and the successful insertion of copper ions by using N3-HST or C_2N-HST as precursors indicate that the organic amines are necessary but their nature (mono amine, or polyamine potentially coordinating) is not a crucial parameter.

The effect of the ratio between reactants (metal ions or complexes and hybrid precursor) has been studied essentially using UV-Vis. spectroscopy. The mechanism involves cation exchange between the positively charged metal ion or complex and the ammonium inserted in the hybrid precursor.

Using this strategy, perspectives are opened to functionalize HST with various kinds of inorganic complexes, for luminescence or spin-transition for instance. This strategy can also be extended to the functionalization by trivalent cations (Fe^{3+} for example, using HST functionalized by 4-pyridinemethanol (***Scheme IV.3***) as a precursor) and to lanthanides in particular.

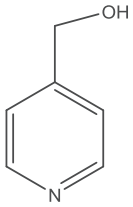

Scheme IV.3. *4-pyridinemethanol.*

Another development of the results obtained in this chapter concerns the use of HST functionalized by "free" metals (such as the green solid). The possibility to insert several different transition metals to obtain heterometallic functionalized hybrids could be studied.
And finally, these systems functionalized by metals may be used to create *in situ* functional coordination networks. One could imagine for instance to connect *in situ* the metals inserted, by an organic ligand (oxalate, dicyanamide…), or by an inorganic complex (hexacyanometallate for instance). In this way it could be possible to build *in situ* a ferromagnetic network, which would then may provide at the end a multiferroic hybrid system.

References

[1] E. C. Subbarao, *J. Phys. Chem. Solids* **1962**, *23*, 665-676.
[2] M. Figlarz, B. Gérand, A. Delahaye-Vidal, B. Dumont, F. Harb, A. Coucou, F. Fievet, *Solid State Ionics* **1990**, *43*, 143-170.
[3] R. E. Schaak, T. E. Mallouk, *Chem. Mater.* **2002**, *14*, 1455-1471.
[4] P. S. Halasyamani, K. R. Poeppelmeier, *Chem. Mater.* **1998**, *10*, 2753-2769.
[5] K. Toda, M. Sato, *J. Mater. Chem.* **1996**, *6*, 1067-1071.
[6] J. Gopalakrishnan, S. Uma, V. Bhat, *Chem. Mater.* **1993**, *5*, 132-136.
[7] J. Gopalakrishnan, V. Bhat, B. Raveau, *Materials Research Bulletin* **1987**, *22*, 413-417.
[8] R. E. Schaak, D. Afzal, J. A. Schottenfeld, T. E. Mallouk, *Chem. Mater.* **2002**, *14*, 442-448.
[9] C. H. Mahler, B. L. Cushing, J. N. Lalena, J. B. Wiley, *Mater. Res. Bull.* **1998**, *33*, 1581-1586.
[10] J. Gopalakrishnan, T. Sivakumar, K. Ramesha, V. Thangadurai, G. N. Subbanna, *J. Am. Chem. Soc.* **2000**, *122*, 6237-6241.
[11] K.-A. Hyeon, S.-H. Byeon, *Chem. Mater.* **1999**, *11*, 352-357.
[12] T. A. Kodenkandath, J. N. Lalena, W. L. Zhou, E. E. Carpenter, C. Sangregorio, A. U. Falster, W. B. Simmons, C. J. O'Connor, J. B. Wiley, *J. Am. Chem. Soc.* **1999**, *121*, 10743-10746.
[13] R. E. Schaak, T. E. Mallouk, *J. Am. Chem. Soc.* **2000**, *122*, 2798-2803.
[14] C. Sanchez, B. Lebeau, F. Chaput, J. P. Boilot, *Adv. Mater.* **2003**, *15*, 1969-1994.
[15] E. Delahaye, S. Eyele-Mezui, M. Diop, C. Leuvrey, P. Rabu, G. Rogez, *Dalton Trans.* **2010**, *39*, 10577-10580.
[16] J. Depas, J. Khaladji, R. Vergoz, *Bull. Soc. Chim. Fr.* **1953**, 1105.
[17] L. Larsson, *Acta Chem. Scand.* **1950**, *4*, 27-38.
[18] K. Nakanishi, T. Goto, M. Ohashi, *Bull. Chem. Soc. Jap.* **1957**, *30*, 403-408.
[19] M.-P. Crosnier-Lopez, F. Le Berre, J.-L. Fourquet, *J. Mater. Chem.* **2001**, *11*, 1146-1151.
[20] S. Tahara, T. Yamashita, G. Kajiwara, Y. Sugahara, *Chem. Lett.* **2006**, *35*, 1292-1293.
[21] D. J. MacLachlan, K. R. Morgan, *J. Phys. Chem. A* **1990**, *94*, 7656-7661.
[22] B. Kamieński, W. Schilf, T. Dziembowska, Z. Rozwadowski, A. Szady-Chełmieniecka, *Solid State Nuclear Magnetic Resonance* **2000**, *16*, 285-289.
[23] Y. Komori, Y. Sugahara, K. Kuroda, *Applied Clay Science* **1999**, *15*, 241-252.
[24] M. Wallau, J. Patarin, I. Widmer, P. Caullet, J. L. Guth, L. Huve, *Zeolites* **1994**, *14*, 402-410.
[25] W. Kolodziejski, J. Klinowski, *Chem. Rev.* **2002**, *102*, 613-628.
[26] A. Pines, M. G. Gibby, J. S. Waugh, *J. Chem. Phys.* **1973**, *59*, 569-590.
[27] M. H. Robbins, R. S. Drago, *Journal of Catalysis* **1997**, *170*, 295-303.
[28] E. Kimura, A. Sakonaka, M. Nakamoto, *Biochimica et Biophysica Acta (BBA) - General Subjects* **1981**, *678*, 172-179.
[29] C. Ziegler, S. Werner, M. Bugnet, M. Wörsching, V. Duppel, G. A. Botton, C. Scheu, B. V. Lotsch, *Chem. Mater.* **2013**, *25*, 4892-4900.
[30] L. Li, R. Ma, Y. Ebina, K. Fukuda, K. Takada, T. Sasaki, *J. Am. Chem. Soc.* **2007**, *129*, 8000-8007.
[31] T. Matsuda, T. Fujita, M. Kojima, *J. Mater. Chem.* **1991**, *1*, 559-562.
[32] T. Steinmetzer, A. Schweinitz, A. Stürzebecher, D. Dönnecke, K. Uhland, O. Schuster, P. Steinmetzer, F. Müller, R. Friedrich, M. E. Than, W. Bode, J. Stürzebecher, *J. Med. Chem.* **2006**, *49*, 4116-4126.
[33] E. K. Barefield, F. Wagner, K. D. Hodges, *Inorg. Chem.* **1976**, *15*, 1370-1377.
[34] K. P. Wainwright, *J. Chem. Soc., Dalton Trans.* **1980**, 2117-2120.
[35] K. P. Wainwright, *J. Chem. Soc., Dalton Trans.* **1983**, 1149-1152.
[36] G. Rogez, Ph-D., Université Paris XI, **2002**.

General conclusion

One of the long-term goals of our laboratory is to synthesize and characterize new hybrid multiferroic materials by functionalizing Aurivillius phases, which could be an interesting alternative to multiferroic oxides obtained in solid state chemistry. As the fundamental part of this overall objective, my thesis work consisted in understanding and improving the soft chemical functionalization of an Aurivillius phase $Bi_2SrTa_2O_9$ (BST).
During the past three years, we have successfully managed to establish several efficient microwave assisted functionalization strategies from insertion/grafting to *in situ* post-modification synthesis, which lead to various organic/inorganic or inorganic/inorganic hybrids based on $H_2Bi_{0.1}Sr_{0.85}Ta_2O_7$ (HST, the protonated form of BST).

New tools for the functionalization of Ta-based Aurivillius phases $Bi_2SrTa_2O_9$ (BST) based on micro-wave heating, which allows to protonate ($H_2Bi_{0.1}Sr_{0.85}Ta_2O_7$ (HST)) and to functionalize the BST phase within 5 hours, have been established.

We have managed to obtain the same compounds functionalized by *n*-alkylamines or *α,ω*-alkyl-diamines as described in the literature, but much faster (5 hours against a dozen days). Comparing with more classical routes described in literature (classical heating or solvothermal), there are not noticeable changes in the yields or crystallinity of the obtained protonated product HST and of the subsequent hybrids. Still using microwave assisted reactions, we have investigated the influence of certain parameters, temperature and solvent, during the functionalization process. The importance of water during the process of inserting HST with amines has been clearly established proved as the first time. In addition, an efficient complementary strategy, the microwave assisted pre-functionalization, has also been developed. This enables us to intercalate HST with various complicated amines, for example polyamines, chiral amines, amines bearing aromatic groups or functionalized cyclam. Although the above established strategies allow overcoming some kinetic restrictions to the insertion of even bulky amines, the thermodynamic limitations cannot be overcome. Among the various amines with which we tried to functionalize HST, phenyl-butylamine (PBA) led to a hybrid material possessing a variable interlayer distance, which can be modulated by the preparation protocols. The influence of the reaction conditions (time, temperature and concentration) on the interlayer distance has been studied.

We have also described the successful rapid microwave-assisted interlayer surface modification of HST via indirect grafting reactions to result in class II hybrids possessing covalent bonds between inorganic host and organic guests. This approach seems to be rather general since the grafting reactions can be carried out with various alcohols (*n*-alcohols, linear diols and bulky alcohols). To the best of our knowledge, this is the first time the grafting behavior of an Aurivillius phase is described. The pillaring arrangement of α,ω-alkanediols in the interlayer space of layered perovskite has also never been described in any layered perovskite. Two different methods of preparation (using an intermediate *n*-alkylamine-HST, or involving an alcohol-exchange-type reaction) have been employed and compared. The presence of *n*-alkyl groups in the interlayer space of layered perovskite is proved to be necessary for the subsequent grafting reactions and it appears that the longer *n*-alkyl groups are advantageous. But we could not prove the necessity of $-NH_3^+$ group, since the intermediate NH_3-HST cannot react with *n*-alcohols and the alcohol exchange reaction also works well when using C_nOH-HST as intermediate with $n \geq 4$. In addition, we have particularly investigated the role of water in the reaction processes. It appears that water

has a key role not only to allow grafting of alcohols, but also to drive the preferential reactivity of HST with amines or alcohols. We have observed an interesting swelling behavior during the reaction processes between C_4N-HST and propan-1-ol, depending on the amount of water. 5-amino-pentan-1-ol has been employed to form bilayer arrangement or a pillaring arrangement by controlling the amount of water. And the transformation from a bilayer to a pillaring arrangement has been realized via thermal post-treatment.

The successful rapid immobilization of 4-pentyn-1-ol or 3-azidopropanol on the interlayer surface of layered perovskites HST by microwave-assisted alcohol-exchange reactions has been described. And the subsequent successful *in situ* post modifications of the obtained precursors via microwave-assisted Copper (I) catalyzed Alkyne-Azide Cycloaddition (CuAAC) reactions have also been described. The relatively general application of this approach has been illustrated through the use of two different azides: 1-azidohexane or 1-azidobenzene. In addition, the microwave-assisted CuAAC reaction between azide-terminated precursor and 1-hexyne is also thought to work, although the residual catalyst is a great obstacle for the characterizations of reaction product. Considering the minimum amount of catalyst, the alkyne-terminated precursor is more suitable than the azide-terminated precursor to perform the post modification of HST. It is noteworthy that there are not noticeable reactivity limitations, although the click reactions, taking places within the interlayer space, may have potential difficulties due to the necessary access of reactants and catalysts. The organic guests in the click reaction products have been successfully deintercalated by alkaline treatment. The characterizations of the collected organic phases further support the successful *in situ* post modifications. To the best of our knowledge, this is the first time microwave-assisted CuAAC reactions are used to post-functionalize the interlayer space of layered perovskite. This post-synthesis modification strategy opens great perspectives to functionalize layered perovskites with a much broader range of molecules, and hence to enrich the properties of the obtained hybrids.

A soft-chemistry route for the insertion of paramagnetic metals (Cu(II) and Ni(II)) into layered perovskite HST has been established using organic amines (bis-(3-aminopropyl)amine (N3) or ethylamine (C_2N)) intercalated HST as intermediates. The microwave-assisted *in situ* reactions between intermediates and aqueous solution of copper nitrate or its complex with bis-(3-aminopropyl)amine lead to a green solid and a blue solid, respectively. A series of characterizations (X-ray diffraction, elemental analysis, UV-Vis spectroscopy, EPR spectroscopy, magnetization measurements, STEM microscopy) allows to precise the environment of Cu(II) in the interlamellar space : only oxygen atoms from the perovskite layers in the case of the green solid, and a complex with bis-(3-aminopropyl)amine in the case of the blue solid. The failure of the direct functionalization of HST with copper ions and the successful insertion of copper ions by using intermediates indicates that the pre-insertion of organic amines is necessary. UV-Vis. spectroscopy and the use of various intermediates, allow to propose a mechanism based on amine catalyzed cation-exchange process, between metal ions or complex and protons of functionalized HST.

As more or less short term perspectives, these works should be completed by various experiments.
First of all, this thesis work has essentially focused on synthetic aspects. But the properties have now to be investigated. Among them, the potential ferroelectric character of the obtained hybrids has to be cleary studied (even though measurement of ferroelectricity on powders is a great challenge). In case of success, we may envision the possibility to finely tune the ferroelectricity of the hybrids by the functionalization of the interlamellar space
Some characterization issues have also to be addressed. For instance, we have shown that PBA-HST possesses a variable interlayer distance depending on the experimental synthetic conditions. However, until now, we have not been able to obtain useful information which could precise the arrangement of the PBA molecules within the interlayer space of HST and the reasons why different arrangements are obtained. 1D electron density maps are currently being extracted from the XRD patterns (collaboration Christine Taviot-Guého, Institut de Chimie de Clermont-Ferrand). We have obtained high quality powder XRD patterns, showing at least ten harmonics for the *00l* diffraction lines. We hope that such analysis will allow to precise the intralayer arrangements.
In order to further demonstrate the general application of our post-synthesis modification strategy, the work of expanding the application scope of CuAAC reactions to Dion-Jacobson phase $HLaNb_2O_7 \cdot xH_2O$ (HLN) has to be finished.
Finally, for the copper intercalated products, High-resolution TEM (HRTEM) as well as STEM-EDX (combining STEM with EDX) and electron energy loss spectroscope (EELS) are currently under progress, which may elucidate the structure and composition of the solid products with a high spatial resolution. In addition, the application scope of this soft chemistry approach is being expanded to other metal ions (Co, Mn, Fe, etc.).

As the medium-term perspectives, the investigation of the applications of soft chemistry on lamellar perovskites, using the tools we have developed and the knowledge acquired, may be continued with a wilder scope.
Firstly, the studied objects can expand from 3D lamellar perovskites to 2D unilamellar sheet units (nanosheets). As previously described, we have observed an interesting swelling behavior during the reaction processes between C_4N-HST and propan-1-ol, depending on the amount of water. This is reminiscent of the swelling phenomenon which has been thoroughly studied by T. Sasaki *et al.*. It is very promising that a microwave-assisted swelling can be obtained, because it opens perspectives for microwave-assisted exfoliation, faster and with better yields than the existing procedures. We could also better control the size of the obtained nanosheets and improve the stability of the suspensions.
Secondly, using the developed tools, we may manage to insert/graft/post-synthesis modify lamellar perovskite with some more interesting molecular, for example C_{60}, to prepare some new multifunctional materials.
Finally, the reactivity of analogues of $Bi_2SrTa_2O_9$, for example $Bi_2SrNb_2O_9$, $Bi_2CaTa_2O_9$ or $Bi_2BaTa_2O_9$ can also be investigated. We believe that this comparative study will improve our understanding of the functionalization mechanism and enrich the candidates for multiferroic materials.

Long-term perspectives can be designed, still focusing on the preparation of new multiferroic, or at least multifunctional, hybrids. We can propose two strategies to finally achieve the above objective. The first one may deal with the elaboration of multiferroic thin

films by combining ferroelectric and ferromagnetic nanosheets by means of Layer-by-Layer (LBL) assembly, or even by click chemistry (pre functionalizing one kind of nanosheets with azides and the other with alkynes). As the second strategy, it may also be also possible to prepare various new ferroelectric Aurivillius phases, where interlayer structure units possessing interesting (ferro)magnetic properties are grown *in situ*.

Annex

A. Synthesis and characterization technics

A.1. Microwave synthesis reactor

Microwave syntheses were performed with a microwave synthesis reactor Monowave 300 (Anton Paar) (non-acidic conditions) and with a microwave synthesis reactor MultiwaveGO (Anton Paar) for the synthesis of **HST** (acidic conditions).

A.2. Elemental analyses

Elemental analyses for Bi, Sr, Cu, La, Nb and Ta were carried out at the Service Central Analyses of the CNRS (USR-59) and at the Analitishe Laboratorien in Lindlar, Germany. The elemental analyses for C, H and N were mainly carried out at the Service d'Analyse of the Institut de Chimie de Strasbourg (CNRS-UdS, UMR 7177).

A.3. Powder X-ray diffraction

The powder XRD patterns were collected with a Bruker D8 diffractometer (CuKα1 = 0.1540598 nm) equipped with a Lynx Eye detector discriminating in energy.

A.4. Thermo Gravimetric and Thermo Differential Analyses (TGA-TDA)

TGA-TDA experiments were performed using a TA instrument SDT Q600 (heating rates of 5°C·min^{-1} under air stream, using alumina crucibles).

A.5. Infrared spectroscopy

FT-IR spectra were collected in ATR mode on a Spectrum II spectrometer (Perkin-Elmer).

A.6. UV-visible spectroscopy

UV-vis/NIR studies were performed on a Perkin-Elmer Lambda 950 spectrometer. For solid compounds, spectra were recorded in the reflection mode, using a 150 mm integrating sphere, with a mean resolution of 2 nm and a sampling rate of 300 nm·min^{-1}. For studies in solution, spectra were recorded in transmission, with a mean resolution of 2 nm and a sampling rate of 300 nm·min^{-1}.

A.7. NMR in solution

NMR spectra in solution were recorded using a Bruker AVANCE 300 (300 MHz) spectrometer.

A.8. Solid state ^{13}C NMR

Solid state NMR ^{13}C (I = 1/2) experiments were performed by Fabrice Leroux, at the Institut de Chimie de Clermont-Ferrand (UMR 6296), with a 300 Bruker spectrometer at 75.47 MHz, using magic angle spinning (MAS) condition at 10 kHz and a 4 mm diameter size zirconia rotor. ^{13}C spectra obtained by proton enhanced cross-polarization method (CP) were referenced to the carbonyl of the glycine calibrated at 176.03 ppm. Recycling and Hartman-

Hahn contact times were 5 s and 1250 µs, respectively. Spinal 64 ^{1}H phase-decoupling was applied during ^{13}C channel acquisition.

A.9. Magnetic measurements

Magnetic measurements were performed using a Quantum Design SQUID-VSM magnetometer. Magnetization measurements at different fields at a given temperature confirm the absence of ferromagnetic impurities. Data were corrected for the sample holder and diamagnetism was estimated using the formula $\chi_{dia} = - M/2 \times 10^{-6}$.

A.10. Electron Paramagnetic Resonance (EPR)

EPR spectra, in continuous wave (cw) and pulsed, in X band (ν = 9.6±0.2 GHz), have been recorded with an ELEXYS spectrometer (BRUKER) with a dielectric resonator whose quality factor *Q* was adapted to the nature of the measurement. A CF935 Oxford Instruments cryostat has been used to work with liquid helium to control the temperature.
In continuous wave, a microwave power of 1 mW, amplitude modulation of 0.1 mT and frequency modulation of 100 kHz have been used.
In pulsed wave, the duration of a $\pi/2$ pulse was settled to 16 ns. The modulations of the Hahn echo decay have been measured, and the Fourier Transformation calculated with the WIN-EPR software (BRUKER). Several τ values (148, 200, 250, 300 and 348 ns) have been used to compensate the "blind spots" problems depending of the nuclei. For τ>348 ns, there is not enough signal. The optimum value to exalt ^{14}N with respect to ^{1}H was τ = 200 ns. A repetition time of 1000 µs was used.

A.11. Scanning Electron Microscopy (SEM)

The SEM images were obtained with a JEOL 6700F microscope equipped with a field emission gun, operating at 3 kV in the SEI mode.

A.12. Transmission Electron Microscopy (TEM) and Scanning Transmission Electron Microscopy (STEM)

The TEM and STEM images were obtained with a JEOL 2100F microscope equipped with analytical configuration:
- Spherical aberrations probe corrector
- EDX (Energy Dispersive X-Rays) spectrometer
- GIF TRIDIEM spectrometer (EELS, EFTEM)
- Classical holders: tilt, tilt rotation, heating
- Specific holders: specialized tomography holders (high tilt, high angle cryogenic), STM-TEM probe current holder
- Holography bi-prism device

Resolution: TEM 0.21 nm, STEM: 0.11 nm, EELS: 0.7 eV

B. Syntheses

B.1. Chapter I

B.1.1. Starting materials

$Bi_2SrTa_2O_9$ (BST): A stoichiometric mixture of Bi_2O_3, $SrCO_3$ and Ta_2O_5 was heated at 900 °C for 4 h and at 1200 °C for 4 h with intermittent grinding according to published procedures.[1] Anal. Calcd. for $Bi_2SrTa_2O_9$ (M = 1011.47 g/mol): Bi, 41.32; Sr, 8.66; Ta, 35.77. Found: Bi, 40.10; Sr, 8.66; Ta, 34.88.

$H_2Bi_{0.1}Sr_{0.85}Ta_2O_7$ (HST): To 20 mL of a 4 M aqueous HCl solution, 200 mg of **BST** were added. The mixture was heated in the microwave oven at T = 70°C during 3 h. In these conditions the mean incident power was about 5 W. The autogenous pressure was too low to be measured (typically below 1.5 bars). The acid-treated product was collected after four centrifugations (14000 rpm, 5 min each) (the supernatant was replaced after each centrifugation by distilled water) and air-dried.
Anal. Calcd. for $H_2Bi_{0.1}Sr_{0.85}Ta_2O_7 \cdot 2\ H_2O$ (M = 607.3 g/mol): H, 1.0; Bi, 3.44; Sr, 12.26; Ta, 59.60. Found: H, 0.25; Bi, 3.70; Sr, 12.13; Ta, 58.00.

B.1.2. Intercalation of mono *n*-alkylamines and *α, ω*-diaminoalkanes

General procedure: ethylamine (C_2N), *n*-propylamine (C_3N), *n*-butylamine (C_4N), *n*-dodecylamine ($C_{12}N$), 1,2-diamino-ethane (C_2N_2), 1,3-diamino-propane (C_3N_2), 1,4-diamino-butane (C_4N_2) and 1,12-diamino-dodecane ($C_{12}N_2$) were used. 100 mg (0.17 mmol) of **HST** (for all amines, except C_2N_2 and C_3N_2) or **C_2N-HST** (for C_2N_2 and C_3N_2) were dispersed in a solution of 20 mmol of amine or diamine in a mixture of 5 mL of THF and 1 mL of water. The mixture was placed in a 30 mL vial and heated by microwave irradiation at 110°C (except $C_{12}N$) / 130°C (for $C_{12}N$), during 1 h (maximum incident power : 90 W). In these conditions, the mean incident power was about 10 W, and the autogenous pressure was about 6 bars. The obtained white powder was collected after three centrifugations (14000 rpm, 5 min each) (the supernatant was replaced after each centrifugation by distilled water (twice) and ethanol (last) in order to wash the product) and air-dried. Detailed reaction conditions and elemental analysis are given in ***Tables B.I.1*** and ***Tables B.I.2*****.**

B.1.3. Intercalation of other amines and diamines

General procedure: cyclohexylamine, (aminomethyl)-cyclohexane, benzylamine, (±)-*trans*-cyclohexane-1,2-diamine ($C_6H_{10}(NH_2)_2$), cyclohexane-1,4-diamine, 1,4-bis(aminomethyl)-cyclohexane and 1,4-bis(aminomethyl)-benzene were used following the conditions described above and in ***Table B.I.1*****.**

Product	Starting compound	Temperature (°C)	Duration (min)
C_2N-HST	HST	110	60
C_3N-HST	HST	110	60
C_4N-HST	HST	110	60
$C_{12}N$-HST	HST	130	60
C_2N_2-HST	C_2N-HST	110	60
C_3N_2-HST	C_2N-HST	110	60
C_4N_2-HST	HST	110	60
$C_{12}N_2$-HST	HST	110	60
cyclohexylamine-HST	HST	130	90
(aminomethyl)-cyclohexane-HST	HST	130	90
benzylamine-HST	HST	130	90
cyclohexane-1,2-diamine-HST	C_2N-HST	90	90
cyclohexane-1,4-diamine-HST	C_2N-HST	130	60
1,4-bis(aminomethyl)-cyclohexane-HST	C_2N-HST	130	60
1,4-bis(aminomethyl)-benzene-HST	C_2N-HST	130	60

Table B.I.1. *Experimental conditions for the insertion of amines into HST.*

Product	Formula	Elemental analysis found (calcd)
Mono-*n*-alkylamines		
C_2N-HST	$(C_2NH)_{0.8}H_{1.2}Bi_{0.1}Sr_{0.85}Ta_2O_7{\cdot}3\ H_2O$ (M = 651 g/mol)	H, 1.51; C, 2.95; N, 1.79; Ta, 54.80 (H, 2.07; C, 2.91; N, 1.69; Ta, 54.72)
C_3N-HST	$(C_3NH)_{0.8}H_{1.2}Bi_{0.1}Sr_{0.85}Ta_2O_7{\cdot}4.9\ H_2O$ (M = 707 g/mol)	H, 1.36; C, 3.58; N, 1.66; Ta, 51.20 (H, 2.71; C, 4.08; N, 1.59; Ta, 51.20)
C_4N-HST	$(C_4NH)_{0.9}H_{1.1}Bi_{0.1}Sr_{0.85}Ta_2O_7{\cdot}3.8\ H_2O$ (M = 706 g/mol)	H, 1.66; C, 6.05; N, 1.69; Ta, 51.70 (H, 2.79; C, 6.13; N, 1.79; Ta, 51.29)
$C_{12}N$-HST	$(C_{12}NH)_{0.7}H_{1.3}Bi_{0.1}Sr_{0.85}Ta_2O_7{\cdot}5.8\ H_2O$ (M = 806 g/mol)	H, 2.94; C, 13.06; N, 1.36; Ta, 44.88 (H, 4.07; C, 12.53; N, 1.22; Ta, 44.93)
α,ω-diaminoalkanes		
C_2N_2-HST	$(C_2N_2H_2)_{0.4}H_{1.2}Bi_{0.1}Sr_{0.85}Ta_2O_7{\cdot}4.6\ H_2O$ (M = 678 g/mol)	H, 1.05; C, 1.36; N, 2.11; Ta, 52.95 (H, 2.14; C, 1.42; N, 1.65; Ta, 53.36)
C_3N_2-HST	$(C_3N_2H_2)_{0.4}H_{1.6}Bi_{0.1}Sr_{0.85}Ta_2O_7{\cdot}3.7\ H_2O$ (M = 668 g/mol)	H, 0.86; C, 1.94; N, 1.57; Ta, 54.21 (H, 2.02; C, 2.16; N, 1.68; Ta, 54.21)
C_4N_2-HST	$(C_4N_2H_2)_{0.6}H_{0.8}Bi_{0.1}Sr_{0.85}Ta_2O_7{\cdot}5.6\ H_2O$ (M = 725 g/mol)	H, 1.31; C, 3.50; N, 2.28; Ta, 49.90 (H, 2.84; C, 3.98; N, 2.32; Ta, 49.91)
$C_{12}N_2$-HST	$(C_{12}N_2H_2)_{0.7}H_{0.6}Bi_{0.1}Sr_{0.85}Ta_2O_7{\cdot}8.7\ H_2O$ (M = 867 g/mol)	H, 2.46; C, 12.50; N, 2.21; Ta, 41.70 (H, 4.37; C, 11.64; N, 2.26; Ta, 41.75)
Other amines		
cyclohexylamine-HST	$(C_6H_{11}NH_3)_{0.8}H_{1.2}Bi_{0.1}Sr_{0.85}Ta_2O_7{\cdot}6.0H_2O$ (M = 759 g/mol)	H, 1.95; C, 7.63; N, 1.66; Ta, 47.78 (H, 3.24; C, 7.60; N, 1.48; Ta, 47.70)
(aminomethyl)-cyclohexane-HST	$(C_6H_{11}CH_2NH_3)_{0.8}H_{1.2}Bi_{0.1}Sr_{0.85}Ta_2O_7{\cdot}1.0H_2O$ (M = 680 g/mol)	H, 2.29; C, 9.50; N, 1.64 (H, 2.35; C, 9.88; N, 1.65)
benzylamine-HST	$(C_6H_5\ CH_2NH_3)_{0.9}H_{1.1}Bi_{0.1}Sr_{0.85}Ta_2O_7{\cdot}5.5H_2O$ (M = 767 g/mol)	H, 1.59; C, 9.57; N, 1.64; Ta, 47.56 (H, 2.77; C, 9.87; N, 1.64; Ta, 47.19)
cyclohexane-1,2-diamine-HST	$(C_6H_{10}\ (NH_3)_2)_{0.8}H_{0.4}Bi_{0.1}Sr_{0.85}Ta_2O_7{\cdot}5.0H_2O$ (M = 753 g/mol)	H, 2.13; C, 7.66; N, 3.00; Ta, 48.0 (H, 3.11; C, 7.66; N, 2.98; Ta, 48.08)
cyclohexane-1,4-diamine-HST	$(C_6H_{10}(NH_3)_2)_{0.4}H_{1.2}Bi_{0.1}Sr_{0.85}Ta_2O_7{\cdot}1.4H_2O$ (M = 651 g/mol)	H, 1.54; C, 4.24; N, 1.78 (H, 1.60; C, 4.42; N, 1.72)
1,4-bis(aminomethyl)-cyclohexane-HST	$(C_6H_{10}(CH_2NH_3)_2)_{0.4}H_{1.2}Bi_{0.1}Sr_{0.85}Ta_2O_7{\cdot}1.2H_2O$ (M = 660 g/mol)	H, 1.70; C, 5.58; N, 1.72 (H, 1.76; C, 5.82; N, 1.70)
1,4-bis(aminomethyl)-benzene-HST	$(C_6H_4(CH_2NH_3)_2)_{0.4}H_{1.2}Bi_{0.1}Sr_{0.85}Ta_2O_7{\cdot}1.3H_2O$ (M = 650 g/mol)	H, 1.30; C, 5.29; N, 1.65 (H, 1.20; C, 5.90; N, 1.72)

Table B.I.2. *Proposed formulae and elemental analyses.*

B.1.4. Preparation of the three phases PBA1-HST, PBA2-HST, PBA3-HST

100 mg (0.17 mmol) of HST (for PBA1-HST, PBA3-HST) or 100 mg (0.15 mmol) of C_2N-HST (for PBA2-HST,) were dispersed in a solution of 20 mmol of PBA (3 mL) in a mixture of 3 mL of THF and 1 mL of water. For the preparation of PBA1-HST or PBA2-HST, the mixture was placed in a 30 mL vial and heated by microwave irradiation at 130°C during 1.5 h (maximum incident power : 70 W). In these conditions, the mean incident power was about 10 W, and the autogenous pressure was about 6 bars. For the preparation of PBA3-HST, the mixture was sealed in a Teflon-lined autoclave (volume 50 mL) and was heated in oven at 130°C during 18 h. The obtained white powders was collected after three centrifugations (14000 rpm, 5 min each) (the supernatant was replaced after each centrifugation by distilled water (twice) and acetone (last) in order to wash the product) and air-dried. The results of elemental analyses and TGA and the proposed formulae are given in ***Table B.I.3***.

Products	Formula	Mass losses water+ organic phase Found (calcd) (%)	Mass losses organic phase Found (calcd) (%)	Mass losses water Found (calcd) (%)	Carbon content Found (calcd) (%)	Hydrogen content Found (calcd) (%)	Nitrogen content Found (calcd) (%)
PBA1-HST	$(C_{10}NH_{16})_{0.5}H_{1.5}Bi_{0.1}Sr_{0.85}Ta_2O_7{\cdot}1.4H_2O$	15.1 (14.9)	11.1 (11.1)	4.0 (3.8)	11.06 (9.0)	1.97 (1.8)	1.28 (1.0)
PBA2-HST	$(C_{10}NH_{16})_{0.6}H_{1.4}Bi_{0.1}Sr_{0.85}Ta_2O_7{\cdot}1.6H_2O$	16.6 (17.2)	12.6 (13.0)	4.0 (4.2)	13.55 (10.4)	2.24 (2.4)	1.52 (1.2)
PBA3-HST	$(C_{10}NH_{16})_{0.5}H_{1.5}Bi_{0.1}Sr_{0.85}Ta_2O_7{\cdot}1.0H_2O$	13.3 (13.9)	10.3 (11.2)	3.0 (2.7)	10.01 (9.0)	1.74 (1.7)	1.25 (1.0)

Table B.I.3. *Mass losses ascribed to the removal of water and of organic phase, elemental micro-analyses (C, H, N) and consistent proposed formulae.*

B.2. Chapter II

B.2.1. Grafting of *n*-alcohols into C_4N-HST

0.1 g (0.15 mmol) of C_4N-HST (HST intercalated by butylamine)) and a mixture of water (0.1 mL, 5.56 mmol) and *n*-alcohols (8 mL, 30-200 mmol) were sealed in a vial (volume 30 mL) (note: for some *n*-alcohols, for example *n*-dodecanol, heating at 70 °C is needed to obtain liquid state). Then the vial was heated in the microwave oven by following an established procedure (heating: from room temperature to 130°C in 2 min; holding time: 2 h; cooling: as fast as possible; stirring speed: 800 rpm; maximum power: 70 W). In these conditions, the mean incident power was about 10 W and the autogenous pressure was in the range 0-6 bars, depending on the alcohol. After reactions, the samples were washed with acetone for three times by using centrifugation (9000 g, 5 min) and air-dried. The results of elemental analyses and TGA and the proposed formulae are given in ***Table B.II.1***.

Products	Formula	Mass losses water+ organic phase Found (calcd) (%)	Mass losses organic phase Found (calcd) (%)	Mass losses water Found (calcd) (%)	Carbon content Found (calcd) (%)	Hydrogen content Found (calcd) (%)
C_1OH-HST	$(C_1O)_{1.5}H_{0.5}Bi_{0.1}Sr_{0.85}Ta_2O_{5.5}\cdot 0.4H_2O$	4.7 (5.0)	3.7 (3.8)	1.0 (1.2)	3.05 (3.0)	1.05 (1.2)
C_2OH-HST	$(C_2O)_{1.1}H_{0.9}Bi_{0.1}Sr_{0.85}Ta_2O_{5.9}\cdot 0.3H_2O$	5.8 (6.1)	4.8 (5.2)	1.0 (0.9)	4.45 (4.3)	1.15 (1.3)
C_3OH-HST	$(C_3O)_{1.1}H_{0.9}Bi_{0.1}Sr_{0.85}Ta_2O_{5.9}\cdot 0.3H_2O$	7.5 (8.4)	6.6 (7.5)	0.9 (0.9)	6.40 (6.3)	1.47 (1.6)
C_4OH-HST	$(C_4O)_{1.0}H_{1.0}Bi_{0.1}Sr_{0.85}Ta_2O_{6.0}\cdot 0.3H_2O$	9.0 (9.8)	8.0 (9.0)	1.0 (0.8)	7.40 (7.6)	1.58 (1.8)
C_7OH-HST	$(C_7O)_{0.9}H_{1.1}Bi_{0.1}Sr_{0.85}Ta_2O_{6.1}\cdot 0.3H_2O$	14.5 (14.2)	13.8 (13.4)	0.7 (0.8)	13.48 (11.3)	2.52 (2.4)
C_{12}OH-HST	$(C_{12}O)_{0.9}H_{1.1}Bi_{0.1}Sr_{0.85}Ta_2O_{6.1}\cdot 0.2H_2O$	19.3 (21.3)	18.9 (20.9)	0.4 (0.4)	17.79 (17.8)	3.20 (3.4)

Table B.II.1. *Mass losses ascribed to the removal of water and of organic phase, elemental micro-analyses (C, H, N) and consistent proposed formulae.*

B.2.2. Alcohol-exchange reactions between C_2OH-HST and *n*-alcohols ($C_nH_{2n+1}OH$, n = 3, 4, 7, 12).

0.1 g (0.17 mmol) of C_2OH-HST is dispersed in a mixture of water (0.1 mL, 5.56 mmol) and *n*-alcohols (8 mL). The mixture was sealed in a microwave vial (volume 30 mL) and heated in the microwave oven by following an established procedure (heating: from room temperature to 130°C within 2 min; holding time: 2 h; cooling: as fast as possible; stirring speed: 800 rpm; maximum power: 70 W). In these conditions, the mean incident power was about 10 W and the autogenous pressure was in the range 0-4 bars, depending on the alcohol. After reactions, the samples were washed with acetone for three times by using centrifugation (9000 g, 5 min) and air-dried.

B.2.3. Grafting of α, ω-alkyldiols ($HOC_nH_{2n}OH$, n = 2, 4, 8, 12) into C_4N-HST

0.1 g (0.14 mmol) of C_4N-HST and a mixture of water (1 mL, 55 mmol) and α, ω-alkyldiols (8 g, 40-130 mmol) were sealed in a microwave vial (volume 30 mL). Then the vial was heated in the microwave oven by following an established procedure (heating: from room temperature to 130°C within 2 min; holding time: 2 h; cooling: as fast as possible; stirring speed: 800 rpm; maximum power: 70 W). In these conditions, the mean incident power was about 5 watts and the autogenous pressure was too low to be measured. After reactions, the samples were washed with acetone for three times by using centrifuge (9000 g, 5 min) and air-dried. The results of elemental analysis and TGA and the proposed formulae are given in ***Table B.II.2***.

Products	Formula	Mass losses water+ organic phase Found (calcd) (%)	Mass losses organic phase Found (calcd) (%)	Mass losses water Found (calcd) (%)	Carbon content Found (calcd) (%)	Hydrogen content Found (calcd) (%)
HOC_2OH-HST	$(HOC_2H_4O)_{0.8}H_{1.2}Bi_{0.1}Sr_{0.85}Ta_2O_{6.3}\cdot 0.9H_2O$	7.6 (8.4)	4.9 (5.8)	2.7 (2.6)	3.75 (3.1)	1.11 (1.1)
HOC_4OH-HST	$(OC_4H_8O)_{0.5}H_{1.0}Bi_{0.1}Sr_{0.85}Ta_2O_6\cdot 0.1H_2O$	5.3 (4.9)	5.0 (4.6)	0.3 (0.3)	4.04 (4.1)	1.13 (0.9)
HOC_8OH-HST	$(OC_8H_{16}O)_{0.3}H_{1.4}Bi_{0.1}Sr_{0.85}Ta_2O_{6.4}\cdot 0.8H_2O$	7.3 (7.7)	5.2 (5.4)	2.1 (2.3)	5.00 (4.6)	1.42 (1.2)
$HOC_{12}OH$-HST	$(OC_{12}H_{24}O)_{0.3}H_{1.4}Bi_{0.1}Sr_{0.85}Ta_2O_{6.4}\cdot 0.8H_2O$	8.4 (10.2)	6.1 (7.9)	2.3 (2.3)	6.99 (6.8)	1.73 (1.6)

Table B.II.2. *Mass losses ascribed to the removal of water and of organic phase, elemental micro-analyses (C, H, N) and consistent proposed formulae.*

B.2.4. Grafting of bulky alcohols (2-propanol, *tert*-butanol and benzyl alcohol) into C_4N-HST

0.1 g (0.14 mmol) of C_4N-HST and a mixture of water and bulky alcohol (8 mL of bulky alcohol, 0.1 mL of water) were sealed in a microwave vial (volume 30 mL). Then the vial was heated in the microwave oven by following an established procedure (heating: from room temperature to 130°C within 2 min; holding time: 2 h; cooling: as fast as possible; stirring speed: 800 rpm; Maximum power: 70 W). In these conditions, the mean incident power was about 10 W and the autogenous pressure was in the range 0-4 bars, depending on the alcohol. After reactions, the samples were washed with acetone for three times by using centrifugation (9000 g, 5 min) and air-dried. The results of elemental analysis and TGA and the proposed formulae are given in ***Table B.II.3***.

Products	Formula	Mass losses water+ organic phase Found (calcd) (%)	Mass losses organic phase Found (calcd) (%)	Mass losses water Found (calcd) (%)	Carbon content Found (calcd) (%)	Hydrogen content Found (calcd) (%)	Nitrogen content Found (calcd) (%)
2-probanol-HST	$(C_3H_7O)_{0.6}H_{1.4}Bi_{0.1}Sr_{0.85}Ta_2O_{6.4}\cdot 0.7H_2O$	6.5 (6.3)	4.5 (4.2)	2.0 (2.1)	4.18 (3.5)	1.33 (1.2)	0
tert-butanol-HST					3.46	1.37	0.82
Benzyl alcohol-HST	$(C_7H_7O)_{0.7}H_{1.3}Bi_{0.1}Sr_{0.85}Ta_2O_{6.3}\cdot 0.3H_2O$	10.2 (10.7)	9.4 (9.9)	0.8 (0.8)	10.90 (9.2)	1.39 (1.1)	0

Table B.II.3. *Mass losses ascribed to the removal of water and of organic phase, elemental micro-analyses (C, H, N) and consistent proposed formulae.*

B.2.5. Reactivity of 5-amino-pentan-1-ol with C_2N-HST as a function of the water content

50 mg of C_2N-HST were dispersed in a solution of 1 mL of 5-amino-1-pentanol in a mixture of 1 mL of THF and water (0.01, 0.02, 0.03, 0.04, 0.1 and 1.0 mL respectively). The mixture was placed in a 10 mL vial and heated by microwave irradiation at 130°C during 1 h (maximum incident power : 70 W). In these conditions, the mean incident power was about 10 W, and the autogenous pressure was about 5 bars. The obtained white powder was collected after

three centrifugations (9000 rpm, 2 min each) (the supernatant was replaced after each centrifugation by acetone in order to wash the product) and air-dried. The results of elemental analysis and TGA and the proposed formulae are given in ***Table B.II.4***.

Products	Formula	Mass losses water + organic phase Found (calcd) (%)	Mass losses organic phase Found (calcd) (%)[a]	Mass losses water Found (calcd) (%)[b]	C Found (calcd) (%)	H Found (calcd) (%)	N Found (calcd) (%)
1 mass %	$(H_3NC_5H_{10}O)_{0.5}H_{1.0}Bi_{0.1}Sr_{0.85}Ta_2O_{6.3}\cdot 0.6H_2O$	8.3 (8.6)	6.6 (6.9)	1.7 (1.7)	6.08 (4.7)	1.49 (1.4)	1.38 (1.2)
2 mass %	$(H_3NC_5H_{10}O)_{0.6}H_{0.8}Bi_{0.1}Sr_{0.85}Ta_2O_{6.4}\cdot 0.9H_2O$	11.4 (10.6)	8.2 (8.1)	3.2 (2.5)	6.11 (5.5)	1.72 (1.6)	1.52 (1.3)
4 mass %	$(H_3NC_5H_{10}OH)_{0.6}H_{1.4}Bi_{0.1}Sr_{0.85}Ta_2O_7\cdot 1.3H_2O$	12.9 (13.5)	7.5 (7.9=9.6-1.7)	5.4 (5.4=3.7+1.7)	5.99 (5.5)	1.77 (1.9)	1.49 (1.3)
10 mass %	$(H_3NC_5H_{10}OH)_{0.5}H_{1.5}Bi_{0.1}Sr_{0.85}Ta_2O_7\cdot 1.4H_2O$	12.6 (12.2)	7.1 (6.9=8.3-1.4)	5.5 (5.3=3.9+1.4)	6.31 (4.7)	2.03 (1.8)	1.47 (1.2)
100 mass %	$(H_3NC_5H_{10}OH)_{0.5}H_{1.5}Bi_{0.1}Sr_{0.85}Ta_2O_7\cdot 1.3H_2O$	12.1 (12.0)	7.1 (6.9=8.3-1.4)	5.0 (5.1=3.7+1.4)	6.08 (4.7)	1.89 (1.7)	1.52 (1.2)

Table B.II.4. *Mass losses ascribed to the removal of water and of organic phase, elemental micro-analyses (C, H, N) and consistent proposed formulae. Note: for low water contents (1 and 2 mass %), 5-amino-pentan-1-ol is pillaring the inorganic layers. For larger water contents, 5-amino-pentan-1-ol forms a bilayer arrangement, with the alcohol function being free. Upon moderate heating it is possible to go from a bilayer to a pillaring arrangement (this hypothesis, made from XRD, still has to be confirmed by NMR spectroscopy). Therefore, for important water contents, mass losses observed at low temperatures are ascribed to the loss of solvation water* and *to the grafting of the alcohol group which leads to the loss of one water molecule per 5-amino-pentan-1-ol.*
a: organic phase content = organic phase content for a bilayer arrangement – quantity of water eliminated by the grafting of the alcohol moiety
b: water content = solvation water + water eliminated by the grafting of the alcohol moiety

B.3. Chapter III

B.3.1. Preparation of precursors based on HST

B.3.1.1. Alkyne-HST

0.1 g (0.17 mmol) of intermediate C_2OH-HST and a mixture of water (25 µL, 1.40 mmol) and 4-pentyn-1-ol (2 mL, 21.50 mmol) were sealed in a vial (volume 10 mL), under a protective argon atmosphere. Then the mixture was heated with microwave irradiation by following an established procedure (heating: from room temperature to 110°C within 2 min; holding time: 2 h; cooling: as fast as possible; stirring speed: 800 rpm; maximum power: 70 W). In these conditions, the mean incident power was about 5 W and the autogenous pressure was too low to be measured. After reaction, the sample was washed with acetone for three times by using centrifugation (9000 g, 5 min) and air-dried. The results of elemental analysis and TGA and the proposed formulae are given in ***Table B.III.1***.

B.3.1.2. Azide-HST

3-azidopropan-1-ol was prepared according to a method described in literature.[2]

3-Chloro-propan-1-ol (10.0 g, 0.11 mol) and sodium azide (17.18 g, 0.26 mol) were reacted in H_2O (100 mL) at 95°C for 24 h. The reaction mixture was cooled to room temperature, and extracted with 100 mL of CH_2Cl_2 for three times. The organic layer was separated, dried over $MgSO_4$, filtered and concentrated to obtain the product. (yield: 98 %).
^{1}H NMR ($CDCl_3$): δ = 1.86 (m, 2H, HO-CH_2-***CH_2***-CH_2-N_3), 3.46 (t, 2H, HO-CH_2-CH_2-***CH_2***-N_3), 3.76 (t, 2H, HO-***CH_2***-CH_2-CH_2-N_3) ppm.
^{13}C NMR ($CDCl_3$): δ = 31.43 (HO-CH_2-***CH_2***-CH_2-N_3), 48.48 (HO-CH_2-CH_2-***CH_2***-N_3), 59.92 (HO-***CH_2***-CH_2-CH_2-N_3) ppm.

Azide-HST: 0.1 g of intermediate (C_2OH-HST, C_4N-HST or C_{12}OH-HST) and a mixture of water (25 µL, 1.40 µmol) and 3-azidopropan-1-ol (2 g, 19.6 mmol) were sealed in a vial (volume 10 mL), under a protective argon atmosphere. Then the reaction mixture was heated with microwave irradiation by following an established procedure (heating: from room temperature to 90°C within 1 min; holding time: 2 h; cooling: as fast as possible; stirring speed: 800 rpm; maximum power: 70 W). In these conditions, the mean incident power was about 2 W and the autogenous pressure was too low to be measured. After reaction, the sample was washed with acetone for three times by using centrifugation (9000 g, 5 min) and air-dried.

B.3.2. Post-modification reactions

B.3.2.1. Post-modification of alkyne-HST

B.3.2.1.1. Hexyl-click-HST

1-azidohexane was prepared according to a method described in literature.[3]
To a solution of 1.73 g (26.6 mmol) of sodium azide (caution, potentially explosive) in 53 mL of DMSO was added 4 g (24.2 mmol) of 1-bromohexane. The solution was stirred at room temperature for 4 h. The resulting solution was then poured into 100 mL of water and extracted twice with 30 mL of diethyl ether. The combined organic layers were dried over $NaSO_4$ and concentrated at reduced pressure to get yellow liquid.
^{1}H NMR ($CDCl_3$): δ = 0.90 (t, 3H, ***CH_3***-CH_2-CH_2-CH_2-CH_2-CH_2-N_3), 1.26-1.42 (m, 6H, CH_3-***CH_2-CH_2-CH_2***-CH_2-CH_2-N_3), 1.60 (m, 2H, CH_3-CH_2-CH_2-CH_2-***CH_2***-CH_2-N_3), 3.26 (t, 2H, CH_3-CH_2-CH_2-CH_2-CH_2-***CH_2***-N_3) ppm.
^{13}C NMR ($CDCl_3$): δ = 13.92 (***CH_3***-CH_2-CH_2-CH_2-CH_2-CH_2-N_3), 22.48 (CH_3-***CH_2***-CH_2-CH_2-CH_2-CH_2-N_3), 26.36 (CH_3-CH_2-***CH_2***-CH_2-CH_2-CH_2-N_3), 28.77 (CH_3-CH_2-CH_2-***CH_2***-CH_2-CH_2-N_3), 31.30 (CH_3-CH_2-CH_2-CH_2-***CH_2***-CH_2-N_3), 51.46 (CH_3-CH_2-CH_2-CH_2-CH_2-***CH_2***-N_3) ppm.

For the CuAAC click reaction, to a dried THF (2 mL) solution of $CuBr(PPh_3)_3$ (1 mol %, 3.0 mg, 3.2 µmol) in a vial (volume 10 mL), 200 mg (0.32 mmol) of alkyne-HST and 0.5 g (3.94 mmol) of 1-azidohexane were added under a protective argon atmosphere. Then the mixture was sealed and then the vial was heated with microwave irradiation by following an established procedure (heating: from room temperature to 80°C within 1 min; holding time: 2 h; cooling: as fast as possible; stirring speed: 800 rpm; maximum power: 70 W). In these conditions, the mean incident power was about 2 W and the autogenous pressure was too low to be measured. After reactions, the sample was washed with THF for two times and acetone for two times, by using centrifugation (9000 g, 5 min), and air-dried. The results of elemental analysis and TGA and the proposed formulae are given in ***Table B.III.1***.

B.3.2.1.2. Benzyl-click-HST

Benzyl azide was prepared according to a method described in literature.[4]
NaN_3 (2.0 equiv) (caution, potentially explosive) in H_2O (0.1 mL/mmol) was added to a stirred solution of the benzyl-bromide (1.0 equiv) in THF (2.5 mL/mmol). The resulting suspension was stirred at 80 °C for 3 h. The mixture was extracted with CH_2Cl_2, washed with water and brine, dried (Na_2SO_4), and filtered, and the solvent was evaporated under reduced pressure. The azide was obtained in quantitative yield and was used without further purification and isolation.
^{1}H NMR ($CDCl_3$): δ = 4.35 (s, 2H, a), 7.27-7.41 (m, 5H, c (c'), d (d'), e) ppm.
^{13}C NMR ($CDCl_3$): δ = 54.8 (a), 128.17 (c (c')), 128.27 (e), 128.79 (d (d')), 135.33 (b) ppm.

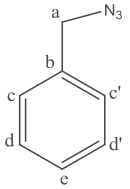

For the CuAAC click reaction, to a dried THF (2 mL) solution $CuBr(PPh_3)_3$ (3.0 mg, 3.2 µmol) in a vial (volume 10 mL), 200 mg (0.32 mmol) of alkyne-HST and 0.52 g (3.94 mmol) of benzyl azide were added under a protective argon atmosphere. Then the mixture was sealed and then the vial was heated with microwave irradiation by following an established procedure (heating: from room temperature to 80°C within 1 min; holding time: 2 h; cooling: as fast as possible; stirring speed: 800 rpm; maximum power: 70 W). In these conditions, the mean incident power was about 2 W and the autogenous pressure was too low to be measured. After reactions, the sample was washed with THF for two times and acetone for two times, by using centrifuge (9000 g, 5 min), and air-dried. The results of elemental analysis and TGA and the proposed formulae are given in ***Table B.III.1***.

B.3.2.2. Post-modification of azide-HST

For the CuAAC click reaction, to a THF (2 mL) solution of $CuBr(PPh_3)_3$ (3.0 mg (3.2 µmol), 60 mg (64 µmol) or 300 mg (320 µmol)) in a vial (volume 10 mL), 200 mg (ca. 0.32 mmol) of azide-HST and 1 mL (8.70 mmol) of 1-hexyne were added under a protective argon atmosphere. Then the vial was heated with microwave irradiation by following an established procedure (heating: from room temperature to 80°C within 1 min; holding time: 2 h; cooling: as fast as possible; stirring speed: 800 rpm; maximum power: 70 W). In these conditions, the mean incident power was about 2 W and the autogenous pressure was too low to be measured. After reactions, the sample was washed with THF for two times and acetone for two times, by using centrifugation (9000 g, 5 min), and air-dried.

products	Formula	Mass losses water + organic phase Found (calcd) (%)	Mass losses Organic phase Found (calcd) (%)	Mass losses Water Found (calcd) (%)	C Found (calcd) (%)	H Found (calcd) (%)	N Found (calcd) (%)
Alkyne-HST	$(C_5H_7O)_{0.7}H_{1.3}Bi_{0.1}Sr_{0.85}Ta_2O_{6.3}\cdot 0.5H_2O$	8.7 (8.9)	7.2 (7.5)	1.5 (1.4)	8.03 (6.7)	1.14 (1.2)	---
Hexyl-click-HST	$(C_{11}N_3H_{20}O)_{0.5}H_{1.5}Bi_{0.1}Sr_{0.85}Ta_2O_{6.5}\cdot 0.3H_2O$	14.8 (15.2)	13.9 (14.3)	0.9 (0.9)	9.05 (9.8)	1.84 (1.8)	2.73 (3.1)
Benzyl-click-HST	$(C_{12}N_3H_{14}O)_{0.6}H_{1.4}Bi_{0.1}Sr_{0.85}Ta_2O_{6.4}\cdot 0.6H_2O$	19.4 (18.6)	17.9 (17.1)	1.5 (1.5)	12.26 (12.3)	1.56 (1.6)	3.35 (3.6)

Table B.III.1. *Mass losses ascribed to the removal of water and of organic phase, elemental micro-analyses (C, H, N) and consistent proposed formulae.*

B.3.3. Deintercalation reactions

To 200 ml of NaOH aqueous solution (6M), 600 mg of the CuAAC reaction product was added. The reaction mixture was then stirred at 80 °C for 48 h. After reaction, the obtained solid and solution were separated via centrifugation (9000 g, 5 min). The obtained solid was washed with water for 3 times and acetone for 2 times by using centrifugation (9000 g, 5 min) and air-dried. The obtained solution was extracted thrice with 100 mL of diethyl ether in the case of hexyl-click-HST or 100 mL of CH_2Cl_2 in the case of benzyl-click-HST. The combined organic layers were dried over Na_2SO_4 and concentrated at reduced pressure.

B.3.3.1. Case of hexyl-click-HST

^{1}H NMR ($CDCl_3$): δ = 0.88 (t, 3H), 1.29-1.32 (m, 6H), 1.87-1.97 (m, 4H), 2.41 (s, 1H), 2.84 (t, 2H), 3.72 (t, 2H), 4.31 (t, 2H), 7.29 (s, 1H) ppm.
^{13}C NMR ($CDCl_3$): δ = 13.92, 22.20, 22.41, 26.17, 30.28, 31.15, 31.97, 50.24, 62.00, 120.63, 147.38 ppm.
Precise attribution of the ^{13}C NMR is given in **Chapter III**.

B.3.3.2. Case of hexyl-click-HST

^{1}H NMR ($CDCl_3$): δ = 1.89 (m, 2H), 2.78 (t, 2H), 3.10 (s, 1H), 3.66 (t, 2H), 5.46 (s, 1H), 7.22-7.25 (m, 3H), 7.27-7.37 (m, 2H) ppm
^{13}C NMR ($CDCl_3$): δ = 22.07, 31.94, 53.99, 61.61, 120.85, 127.93, 128.60, 129.02, 134.78, 147.97 ppm.
Precise attribution of the ^{13}C NMR is given in **Chapter III**.

B.3.4. Preparation of precursors based on $HLaNb_2O_7\cdot xH_2O$ (HLN)

B.3.4.1. Preparation of HLN

A stoichiometric mixture of K_2CO_3, La_2O_3 and Nb_2O_5 was heated at 1100 C for 72 h according to published procedures to obtain a precursor $KLaNb_2O_7$ (KLN).[5]

Then to 400 mL of a 6.5 M aqueous HNO_3 solution, 2 g of KLN was added. The mixture was stirred at room temperature for 24 h. After reactions, the sample was washed with water for four times and acetone for one time by using centrifugation (9000 g, 5 min) and air-dried.

B.3.4.2. C_3OH-HLN.

0.1 g (0.23 mmol) of HLN and a mixture of water and propan-1-ol (8 mL (107 mmol) of propan-1-ol, 1 mL (56 mmol) of water) were sealed in a vial (volume 30 mL). Then the vial was heated in microwave by following an established procedure (heating: from room temperature to 130°C within 2 min; holding time: 2 h; cooling: as fast as possible; stirring speed: 800 rpm; maximum power: 70 W). After reaction, the sample was washed with acetone for three times by using centrifugation (9000 g, 5 min) and air-dried.

B.3.4.3. alkyne-HLN

0.1 g (0.16 mmol) of intermediate C_3OH-HLN and a mixture of water and 4-pentyn-1-ol (2 mL (21.5 mmol) of 4-pentyn-1-ol, 0.5 mL (28 mmol) of water) were sealed in a vial (volume 10 mL), under a protective argon atmosphere. Then the vial was heated with microwave irradiation by following an established procedure (heating: from room temperature to 110°C within 2 min; holding time: 2 h; cooling: as fast as possible; stirring speed: 800 rpm; maximum energy: 70 W). After reaction, the sample was washed with acetone for three times by using centrifugation (9000 g, 5 min) and air-dried.
Anal. Calcd. for $(C_5H_7O)_{0.6}H_{0.4}LaNb_2O_{6.4}\cdot 0.4H_2O$ (M = 470 g/mol): H, 1.1; C, 7.6. Found: H, 0.98; C, 7.09.

B.3.4.4. azide-HLN

0.1 g (0.16 mmol) of intermediate C_3OH-HLN and a mixture of water and 3-azidopropan-1-ol (2 g (19.6 mmol) of 3-azidopropan-1-ol, 0.5 mL (26 mmol) of water) were sealed in a vial (volume 10 mL), under a protective argon atmosphere. Then the vial was heated with microwave irradiation by following an established procedure (heating: from room temperature to 90°C within 1 min; holding time: 2 h; cooling: as fast as possible; stirring speed: 800 rpm; maximum power: 70 W). After reaction, the sample was washed with acetone for three times using centrifugation (9000 g, 5 min) and air-dried.
Anal. Calcd. for $(C_3H_6N_3O)_{0.5}H_{0.5}LaNb_2O_{6.5}\cdot 0.3H_2O$ (M = 470 g/mol): H, 0.9; C, 3.8; N, 4.4. Found: H, 1.04; C, 4.16; N, 4.31.

B.3.5. Post-modification of azide-HLN via microwave-assisted CuAAC click reaction with 1-hexyne.

To a THF (2 mL) solution of $CuBr(PPh_3)_3$ (93 mg (0.10 mmol), 186 mg (0.20 mol), 372 mg (0.40 mmol)) in a microwave vial (volume 10 mL), 50 mg (0.10 mmol) of azide-HLN and 1 mL (8.70 mmol) of 1-hexyne were added under a protective argon atmosphere. Then the vial was heated with microwave irradiation by following an established procedure (heating: from room temperature to 110°C within 2 min; holding time: 2 h; cooling: as fast as possible; stirring speed: 800 rpm; maximum power: 70 W). After reactions, the sample was washed

with THF for three times and acetone for two times, by using centrifugation (9000 g, 5 min) and air-dried.

B.4. Chapter IV

B.4.1. Non-linear optical measurements

As our simples are obtained as powders, it is difficult to measure the ferroelectric behavior since electrical contacts are required. Therefore, we first use non-linear optical measurements and more particularly Second Harmonic Generation (SHG). Since the symmetry requirements for SHG are less restrictive than those for ferroelectric and SHG requires neither cooperative interactions nor electrical contacts, SHG activity can be used as a first positive indication of possible ferroelectric behavior. On the contrary, the absence of SHG activity is a definitive proof of the absence of ferroelectric behavior.

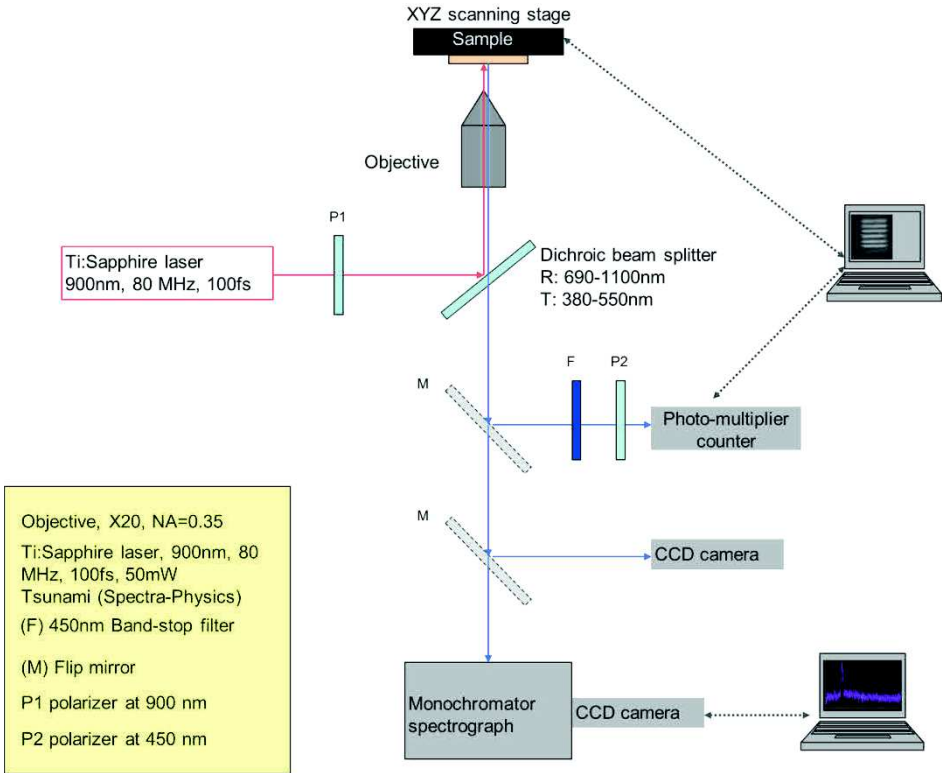

Figure B.IV.1. *Experimental setup used for the SHG measurements.*

The experimental setup used for the SHG measurements of our starting materials BST and HST is shown in ***Figure B.IV.1***. The whole experimental procedure was carried out at room temperature. The incident radiation (900 nm) was provided by a Ti:sapphire laser (pluse width: 100 fs; repetition, 80 MHz). The reflected SHG light (450 nm) was detected by a photo-multiplier counter through color filters.

The obtained results for BST and HST are displayed in ***Figure B.IV.2***. The observed peaks appeared at 450 nm. This indicates that both compounds may present ferroelectricity. Observation of SHG is thus a positive indication that HST may be ferroelectric just like the parent compound BST.

The SHG intensity of HST was found to be weaker than BST. Yet this reduced SHG intensity of HST do not necessarily indicate a weaker ferroelectric behavior, if any.

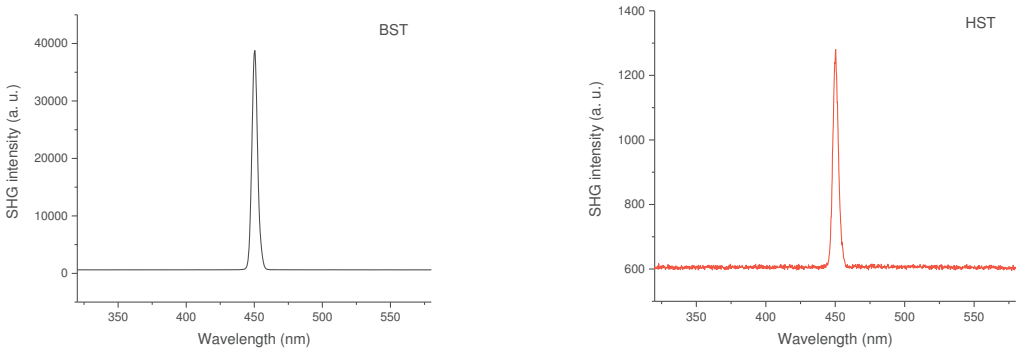

Figure B.IV.2. *Second Harmonic Generation measurement for BST (left) and HST (right).*

B.4.2. In situ reactions between N3-HST and $Cu(NO_3)_2 \cdot 2.5H_2O$ or $CuN3(NO_3)_2$

B.4.2.1. Preparation N3-HST

0.1 g of HST and a mixture of water, THF and bis-(3-aminopropyl)amine (N3) (6 mL of N3, 4 mL of THF and 1 mL of water) were sealed in a microwave vial (volume 30 mL). Then the vial was heated by following an established procedure (heating: from room temperature to 130°C within 2 min; holding time: 1.5 h; cooling: as fast as possible; stirring speed: 800 rpm; maximum power: 70 W). In these conditions, the mean incident power was about 10 W and the autogenous pressure was about 6 bars. After reactions, the sample was washed with acetone for three times by using centrifugation (9000 g, 5 min) and air-dried.
Anal. Calcd. for $(C_6N_3H_{18})_{0.43}H_{1.57}Bi_{0.1}Sr_{0.85}Ta_2O_7 \cdot 2.0H_2O$ (M = 664.53 g/mol): H, 2.10; C, 4.66; N, 2.72; Ta, 54.45. Found: H, 1.99; C, 4.70; N, 2.74; Ta, 54.00.

B.4.2.2. Reaction between N3-HST and $Cu(NO_3)_2 \cdot 2.5H_2O$ (green solid)

$Cu(NO_3)_2 \cdot 2.5H_2O$ (20 mg, 0.086 mmol) was dissolved in 6 mL of water. Then to the solution, 50 mg (0.075 mmol) of the precursor N3-HST was added. The mixture was sealed in a microwave vial (volume 30 mL). Then the mixture was heated in the microwave oven by following an established procedure (heating: from room temperature to 80°C within 2 min; holding time: 0.5 h; cooling: as fast as possible; stirring speed: 800 rpm; maximum power: 70 W). In these conditions, the mean incident power was about 1 W and the autogenous pressure was too low to be measured. After reaction, the samples was washed with water for two times and with acetone for two times by using centrifugation (9000 g, 5 min) and air-dried. A green solid was obtained.
Anal. Calcd. for $Cu_{0.60}(C_6N_3H_{18})_{0.08}H_{0.72}Bi_{0.1}Sr_{0.85}Ta_2O_7 \cdot 4.12H_2O$ (M = 694.59 g/mol): H, 1.50; C, 0.96; N, 0.51; Cu, 5.53; Ta, 52.10. Found: H, 0.75; C, 0.97; N, 0.51; Cu, 5.52; Ta, 52.11.

B.4.2.3. Reaction between N3-HST and $CuN3(NO_3)_2$ (blue solid)

$CuN3(NO_3)_2$: $Cu(NO_3)_2 \cdot 2.5H_2O$ (20 mg, 0.086 mmol) was dissolved in 6 mL of water. Then to the stirred solution, 11.27 mg (0.086 mmol) of N3 was added drop by drop at room temperature. The obtained blue solution was stirred for 5 min and used without further purification.

To the blue solution of $CuN3(NO_3)_2$, 50 mg (0.075 mmol) of N3-HST was added. The mixture was sealed in a microwave vial (volume 30 mL). Then the vial was heated in microwave oven by following an established procedure (heating: from room temperature to 80°C within 2 min; holding time: 0.5 h; cooling: as fast as possible; stirring speed: 800 rpm; maximum power: 70 W). In these conditions, the mean incident power was about 2 W and the autogenous pressure was too low to be measured. After reaction, the sample was washed with water for two times and with acetone for two times by using centrifugation (9000 g, 5 min) and air-dried. A blue solid was obtained.
Anal. Calcd. for $Cu_{0.35}(C_6N_3H_{17})_{0.35}H_{1.30}Bi_{0.1}Sr_{0.85}Ta_2O_7 \cdot 2.06H_2O$ (M = 676.41 g/mol): H, 1.67; C, 3.73; N, 2.17; Cu, 3.31; Ta, 53.50. Found: H, 1.49; C, 4.01; N, 2.16; Cu, 3.28; Ta, 53.50.

B.4.3. In situ reactions between C_2N-HST and $Cu(NO_3)_2 \cdot 2.5H_2O$ or $CuN3(NO_3)_2$

B.4.3.1. Reaction between C_2N-HST and $Cu(NO_3)_2 \cdot 2.5H_2O$ (green solid-2)

$Cu(NO_3)_2 \cdot 2.5H_2O$ (20 mg, 0.086 mmol) was dissolved in 6 mL of water. Then to the solution, 50 mg (0.077 mmol) of the precursor C_2N-HST was added. The mixture was sealed in a microwave vial (volume 30 mL). Then the mixture was heated in the microwave oven by following an established procedure (heating: from room temperature to 80°C within 2 min; holding time: 0.5 h; cooling: as fast as possible; stirring speed: 800 rpm; maximum power: 70 W). In these conditions, the mean incident power was about 1 W and the autogenous pressure was too low to be measured. After reaction, the sample was washed with water for two times and with acetone for two times by using centrifugation (9000 g, 5 min) and air-dried. A green solid was obtained.
Anal. Calcd. for $Cu_{0.30}H_{1.40}Bi_{0.1}Sr_{0.85}Ta_2O_7 \cdot 2.74H_2O$ (M = 640.49 g/mol): H, 1.01; Cu, 2.99; Ta, 56.50. Found: H, 0.75; Cu, 2.96; Ta, 56.50.

B.4.3.2. Reaction between C_2N-HST and $CuN3(NO_3)_2$ (blue solid-2)

To the blue solution of complex $CuN3(NO_3)_2$ ($Cu(NO_3)_2 \cdot 2.5H_2O$ (20 mg, 0.086 mmol) dissolved in 6 mL of water), 50 mg (0.077 mmol) of the precursor C_2N-HST was added. The mixture was sealed in a microwave vial (volume 30 mL). Then the vial was heated in microwave oven by following an established procedure (heating: from room temperature to 80°C within 2 min; holding time: 0.5 h; cooling: as fast as possible; stirring speed: 800 rpm; maximum energy: 70 W). In these conditions, the mean incident power was about 2 W and the autogenous pressure was too low to be measured. After reaction, the sample was

washed with water for two times and with acetone for two times by using centrifugation (9000 g, 5 min) and air-dried. A blue solid was obtained.
Anal. Calcd. for $Cu_{0.39}(C_6N_3H_{17})_{0.37}H_{1.22}Bi_{0.1}Sr_{0.85}Ta_2O_7 \cdot 2.40H_2O$ (M = 687.98 g/mol): H, 1.80; C, 3.90; N, 2.26; Cu, 3.63; Ta, 52.60. Found: H, 1.51; C, 4.47; N, 2.28; Cu, 3.61; Ta, 52.60.

B.4.4. In situ reactions between N3-HST and $Ni(NO_3)_2 \cdot 6H_2O$ or $NiN3(NO_3)_2$

B.4.4.1. Reaction between N3-HST and $Ni(NO_3)_2 \cdot 6H_2O$

$Ni(NO_3)_2 \cdot 6H_2O$ (25 mg, 0.086 mmol) was dissolved in 6 mL of water. Then to the solution, 50 mg (0.075 mmol) of the precursor N3-HST was added. The mixture was sealed in a microwave vial (volume 30 mL). Then the mixture was heated in the microwave oven by following an established procedure (heating: from room temperature to 80°C within 2 min; holding time: 0.5 h; cooling: as fast as possible; stirring speed: 800 rpm; maximum power: 70 W). In these conditions, the mean incident power was about 1 W and the autogenous pressure was too low to be measured. After reaction, the sample was washed with water for two times and with acetone for two times by using centrifugation (9000 g, 5 min) and air-dried.

B.4.4.2. Reaction between N3-HST and $NiN3(NO_3)_2$

In order to prepare the complex $NiN3(NO_3)_2$: $Ni(NO_3)_2 \cdot 6H_2O$ (25 mg, 0.086 mmol) was dissolved in 6 mL of water. Then to the stirred solution, 11 mg (0.086 mmol) of N3 was added drop by drop at room temperature. The obtained light blue solution was stirred for 5 min and used without further purification.

To the solution of complex $NiN3(NO_3)_2$, 50 mg (0.075 mmol) of the precursor N3-HST was added. The mixture was sealed in a microwave vial (volume 30 mL). Then the mixture was heated in the microwave oven by following an established procedure (heating: from room temperature to 80°C within 2 min; holding time: 0.5 h; cooling: as fast as possible; stirring speed: 800 rpm; maximum power: 70 W). In these conditions, the mean incident power was about 1 W and the autogenous pressure was too low to be measured. After reaction, the sample was washed with water for two times and with acetone for two times by using centrifugation (9000 g, 5 min) and air-dried.

B.4.5. Other precursors N4-HST, PA-HST and $cyclam(NH_2)_4$-HST

N,N'-bis(3-aminopropyl)-ethylenediamine (N4) was used from commercial sources.
4-(2-aminoethyl)-pyridine (PA) was synthesized from published procedures.[6]
N,N',N'',N'''-tetra(3-aminopropyl)-1,4,8,11-tetra-azacyclotetradecane ($cyclam(NH_2)_4$) was prepared according to described protocols.[7-10]

0.1 g (0.15 mmol) of C_2N-HST and a mixture of water (1 mL for N4 and 5 mL for PA and $cyclam(NH_2)_4$), THF (4 mL for N4 or $cyclam(NH_2)_4$ and 1 mL for PA) and amines (6 mL, (33 mmol) of N4; 5 g (41 mmol) of PA; 500 mg (1.3 mmol) of $cyclam(NH_2)_4$) were sealed in a microwave vial (volume 30 mL). Then the vial was heated by following an established

procedure (heating: from room temperature to 130°C within 2 min; holding time: 1.0 h; cooling: as fast as possible; stirring speed: 800 rpm; maximum power: 70 W). In these conditions, the mean incident power was about 10 W and the autogenous pressure was around 2 bars. After reactions, the sample was washed with acetone for three times by using centrifugation (9000 g, 5 mins) and air-dried. The results of elemental analysis and the proposed formulae are given in ***Table B.IV.1***.

Products	Formula	C Found (calcd) (%)	H Found (calcd) (%)	N Found (calcd) (%)
N4-HST	$(C_8N_4H_{24})_{0.3}H_{1.4}Bi_{0.1}Sr_{0.85}Ta_2O_7{\cdot}1.0H_2O$	4.90 (4.4)	1.74 (1.6)	2.90 (2.6)
PA-HST	$(C_7N_2H_{11})_{0.4}H_{1.6}Bi_{0.1}Sr_{0.85}Ta_2O_7{\cdot}0.9H_2O$	5.10 (5.3)	1.21 (1.2)	1.98 (1.8)
cyclam$(NH_2)_4$-HST	$(C_{20}N_8H_{52})_{0.2}H_{1.2}Bi_{0.1}Sr_{0.85}Ta_2O_7{\cdot}0.5H_2O$	7.57 (7.3)	2.05 (1.9)	3.17 (3.4)

Table B.IV.1. *Elemental micro-analyses (C, H, N) and consistent proposed formulae.*

.

References

[1] S. Ida, C. Ogata, U. Unal, K. Izawa, T. Inoue, O. Altuntasoglu, Y. Matsumoto, *J. Am. Chem. Soc.* **2007**, *129*, 8956-8957.

[2] Y.-S. Ye, W.-C. Shen, C.-Y. Tseng, J. Rick, Y.-J. Huang, F.-C. Chang, B.-J. Hwang, *Chem. Commun.* **2011**, *47*, 10656-10658.

[3] J. Sinha, R. Sahoo, A. Kumar, *Macromolecules* **2009**, *42*, 2015-2022.

[4] C. Zanato, M. G. Cascio, P. Lazzari, R. Pertwee, A. Testa, M. Zanda, *Synthesis* **2015**, *47*, 817-826.

[5] S. Takahashi, T. Nakato, S. Hayashi, Y. Sugahara, K. Kuroda, *Inorg. Chem.* **1995**, *34*, 5065-5069.

[6] T. Steinmetzer, A. Schweinitz, A. Stürzebecher, D. Dönnecke, K. Uhland, O. Schuster, P. Steinmetzer, F. Müller, R. Friedrich, M. E. Than, W. Bode, J. Stürzebecher, *J. Med. Chem.* **2006**, *49*, 4116-4126.

[7] E. K. Barefield, F. Wagner, K. D. Hodges, *Inorg. Chem.* **1976**, *15*, 1370-1377.

[8] K. P. Wainwright, *J. Chem. Soc., Dalton Trans.* **1980**, 2117-2120.

[9] K. P. Wainwright, *J. Chem. Soc., Dalton Trans.* **1983**, 1149-1152.

[10] G. Rogez, Ph-D., Université Paris XI, 2002.

Extended abstract (in French)

Introduction générale

Mon travail de thèse a pour cadre général le domaine de la Chimie Douce,[1] qui a connu un succès croissant ces quarante dernière années en chimie des matériaux.[2-8] La voie de synthèse "chimie douce" a permis un développement considérable de la synthèse de matériaux multifonctionnels par une approche matériaux hybrides.[7] L'approche matériaux hybrides, qui consiste en l'assemblage contrôlé à l'échelle nanoscopique d'au moins deux composants fonctionnels, qui combinent ainsi leurs propriétés dans le matériau final, soit de manière composite, soit en synergie,[9,10] est devenue l'une voies les plus efficaces pour l'obtention de matériaux multifonctionnels (***Figure EA.1***).[10,11] En effet, la synthèse de composés hybrides par voie chimie douce présente de nombreux avantages: elle permet la fonctionnalisation relativement facile par les espèces moléculaires, elle permet de faire appel à diverses réactions et enfin elle permet l'ajustement fin des propriétés. En fonction de la nature de l'interface, les hybrides organiques-inorganiques peuvent être divisés en deux classes distinctes. Les hybrides de classe I mettent en jeu des liaisons faibles (liaisons hydrogène, de van der Waals ou liaisons ioniques) tandis que les hybrides de classe II impliquent des liaisons chimiques fortes (liaisons covalentes ou iono-covalentes).[12]

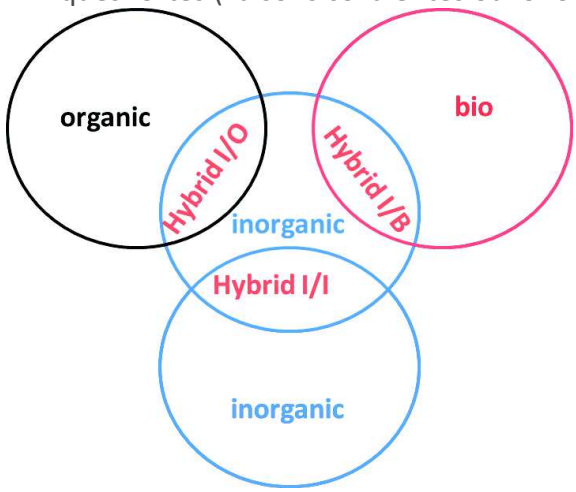

Figure EA.1. *Illustration schématique des principaux types de matériaux hybrides.*

Dans le domaine des matériaux multifonctionnels, les composés multiferroïques (c'est-à-dire des matériaux présentant la coexistence d'au moins eux ordres parmi les ordres électrique, magnétique ou élastique) ont reçu beaucoup d'attention (***Figure EA.2.***).[13,14] En termes d'applications possibles, les composés comportant un couplage magnéto-électrique sont les plus intéressants. Cependant, les matériaux multiferroïques intrinsèques sont rares, ce qui est expliqué par le fait que les ordres électriques et magnétiques ont tendance à être mutuellement exclusifs.[15]

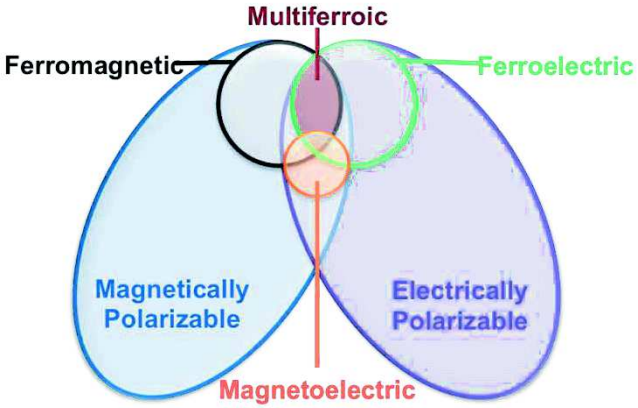

Figure EA.2. *Illustration schématique des composés multiferroïques.*

L'utilisation de l'approche hybride, basée sur la voie chimie douce, pour concevoir et préparer des composés multiferroïques potentiels semble une approche prometteuse.[16] En effet les hybrides présentent de nombreux avantages d'hybrides tels que la possibilité de concevoir des blocs de construction moléculaires pour induire un comportement ferroélectrique, une aimantation plus élevée ou la présence de sous-réseaux imbriqués susceptibles d'induire un couplage magnéto-électrique. Cependant, en dehors de quelques exemples (MOF de type pérovskite,[16-20] pérovskites lamellaires de type AMX_4 ou A_2MX_4[21] et oxalates bimétalliques[22,23]), l'approche matériaux hybrides par des voies de chimie douce n'a pas encore été beaucoup explorée dans le domaine des composés multiferroïques.
Les systèmes lamellaires sont particulièrement adaptés à l'approche hybride, en raison de la polyvalence des réactions d'insertion qui peuvent être réalisées et la multiplicité des propriétés qui en résulte.[24] Parmi les matériaux lamellaires, les pérovskites lamellaires ou les composés lamellaires à structure proche de celle des pérovskites demeurent un sujet de prédilection des études en chimie du solide et en science des matériaux. Ils présentent des propriétés physiques particulièrement intéressantes telles que la ferroélectricité avec faible fatigabilité,[25-30] la luminescence,[31] des propriétés photovoltaïques,[32] photocatalytiques,[33] photoelectrochimiques[34] ou encore magnétiques.[35] Par conséquent, les hybrides organiques-inorganiques basés sur les pérovskites lamellaires sont des candidats prometteurs pour présenter un ordre multiferroïque car ils possèdent en même temps des structures flexibles et des propriétés magnétiques ou électriques.
La formule générale des pérovskites peut s'écrire ABX_3, où A est un gros cation électropositif (du bloc s, d ou f),[5] B est un cation de métal de transition et X est un anion. Les oxydes étant majoritaires dans cette famille, la formule peut également s'écrire directement ABO_3. La ***Figure EA.3*** représente la structure perovskite de base. Le cation B est situé au centre d'un site octaédrique formé d'anion oxygène. Le cation A est situé au centre des cavités interstitielles, et est entouré de 8 octaèdres BO_6. Parmi les pérovskites oxydes, les pérovskites lamellaires sont particulièrement intéressantes pour nous pour leur fonctionnalisation. Les oxydes pérovskites lamellaires sont classés en trois familles principales: Dion-Jacobson, Ruddlesden-Popper et Aurivillius.[5] Ces différentes phases ont connu un intérêt croissant dans les dernières décennies, à cause de leurs propriétés d'échange d'ion, et leurs nombreuses propriétés physiques intéressantes (photocatalyse,[33] photovoltaïque[32] etc…). Les phases d'Aurivillius, par exemple $Bi_2SrTa_2O_9$ qui est bien connue pour ses propriétés ferroélectriques,[25] ont naturellement retenu notre attention.

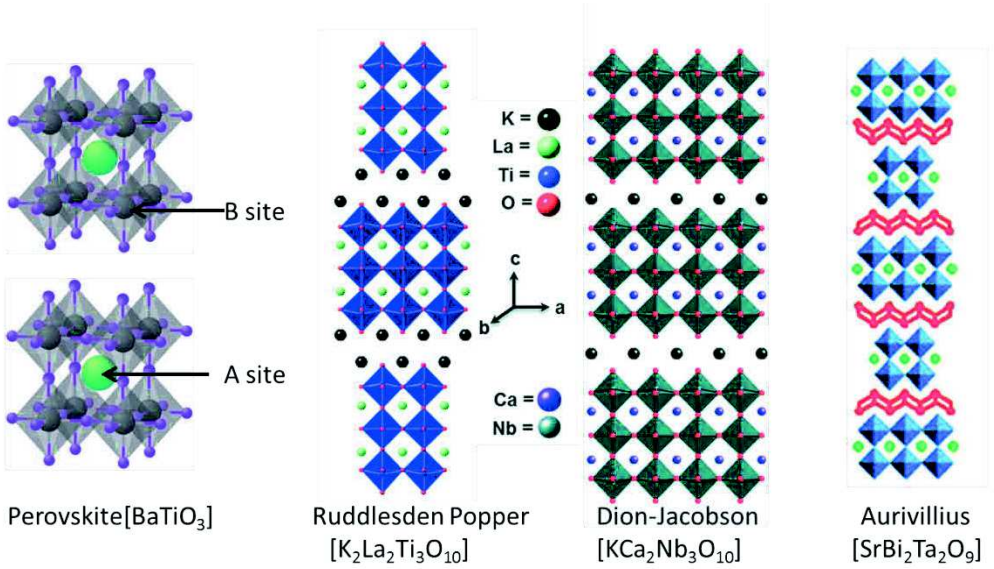

Figure EA.3. *Structures représentatives des pérovskites et pérovskites lamellaires.*[5,36,37]

Récemment, des voies chimie douce ont été développées pour la synthèse de nouveaux matériaux basés sur des structures pérovskites.[5,38] Les pérovskites lamellaires sont ainsi considérés comme des candidats prometteurs pour l'obtention de nouveaux matériaux multiferroïques. Les voies de synthèse possibles sont essentiellement l'échange ionique, l'insertion, le greffage et l'exfoliation (***Figure EA.4***.)

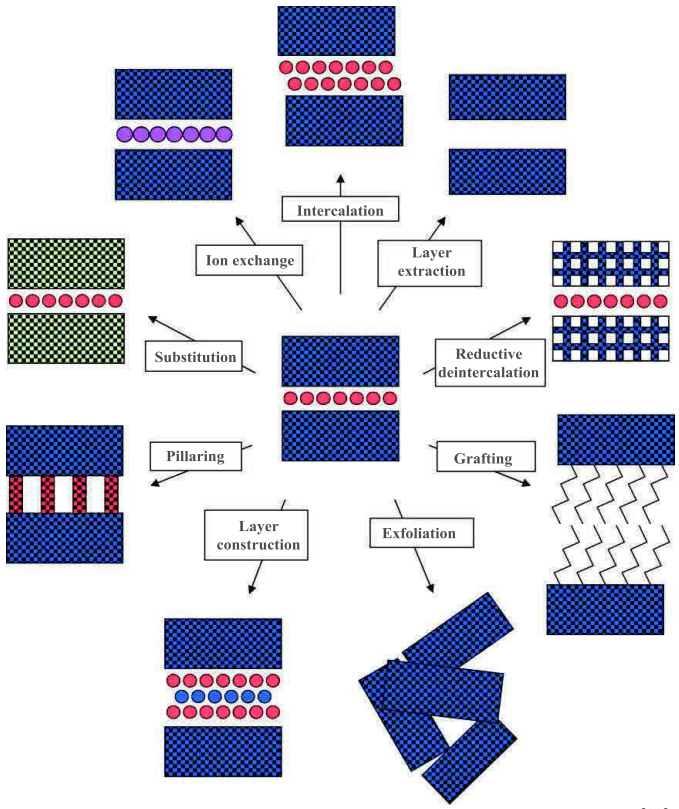

Figure EA.4*. Voies de synthèse pour la fonctionnalisation de pérovskites lamellaires.*[38]

L'un des objectifs à long terme du laboratoire consiste à synthétiser et à caractériser de nouveaux matériaux hybrides multiferroïques par la fonctionnalisation de phases Aurivillius. En effet de tels matériaux hybrides multiferroïques pourraient constituer une alternative

intéressante aux multiferroïques oxydes obtenus en chimie du solide.[20,22,39] Dans le cadre de cet objectif général, mon travail de thèse a consisté en la compréhension et l'amélioration des mécanismes de fonctionnalisation d'une phase Aurivillius $Bi_2SrTa_2O_9$ (BST). La littérature rapporte en effet la fonctionnalisation de telles phases pérovskites lamellaires, mais le mode opératoire utilisé est extrêmement long (plus d'une semaine de réaction), et les molécules insérées jusque-là sont extrêmement simples (amines ou alcools aliphatiques uniquement).

Travail de thèse

Dans la première partie de mon travail de thèse, nous avons donc développé de nouveaux outils pour la fonctionnalisation d'une phase Aurivillius $Bi_2SrTa_2O_9$ (BST), basé sur le chauffage micro-ondes, ce qui permet de protoner et fonctionnaliser la phase de BST en environ 5 heures de réaction.
L'acidification assistée par micro-ondes de la phase BST conduit à un composé (***Figure EA.5***) de formule élémentaire $H_2Bi_{0.1}Sr_{0.85}Ta_2O_7$, ci-après désigné par HST. La formule est en bon accord avec celle obtenue par traitement de BST dans les conditions classiques, à température ambiante, utilisées par *Tsunoda et al.*.[40] La petite différence dans le rapport final Bi:Sr:Ta peut être attribuée à une petite différence dans le désordre de cations (Bi↔Sr) dans les composés BST initiaux.[40-42] La taille des cristallites peut être évaluée en utilisant la formule de Scherrer, et comparée avec celle obtenue lorsque le procédé classique de protonation est utilisé (HCl à 4 M, température ambiante, 5 jours).[40] Il apparaît que la protonation assistée par micro-ondes ne modifie pas sensiblement la taille des cristallites dans les dimensions latérales. Dans la direction 00l la taille est réduite par rapport à un composé HST synthétisé dans les conditions classiques, mais reste dans la fourchette de ce qui a été rapporté dans la littérature pour HST.[40,43] Il convient de noter cependant qu'une température supérieure à 70 ° C conduit très rapidement à une diminution sensible de la cristallinité.

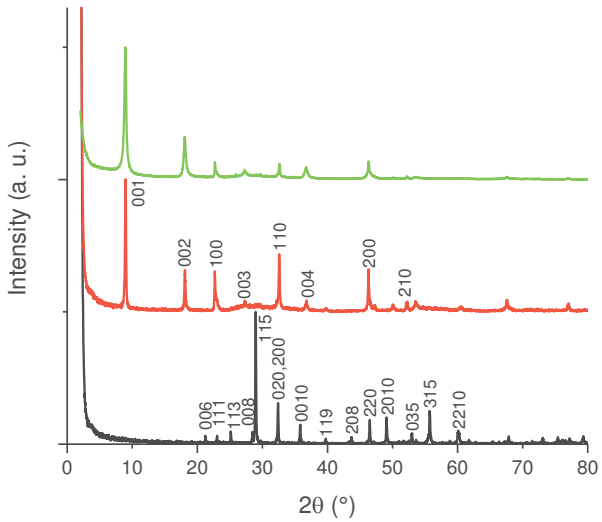

Figure EA.5. *Diagrammes de diffraction des rayons X sur poudre de BST (noir), HST "par voie classique" (rouge) et HST synthétisé par voie micro-onde (vert).*

Nous avons ainsi réussi à obtenir des composés fonctionnalisés par des *n*-alkylamines ou des α,ω-alkyldiamines identiques à ceux décrits dans la littérature,[44,45] mais de manière beaucoup plus rapide (5 heures contre une dizaine de jours).
Grâce à cette accélération considérable des processus réactionnels, nous avons pu étudier l'influence de certains paramètres tels que le solvant et la température de réaction. Nous avons par ailleurs mis au point une stratégie particulièrement efficace, dite de pré-intercalation. La phase protonée HST est pré-fonctionnalisé avec de l'éthylamine et la phase ainsi obtenue C_2N-HST est ensuite utilisée comme produit de départ à la place de HST. Cette stratégie nous a permis d'insérer des amines beaucoup plus complexes, telles que des polyamines, la cyclohexylamine, ou des amines portant des groupes aromatiques (***Figure 6***).

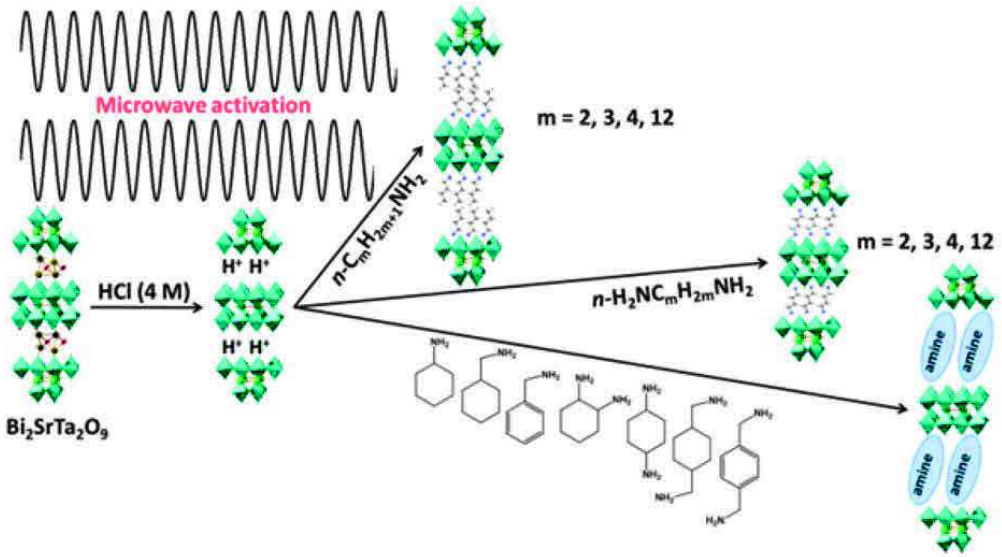

Figure EA.6. *Fonctionnalisation de HST assistée par micro-onde par des n-alkylamines, α,ω-alkyldiamines ou des amines beaucoup plus complexes.*

Parmi les matériaux hybrides obtenus, HST intercalé par la phényl-butylamine (PBA) peuvent présenter plusieurs distances inter-lamellaires, ce qui peut être contrôlé par les protocoles de préparation (***Figure EA.7***). Les phases obtenues par reaction d'intercalation directe entre HST et PBA *via* activation micro-one (130 °C, 1,5 h) ou par chauffage classique (130 °C, 18 h) sont notées PBA1-HST et PBA3-HST respectivement. La phase PBA2-HST est obtenue par irradiation micro-onde (130 °C, 1,5 h) en utilisant C_2N-HST comme intermédiaire. Après réaction, la distance interlamellaire augmente depuis celle de HST (0,98 nm) à 2,20 nm pour PBA1-HST et jusqu'à 3,00 nm pour PBA3-HST. Pour PBA2-HST, la distance interlamellaire passe de 1,57 nm dans C_2N-HST à 2,67 nm.

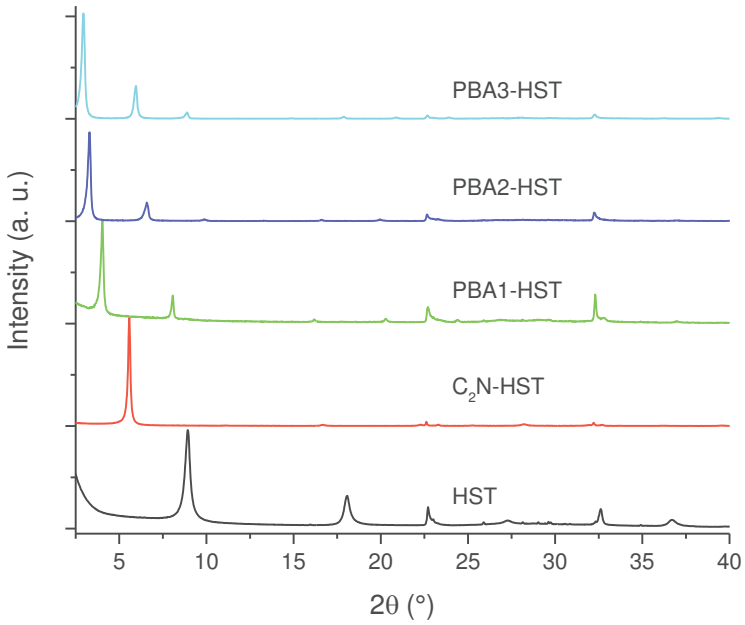

Figure EA.7. *Diagrammes de diffraction des rayons X sur poudre de HST, C_2N-HST, PBA1-HST, PBA2-HST et PBA3-HST.*

Jusqu'à présent, nous n'avons pas pu obtenir des informations qui pourraient aider à préciser la disposition des molécules PBA dans l'espace interlamellaire de HST ni à établir les raisons pour lesquelles des arrangements différents sont obtenus en fonction des conditions de réaction. Des profils de densité électronique 1D sont actuellement extraites diagrammes de diffraction (collaboration C. Taviot-Guého, Institut de Chimie de Clermont-Ferrand) (des diagrammes de poudre de grande qualité ont été obtenus, montrant au moins dix harmoniques pour la famille 00l). Nous espérons que cette analyse permettra de préciser les arrangements intracouche.[46]

Dans une deuxième partie, nous avons étendu cette approche au greffage de divers alcools dans HST, toujours en utilisant des réactions assistées par micro-ondes. La modification de surface de composés lamellaires par des reactions de greffage pour preparer divers matériaux hybrides organique-inorganic a été largement étudiée.[47-53] Les hybrids obtenus possèdent des liaisons fortes, de type iono-covalent entre les molecules et les couches inorganiques.[54] Cette stratégie de modification de surface par l'intermédiaire de réactions de greffage est adaptée aux couches perovskites à ions échangeables qui comprennent les phases Dion-Jacobson et les phases Ruddlesden-Popper. Cependant, les méthodes publiées sont limitées à l'utilisation de reflux et d'autoclave, et ont l'inconvénient majeur d'être très longues (typiquement de plusieurs jours).
Les tentatives de modification directe de HST par EtOH ont échoué. Selon les travaux de *P. van der Voort et al.*, les amines primaires sont connues comme catalyseurs pour favoriser la silylation de la surface de la silice et de la formation de liaisons Si-O-Si.[55] De plus, une phase très similaire, une perovskite protonée $H_2CaTa_2O_7$, a pu être fonctionnalisée par greffage de *n*-alcools en utilisant comme intermédiaire le compose $H_2CaTa_2O_7$ fonctionnalisé par une *n*-alkylamine.[56,57] Par conséquent, la réactivité de HST avec des *n*-alkylamines, étudiée dans la première partie, offre une possibilité de fonctionnalisation de ce type de pérovskites par des

alcools en deux étapes. Trois intermédiaires différents ont été choisis comme composés de départ: NH_3-HST (HST intercalés par un ion ammonium), C_2N-HST (HST fonctionnalisé par l'éthylamine) et C_4N-HST (HST fonctionnalisé par la butylamine). Il apparaît que l'intermédiaire NH_3-HST ne réagit pas avec les *n*-alcools (partiellement avec du méthanol), ce qui montre que la présence d'un groupe NH_3^+ est insuffisante pour favoriser les réactions de greffage dans HST. Cependant, l'intermédiaire C_2N-HST peut réagir avec certains *n*-alcools relativement courts (méthanol, éthanol, propan-1-ol et butan-1-ol) et l'intermédiaire C_4N-HST peut réagir avec de nombreux $_n$-alcools (au moins jusqu'au dodécan-1-ol) (***Figure EA.8***). Cela prouve l'importance des groupes *n*-alkyle dans l'espace inter-couches de perovskite en couches. Et il apparaît que les groupes $_n$-alkyle les plus longs sont les plus efficaces.

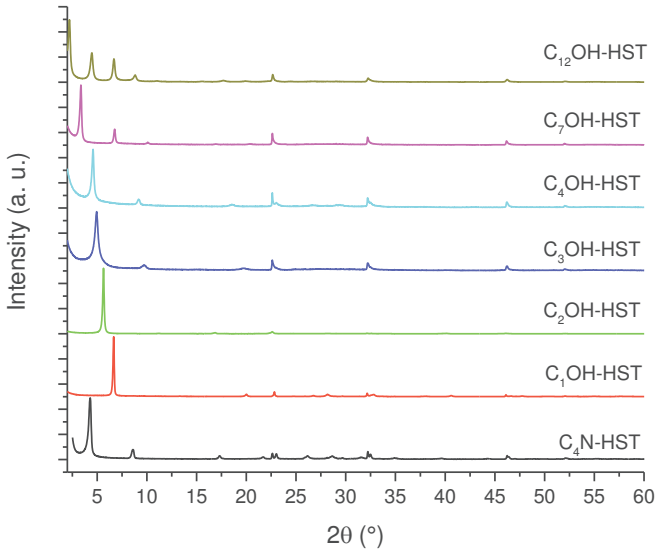

Figure EA.8. *Diagrammes de diffraction des rayons X sur poudre de C_4N-HST et de ses produits de reaction avec divers n-alcohols (C_nOH, n = 1, 2, 3, 4, 7, 12).*

Il a déjà été décrit que de nombreux dérivés alkoxy de $HLaNb_2O_7{\cdot}xH_2O$, $HCa_2Nb_3O_{10}{\cdot}xH_2O$ et $H_2La_2Ti_3O_{10}$ peuvent être obtenus par des réactions d'échange d'alcool, avec un dérivé *n*-alkoxy comme compose de départ.[58-60] Ici aussi, il nous a semblé raisonnable d'essayer de préparer des dérivés *n*-alkoxy de HST en utilisant des réactions d'échange d'alcool, puisque des dérivés *n*-alkoxy similaires ont pu être obtenus à partir de C_2N-HST ou de C_4N-HST. Parmi les dérivés *n*-alkoxy obtenus, C_2OH-HST a été choisi comme composé de départ pour réagir avec quelques *n*-alcohols (C_nOH, n = 3, 4, 7, 12) en utilisant l'irradiation micro-onde. Ainsi, ls dérivés *n*-alkoxy de of HST ont pu être obtenus par reaction d'échange à partir de C_2OH-HST, et ces composés sont exactement identiques à ceux obtenus en utilisant C_4N-HST comme intermédiaire.

La réactivité de HST vis-à-vis des α, ω-alkyldiamines[45] nous a conduit à explorer le greffage de ω-alkanediols dans HST. C_4N-HST a été choisi comme intermédiaire (ce composé est facile à préparer et sa réactivité vis-à-vis des alcools a été démontrée) pour réagir avec quelques α, ω-alkanediols ($C_n(OH)_2$, n = 2, 4, 8, 12) en utilisant l'irradiation micro-onde. A notre connaissance, la réactivité des pérovskites lamellaires vis-à-vis des diols n'a été décrite qu'une seule fois, lors du greffage d'éthylène glycol dans une phase Dion-Jacobson $HLaNb_2O_7$.[58]

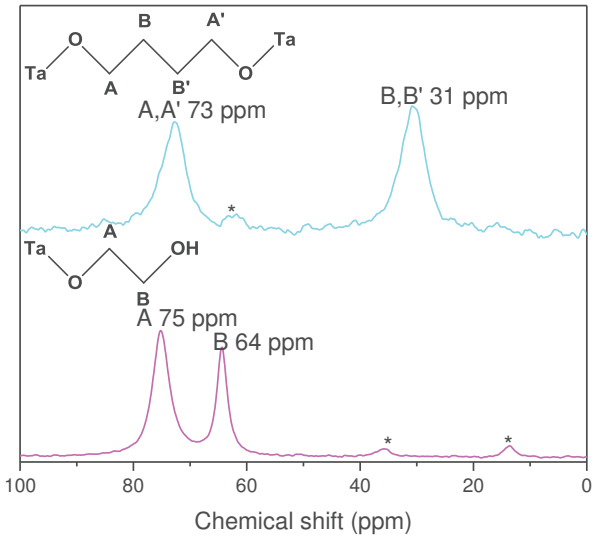

Figure EA.9. *Spectre RMN solide ^{13}C CP/MAS NMR de $C_2(OH)_2$-HST et de $C_4(OH)_2$-HST.*

L'arrangement en double couche de $C_2(OH)_2$ dans l'espace interlamellaire de HST (***Figure EA.9***) est en bon accord avec la littérature sur la phase Dion-Jacobson phase $HLaNb_2O_7 \cdot xH_2O$.[58] Cependant, à notre connaissance, l'arrangement en piliers de α, ω-alkanediols dans l'espace interlamellaire de pérovskites lamellaires n'a jamais été décrit dans la littérature. La modification de la Kaolinite par des propanediols a été décrite.[61] Seul l'un des deux groupes –OH des 1, 2- et 1, 3-propanediol est lié aux couches inorganiques. Lorsque le temps de réaction est augmenté, les molécules de 1, 3-propanediols forment un arrangement où les deux groupes OH sont liés à la même couche inorganique. Le modification de la Kaolinite par des butanediols a également été rapportée, et ne montre pas d'arrangement en pilier.[62] Les reactions de greffage entre $HLaNb_2O_7 \cdot xH_2O$ et des polyethylene glycols (PEGs) de différentes masses moléculaires ont été explores et montrent uniquement des arrangements mono-greffage.[63] Enfin, la fonctionnalisation de la phase Dion-Jacobson phase $HLaNb_2O_7$ par le D-glucopyranose montre également un mono-greffage.[64]

Afin d'étendre la plage d'application des réactions de greffage entre HST et les alcools, nous avons testé des alcools plus encombrés, autres que des alcools aliphatiques linéaires. Ainsi, le 2-propanol, *tert*-butanol et l'alcool benzylique ont été testé. Des hybrides monophasiques purs ont été obtenus, sauf pour le *tert*-butanol, ce qui sûrement dû à son encombrement stérique important.

Pendant l'exploration des conditions de réaction appropriées pour le greffage, le role de l'eau a été mis en évidence, que l'on utilise C_4N-HST ou C_2OH-HST comme compose de départ. Cette importance de l'eau avait déjà été mise en évidence dans le premier chapitre sur l'insertion d'amines. Son rôle a également déjà été souligné dans la littérature.[56,59,65]

Une série de réaction a été testée en faisant varier la quantité d'eau utilisée (0, 1 ou 20 % en masse par rapport à l'alcool)

Pour C_4N-HST (***Figure EA.10***), quand on n'ajoute pas d'eau, aucune réaction ne se produit. En revanche, l'utilisation de 1% en masse d'eau conduit à la diminution de la distance interlamellaire, en accord avec celle obtenue pour la formation de C_3OH-HST (1,77 nm). Pour les quantités d'eau importante (20% en masse), la distance interlamellaire augmente de 2,05

nm pour C_4N-HST à 2,80 nm, et la cristallinité diminue. Cela peut suggérer un phénomène de swelling, tel que décrit par T. Sasaki *et al.*.[66] Pendant la durée de cette these, je n'ai pas eu le temps d'étudier ce phénomène de manière plus approfondie. Cependant, il est très prometteur qu'un phénomène de swelling assisté par micro-onde puisse être apparemment être observé, car cela ouvre la voie à l'exfoliation assistée par micro-onde, qui serait plus rapide, et éventuellement avec de meilleurs rendements que les procédures classiques.

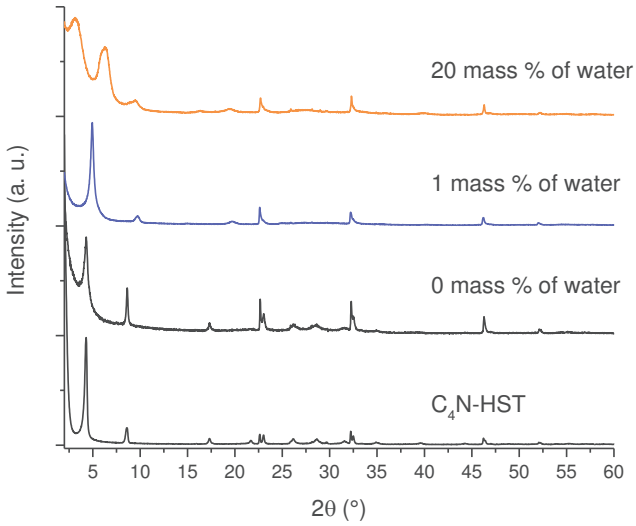

Figure EA.11. *Diagrammes de diffraction des rayons X sur poudre de C_4N-HST et des produits de réactions avec le propan-1-ol et l'eau (0% en masse, 1% et 20%).*

Les réactions de greffage d'alcools semblent donc relativement sensible à la quantité d'eau. Pour l'insertion d'amines, l'eau est nécessaire, mais contrairement aux alcools, il semble que la quantité d'eau ne soit pas un paramètre crucial (même si nous n'avons pas effectué d'étude exhaustive sur ce point). De plus, les insertions d'amines ont essentiellement été réalisée dans le THF, tandis que le greffage d'alcools utilise l'alcool comme solvant. Par conséquent, il semble nécessaire d'étudier la réactivité comparée des amines et des alcools et comment les conditions de réaction (la quantité d'eau par exemple) peuvent influer sur la réactivité préférentielle de HST envers les amines ou les alcools. Cette étude est particulièrement intéressante en vue de l'insertion de molécules complexes, comportant plusieurs groupes réactionnels.
Nous avons alors entrepris une série de réactions en utilisant le 5-amino-pentan-1-ol dissout dans le THF (1/1 v:v), avec comme variable la quantité d'eau (de 1% à 100% en masse par rapport au 5-amino-pentan-1-ol).

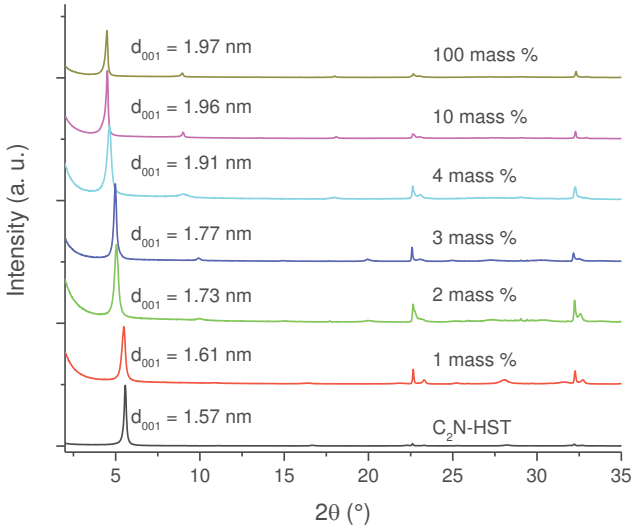

Figure EA.11. *Diagrammes de diffraction des rayons X sur poudre de C_2N-HST et des produits issus de la reaction avec le 5-amino-1-pentanol et différentes quantités d'eau.*

La distance interlamellaire des composés obtenus varie entre 1,6 nm et 2,0 nm (***Figure 11***), ce qui est attribué à un changement de l'arrangement du 5-amino-1-pentanol dans l'espace interlamellairen d'un arrangement en connecteur (pilier) à un arrangement en double couche.

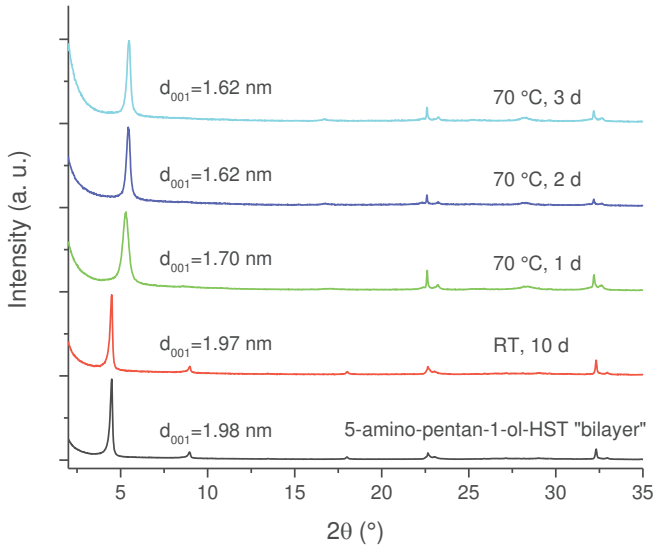

Figure EA.12. *Diagrammes de diffraction des rayons X sur poudre de 5-amino-pentan-1-ol-HST en double couche, et des produits obtenus après différents traitements thermiques.*

L'arrangement en double couche du 5-amino-pentan-1-ol dans l'espace interlamellaire de HST laisse du même coup les groupes OH libres. Ces groupes peuvent potentiellement se greffer par la suite dans l'espace interlamellaire de HST, conduisant à un arrangement en pilier ou connecteur. L'hybride possédant un arrangement en bicouche a ainsi été soumis à différents traitements thermiques à 70°C pendant 1, 2 ou 3 jours. La stabilité de cet hybride

a également été testée sur 10 jours à température ambiante. Quand le composé est chauffé à 70°C pendant une journée, la distance interlamellaire diminue de 1,98 nm à 1,70 nm, et diminue encore à 1,62 nm quand le chauffage est prolongé jusqu'à 2 jours (***Figure 12***). Des temps de chauffage plus longs ne conduisent pas à d'autres modifications de la distance interlamellaire. Il est remarquable que la distance qui est obtenue après chauffage (1,62 nm) est identique à celle obtenue par réaction entre C_2N-HST et le 5-amino-pentan-1-ol avec 1% en masse d'eau, ce qui correspond à un arrangement en pilier du 5-amino-pentan-1-ol.

Dans la troisième partie, nous avons développé une réaction *in situ*, pour ne plus être limités aux réactions d'insertion ou de greffage. La réaction qui a été choisie est la cyclo-addition 1,3-dipolaire catalysée (ou réaction "click"), assistée par micro-onde (***Figure EA.13***).

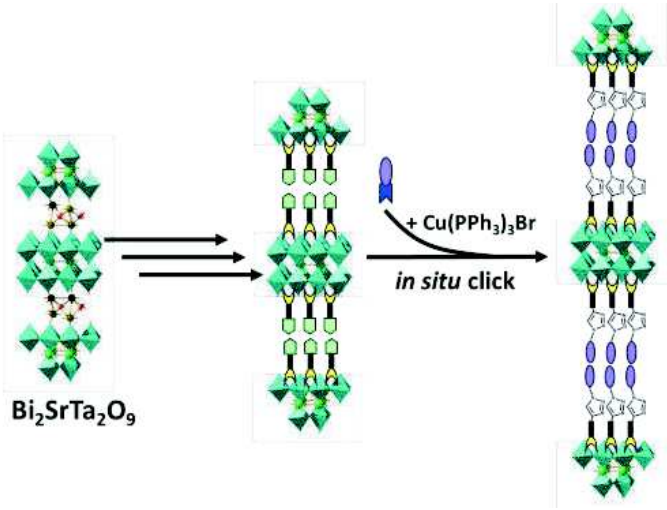

Figure EA.13. *Modification post-synthèse de la phase d'Aurivillius $Bi_2SrTa_2O_9$ par une cycloaddition alcyne-azide catalysée par le cuivre(I).*

La modification post-synthèse peut en effet être propose pour surmonter la difficulté à insérer directement des espèces moléculaires complexes ou peu réactives. Selon cette stratégie, la molécule désirée est synthétisée *in situ*, dans l'espace interlamellaire. La stratégie de modification post-synthèse (PSM) a été proposée au début des années 90,[67] et réellement développée dans le cadre des MOFs dix ans plus tard.[68] L'utilisation de la PSM a fait l'ojet de plusieurs revues récentes.[69-71] La PSM a également été employée pour les matériaux micro-poreux[72] ou pour les silices mésoporeuses.[73,74]
Dans le domaine des matériaux lamellaires, la PSM a été peu utilisée : dans les argiles,[75,76] les silicates lamellaires,[77] les Hydroxydes Doubles Lamellaires[78,79] et plus récemment dans les Hydroxydes Simple Lamellaires.[80] A notre connaissance, la stratégie de modification post-synthèse n'a été utilisée qu'une seule fois dans le domaine des pérovskites lamellaires, pour l'hydrosilylation *in situ* d'une phase Dion-Jacobson.[81]
Les réactions "click" (ou CuAAC) se sont révélées être particulièrement utiles en chimie moléculaire, en ce qu'elles sont très efficaces, avec d'excellents rendements, peu de sous-produits et compatibles avec la plupart des groupes fonctionnels.[82] Comme pour d'autres réactions,[83,84] l'utilisation des micro-onde pour les réactions de chimie click a été beaucoup développée récemment en synthèse moléculaire.[83-88] Dans les dernières années, les

réactions CuAAC ont été utilisées pour la PSM dans un grand nombre de MOFs, soit la modification sélective de surface,[89] soit pour la fonctionnalisation interne.[90-95]
Afin de réaliser notre objectif de post-modification *in situ*, la première étape est de synthétiser un précurseur fonctionnalisé, par un alkyne terminal ou par un groupe azide. A la suite des résultats obtenus sur l'insertion d'amines par activation micro-onde,[96] nous avons tout d'abord cherché à fonctionnaliser HST par des amines portant un groupe alcyne terminal (4-pentyn-1-amine[97]). Malheureusement, ces réactions ont échoué, du fait de l'instabilité des molécules organiques dans les conditions de greffage. Par conséquent nous avons mis à profit les possibilités de greffage d'alcools dans l'espace interlamellaire.[58,60,98]
Dans ce troisième chapitre, nous présenterons tout d'abord l'immobilisation rapide du 4-pentyn-1-ol et du 3-azidopropan-1-ol dans l'espace interlamellaire de HST. Malheureusement, nous avons montré que la modification de HST par le 3-azidopropan-1-ol était incomplète (***Figure EA.14***).

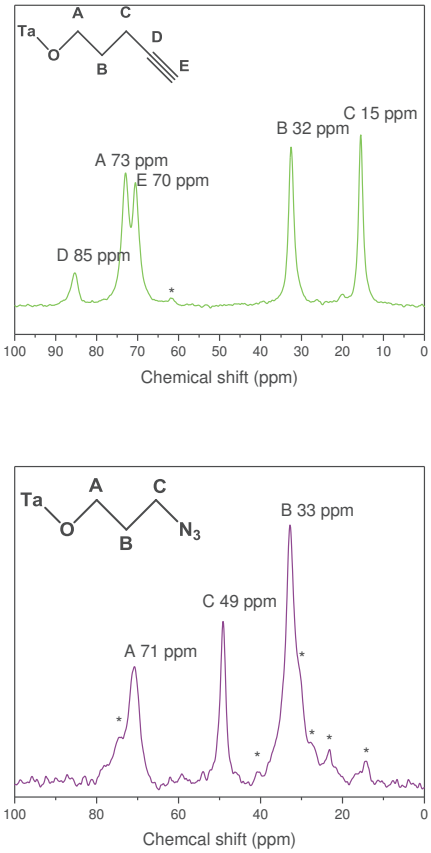

Figure EA.14. *Spectres RMN solide ^{13}C CP/MAS de alkyne-HST (gauche) et de azide HST (droite).*

La reaction suivante, la CuAAC entre le précurseur alkyne-HST et l'azidohexane ou l'azidobenzene a été ensuite menu *in situ* et par activation micro-ondes (***Figure EA.13***). Plusieurs catalyseurs différents ont été testés, tels que le Cu métal,[99] Cu métal/$CuSO_4$,[100] CuI,[101,102] CuI/EtN,[103-105] et CuBr/CH_3SCH_3,[106,107] malheureusement sans résultat positif, quels que soient le solvant ou les conditions de température. L'utilisation du célèbre catalyseur $CuSO_4$/acorbate de sodium ascorbate conduit à un succès seulement partiel de la réaction click, avec la présence notamment du composé de départ et de HST dans le produit final. Ceci est probablement dû à l'utilisation d'eau, nécessaire avec ce catalyseur, qui

conduit à l'hydrolyse de la liaison alcool-Ta.[58] En effet le précuseur peut être vu comme un oxoalkoxyde macromoléculaire hétérométallique,[59] qui est donc sensible à l'hydrolyse, spécialement à hautes températures.[58,59] Notre choix de catalyseur s'est donc porté sur $CuBr(PPh_3)_3$ qui peut être utilisé dans des solvants non-acqueux ou aprotiques, typiquement le THF sec.[108-110] Nous avons particulièrement détaillé l'optimisation de la quantité de catalyseur, car un excés de catalyseur dans le produit final peut-être un grand obstacle à la caractérisation du matériau, par RMN du solide par exemple.

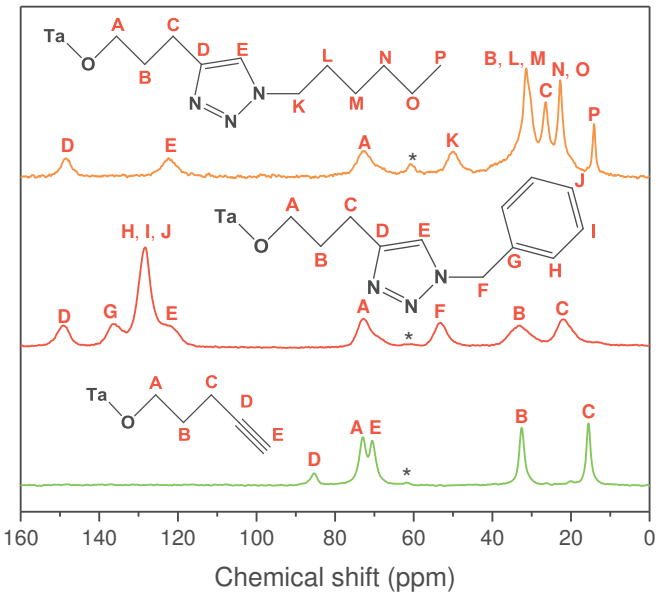

Figure EA.15. *Spectres RMN solide ^{13}C CP/MAS de alkyne-HST et de ses produits de réaction avec le 1-azidohexane ou le benzyl azide.*

Les analyses effectuées (par exemple par RMN du solide, ***Figure EA.15***) montrent le succès de l'approche de fonctionnalisation post-synthèse de HST. A notre connaissance, c'est la première fois qu'une telle stratégie est utilisée pour les pérovskites lamellaires à ion échangeable. Nous avons montré que $CuBr(PPh_3)_3$ était le catalyseur le plus adapté, car il peut être utilisé en solvant non-aqueux. Une quantité de 1% molaire de catalyseur s'est révélée suffisante pour une réaction *in situ* complète. Il s'agit de la limite inférieure des quantités rencontrées dans la littérature (1 mol % -20 mol %).[108,111,112] Dans notre cas, le problème de la quantité de catalyseur est un aspect crucial, parce que le catalyseur est susceptible de rester piégé au sein de la pérovskite lamellaire et d'être difficile à éliminer s'il est présent en grosses quantités. Son élimination est pourtant absolument nécessaire pour pouvoir caractériser les matériaux par RMN du solide. Il faut souligner que l'ajout d'une base, telle que la triéthylamine (TEA) ou la N, N-diisopropyléthylamine (DIPEA), n'a pas été nécessaire, alors que de nombreux exemples dans la littérature décrivent l'utilisation d'une base organique. [86,109,111,112] La raison d'une telle non-nécessité d'une base est pour l'instant inconnue.

La réaction CuAAC activée par micro-onde utilisée ici *in situ* est rapide et particulièrement efficace. Il faut souligner que la réaction a lieu dans l'ensemble de l'espace interlamellaire, sans limitations notables dues aux éventuelles difficultés d'accès des réactifs (azide, même

encombré) et du catalyseur. Cette stratégie complète celles utilisées jusqu'à présent pour fonctionnaliser les pérovskites lamellaires (insertion d'amine, greffage d'alcool… décrites dans les chapitres précédents. Cette approche "modification post-synthèse" permet d'envisager la fonctionnalisation des pérovskites lamellaires par un panel de molécules beaucoup plus vaste, et donc d'étendre les propriétés et les fonctionnalités des hybrides obtenus.

Dans la quatrième et dernière partie du travail, nous avons développé une voie de chimie douce pour l'insertion de métaux paramagnétiques (Cu(II) essentiellement pour l'instant). La phase d'Aurivillius $Bi_2SrTa_2O_9$ est bien connue pour ses propriétés ferroélectriques.[25] Puisque sa phase protonnée (HST) est particulièrement adaptée pour être fonctionnalisée par de nombreuses molécules, elle peut-être un candidat prometteur pour être converti en matériau multiferroïque *via* une approche chimie douce.[5,113]
Même si nous n'avons pas encore de preuve que HST est ferroélectrique (les mesures de propriétés diélectriques sur des poudres sont particulièrement délicates), nous avons montré qu'il présente une activité ONL importante (***Figure EA.16***).

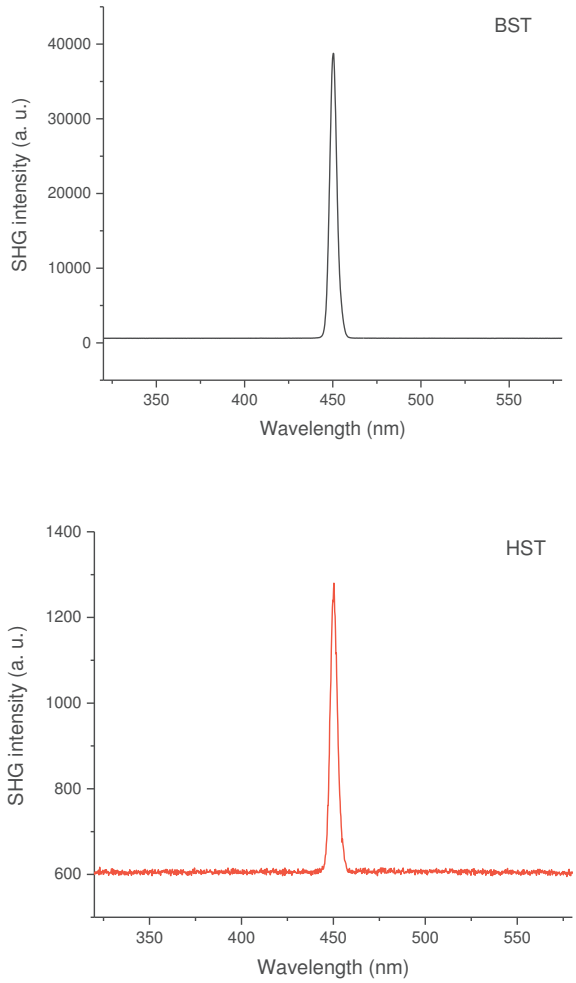

Figure EA.16. *Mesures de Génération de Seconde Harmonique pour BST (haut) et HST (bas).*

Les conditions de symétrie pour la Génération de Seconde Harmonique (GSH) sont moins restrictives que celles requises pour la ferroélectricité, l'observation de GSH est une

condition nécessaire à remplir pour qu'un compose soit ferroélectrique.[114] L'observation de GSH est donc un indice positif que HST est ferroélectrique comme le composé parent BST. Notre idée est donc ici de synthétiser de nouveaux hybrides multiferroïques par fonctionnalisation du composé potentiellement ferroélectrique HST. La première étape de cette stratégie est de conférer à HST des propriétés magnétiques, même simplement paramagnétiques. Une deuxième étape, non-abordée pendant ma thèse, sera alors la synthèse *in situ* d'un réseau ferromagnétique.
Nous avons donc décidé de préparer un précurseur HST fonctionnalisé par un ligand polydente, qui peut par la suite coordiner des métaux de transition paramagnétiques (Cu (II), Ni (II)…). Nous avons alors intercalé HST avec une polyamine commercial, la bis-(3-aminopropyl) (notée N3), en utilisant les outils développés plus haut. Le précurseur hybride N3-HST a été complètement caractérisé (***Figure EA.17***). L'idée est que les deux groupes terminaux NH_2 jouent le rôle de piliers entre les couches inorganiques, laissant l'amine secondaire centrale libre pour la coordination d'ions métalliques ou de complexes.

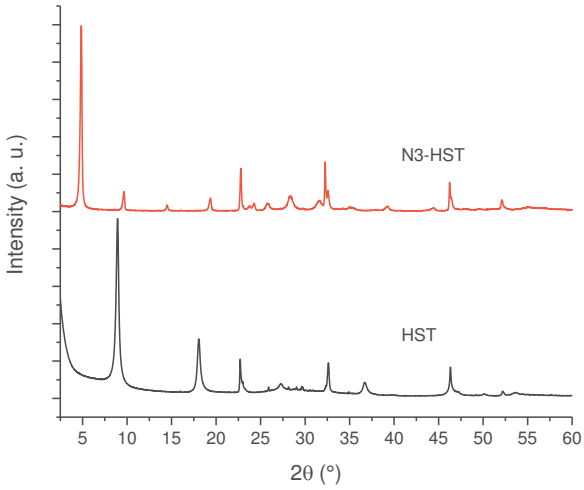

Figure EA.17. *Diagrammes de diffraction des rayons X sur poudre de HST et de N3-HST.*

Le spectre RMN ^{13}C CP/MAS NMR montre qu'il y a probablement deux formes de N3 dans l'espace interlamellaire de HST, toutes deux avec les groupes $–NH_2$ terminaux protonnés, mais une phase majoritaire où l'amine centrale est libre, et une phase minoritaire où cette amine secondaire centrale est protonnée.
Afin d'immobiliser des ions Cu(II) dans l'espace interlamellaire de HST, deux réactions différentes utilisant HST ont été menées, l'une avec $Cu(NO_3)_2{\cdot}2{,}5H_2O$, l'autre avec le complexe $CuN3(NO_3)_2$. Après réactions, un solide vert et un solide bleu sont isolés (***Figure EA.18***).

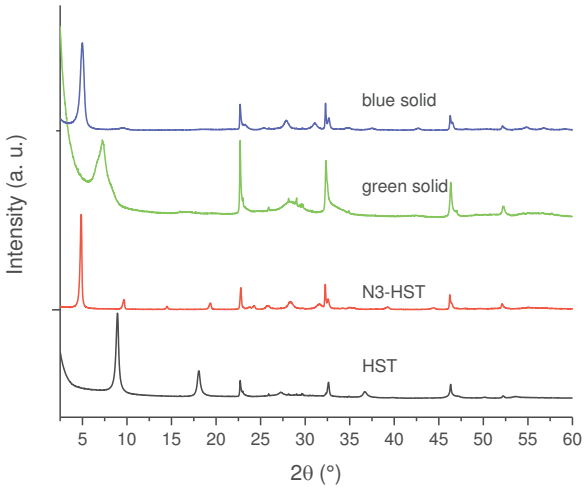

Figure EA.18. *Diagrammes de diffraction des rayons X sur poudre de HST, N3-HST, solide vert et solide bleu.*

Les diffractogrammes du solide vert et de N3-HST (***Figure EA.18***) montre que la distance interlamellaire diminue de 1,82 nm à 1,25 nm. Par ailleurs, la cristallinité est considérablement réduite. Les diffractogrammes du solide bleu et de N3-HST montrent que la distance interlamellaire diminue de 1,82 nm à 1,76 nm, sans réduction significative de la cristallinité.

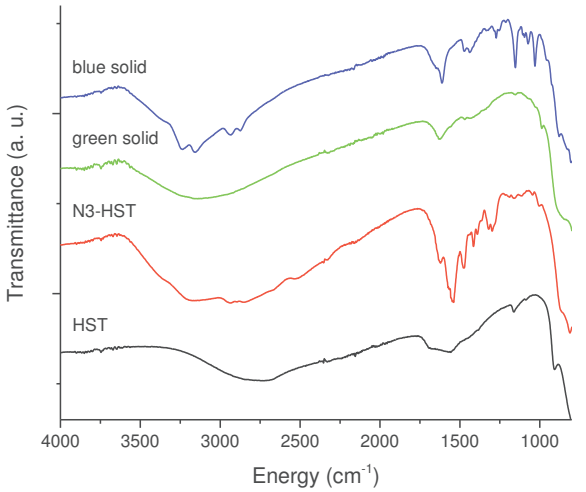

Figure EA.19. *Spectres infrarouges de HST, N3-HST, solide vert et solide bleu.*

La comparaison des spectres IR du solide vert et de N3-HST (***Figure EA.19***) montre la disparition du ligand N3. La comparaison des spectres IR du solide bleu et de N3-HST montre la rétention et la déprotonation de la polyamine N3 dans le solide bleu.

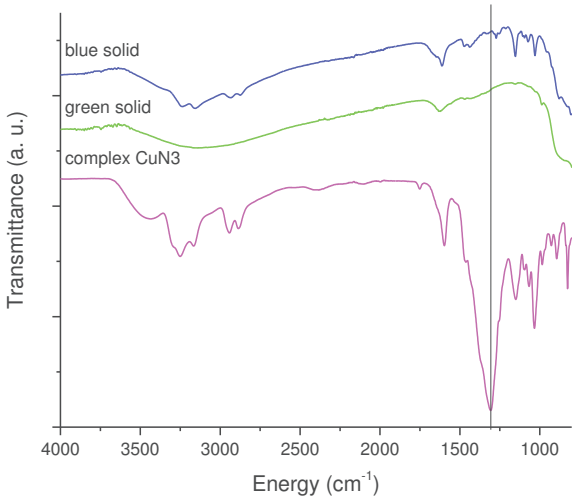

Figure EA.20. *Spectres infrarouges du solide vert, solide bleu et complexe CuN3(NO$_3$)$_2$.*

La ***Figure EA.20*** présente une comparaison des spectres IR des solides bleus et verts, ainsi que le spectre du complexe CuN3(NO$_3$)$_2$ (obtenu par evaporation à sec de la solution aqueuse correspondante sous pression réduite). La première observation marquante est la disparition dans les spectres des solides vert et bleu de la bande d'élongation des nitrates (autour de 1308 cm^{-1}), qui est pourtant très intense dans CuN3(NO$_3$)$_2$.
Si on prend en compte le nécessaire équilibre de charges, l'observation précédente indique qu'il y a un échange cationique entre le Cu(II) et les protons de HST.
De plus, l'observation détaillée des spectres du solide bleu et du complexe CuN3(NO$_3$)$_2$ montre qu'ils sont très semblables, mise à part l'absence de bandes de nitrate dans le spectre du solide bleu. Ceci indique donc que l'espèce présente dans l'espace interlamellaire du solide bleu ressemble au complexe [CuN3]$^{2+}$.
Une étude complémentaire des solides bleu et vert a été menée par spectroscopie STEM. La ***Figure EA.21*** illustre quelques vues en STEM d'un coupe du solide bleu. Les bandes sombres sont attribuées aux couches pérovskites, mais la nature de l'espèce interlamellaire n'a pas pu être clairement identifiée.

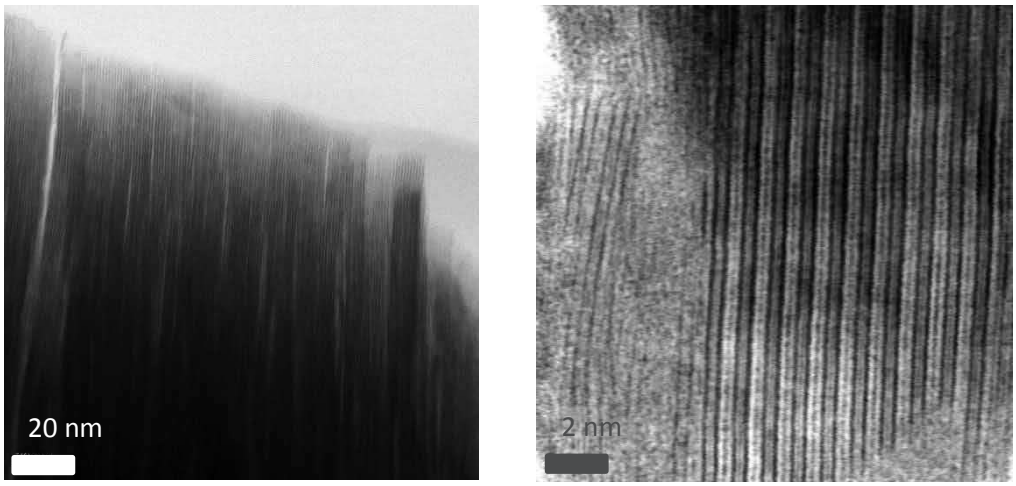

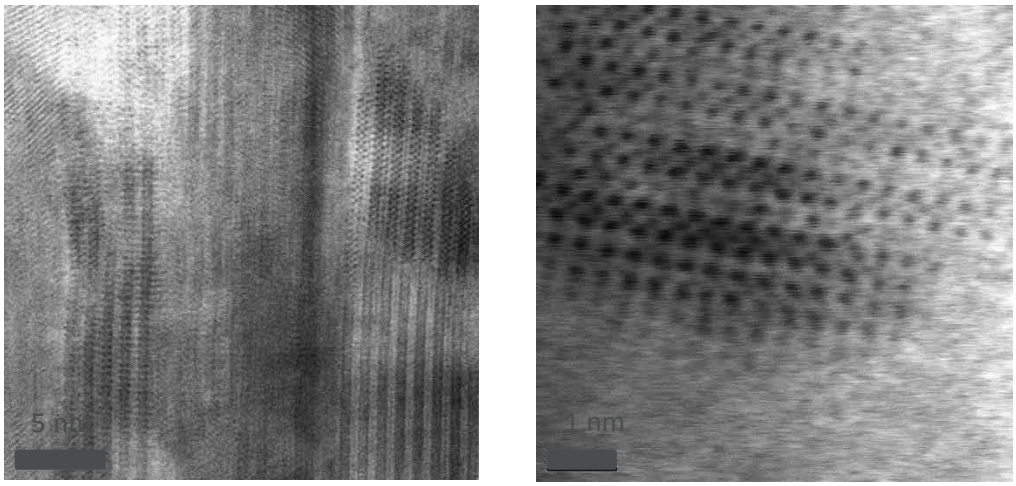

Figure EA.21. *Images STEM d'une coupe du solide bleu.*

Les analyses élémentaires des solides vert et bleu, ainsi que les observations précédentes permettent de proposer les formules suivantes : $Cu_{0.60}(C_6N_3H_{17})_{0.08}H_{0.80}Bi_{0.1}Sr_{0.85}Ta_2O_7{\cdot}4H_2O$ pour le solide vert et $Cu_{0.35}(C_6N_3H_{17})_{0.35}H_{1.30}Bi_{0.1}Sr_{0.85}Ta_2O_7{\cdot}2H_2O$ pour le solide bleu. Les analyses élémentaires confirment donc la disparition quasi-totale de N3 dans le solide vert, alors que la polyamine est encore présente dans le solide bleu. De plus, les analyses élémentaires confirment l'absence de nitrate, en accord avec les observations en spectroscopie IR. Enfin, pour le solide bleu, le rapport molaire Cu/N3 est de 1, comme pour le complexe $CuN3^{2+}$.[115,116]

Les comportements magnétiques des solides vert et bleu ont été étudiés par magnétométrie à Squid. Les mesures en température ont été effectuées sous un champ de 5000 G. Les données ont été corrigées de la contribution du porte-échantillon, et le diamagnétisme a été estimé en considérant la formule $\chi_{dia} = - M/2 \times 10^{-6}$.

La ***Figure EA.22*** montre les courbes χT = f(T) pour les solides vert et bleu. Les courbes ont été rapportée à un cuivre.

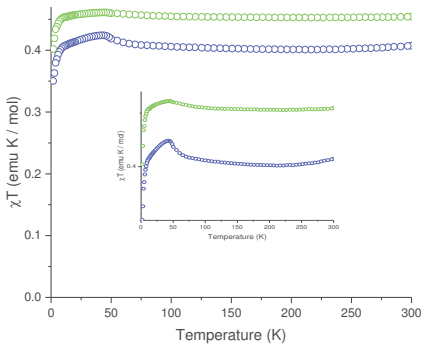

Figure EA.22. *Courbes χT = f(T) pour les solides vert et bleu sous un champ de 5000 G.*

L'ajustement des courbes 1/χ = f(T) en utilisant la loi de Curie-Weiss amène une constant de Curie de 0.45 $emu{\cdot}K{\cdot}mol^{-1}$ et 0.40 $emu{\cdot}K{\cdot}mol^{-1}$ pour les solides vert et bleu respectivement, en très bon accord avec la valeur attendue pour un ion Cu(II). A haute température du moins, les propriétés magnétiques sont donc en très accord avec les formules proposées.

Les solides vert et bleu ont des comportements magnétiques très semblables. Le produit χT augmente légèrement depuis la temperature ambiante jusque vers 50 K. Puis, quand la temperature diminue encore, le produit χT décroit d'abord légèrement, puis de manière plus

prononcée en dessous de 10 K. Pour l'instant, nous ne sommes pas parvenus à expliquer ce comportement. La légère décroissance de χT de 300 K jusque vers 200 K est très probablement due à une correction de magnétisme surévaluée.
Les courbes M = f(H) sont présentées ***Figure EA.23*** (et ramenées à 1 Cu). Elles peuvent être modélisées en utilisant une function de Brillouin, qui amène g = 2.11(5) et g = 1.95(5) pour les solides vert et bleu respectivement. Le facteur g déterminé pour le solide bleu est clairement trop petit. Ceci est probablement dû à une erreur, inévitable dans la formule élémentaire déterminée. Le fait que ces courbes M = f(H) puissent être ajustées par une loi de Brillouin en bon accord avec les formules élementaires confirme le comportement paramagnétique (avec très faible couplage) des solides vert et bleu.

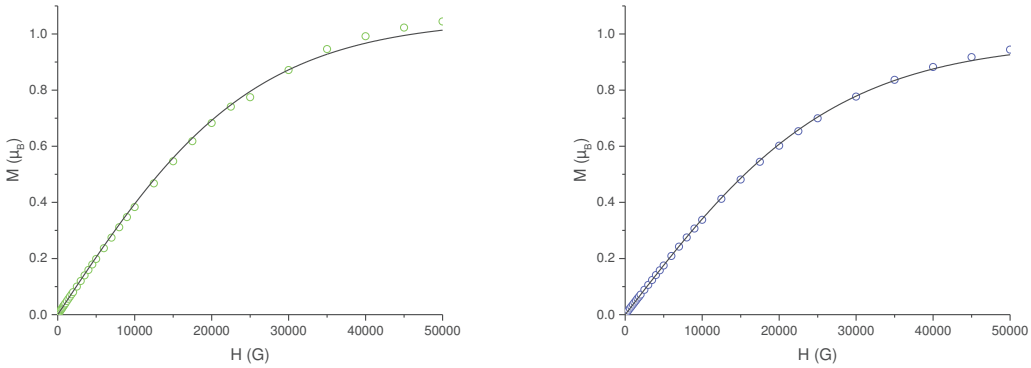

Figure EA.23. *Courbes M = f(H) pour les solides vert et bleu à 1.8 K. Les courbes en trait plein représentent les meilleurs fit aves une loi de Brillouin.*

L'environnement des ions cuivre dans les deux solides a été ensuite caractérisé par RPE onde continue et impulsionnelle (ESEEM-2P) (collaboration avec Nathalie Parizel et Philippe Turek, Institut de Chimie de Strasbourg).
Les spectres en bande X (ν ≈ 9.8 GHz) des deux composés ont été enregistrés en fonction de la température depuis la température ambiante jusque vers 10 K.
Pour le solide bleu, le spectre ne change pratiquement pas quand la température décroit (***Figure EA.24***). Il présente un seul signal, symétrique, centré autour de g = 2, et avec une largeur de raie pic à pic de environ 100 G.

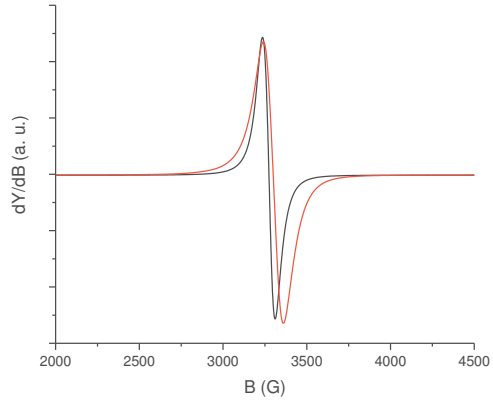

Figure EA.24. *Spectres en bande X du solide bleu à température ambiante (noir, ν = 9.546 GHz) (g = 2.083, ΔB_{pp} = 70 G) et à 10 K (rouge, ν = 9.727 GHz) (g = 2.105, ΔB_{pp} = 112 G).*

Les spectres du solide bleu sont très étroits, pas caractéristiques d'espèces Cu(II) isolées. Les ions Cu(II) interagissent de manière relativement forte entre eux (probablement *via* des interactions dipolaires).
Pour le solide vert, les spectres en bande X à temperature ambiante et à 10 K sont clairement axiaux (***Figure EA.25***). L'interaction hyperfine ne peut pas être déterminée à partir du spectre, qui est modélisé en utilisant des paramètres B_{strain} (largeur de raie résiduelle dans la simulation par une gaussienne) différents pour les parties parallèle et perpendiculaire afin de tenir compte de la non-résolution de l'interaction hyperfine.

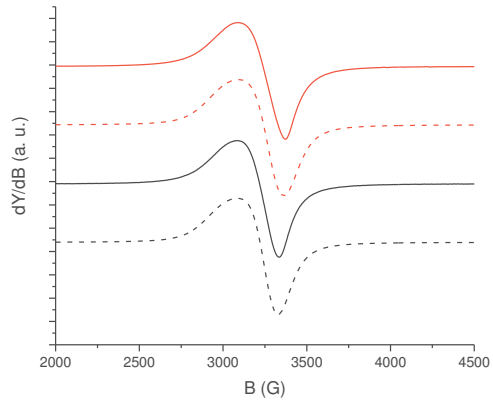

Figure EA.25. *Spectres en bande X du solide vert à température ambiante (noir, v = 9.596 GHz) et à 10 K (rouge, v = 9.744 GHz). Les lignes pleines correspondent aux spectres expérimentaux, les lignes en tirets correspondent au meilleur fit (à température ambiante : $g_{//}$ = 2.283, $g_{\perp}$ = 2.092, $Bstrain_{//}$ = 671 MHz, $Bstrain_{\perp}$ = 348 MHz, largeur de raie = 95 G t à 10 K : $g_{//}$ = 2.311, $g_{\perp}$ = 2.105, $Bstrain_{//}$ = 706 MHz, $Bstrain_{\perp}$ = 431 MHz, largeur de raie = 95 G).*

Afin de caractériser l'environnement de l'électron célibataire des ions Cu(II) détectés en RPE à onde continue, nous avons réalisé des études en RPE pulsée (ESEEM-2P) (Electron Spin Echo Envelope Modulation-2 Pulses) à 10 K. Les modulations de l'écho de Hahn sont enregistrées en fonction du l'écart temporel entre les deux pulses (at 90° and 180°). La transformée de Fourier du signal après soustraction du déclin dû à la relaxation transverse donne les fréquences des noyaux sur lesquels l'électron est délocalisé (***Figure EA.26***).

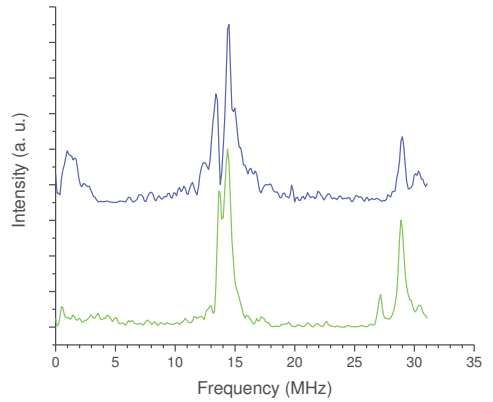

Figure EA.26. *Spectre ESEEM-2P du solid vert (vert) et du solide bleu (bleu) à 10K.*

Pour le solide bleu, le spectre ESEEM-2P montre un signal dû à ^{14}N autour de v = 1.1 MHz, avec la double résonnance autour de 2.2 MHz. De plus, on peut voir le signal de ^{1}H autour de v = 14.5 MHz, avec la double résonnance autour de 29 MHz.

En comparaison, le spectre ESEEM-2P du solide vert montre seulement le signal de ^{1}H et sa double résonnance. Par ailleurs, le signal du ^{1}H est moins large que pour le solide bleu, ce qui indique une interaction moins forte entre les ions Cu(II) et les protons. En outre, le signal de ^{14}N est clairement absent.
La RPE en onde continue et la RPE pulsée indiquent donc que dans le solid bleu, les ions Cu(II) sont entourés de N et de H (comme attendu dans le cas d'une coordination par le ligand N3) et qu'ils interagissent (probablement par interactions dipolaires). Pour le solide vert, les ions Cu(II) sont un peu plus isolés les uns des autres (en accord avec ce qui a été observé par des mesures squid), et leur environnement ne contient pas de N. Des expériences sont en cours avec des échantillon où les ions Cu(II) sont dilués.

A plus ou moins long terme, ces travaux pourront être completés par différentes expériences.
Tout d'abord, ce travail de thèse a essentiellement porté sur des problématiques de synthèse. Mais les propriétés des matériaux obtenus vont devoir désormais être étudiées. Parmi celles-ci, le potentiel caractère ferroélectrique des hybrides obtenus devra être précisément étudié (malgré le défi que cela représente).En cas de succès, on pourra alors envisager d'ajuster finement la ferroélectricité des hybrides par la fonctionnalisation de l'espace interlamellaire.
Des problèmes de caractérisation non résolus doivent aussi être traités. Par exemple, nous avons montré que la distance interlamellaire de PBA-HST dépendait des conditions expérimentales de synthèse. Cependant, nous n'avons pas encore pu obtenir d'information pertinente sur l'arrangement des molécules de PBA dans l'espace interlamellaire de HST et les raisons conduisant à de tels arrangements. Des profils de densité électronique 1D sont actuellement en court d'extraction (collaboration Christine Taviot-Guého, Institut de Chimie de Clermont-Ferrand).
Pour démontrer plus avant le caractère general de notre approche de modification post-synthèse, il faudra poursuivre le travail entamé sur l'application de la CuAAC *in situ* dans des phases de Dion-Jacobson phase telles que $HLaNb_2O_7{\cdot}xH_2O$ (HLN).
Enfin, pour les composés intercalés par du cuivre, du TEM haute résolution, ainsi que du STEM-EDX et de la spectroscopie de perte d'énergie sont actuellement en cours. Cla permettrait d'élucider la structure et la composition des hybrides obtenus avec une excellente résolution spatiale. Par ailleurs, cette approche est en cours d'extension à d'autres ions métalliques (Co, Mn, Fe, etc.).
Les perspectives à moyen terme concernent les applications de cette approche de fonctionalistion de pérovskites lamellaire à une plus large échelle.
Tout d'abord, il est possible d'étendre le champ d'étude depuis les pérovskites lamellaires 3D à des pérovskites 2D unilamellaires (nanofeuillet). Nous avons ainsi pu observer un phénomène de swelling intéressant lors de la réaction entre C_4N-HST et le propan-1-ol, selon la quantité d'eau. Il est très prometteur qu'un swelling assisté par microonde puisse être observé, car cela ouvre des perspectives pour l'exfoliation assistée par microonde, plus rapide et avec de meilleurs rendements que par les procédures classiques. Il serait éventuellement possible de mieux contrôler la taille des nanofeuillets et d'améliorer la stabilité des suspensions.
En utilisant les outils développés, il sera également envisageable d'insérer/greffer/modifier par psm ces pérovskites lamellaires par des molécules plus intéressantes, par exemple des dérivés du C_{60}, afin de préparer de nouveaux matériaux multifonctionnels.

A plus long terme, d'autres perspectives peuvent être envisagées, toujours basées sur la préparation de nouveaux objets multiferroïques, ou plus généralement multifonctionnels. Nous pouvons proposer deux stratégies. La première consisterait à obtenir des composés multiferroïque par combinaison de feuillets ferroélectriques et ferromagnétiques, par assemblage Layer by Layer, ou par chimie click. La deuxième stratégie consisterait à developper par réaction *in situ* dans l'espace interlamellaire un réseau ferromagnétique.

Bibliographie

[1] C. Delmas, Y. Borthomieu, C. Faure, *Solid State Ionics* **1988**, *26*, 152.
[2] J. Gopalakrishnan, *Chem. Mater.* **1995**, *7*, 1265-1275.
[3] D. M. Schleich, *Solid State Ionics* **1994**, *70*, 407-411.
[4] J. Rouxel, M. Tournoux, *Solid State Ionics* **1996**, *84*, 141-149.
[5] R. E. Schaak, T. E. Mallouk, *Chem. Mater.* **2002**, *14*, 1455-1471.
[6] G. A. Seisenbaeva, V. G. Kessler, *Nanoscale* **2014**, *6*, 6229-6244.
[7] C. Sanchez, G. J. d. A. A. Soler-Illia, F. Ribot, T. Lalot, C. R. Mayer, V. Cabuil, *Chem. Mater.* **2001**, *13*, 3061-3083.
[8] S. Gai, C. Li, P. Yang, J. Lin, *Chem. Rev.* **2014**, *114*, 2343-2389.
[9] P. Gomez-Romero, *Adv. Mater.* **2001**, *13*, 163-174.
[10] E. Delahaye, S. Eyele-Mezui, M. Diop, C. Leuvrey, P. Rabu, G. Rogez, *Dalton Trans.* **2010**, *39*, 10577-10580.
[11] *Functional Hybrid Materials*; P. Gómez-Romero, C. Sanchez, Eds.; Wiley-VCH: Weinheim, 2004.
[12] P. Judeinstein, C. Sanchez, *J. Mater. Chem.* **1996**, *6*, 511-525.
[13] W. Eerenstein, N. D. Mathur, J. F. Scott, *Nature* **2006**, *442*, 759-765.
[14] S.-W. Cheong, M. Mostovoy, *Nat. Mater.* **2007**, *6*, 13-20.
[15] N. A. Hill, *J. Phys. Chem. B* **2000**, *104*, 6694-6709.
[16] P. Jain, V. Ramachandran, R. J. Clark, H. D. Zhou, B. H. Toby, N. S. Dalal, H. W. Kroto, A. K. Cheetham, *J. Am. Chem. Soc.* **2009**, *131*, 13625-13627.
[17] X.-Y. Wang, L. Gan, S.-W. Zhang, S. Gao, *Inorg. Chem.* **2004**, *43*, 4615-4625.
[18] X.-Y. Wang, Z.-M. Wang, S. Gao, *Chem. Commun.* **2008**, 281-294.
[19] A. Stroppa, P. Jain, P. Barone, M. Marsman, J. M. Perez-Mato, A. K. Cheetham, H. W. Kroto, S. Picozzi, *Angew. Chem. Int. Ed.* **2011**, *50*, 5847-5850.
[20] G. Rogez, N. Viart, M. Drillon, *Angew. Chem. Int. Ed.* **2010**, *49*, 1921-1923.
[21] A. O. Polyakov, A. H. Arkenbout, J. Baas, G. R. Blake, A. Meetsma, A. Caretta, P. H. M. van Loosdrecht, T. T. M. Palstra, *Chem. Mater.* **2012**, *24*, 133-139.
[22] E. Pardo, C. Train, H. Liu, L.-M. Chamoreau, B. Dkhil, K. Boubekeur, F. Lloret, K. Nakatani, H. Tokoro, S.-i. Ohkoshi, M. Verdaguer, *Angew. Chem. Int. Ed.* **2012**, *51*, 8356-8360.
[23] B. Kundys, A. Lappas, M. Viret, V. Kapustianyk, V. Rudyk, S. Semak, C. Simon, I. Bakaimi, *Phys. Rev. B* **2010**, *81*, 224434.
[24] P. Rabu, M. Drillon, *Adv. Eng. Mater.* **2003**, *5*, 189-210.
[25] E. C. Subbarao, *J. Phys. Chem. Solids* **1962**, *23*, 665-676.
[26] S. M. Blake, M. J. Falconer, M. McCreedy, P. Lightfoot, *J. Mater. Chem.* **1997**, *7*, 1609-1613.
[27] N. C. Bristowe, J. Varignon, D. Fontaine, E. Bousquet, P. Ghosez, *Nat. Commun.* **2015**, *6*.
[28] C. A. P. de Araujo, J. D. Cuchiaro, L. D. McMillan, M. C. Scott, J. F. Scott, *Nature* **1995**, *374*, 627-629.
[29] K. Amanuma, T. Hase, Y. Miyasaka, *Appl. Phys. Lett.* **1995**, *66*, 221-223.
[30] A. Kingon, *Nature* **1999**, *401*, 658-659.
[31] H. Abid, A. Samet, T. Dammak, A. Mlayah, E. K. Hlil, Y. Abid, *J. Lumin.* **2011**, *131*, 1753-1757.
[32] A. Kojima, K. Teshima, Y. Shirai, T. Miyasaka, *J. Am. Chem. Soc.* **2009**, *131*, 6050-6051.
[33] M. Kudo, S. Tsuzuki, K.-i. Katsumata, A. Yasumori, Y. Sugahara, *Chem. Phys. Lett.* **2004**, *393*, 12-16.
[34] K. Gurunathan, P. Maruthamuthu, *J. Solid State Electrochem.*, *2*, 176-180.
[35] S. Kataoka, S. Banerjee, A. Kawai, Y. Kamimura, J.-C. Choi, T. Kodaira, K. Sato, A. Endo, *J. Am. Chem. Soc.* **2015**, *137*, 4158-4163.
[36] J. Boltersdorf, N. King, P. A. Maggard, *CrystEngComm* **2015**, *17*, 2225-2241.
[37] Z. Tong, G. Zhang, S. Takagi, T. Shimada, H. Tachibana, H. Inoue, *Chem. Lett.* **2005**, *34*, 632-633.

[38] K. G. Sanjaya Ranmohotti, E. Josepha, J. Choi, J. Zhang, J. B. Wiley, *Adv. Mater.* **2011**, *23*, 442-460.
[39] P. Jain, V. Ramachandran, R. J. Clark, H. D. Zhou, B. H. Toby, N. S. Dalal, H. W. Kroto, A. K. Cheetham, *J. Am. Chem. Soc.* **2009**, *131*, 13625-13627.
[40] Y. Tsunoda, M. Shirata, W. Sugimoto, Z. Liu, O. Terasaki, K. Kuroda, Y. Sugahara, *Inorg. Chem.* **2001**, *40*, 5768-5771.
[41] S. M. Blake, M. J. Falconer, M. McCreedy, P. Lightfoot, *J. Mater. Chem.* **1997**, *7*, 1609-1613.
[42] W. Sugimoto, M. Shirata, Y. Sugahara, K. Kuroda, *J. Am. Chem. Soc.* **1999**, *121*, 11601-11602.
[43] Z. Peng, X. Xing, X. Chen, *J. Alloys Compd.* **2006**, *425*, 323-328.
[44] Y. Tsunoda, W. Sugimoto, Y. Sugahara, *Chem. Mater.* **2003**, *15*, 632-635.
[45] S. Tahara, T. Yamashita, G. Kajiwara, Y. Sugahara, *Chem. Lett.* **2006**, *35*, 1292-1293.
[46] J. Demel, J. Hynek, P. Kovář, Y. Dai, C. Taviot-Guého, O. Demel, M. Pospíšil, K. Lang, *J. Phys. Chem. C* **2014**, *118*, 27131-27141.
[47] I. Fujita, K. Kuroda, M. Ogawa, *Chem. Mater.* **2003**, *15*, 3134-3141.
[48] J. J. Tunney, C. Detellier, *J. Mater. Chem.* **1996**, *6*, 1679-1685.
[49] J.-H. Choy, J.-B. Yoon, D.-K. Kim, S.-H. Hwang, *Inorg. Chem.* **1995**, *34*, 6524-6531.
[50] S. Bruzaud, G. Levesque, *Chem. Mater.* **2002**, *14*, 2421-2426.
[51] P. M. Forster, M. M. Tafoya, A. K. Cheetham, *J. Phys. Chem. Solids* **2004**, *65*, 11-16.
[52] S. Si, A. Taubert, A. Mantion, G. Rogez, P. Rabu, *Chem. Sci.* **2012**, *3*, 1945-1957.
[53] S. Eyele-Mezui, E. Delahaye, G. Rogez, P. Rabu, *Eur. J. Inorg. Chem.* **2012**, *2012*, 5225-5238.
[54] E. Ruiz-Hitzky, *Chem. Record* **2003**, *3*, 88-100.
[55] P. V. Der Voort, E. F. Vansant, *J. Liq. Chromatogr.Relat. Technol.* **1996**, *19*, 2723-2752.
[56] Y. Wang, C. Wang, L. Wang, Q. Hao, X. zhu, X. Chen, K. Tang, *RSC Adv.* **2014**, *4*, 4047-4054.
[57] S. Akbarian-Tefaghi, E. Teixeira Veiga, G. Amand, J. B. Wiley, *Inorg. Chem.* **2016**, *55*, 1604-1612.
[58] H. Suzuki, K. Notsu, Y. Takeda, W. Sugimoto, Y. Sugahara, *Chem. Mater.* **2003**, *15*, 636-641.
[59] S. Tahara, Y. Sugahara, *Langmuir* **2003**, *19*, 9473-9478.
[60] S. Tahara, T. Ichikawa, G. Kajiwara, Y. Sugahara, *Chem. Mater.* **2007**, *19*, 2352-2358.
[61] T. Itagaki, K. Kuroda, *J. Mater. Chem.* **2003**, *13*, 1064-1068.
[62] J. Murakami, T. Itagaki, K. Kuroda, *Solid State Ionics* **2004**, *172*, 279-282.
[63] S. Hotta, N. Idota, Y. Sugahara, *Key Engineering Materials* **2014**, *616*, 82-86.
[64] C. Wang, K. Tang, D. Wang, Z. Liu, L. Wang, Y. Zhu, Y. Qian, *J. Mater. Chem.* **2012**, *22*, 11086-11092.
[65] N. Toihara, Y. Yoneyama, A. Shimada, S. Tahara, Y. Sugahara, *Dalton Trans.* **2015**, *44*, 3002-3008.
[66] F. Geng, R. Ma, Y. Ebina, Y. Yamauchi, N. Miyamoto, T. Sasaki, *J. Am. Chem. Soc.* **2014**, *136*, 5491-5500.
[67] B. F. Hoskins, R. Robson, *J. Am. Chem. Soc.* **1990**, *112*, 1546-1554.
[68] J. S. Seo, D. Whang, H. Lee, S. I. Jun, J. Oh, Y. J. Jeon, K. Kim, *Nature* **2000**, *404*, 982-986.
[69] S. M. Cohen, *Chem. Rev.* **2012**, *112*, 970-1000.
[70] K. K. Tanabe, S. M. Cohen, *Chem. Soc. Rev.* **2011**, *40*, 498-519.
[71] Z. Wang, S. M. Cohen, *Chem. Soc. Rev.* **2009**, *38*, 1315-1329.
[72] V. Valtchev, G. Majano, S. Mintova, J. Perez-Ramirez, *Chem. Soc. Rev.* **2013**, *42*, 263-290.
[73] D. Bruhwiler, *Nanoscale* **2010**, *2*, 887-892.
[74] A. Mehdi, C. Reye, R. Corriu, *Chem. Soc. Rev.* **2011**, *40*, 563-574.
[75] J. Zhu, A. B. Morgan, F. J. Lamelas, C. A. Wilkie, *Chem. Mater.* **2001**, *13*, 3774-3780.
[76] D. R. Robello, N. Yamaguchi, T. Blanton, C. Barnes, *J. Am. Chem. Soc.* **2004**, *126*, 8118-8119.
[77] M. W. Weimer, H. Chen, E. P. Giannelis, D. Y. Sogah, *J. Am. Chem. Soc.* **1999**, *121*, 1615-1616.
[78] E. Coronado, C. Martí-Gastaldo, E. Navarro-Moratalla, A. Ribera, *Inorg. Chem.* **2010**, *49*, 1313-1315.
[79] G. Layrac, D. Tichit, J. Larionova, Y. Guari, C. Guérin, *J. Phys. Chem. C* **2011**, *115*, 3263-3271.
[80] O. Palamarciuc, E. Delahaye, P. Rabu, G. Rogez, *New J. Chem.* **2014**, *38*, 2016-2023.

[81] S. Yoshioka, Y. Takeda, Y. Uchimaru, Y. Sugahara, *J. Organomet. Chem.* **2003**, *686*, 145-150.
[82] *Chem. Soc. Rev.* **2010**, *39*, Applications of click chemistry themed issue.
[83] C. O. Kappe, *Chem. Soc. Rev.* **2008**, *37*, 1127-1139.
[84] C. O. Kappe, A. Stadler, D. Dallinger, *Microwaves in Organic and Medicinal Chemistry, 2nd edition*; Wiley-VCH, 2012.
[85] W. J. Sommer, M. Weck, *Langmuir* **2007**, *23*, 11991-11995.
[86] F. Amblard, J. H. Cho, R. F. Schinazi, *Chem. Rev.* **2009**, *109*, 4207-4220.
[87] K. Bürglová, N. Moitra, J. Hodačová, X. Cattoën, M. Wong Chi Man, *J. Org. Chem.* **2011**, *76*, 7326-7333.
[88] R. Guezguez, K. Bougrin, K. El Akri, R. Benhida, *Tetrahedron Lett.* **2006**, *47*, 4807-4811.
[89] T. Gadzikwa, G. Lu, C. L. Stern, S. R. Wilson, J. T. Hupp, S. T. Nguyen, *Chem. Commun.* **2008**, 5493-5495.
[90] C. Liu, T. Li, N. L. Rosi, *J. Am. Chem. Soc.* **2012**, *134*, 18886-18888.
[91] F.-G. Xi, H. Liu, N.-N. Yang, E.-Q. Gao, *Inorg. Chem.* **2016**, *55*, 4701-4703.
[92] P.-Z. Li, X.-J. Wang, J. Liu, J. S. Lim, R. Zou, Y. Zhao, *J. Am. Chem. Soc.* **2016**, *138*, 2142-2145.
[93] S. Castellanos, K. B. Sai Sankar Gupta, A. Pustovarenko, A. Dikhtiarenko, M. Nasalevich, P. Atienzar, H. García, J. Gascon, F. Kapteijn, *Eur. J. Inorg. Chem.* **2015**, *2015*, 4648-4652.
[94] S. Wu, L. Chen, B. Yin, Y. Li, *Chem. Commun.* **2015**, *51*, 9884-9887.
[95] X.-C. Yi, F.-G. Xi, Y. Qi, E.-Q. Gao, *RSC Adv.* **2015**, *5*, 893-900.
[96] Y. Wang, E. Delahaye, C. Leuvrey, F. Leroux, P. Rabu, G. Rogez, *Inorg. Chem.* **2016**, *55*, 4039-4046.
[97] G. Chouhan, K. James, *Org. Lett.* **2013**, *15*, 1206-1209.
[98] A. Shimada, Y. Yoneyama, S. Tahara, P. H. Mutin, Y. Sugahara, *Chem. Mater.* **2009**, *21*, 4155-4162.
[99] F. Himo, T. Lovell, R. Hilgraf, V. V. Rostovtsev, L. Noodleman, K. B. Sharpless, V. V. Fokin, *J. Am. Chem. Soc.* **2005**, *127*, 210-216.
[100] P. Appukkuttan, W. Dehaen, V. V. Fokin, E. Van der Eycken, *Org. Lett.* **2004**, *6*, 4223-4225.
[101] G. A. Molander, J. Ham, *Org. Lett.* **2006**, *8*, 2767-2770.
[102] Z. Li, R. Bittman, *J. Org. Chem.* **2007**, *72*, 8376-8382.
[103] C. W. Tornøe, C. Christensen, M. Meldal, *J. Org. Chem.* **2002**, *67*, 3057-3064.
[104] D. Giguere, R. Patnam, M.-A. Bellefleur, C. St-Pierre, S. Sato, R. Roy, *Chem. Commun.* **2006**, 2379-2381.
[105] D. Font, C. Jimeno, M. A. Pericàs, *Org. Lett.* **2006**, *8*, 4653-4655.
[106] P. G. Andersson, H. E. Schink, K. Österlund, *J. Org. Chem.* **1998**, *63*, 8067-8070.
[107] Y. Liu, D. D. Díaz, A. A. Accurso, K. B. Sharpless, V. V. Fokin, M. G. Finn, *J. Polym. Sci.* **2007**, *45*, 5182-5189.
[108] J. E. Hein, V. V. Fokin, *Chem Soc Rev.* **2010**, *39*, 1302-1315.
[109] D. Toulemon, B. P. Pichon, C. Leuvrey, S. Zafeiratos, V. Papaefthimiou, X. Cattoën, S. Bégin-Colin, *Chem. Mater.* **2013**, *25*, 2849-2854.
[110] J. E. Hein, V. V. Fokin, *Chem. Soc. Rev.* **2010**, *39*, 1302-1315.
[111] M. I. Montañez, Y. Hed, S. Utsel, J. Ropponen, E. Malmström, L. Wågberg, A. Hult, M. Malkoch, *Biomacromolecules* **2011**, *12*, 2114-2125.
[112] M. Meldal, C. W. Tornøe, *Chem. Rev.* **2008**, *108*, 2952-3015.
[113] M. Figlarz, B. Gérand, A. Delahaye-Vidal, B. Dumont, F. Harb, A. Coucou, F. Fievet, *Solid State Ionics* **1990**, *43*, 143-170.
[114] P. S. Halasyamani, K. R. Poeppelmeier, *Chem. Mater.* **1998**, *10*, 2753-2769.
[115] M. H. Robbins, R. S. Drago, *Journal of Catalysis* **1997**, *170*, 295-303.
[116] E. Kimura, A. Sakonaka, M. Nakamoto, *Biochimica et Biophysica Acta (BBA) - General Subjects* **1981**, *678*, 172-179.

Yanhui WANG

Hybridation d'oxydes lamellaires: de l'insertion à la synthèse *in situ*

Résumé

Dans cette thèse, nous avons développé l'utilisation de l'activation microondes pour fonctionnaliser des pérovskites lamellaires et notamment la phase d'Aurivillius $Bi_2SrTa_2O_9$ (BST), connue pour ses propriétés ferroélectriques. Nous sommes parvenus à protoner cette phase (HST) et à la fonctionnaliser par diverses amines et polyamines, avec des temps de réaction considérablement réduits par rapport aux fonctionnalisations en conditions classiques. Cette approche nous a permis de fonctionnaliser HST par des amines plus encombrées et plus complexes. Cette stratégie a ensuite été étendue au greffage d'alcools et de polyols. Nous avons également établi une stratégie de modification post-synthèse, pour synthétiser *in situ* la molécule désirée, en utilisant la chimie "click" et l'activation microondes. Enfin, nous sommes parvenus à insérer des ions métalliques et des complexes de métaux de transition, ce qui constitue une première étape vers la synthèse de nouveaux hybrides multiferroïques.

Mots-clés: pérovskites lamellaires, synthèse micro-onde, modification post-synthèse, chimie click

Abstract

During this PhD thesis, we have developed the use of microwave activation to functionalize layered perovskites, among which the Aurivillius phase $Bi_2SrTa_2O_9$ (BST), known for its ferroelectric properties. We managed to protonate this phase (leading to HST) and to functionalize it by various amines and polyamines, with reaction times much shorter than using classical conditions. This approach allowed us to functionalize HST by bulkier and more complex amines. This strategy has further been extended to the grafting of alcohols and polyols. We have also established a post-synthesis modification strategy, in order to synthesize the desired molecule *in situ*, within the interlamellar space, using "click" chemistry and microwave activation. Finally, we managed to insert transition metal ions and complexes, which constitutes a promising step towards the synthesis of new multiferroic hybrid materials.

Keywords: layered perovskites, microwave synthesis, post-synthesis modification, click chemistry